WIDEBAND PHASED ARRAY

&

RECTENNA DESIGN AND MODELING FOR

WIRELESS POWER TRANSMISSION

A Dissertation

by

JONATHAN NOEL HANSEN

Submitted to the Office of Graduate Studies of
Texas A&M University
in partial fulfillment of the requirements for the degree of

DOCTOR OF PHILOSOPHY

December 2011

Major Subject: Electrical Engineering

Wideband Phased Array &

Rectenna Design and Modeling for Wireless Power Transmission

WIDEBAND PHASED ARRAY

&

RECTENNA DESIGN AND MODELING FOR

WIRELESS POWER TRANSMISSION

A Dissertation

by

JONATHAN NOEL HANSEN

Submitted to the Office of Graduate Studies of
Texas A&M University
in partial fulfillment of the requirements for the degree of

DOCTOR OF PHILOSOPHY

Approved by:

Chair of Committee,	Kai Chang
Committee Members,	Krzysztof Michalski
	Laszlo Kish
	Kenith Meissner
Head of Department,	Costas Georghiades

December 2011

Major Subject: Electrical Engineering

ABSTRACT

Wideband Phased Array &

Rectenna Design and Modeling for Wireless Power Transmission.

(December 2011)

Jonathan Noel Hansen, B.S., Texas A&M University

Chair of Advisory Committee: Dr. Kai Chang

Microstrip patch antennas are the most common type of printed antenna due to a myriad of advantages which encourage use in a wide range of applications such as: wireless communication, radar, satellites, remote sensing, and biomedicine. An initial design for a stacked-patch, broadband, dual-polarized, aperture-fed antenna is tested, and some adjustments are made to improve performance. The design goal is to obtain a 3 GHz bandwidth centered at 10 GHz for each polarization.

Once the single-element design is finalized, it is used in a 4x1 array configuration. An array increases the gain, and by utilizing variable phase-shifters to each element, the pattern can be electronically steered in a desired direction. The phase-shifters are controlled by a computer running LabVIEW so that the array's steering angle can be easily adjusted. The result of this new phased array design is a wide bandwidth system with dual-polarization which can be electronically steered.

Rectennas (rectifying antennas) are used in wireless power transmission (WPT) systems to collect microwave power and convert this power into useable DC power.

They find use in many areas such as space power transmission, RFID tags, wireless sensors, and recycling ambient microwave energy.

The ability to simulate rectenna designs will allow for an easier method of analysis and tuning without the time and expense of repetitive fabrication and measurement. The most difficult part of rectenna simulation is a good diode model, and since different diodes have dissimilar properties, a model must be specific to a particular diode. Therefore, a method of modeling an individual diode is the most critical part of rectenna simulation. A diode modeling method which is based on an equivalent circuit and compatible with harmonic balance simulation is developed and presented. The equivalent circuit parameters are determined from a series of S-parameter measurements, and the final model demonstrates S-parameters in agreement with the measured data.

An aperture-coupled, high-gain, single-patch rectenna is also designed and measured. This rectenna is modeled using the presented method, and the simulation shows good agreement with the measured results. This further validates the proposed modeling technique.

ACKNOWLEDGEMENTS

I would like to express my appreciation to Dr. Kai Chang for his guidance and support throughout my graduate studies and research at Texas A&M University. I would also like to thank Dr. Michalski, Dr. Kish, and Dr. Meissner for serving on my committee and for their helpful comments.

I am grateful to Mr. Li and other members of the Electromagnetic and Microwaves Laboratory at Texas A&M University for their invaluable technical assistance. I also want to extend my gratitude for the generous support of Raytheon and the guidance of Dr. James McSpadden throughout the phased array project.

Lastly, I would like to thank my family, especially my father, who has been a continuing source of guidance, support, and encouragement.

TABLE OF CONTENTS

Page

Page

LIST OF FIGURES

Page

Page

Page

Page

Page

LIST OF TABLES

1. INTRODUCTION

This dissertation is divided into two main topics. The first topic covers the design of a patch antenna and the subsequent development of this antenna into a phased array system. The second topic discusses rectenna theory, design, and modeling.

Section 2 discusses the design of a stacked-patch, broadband, dual-polarized, aperture-fed antenna. Background on patch antennas and the utilized design features are given, and reasons for all design decisions are addressed. Design goals, fabrication techniques, and measurement results which characterize the final design are also discussed.

Section 3 presents background information on array theory. Advantages of phased arrays are first discussed, followed by a brief mathematical description of how they operate. A few characteristics of phased arrays are addressed, and finally a discussion of design choices which will affect these characteristics is given.

Section 4 discusses the development of a phased array system which utilizes the single-element antenna designed in Section 2. A 4x1 array configuration is created which requires a power divider to be designed and fabricated to properly distribute power to each of the antenna elements. Phase-shifters must also be integrated into the system in order to control the phased array, and these phase-shifters are controlled by using LabVIEW to control a Data Acquisition (DAQ) device which is linked to a

---

This dissertation follows the style of *IEEE Transactions on Microwave Theory and Techniques*.

connector box and a logic-conversion circuit. The phased array is integrated into a useable system, calibrated, and measured for various settings. The results are then analyzed and discussed.

Section 5 gives a history of rectennas and their use in wireless power transmission systems. A definition for the term "rectenna" is first given, and some typical applications of rectennas are listed. A chronological history of rectenna development is then provided, starting with Hertz and Tesla in the 1800's and concluding with today's interest in a space solar-power satellite.

Section 6 provides a theoretical discussion of rectenna and wireless power transmission technology. The wireless power transmission system as a whole is first discussed, and the rectenna is then described in more detail. A rectenna is analogous to a half-wave rectifier, so a mathematical explanation of this is provided. An analytical model of rectenna efficiency is also derived and presented. The section concludes with a discussion on the effect of input power and diode selection.

Section 7 discusses rectenna simulation and its impact on rectenna design. A rectenna model is then proposed which will aid in simulation and simplify rectenna analysis and tuning. The model is based on a series of S-parameter measurements which allow the extraction of equivalent circuit model parameters. The final model is analyzed for usability and its match to the measurements on which it is based.

Section 8 proposes a new rectenna design and discusses its design, fabrication, and measurement. The new design is also modeled using the method proposed in

Section 7, and the simulation results are compared to the measured results to further validate the proposed rectenna model.

Section 9 concludes this dissertation with a summary, a discussion of accomplishments, and recommendations for future work.

The appendices provide LabVIEW and Matlab code developed to aid in the work presented here.

2. SINGLE-ELEMENT ANTENNA DEVELOPMENT

A. Background

The microstrip patch antenna is widely used because of its many advantages and is "often described as one of the most exciting developments in antenna and electromagnetic history [1]." These advantages include: lightweight, small size, conformability, easy fabrication, low cost, efficiency, and simple integration with microwave integrated circuits. However, there are some disadvantages which include: narrow impedance bandwidth, low gain, and the excitation of surface waves (decreases efficiency) [1]-[4]. A thorough history can be found in [1].

Radiation of the microstrip patch antenna is determined from the electromagnetic field distribution between the patch and the ground plane. The radiation can also be described in terms of the surface currents which exist on the patch [2]. Radiation arises from discontinuities at the patch edges, and resonance is created when the patch length is approximately a half-wavelength. However, some of the field extends outside the bounds of the physical patch. This is called the fringing effect, and it causes the patch to behave slightly larger than its physical dimensions. The length of the patch can be approximated as [5]

$$L \approx 0.49\lambda_d = 0.49\frac{\lambda_0}{\sqrt{\varepsilon_r}} \tag{2.1}$$

where λ_d is the wavelength in the dielectric, λ_0 is the free space wavelength, and ε_r is the relative permittivity of the dielectric.

Stacked patches can be used to increase the bandwidth. By stacking a parasitic patch (of different size) on top of the fed patch, two resonant frequencies will now exist as a result of the two different sized patches. This will effectively widen the bandwidth [6].

The most common methods of feeding early microstrip antennas were by means of a microstrip line contacting the patch edge or a coaxial probe extending through the ground plane and contacting the patch. However, microstrip feeds promote spurious radiation which limits bandwidth [4], and coaxial probes require long probes which increase spurious radiation from the probe, amplify surface waves, and increase feed inductance [2]. Microstrip feeds and coaxial probes also produce cross-polarized radiation due to inherent asymmetries which produce higher order modes [4]. Alternatively, an aperture-coupled feed electromagnetically couples from a microstrip line on the lower substrate to the patch through an aperture in the ground plane. This method isolates the feedline from the patch so that the feedline does not interfere with the radiating element (due to the shielding effect of the ground plane). This also has the benefit of increasing polarization purity. Coupling and bandwidth can be improved by adjusting the shape and size of the aperture, the feedline dimensions, and the stub length [2]. It has been shown that the best coupling is achieved when the aperture is in the shape of a bowtie [7].

Substrate choice is an important design decision. In general, substrates with a lower dielectric constant will give higher efficiency and a larger bandwidth. Also, as substrate thickness is increased, bandwidth tends to increase while efficiency decreases [8]. Therefore, tradeoffs must be made in selecting a suitable substrate.

Polarization of a wave is described by the direction of the electric field as time advances. If the electric field is oriented in a single direction then the wave is linearly polarized; if it rotates as time advances then the wave is circularly or elliptically polarized [3]-[4]. Dual linear polarization indicates that the wave is composed of two independent orthogonal linear polarizations. An antenna with dual-polarization allows two separate signals to be transmitted or received on the same antenna. Since both polarizations should operate at the same frequency bandwidth, both dimensions of the patch should be the same length. This has a negative effect on the bandwidth of the antenna since unequal dimensions of a patch can be used to increase bandwidth [9].

B. Initial Design

The design goals are to create a flat-panel, dual-polarized antenna which is centered at 10 GHz and has a 3 GHz bandwidth. A high cross-polarization isolation of greater than 20 dB is also desirable.

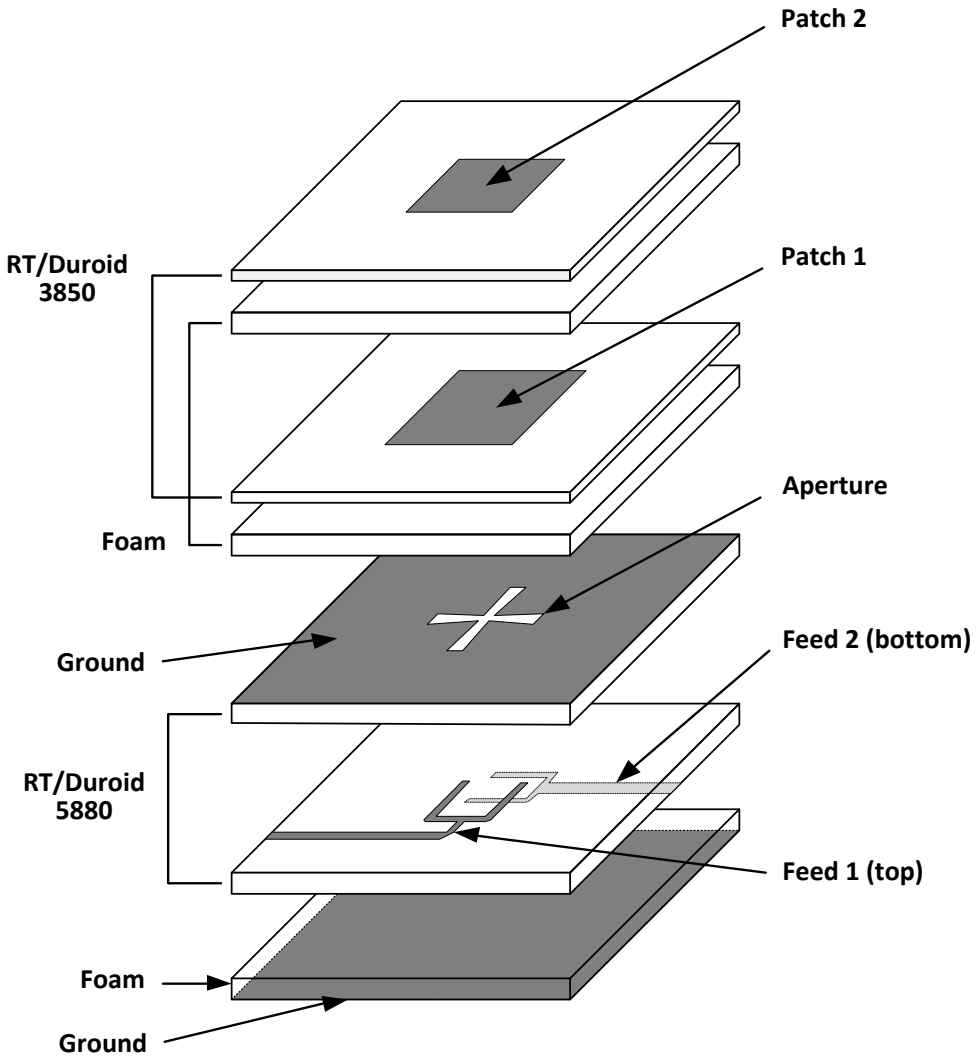

Figure 2.1. Single-element design (stacked-patch, aperture-fed, dual-polarized stripline).

The initial design of the single-element antenna [10] is a stacked-patch, aperture-fed, dual-polarized stripline design which is illustrated in Fig. 2.1. The patches are etched on 2 mil RT/Duroid 3850 substrate with a dielectric constant of 2.9. The top patch is supported by a 1.6 mm thick layer of lightweight foam, and the bottom patch is supported by a 3.2 mm thick layer of the same foam. This foam (Cuming C-FOAM PF-4/PSA) is specially made for microwave applications and has a low dielectric constant of 1.06. The apertured-ground plane and the feedlines are etched on 20 mil RT/Duroid 5880 substrate with a dielectric constant of 2.2. This places the top feed 20 mil from the apertured-ground plane and the bottom feed 40 mil from the apertured-ground plane.

There is also a second ground plane for the stripline design which is separated from the bottom feed by a 4.8 mm thick layer of the previously mentioned foam. The stripline scheme provides ground planes on both sides of the feedlines thereby shielding them from outside influences. The stripline structure also confines all of the electromagnetic field to the dielectric which allows it to support TEM waves and higher order TM/TE modes. This is in contrast to the microstrip design which has only one ground plane; this permits some of its field to exist in the air surrounding the dielectric which prevents the microstrip line from supporting pure TEM waves [11]. The downside to the stripline scheme is that since the field is distributed between two ground planes, the coupling through the aperture is reduced. However, by separating the second ground plane from the feedlines by a thick 4.8 mm layer of foam, most of the field is distributed toward the apertured-ground plane. This retains some of the benefit of a stripline feed while still maintaining good coupling through the aperture.

Dual-offset feedlines are used to improve impedance matching and decrease coupling between the feeds which reduces cross-polarization [9]. This feeding method also allows both feeds to share a single aperture. The feeding design can be seen in Fig. 2.2. It uses a simple two-way power divider with a mitered junction to split the power between the two feeds. The single input is a 50 Ω line which is split into two 100 Ω lines. Rather than extending straight to the edge of the structure as feed 2 does, feed 1 makes a 90° turn so that it exits the structure on the opposite side from feed 1. This is to ease its use in an array in which the feeds must exit on opposite sides.

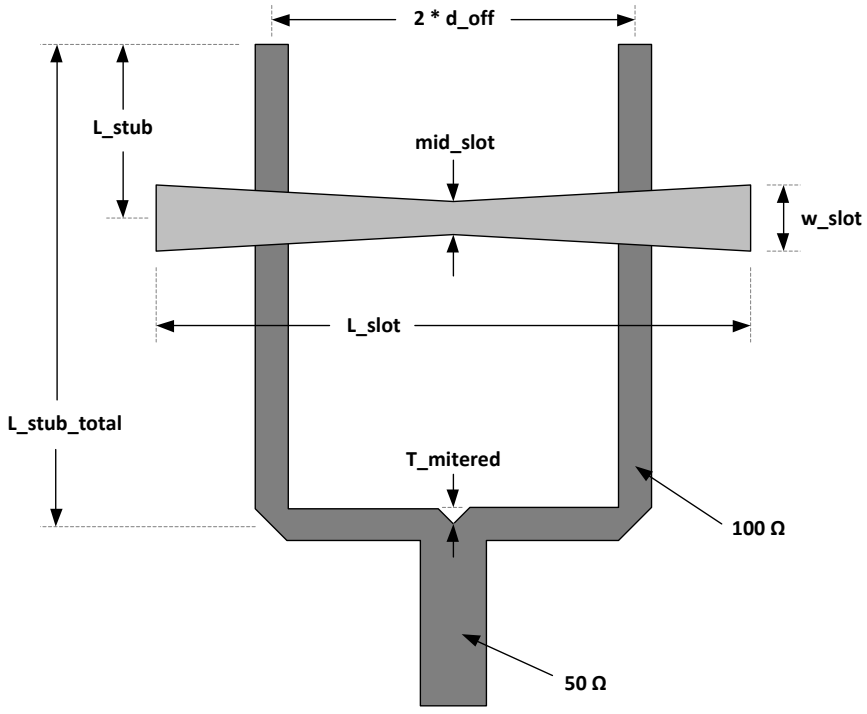

Figure 2.2. Dual-offset feedline with a bowtie aperture.

The design is tuned for a center frequency of 10 GHz and wide bandwidth. The dimensions of this design are given in Table 2.1.

Table 2.1. Initial antenna design parameters.

Variable	**Value**	**Variable**	**Value**
Height of feed 1 (top) substrate (h_feed1)	0.508 mm	Feed 1 (top) matching stub length (L_stub1)	1.98 mm
Height of feed 2 (bottom) substrate (h_feed2)	0.508 mm	Feed 2 (bottom) matching stub length (L_stub2)	2.07 mm
Height of patch 1 (bottom) foam (h_ant1)	3.2 mm	Feed 1 (top) total matching stub length (L_stub_total1)	8.6215 mm
Height of patch 2 (top) foam (h_ant2)	1.6 mm	Feed 2 (bottom) total matching stub length (L_stub_total2)	9.0165 mm
Feed 1 (top) width (100 Ω) (f1w_100)	0.403 mm	Aperture 1 length (L_slot1)	9.75 mm
Feed 1 (top) width (50 Ω) (f1w_50)	1.578 mm	Aperture 1 end-width (w_slot1)	1 mm
Feed 2 (bottom) width (100 Ω) (f2w_100)	1.013 mm	Aperture 1 mid-width (mid_slot1)	0.6 mm
Feed 2 (bottom) width (50 Ω) (f2w_50)	3.3 mm	Aperture 2 length (L_slot2)	10 mm
Offset feed 1 (top) separation (d_off1)	2.5 mm	Aperture 2 end-width (w_slot2)	1 mm
Offset feed 2 (bottom) separation (d_off2)	2.5 mm	Aperture 2 mid-width (mid_slot2)	0.6 mm
Mitered T-Junction Feed 1(top) (T1_mitered)	0.2015 mm	Patch 1 (bottom) length (L_p1)	11.3 mm
Mitered T-Junction Feed 2 (bottom) (T2_mitered)	0.5065 mm	Patch 2 (top) length (L_p2)	10.2 mm
Height of bottom foam (h_foam)	4.8 mm		

This design shows good simulation results using IE3D [12] as seen in Fig. 2.3. Using a standard VSWR cutoff value of 2.0, feed 1 shows a VSWR bandwidth of 42% (7.9 – 12.1 GHz) (f_0 = 10.0 GHz), and feed 2 shows a VSWR bandwidth of 44% (7.7 – 12.0 GHz) (f_0 = 9.85 GHz). The isolation between the two feeds is greater than 20 dB throughout the VSWR bandwidth.

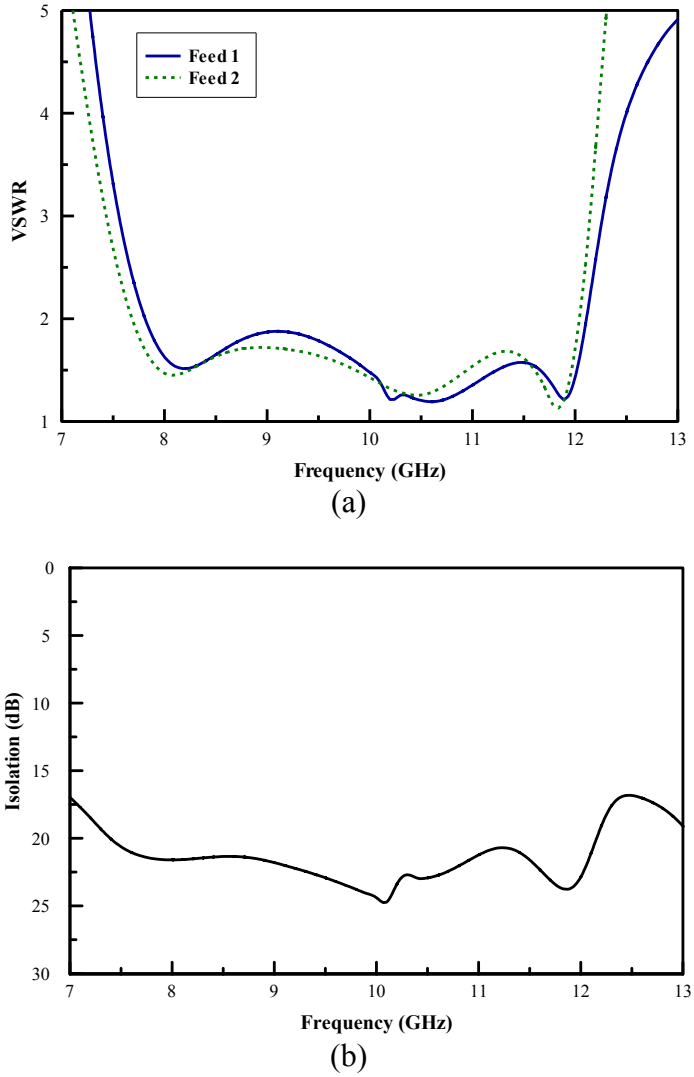

Figure 2.3. Simulation of the original single-element design. (a) VSWR and (b) isolation.

C. Fabrication of Initial Design

For optimal performance, the patches would be floating in the air or etched on top of the foam. Since this is not practical, a very thin substrate (2 mil) is placed on top of the foam layers. All patches, apertures, and feeds are etched using a photolithography process in which ultraviolet light and etching chemicals are used to remove specified areas of copper from the substrates.

All substrate and foam layers are cut as precisely as possible to the same dimensions as the ground planes (26 oz. zinc-plated steel is used as the bottom ground plane). The layers are then aligned and fixed together using 3M Super 77 Multipurpose Spray Adhesive. SMA connectors must also be soldered to the feedlines and both ground planes. Precise alignment is difficult, and care must be taken during this step since the alignment has a dramatic impact on performance of the antenna. A photograph of the fabricated antenna can be seen in Fig. 2.4.

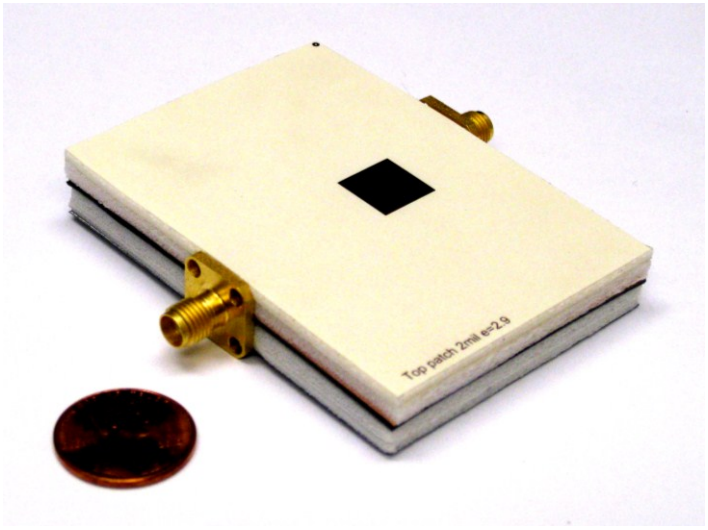

Figure 2.4. Photograph of the single-element antenna.

S-parameter measurements of the antenna can be seen in Fig. 2.5. Ignoring a small overrun in feed 2's VSWR, feed 1 has a measured bandwidth of 35% (7.8 – 11.1 GHz) (f_0 = 9.45 GHz), and feed 2 has a measured VSWR bandwidth of 37% (7.6 – 11.0 GHz) (f_0 = 9.3 GHz). The isolation between the two feeds is measured to be greater than 17 dB throughout the VSWR bandwidth. The measured results show a decrease in performance from the simulated values which is to be expected due to fabrication errors and extreme alignment difficulty. There is, however, one particularly troubling deviation from simulated data. The bandwidth's upper cutoff frequency is reduced by 1 GHz. For comparison, a number of devices were fabricated using the same procedure, and they all showed the same trend.

As a check on the IE3D [12] simulation results, another simulator, HFSS [13] was used to verify the solution. IE3D uses a method-of-moments analysis while HFSS uses a 3D finite element method. The simulated results from HFSS were very similar to the results from IE3D as can be seen in Fig. 2.6. Hence, comparable results were obtained from two different types of simulations, so simulator problems cannot explain the deviation in measured results.

As an attempt to increase alignment accuracy and possibly reduce any air gap errors in fabrication, a new fabrication method was tested in which feed 1 is etched on the bottom side of the apertured-ground plane substrate rather than on the top side of the feed 2 substrate. Several devices using this method were fabricated and compared to the previous method. This new method did show more consistent results, but the results were similar to the previous method, and the frequency-shifting problem still persisted.

Adhesive effects on multi-layer antenna performance have been analyzed in [14]-[15], and an explanation for the type of fabrication error appearing here is presented in the analysis. The authors theorize that the lossy adhesive used to bond the layers is the cause of the VSWR bandwidth's upper frequency shift. As an attempt to avoid adhesive losses, antennas were fabricated using double-sided tape to bond the layers instead of spray adhesive. The tape was strategically placed to avoid the areas where electromagnetic waves are coupling between layers. Measurements showed that this did not correct the problem, and the results were less consistent. This is probably due to air gaps introduced by the taping method.

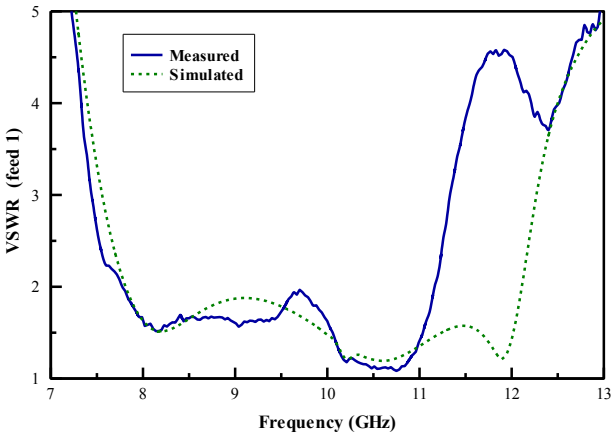

(a)

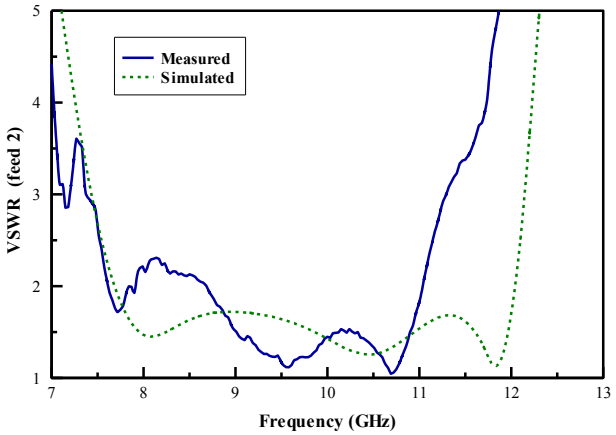

(b)

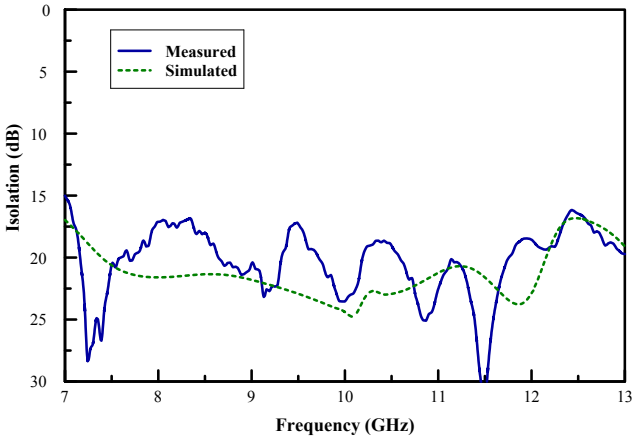

(c)

Figure 2.5. Measured and simulated VSWR and isolation of the original single-element design.

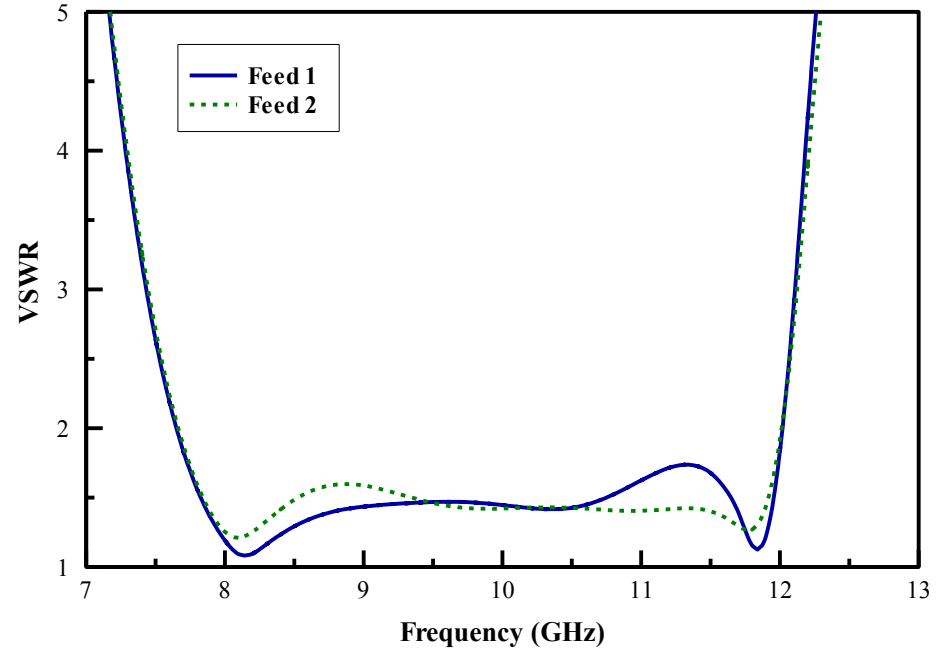

(a)

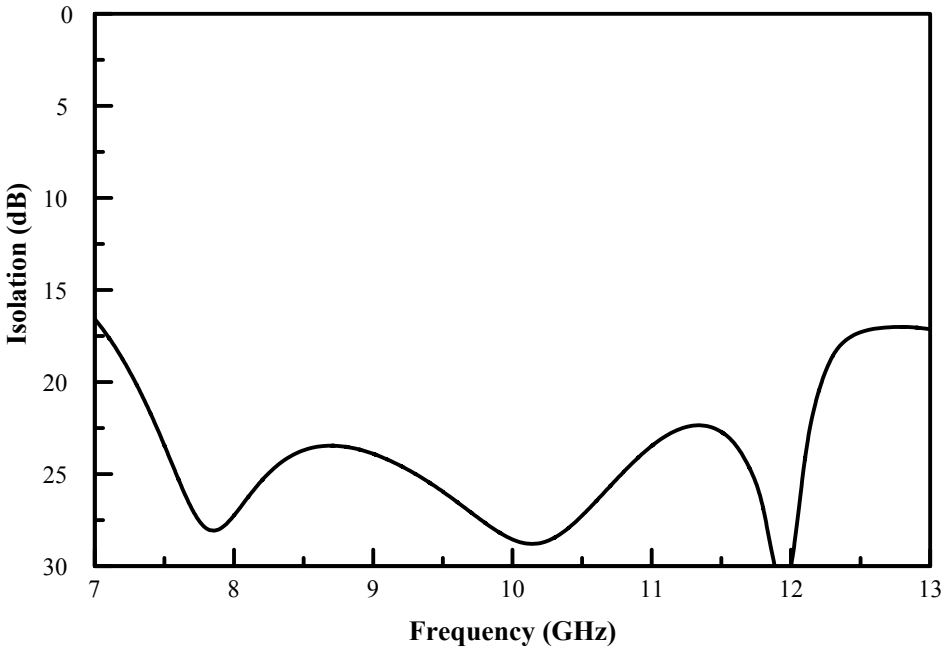

(b)

Figure 2.6. HFSS simulation of the original single-element design. (a) VSWR and (b) isolation.

D. Redesign (Dimension Adjustment) (Final Design)

Since a fabrication method to correct the problem could not be found, the antenna was redesigned to give a higher upper frequency cutoff. The main change was a reduction in patch size which raised the resonant frequency. Some other parameters were then altered to fine tune the new design. The dimensions of the new design are given in Table 2.2.

Table 2.2. Final antenna design parameters.

Variable	**Value**	**Variable**	**Value**
Height of feed 1 (top) substrate (h_feed1)	0.508 mm	Feed 1 (top) matching stub length (L_stub1)	1.96 mm
Height of feed 2 (bottom) substrate (h_feed2)	0.508 mm	Feed 2 (bottom) matching stub length (L_stub2)	2.07 mm
Height of patch 1 (bottom) foam (h_ant1)	3.2 mm	Feed 1 (top) total matching stub length (L_stub_total1)	8.6015 mm
Height of patch 2 (top) foam (h_ant2)	1.6 mm	Feed 2 (bottom) total matching stub length (L_stub_total2)	9.0165 mm
Feed 1 (top) width (100 Ω) (f1w_100)	0.403 mm	Aperture 1 length (L_slot1)	9.7 mm
Feed 1 (top) width (50 Ω) (f1w_50)	1.578 mm	Aperture 1 end-width (w_slot1)	1 mm
Feed 2 (bottom) width (100 Ω) (f2w_100)	1.013 mm	Aperture 1 mid-width (mid_slot1)	0.6 mm
Feed 2 (bottom) width (50 Ω) (f2w_50)	3.3 mm	Aperture 2 length (L_slot2)	9.6 mm
Offset feed 1 (top) separation (d_off1)	2.5 mm	Aperture 2 end-width (w_slot2)	1 mm
Offset feed 2 (bottom) separation (d_off2)	2.5 mm	Aperture 2 mid-width (mid_slot2)	0.6 mm
Mitered T-Junction Feed 1(top) (T1_mitered)	0.2015 mm	Patch 1 (bottom) length (L_p1)	10.9 mm
Mitered T-Junction Feed 2 (bottom) (T2_mitered)	0.5065 mm	Patch 2 (top) length (L_p2)	9.5 mm
Height of bottom foam (h_foam)	4.8 mm		

S-parameter simulation results and measurements of the new antenna design can be seen in Fig. 2.7. For the simulation, using a standard VSWR cutoff value of 2.0, feed 1 shows a VSWR bandwidth of 47% (7.9 – 12.7 GHz) (f_0 = 10.3 GHz), and feed 2 shows a VSWR bandwidth of 45% (8.0 – 12.6 GHz) (f_0 = 10.3 GHz). The isolation between the two feeds is greater than 20 dB throughout the VSWR bandwidth.

Ignoring a small overrun in feed 2's VSWR, feed 1 has a measured bandwidth of 42% (7.9 – 12.1 GHz) (f_0 = 10.0 GHz), and feed 2 has a measured VSWR bandwidth of 38% (8.2 – 12.0 GHz) (f_0 = 10.1 GHz). The isolation between the two feeds is measured to be greater than 17 dB throughout the VSWR bandwidth. The measured results still show a shift in the bandwidth's upper cutoff frequency, but now that shift is accounted for, so the measured center frequencies for feeds 1 and 2 are 10.0 GHz and 10.1 GHz, respectively. This dimension adjustment has corrected the fabricated antenna and shifted the bandwidth to the desired location.

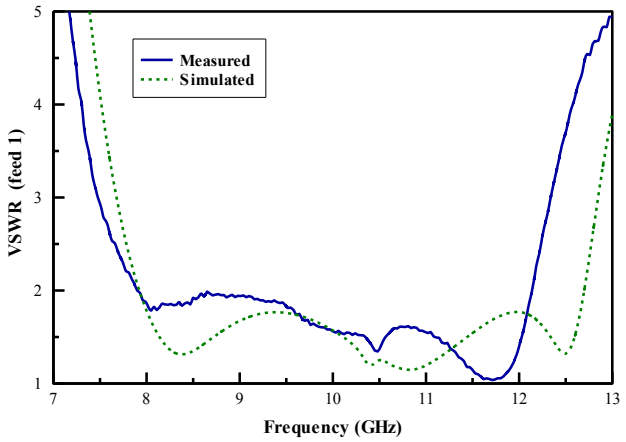

(a)

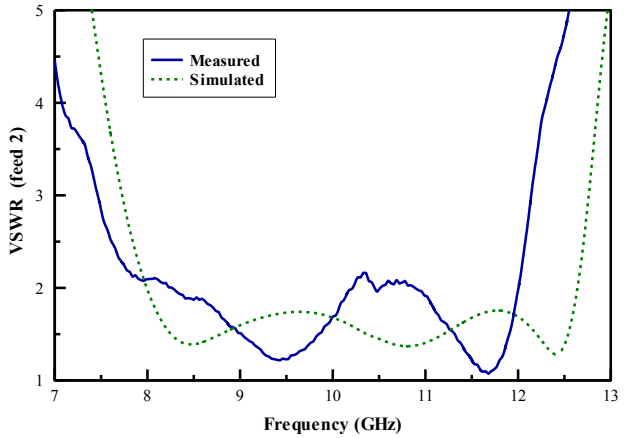

(b)

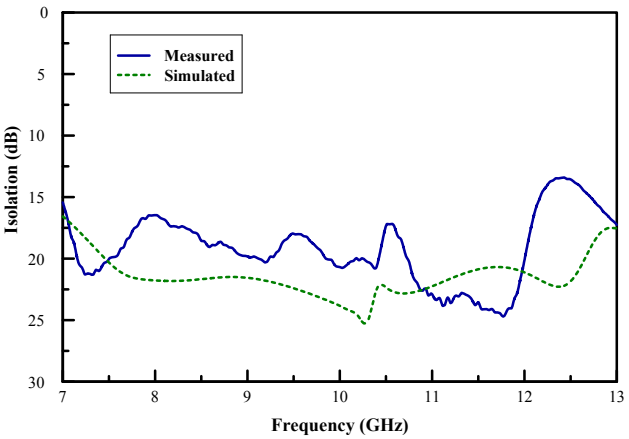

(c)

Figure 2.7. Measured and simulated VSWR and isolation of the redesigned (final) single-element with new dimensions.

E. Radiation Pattern Measurement

The radiation pattern of the redesigned (final) antenna was measured in an anechoic chamber. Each feed is measured separately, and when one feed is being measured, the other is terminated with a 50 Ω load to prevent reflections. Also, during measurement it is important to cover the antenna's connectors with absorber to prevent reflections. If this is not done, results similar to Fig. 2.8 will be obtained.

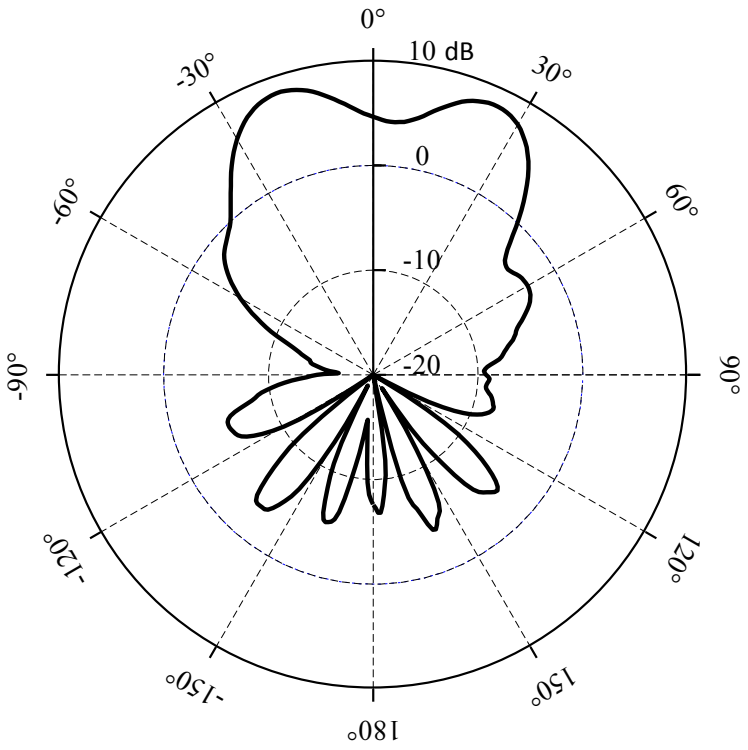

Figure 2.8. Radiation pattern with no absorber (10 GHz / Port 1 / co-pol E-plane).

After a complete set of antenna measurements was taken, a comparison was made to simulated results (Fig. 2.9), and it was noticed that the absorber covering the connectors might be disturbing some of the measured pattern at larger measurement angles and artificially reducing the beamwidth of the antenna. This was corrected by fabricating a new antenna with a larger ground plane (Fig. 2.10). This placed the connectors farther away from the patch so that when they are covered with absorber, it does not interfere with the pattern measurement. This adds approximately 15-25° of beamwidth to the measured pattern. This is illustrated in Fig. 2.11.

Measured radiation patterns of the antenna are displayed in Fig. 2.12 for 8.5, 10, and 11.5 GHz. The patterns are well behaved, and the cross-polarization isolation is greater than 20 dB for all cases. Also, graphs of gain and half-power beamwidth (HPBW) versus frequency are displayed in Figs. 2.13-2.14. The measured gain ranges from 5 - 8 dBi, and the measured HPBW is 50 - 70° for the E-plane and 70 - 90° for the H-plane. Accounting for measurement error and alignment difficulties during fabrication, these results match well to the simulation.

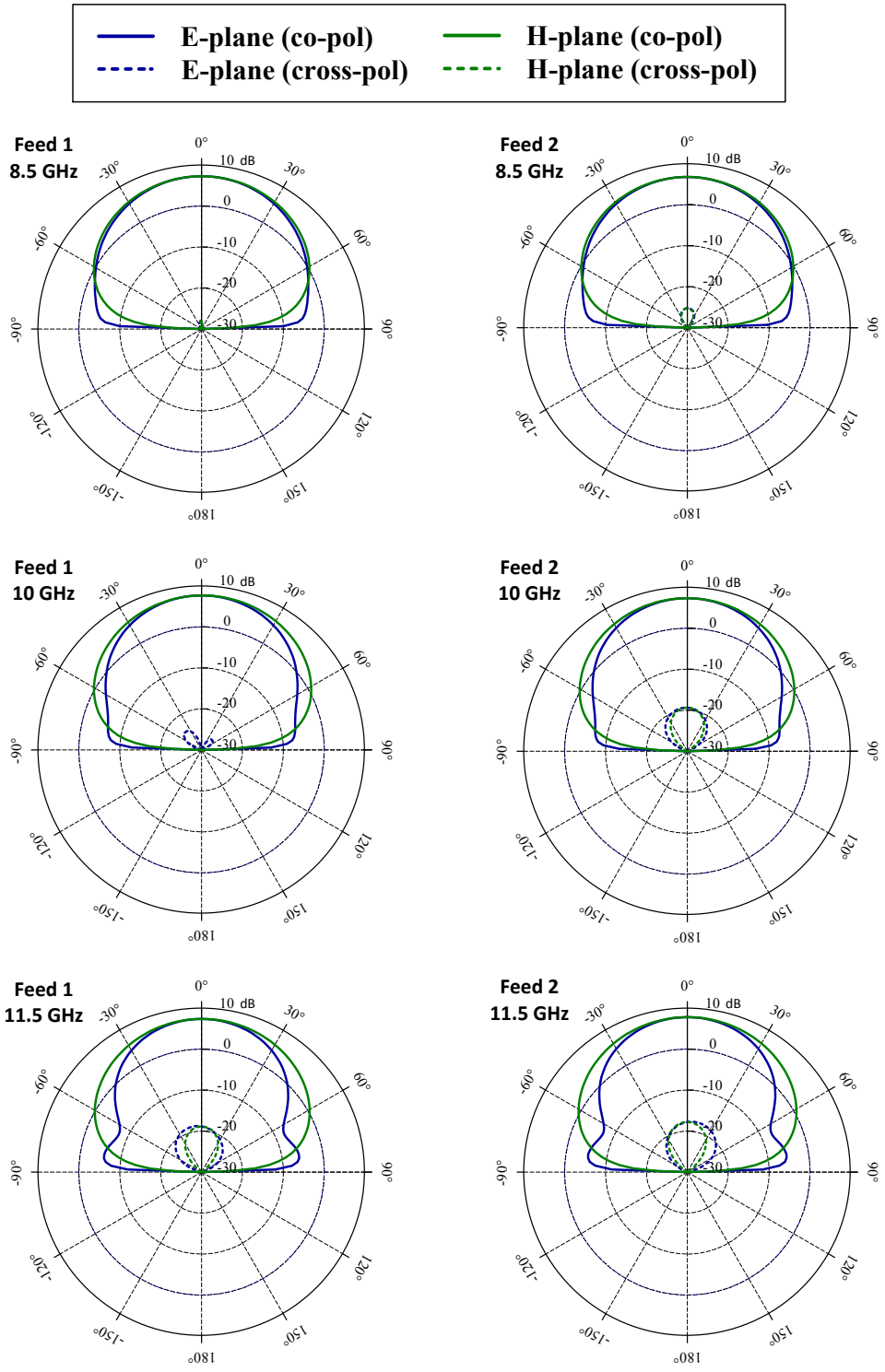

Figure 2.9. Simulated radiation pattern of the single-element final design.

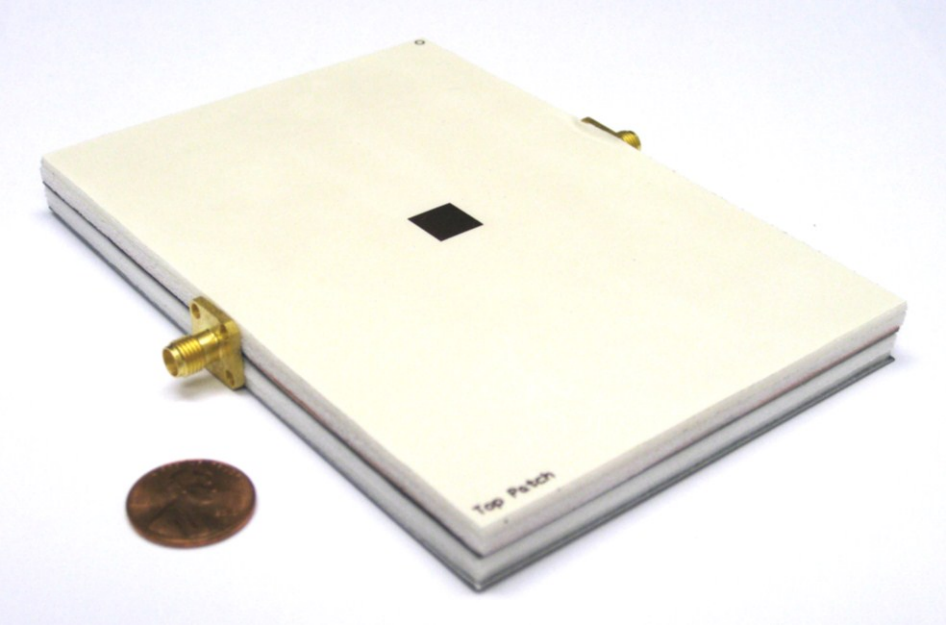

Figure 2.10. Photograph of the single-element antenna with larger ground plane.

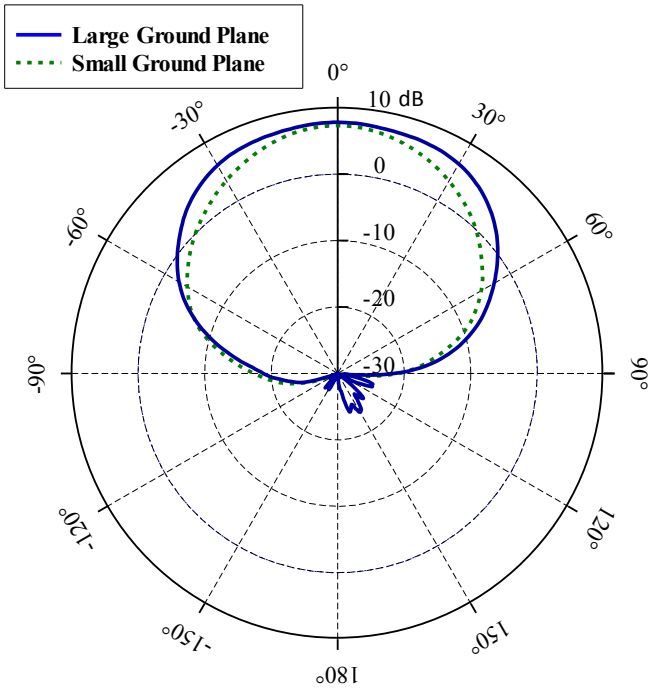

Figure 2.11. Measured radiation pattern comparison of ground plane size (10 GHz / Port 2 / co-pol H-plane).

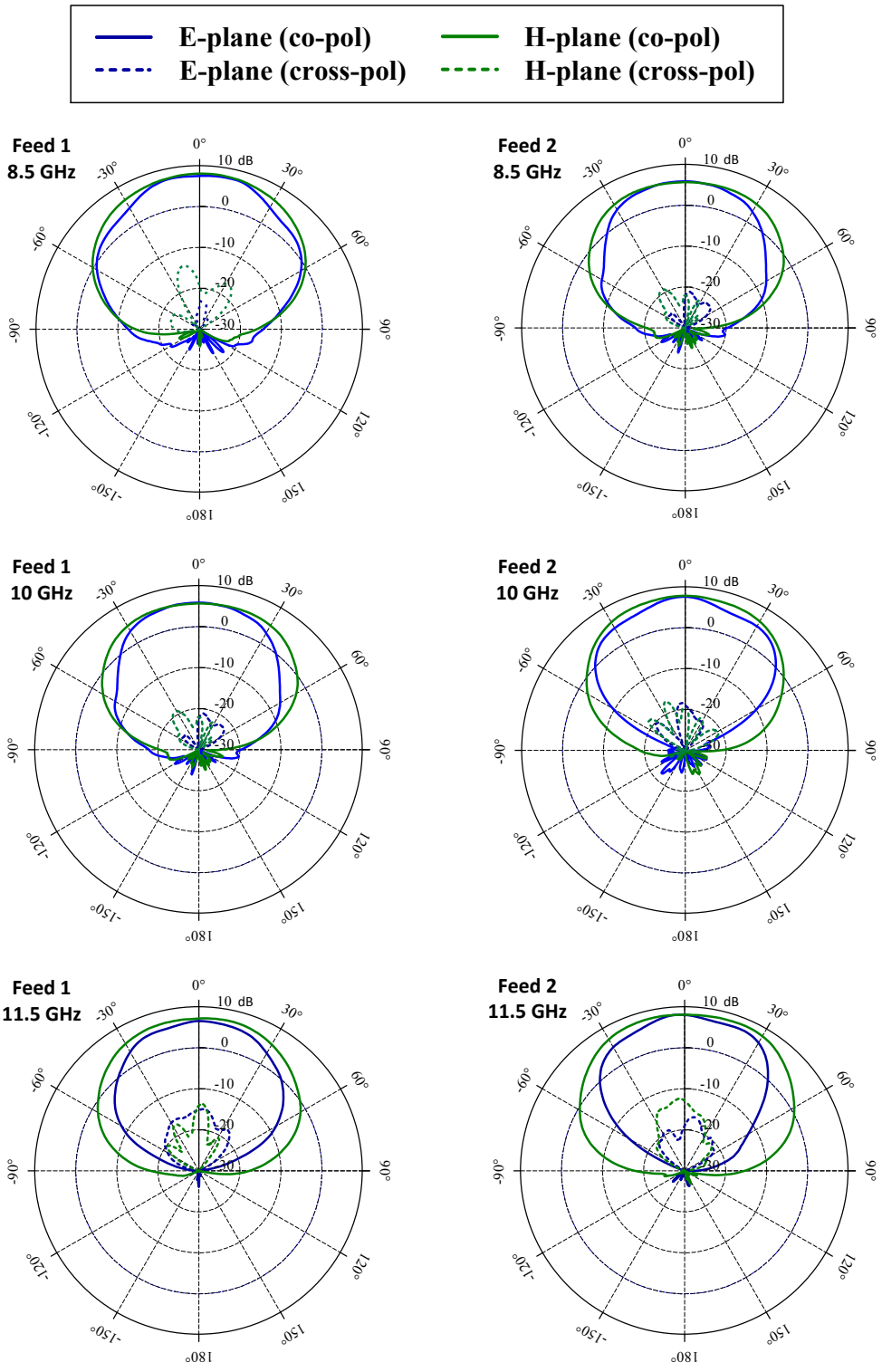

Figure 2.12. Measured radiation pattern of the single-element final design.

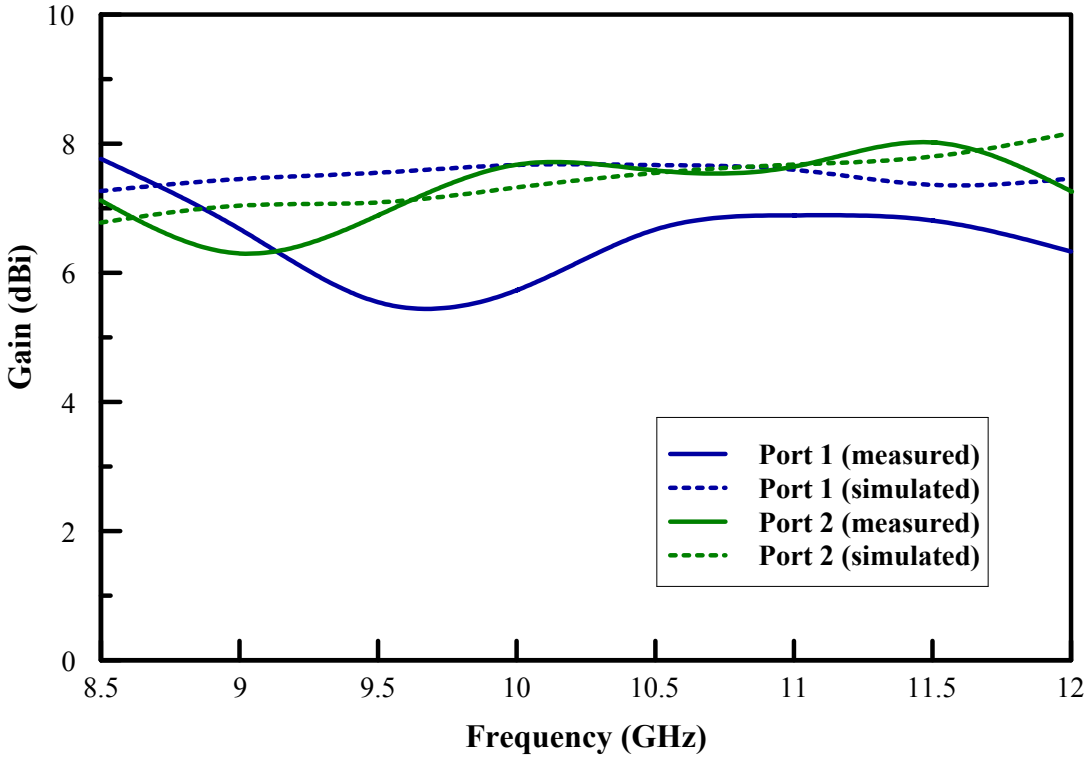

Figure 2.13. Gain versus frequency of the radiation pattern for the single-element final design.

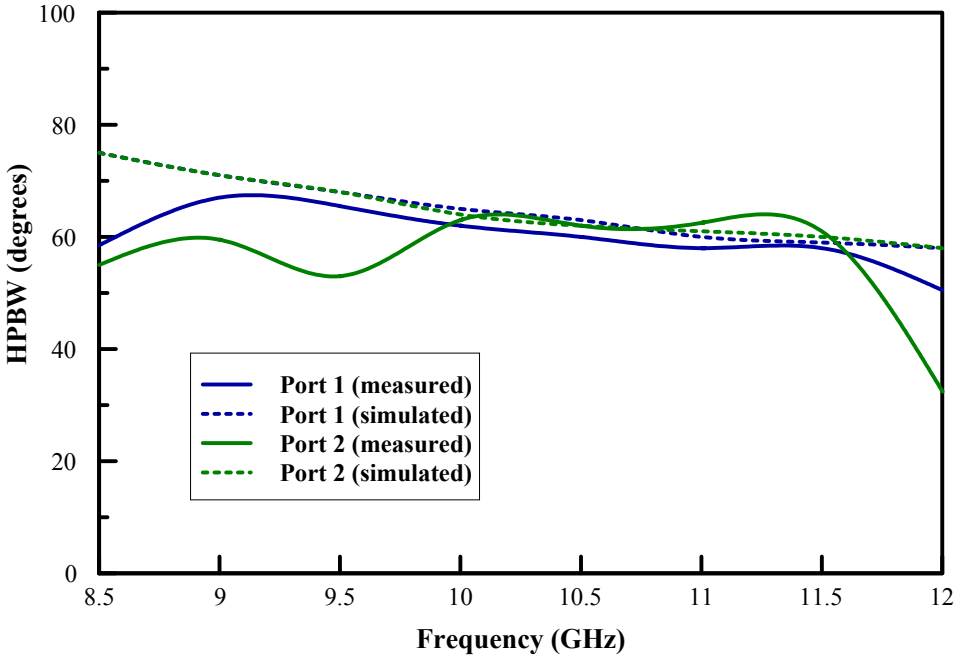

(a)

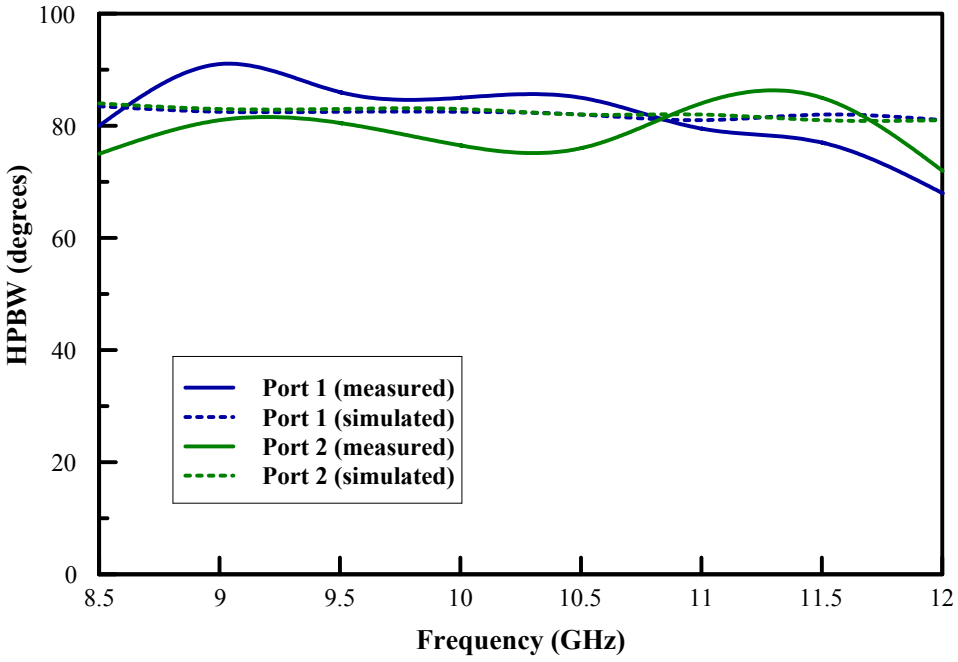

(b)

Figure 2.14. Half-power beamwidth (HPBW) versus frequency of the radiation pattern for the single-element final design. (a) E-plane and (b) H-plane.

F. Conclusion

S-parameter measurements of the initial single-element design showed a shift in the VSWR bandwidth's upper frequency cutoff which shifted the bandwidth out of the desired range of 8.5 – 11.5 GHz. Some adjustments to the antenna dimensions corrected for this unavoidable shift, and the new design was shown to perform well in the target bandwidth and beyond. The VSWR bandwidth of feed 1 was measured as 42% with f_0=10.0 GHz, and the VSWR bandwidth of feed 2 was measured as 38% with f_0=10.1 GHz. S-parameter isolation between the feeds was measured to be greater than 17 dB, and gain measurements showed a cross-polarization isolation of greater than 20 dB. Gain was measured to be 5 – 8 dBi throughout the target bandwidth, and HPBW was measured to be 50 – 90°. Measurements and simulation of the antenna show a good match, and the antenna should work well in a phased array application.

3. ARRAY THEORY

A. Introduction

Single-element antennas have two significant drawbacks: a large beamwidth and a fixed beam direction. This can be overcome with an array of antenna elements which is able to focus energy in a desired direction to narrow the beam and increase range. In order to increase the directivity, the electrical size of an antenna must be increased, and creating an array of elements is a simple and effective way of doing this [4]. An antenna can be mechanically steered, but this is slow and prone to breakage [16]. Alternatively, an antenna array can be fitted with phase shifting devices which will allow the real-time adjustment of individual elements so that the elements will interfere constructively in the desired direction and interfere destructively in all other directions.

Phased arrays were first used in the 1930s for communications between the United States and England. It was, however, the radar and radioastronomy communities that were responsible for the large advances in phased array technology [17]. Since a phased array radar steers without movement and inertia, it has the ability to pause scans to check detections, track multiple targets by switching back and forth, and simultaneously survey and track [16].

B. Array Factor

An *N*-element linear array can be formed by aligning *N* identical antenna elements along the z-axis with each element separated by a distance *d* and phase β. This *N*-element array will form a plane wave whose direction is determined by the progressive phase shift between elements [3]. This is illustrated in Fig. 3.1 where each element has a phase-shifter with a shifting value of β degrees greater than the previous element. This phase shift offset will align the phases to form a wave front and create a plane wave traveling at an angle θ_0 with respect to the array's broadside. The angle θ is with respect to the z-axis on which the elements are positioned.

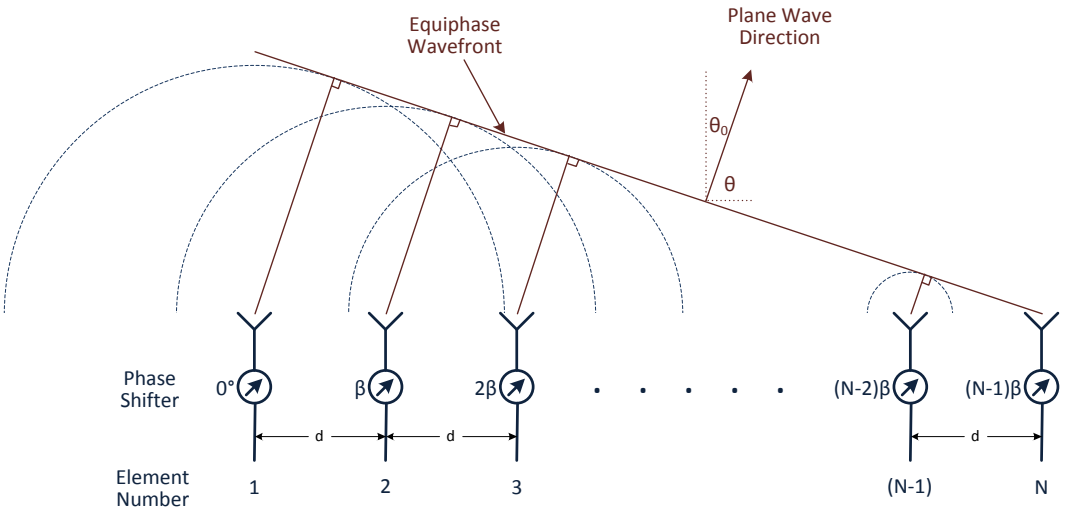

Figure 3.1. An *N*-element linear array with each element separated by a distance *d* and phase β.

The total radiated field from an array of identical single-elements can be calculated as the sum of all the individual elements. The far-field approximation [4][3]:

$$\theta_1 = \theta_2 = \ldots = \theta_N = \theta \tag{3.1}$$

$$\left.\begin{aligned} r_1 &= r \\ r_2 &= r + d\cos\theta \\ &\vdots \\ r_N &= r + (N-1)d\cos\theta \end{aligned}\right\} \text{ for phase variation} \tag{3.2}$$

$$r_1 = r_2 = \ldots = r_N = r \qquad \text{for amplitude variation} \tag{3.3}$$

can be applied in order to express the total field from the array as

$$E_{\text{total}} = E_{\text{single-element}} \times AF \tag{3.4}$$

where $E_{\text{single-element}}$ is the electric field of the single-element at the reference point and AF is the array factor. For an array of uniform amplitude and spacing, the array factor can be expressed as [4]

$$AF = \sum_{n=1}^{N} e^{j(n-1)\psi} \tag{3.5}$$

$$\text{where} \qquad \psi = kd\cos\theta + \beta \ . \tag{3.6}$$

The parameter k is the wave number, d is the distance between elements, and β is the progressive phase shift between elements. By setting the reference point to the center of the array, applying complex exponential identities, and normalizing [4], the array factor can also be expressed as

$$AF = \frac{1}{N}\left[\frac{\sin\left(\frac{N}{2}\psi\right)}{\sin\left(\frac{1}{2}\psi\right)}\right] \quad . \tag{3.7}$$

As described in Fig. 3.1, the progressive phase shift β produces a wave front moving in the direction of the angle θ_0 (where $\theta_0 = 90° - \theta$). The array can then be steered by adjusting β. As seen in (3.5), the array factor (*AF)* is maximum when $\psi=0$, so the array's scan angle can be calculated by

$$\beta = -kd\cos\theta = -kd\sin\theta_0 . \tag{3.8}$$

For an N-element array with elements separated by half-wavelengths, the half-power (3 dB) beamwidth can be estimated [3] as

$$\theta_{HPBW} \approx \frac{100}{\sqrt{N}} \tag{3.9}$$

where θ_{HPBW} is in degrees. It should also be mentioned that the AF's beamwidth increases some with increasing scan angles.

C. Grating Lobes

Since the array factor is a periodic function, it is possible for constant phase wave fronts to form by constructive interference in more than one direction. The additional wave fronts which appear are known as grating lobes which occur when the array factor's exponential in (3.5) is equal to a multiple of 2π, so grating lobes appear when

$$\psi = \pm 2\pi m \quad , \quad \text{m} = 0, 1, 2, \ldots \tag{3.10}$$

Then to scan to an angle θ_0, the condition in (3.8) must hold, so (3.6) and (3.10) can be equated and (3.8) substituted for β resulting in the condition

$$\psi = kd\cos\theta - kd\sin\theta_0 = \pm 2\pi m \quad . \tag{3.11}$$

Next, the observation angle θ (relative to the z-axis) will be changed to an angle relative to broadside and identified as the grating lobe angle such that $\theta_g = 90° - \theta$. Then the condition for grating lobes becomes

$$kd(\sin\theta_g - \sin\theta_0) = \pm 2\pi m \quad , \tag{3.12}$$

and since $k=2\pi/\lambda$,

$$\frac{d}{\lambda}\left(\sin\theta_g - \sin\theta_0\right) = \pm m \ . \tag{3.13}$$

Then the grating lobe angles can be found from

$$\sin\theta_g = \pm m\frac{\lambda}{d} + \sin\theta_0 \quad , \tag{3.14}$$

and the condition for avoiding grating lobes in all of real space is

$$\left|\sin\theta_0 \pm \frac{\lambda}{d}\right| > 1 \tag{3.15}$$

which is satisfied if

$$\frac{\lambda}{d} > 1 + \sin\theta_0 \tag{3.16}$$

which can be rewritten as

$$\frac{d}{\lambda} < \frac{1}{1+\sin\theta_0} \quad . \tag{3.17}$$

Since the maximum scan is 90°, the condition to avoid grating lobes (in all visible space) for all scan angles is

$$d < \lambda/2 \quad . \tag{3.18}$$

It should be noted that the θ in (3.8) and the θ in (3.11) represent observation angles for different pattern features. The θ in (3.8) denotes the scan angle, and the θ in (3.11) denotes grating lobe angles. Both θs are with respect to the z-axis.

D. Non-Uniform Amplitude

Non-uniform amplitude distributions can be used to adjust the beamwidth and sidelobe levels of a phased array. The equation for the array factor in (3.5) can be modified to include the effect of element amplitudes a_n as

$$AF = \sum_{n=1}^{N} a_n e^{j(n-1)\psi} \quad . \tag{3.19}$$

By setting the reference point to the center of the array, applying complex exponential identities, and normalizing [4], the array factor can also be expressed as

$$(AF)_{2M}(\text{even}) = \sum_{n=1}^{M} a_n \cos\left[(2n-1)u\right] \tag{3.20}$$

$$(AF)_{2M+1}(\text{odd}) = \sum_{n=1}^{M+1} a_n \cos\left[2(n-1)u\right] \tag{3.21}$$

$$\text{where} \qquad u = \frac{\pi d}{\lambda}\cos\theta \ . \tag{3.22}$$

In these equations, the total number of elements for an even array is $2M$ and for an odd array is $2M+1$. Also, the amplitude excitation of the center element for an odd numbered array as described in (3.21) is $2a_1$.

Amplitude coefficients for each element can then be chosen and used in (3.19)-(3.22) to determine the array factor. Two of the most popular amplitude distributions are discussed here, but there are many others.

Binomial Distribution

A binomial distribution [4] can be found by expanding the function $(1\text{-}x)^{m-1}$ using a binomial expansion as

$$(1+x)^{m-1} = 1 + (m-1)x + \frac{(m-1)(m-2)}{2!}x^2 + \frac{(m-1)(m-2)(m-3)}{3!}x^3 + \cdots \qquad (3.23)$$

The positive coefficients of the series can then be used as amplitude coefficients for an array of *m* elements. These coefficients for increasing values of *m* form a Pascal triangle as:

m = 1				1				
m = 2				1	1			
m = 3			1	2	1			
m = 4		1	3	3	1			
m = 5		1	4	6	4	1		
m = 6	1	5	10	10	5	1		
m = 7	1	6	15	20	15	6	1	
m = 8	1	7	21	35	35	21	7	1

(3.24)

Dolph-Tschebyscheff Distribution

The Dolph-Tschebyscheff distribution [4] is formed from the Tschebyscheff polynomials and is a compromise between a uniform and a binomial distribution. Its amplitude coefficients can be chosen to create sidelobes of any desired level, and when a Dolph-Tschebyscheff array with no sidelobes is chosen, it reduces to a binomial array. The Dolph-Tschebyscheff polynomial [18] is defined as

$$T_m(z) = \cos\left[m\cos^{-1}(z)\right], \qquad -1 \le z \le 1 \tag{3.25}$$

$$T_m(z) = \cosh\left[m\cosh^{-1}(z)\right], \qquad |z| > 1 \quad . \tag{3.26}$$

The method of finding the Dolph-Tschebyscheff coefficients involves expanding (3.25)-(3.26) and the array factor to be of the same form and equating the coefficients. The complete procedure is explained in detail in [4] and [18]. The Dolph-Tschebyscheff coefficients will give an array with all sidelobes at a level specified in the design procedure. However, decreasing the sidelobe level increases the beamwidth and the difference in coefficient magnitudes.

E. Phase Quantization

Most recent phased array systems use digital phase-shifters to control the phase of each element. This effectively quantizes the phase so that the realized phase is only an approximation of the ideal phase. For an *N*-bit phase-shifter, the phase states are separated by the least significant phase ϕ_0 which is given by

$$\phi_0 = \frac{2\pi}{2^N} \quad . \tag{3.27}$$

This phase approximation creates phase quantization grating lobes, and the first detailed analysis of this effect was performed by Miller [19]-[20]. He evaluated the level of the first grating lobe by assuming that the array current distribution is continuous (i.e., there is not a discrete number of elements). From this analysis, the level of the first phase quantization lobe can be expressed as

$$P_{QL} = \frac{1}{2^{2N}} \approx -6N \text{ (dB)} . \tag{3.28}$$

The continuous array approximation used by Miller led to an underestimation of the actual peak phase quantization lobes [21]. More accurate equations have been given by various authors including Hansen [22] and Mailloux [23]. Mailloux gives an estimate for the upper bound on the phase quantization sidelobe level as

$$P_{QL} < -20\log M + 9.94 - 6.02N \text{ (dB)} \quad \text{for } M \geq 2 \text{ and } N \geq 3 \tag{3.29}$$

where N is still the number of bits and M is the number of array elements. The equations for phase quantization sidelobe levels as proposed by Miller (3.28) and Mailloux (3.29) are plotted in Fig. 3.2.

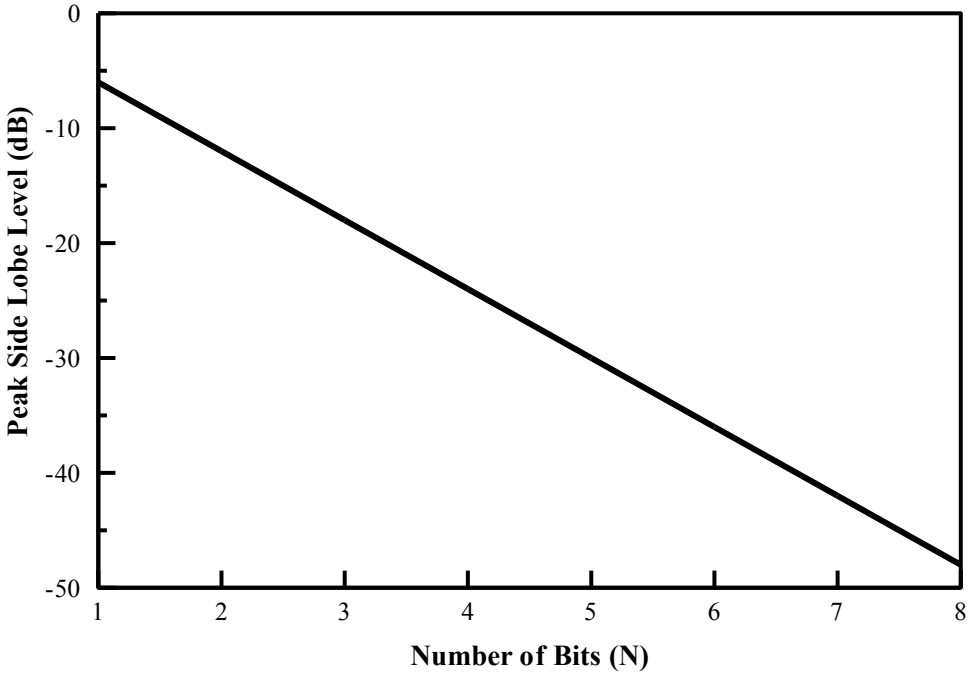

(a)

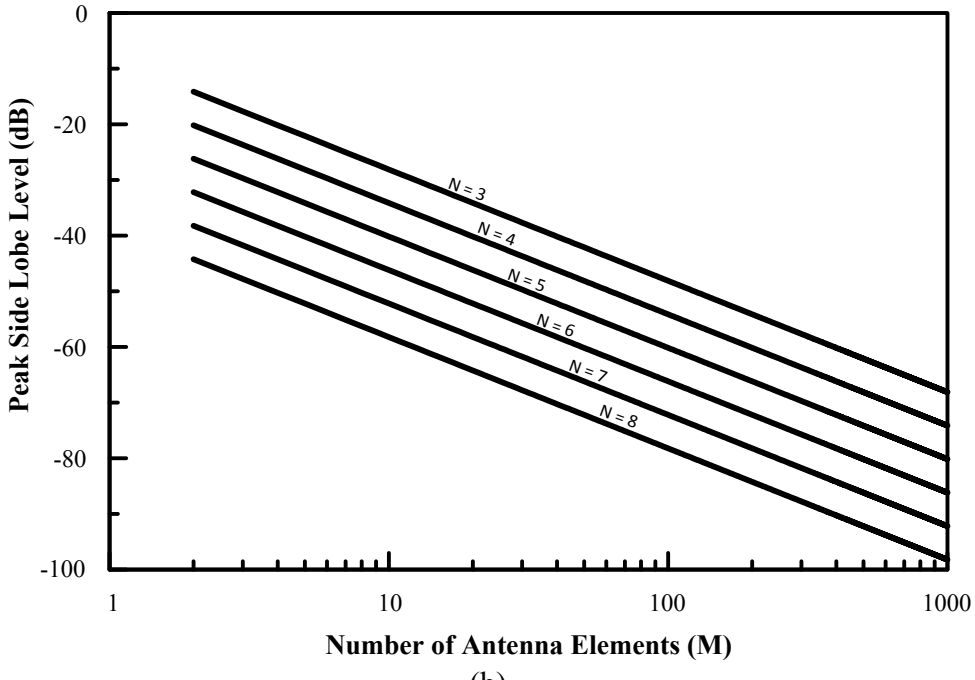

(b)

Figure 3.2. Maximum phase quantization sidelobe levels as proposed by (a) Miller and (b) Mailloux.

F. Design Choices

When designing a phased array, decisions must be made which balance the tradeoffs between performance and cost/complexity. Assuming that the single-element is already designed, these decisions involve the amplitude distribution, the number of elements, element spacing, and the number of phase-shifter bits.

Amplitude Distribution

As previously mentioned, there are many choices for an array's amplitude distribution, of which the most popular are: uniform, binomial, and Dolph-Tschebyscheff. Examples of these are illustrated in Fig. 3.3. One of the uniform distribution's advantages is that it has a beamwidth which is narrower than the other distributions. The downside is that the sidelobes are relatively large. The uniform distribution is also simple to implement; since all of the elements' amplitudes are equal, there is no need for an amplifier or attenuator for each feed. For non-uniform distributions, individual element amplitudes must be controlled, which leads to increased system complexity and cost.

The binomial distribution eliminates sidelobes, but it does this at the expense of a wide beamwidth. Also, the difference in element amplitudes is quite large, and this can be difficult to implement in a practical system.

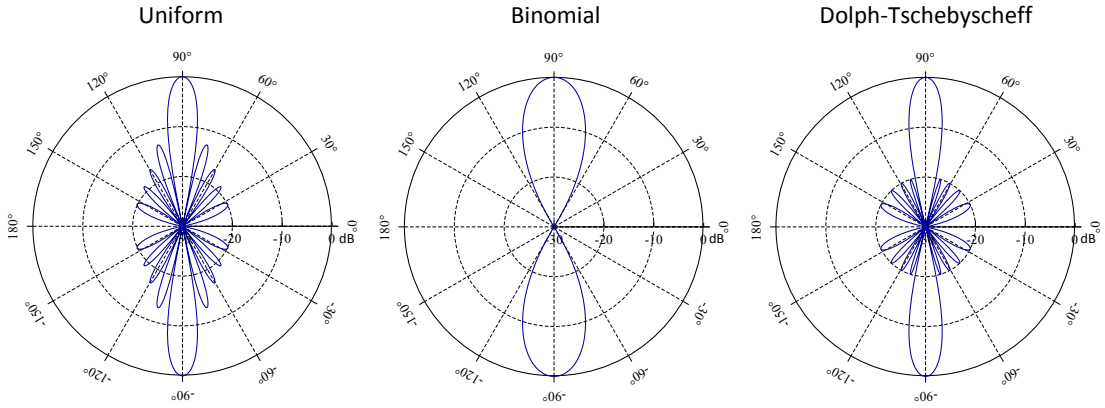

N = 10 d = λ/2

	Uniform	Binomial	Dolph-Tschebyscheff
	1	1	1
	1	9	1.67
	1	36	2.60
	1	84	3.41
Amplitude	1	126	3.88
Distribution	1	126	3.88
	1	84	3.41
	1	36	2.60
	1	9	1.67
	1	1	1
HPBW	10.2°	20.2°	11.2°

Figure 3.3. AF for different amplitude distributions: uniform, binomial, and Dolph-Tschebyscheff (20 dB SLL). An array with $N = 10$ elements and element spacing $d = \lambda/2$ is used. The amplitude distribution and half-power beamwidth (HPBW) are also given for each distribution.

The Dolph-Tschebyscheff distribution is somewhat of a compromise between the uniform and binomial distribution. When implementing this distribution, the SLL (sidelobe level) is specified, and when the sidelobes are eliminated, it reduces to a binomial distribution. When using this distribution, all sidelobes are at a constant level as opposed to the uniform distribution where the SLL decreases for lobes farther from the main beam. Specifying lower sidelobes widens the beamwidth and increases the disparity between individual element amplitudes. Therefore, the Dolph-Tschebyscheff distribution allows a compromise to be chosen between SLL, beamwidth, and amplitude disparity.

Number of Elements

The number of elements greatly affects a phased array's performance and cost. Adding elements to an array reduces its beamwidth, and an array with a large number of elements can produce a very narrow beamwidth. This is illustrated in Fig. 3.4.

However, more elements means that the system will be larger and more expensive. Phase-shifters can be quite expensive, and since each element must have its own phase-shifter and controlling mechanism, the expense can add up very quickly.

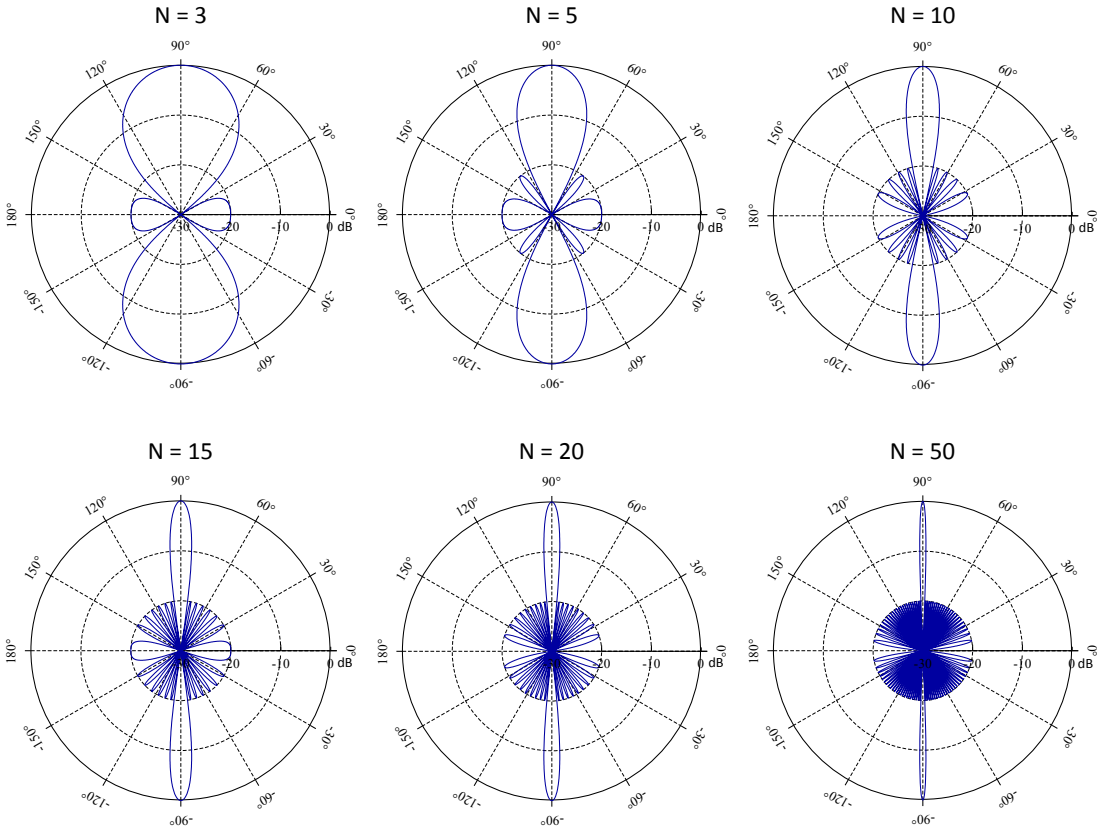

Dolph-Tschebyscheff d = λ/2

N	3	5	10	15	20	50
HPBW	**40.4°**	**23.6°**	**11.2°**	**7.2°**	**5.4°**	**2.1°**

Figure 3.4. Illustration of the effect of N (number of elements) on the AF's beamwidth. A Dolph-Tschebyscheff (20 dB SLL) array with element spacing $d = \lambda/2$ is used for comparison.

Element Spacing

As previously mentioned, close element spacing will delay the onset of grating lobes as illustrated in Fig. 3.5; and (3.17) can be used to find the maximum element spacing (for a given scan angle) which will prevent grating lobes.

The tradeoff is that closer element spacing will also increase the beamwidth as illustrated in Fig. 3.6. Therefore close element spacing is desired to eliminate grating lobes, but large element spacing is desirable for a narrow beamwidth. Also, the element spacing is expressed as a function of wavelength, so if the array is to operate at multiple frequencies, the effective element separation will be different for each frequency. This effect should be taken into consideration in the design.

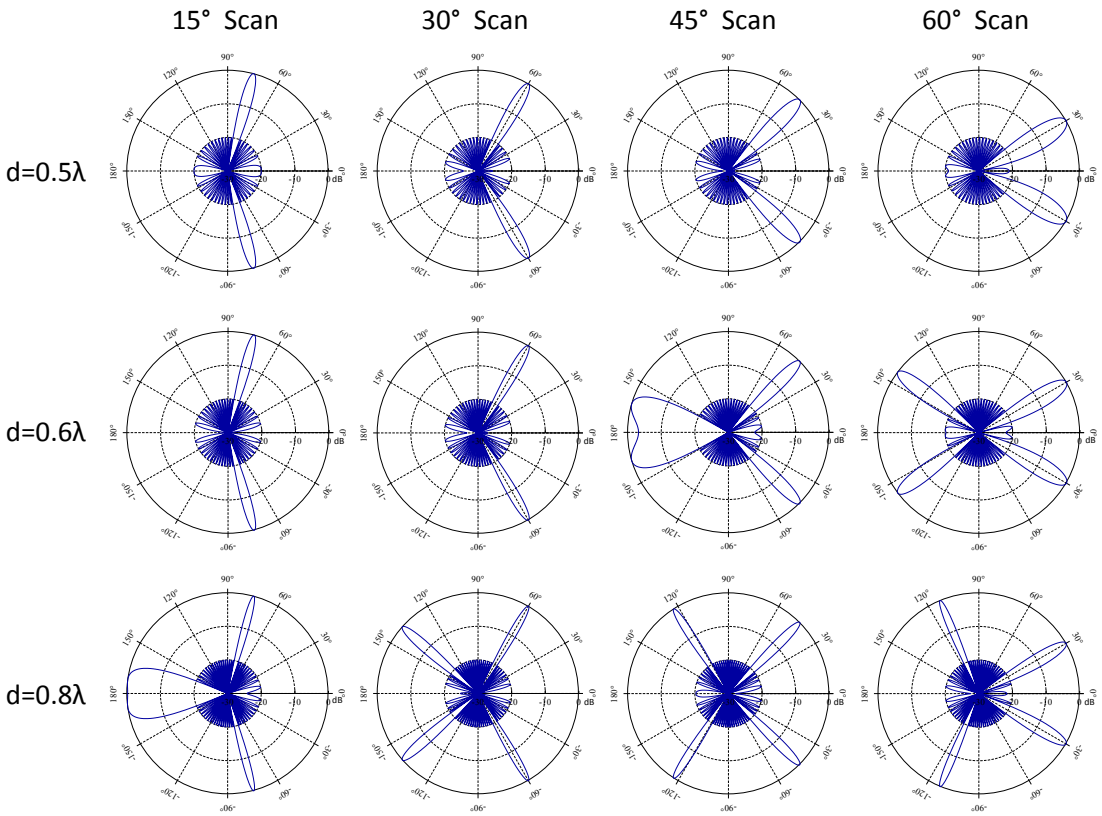

Figure 3.5. Illustration of the effect of d (element spacing) on grating lobes in the AF. A Dolph-Tschebyscheff (20 dB SLL) array with $N = 20$ elements is used for comparison.

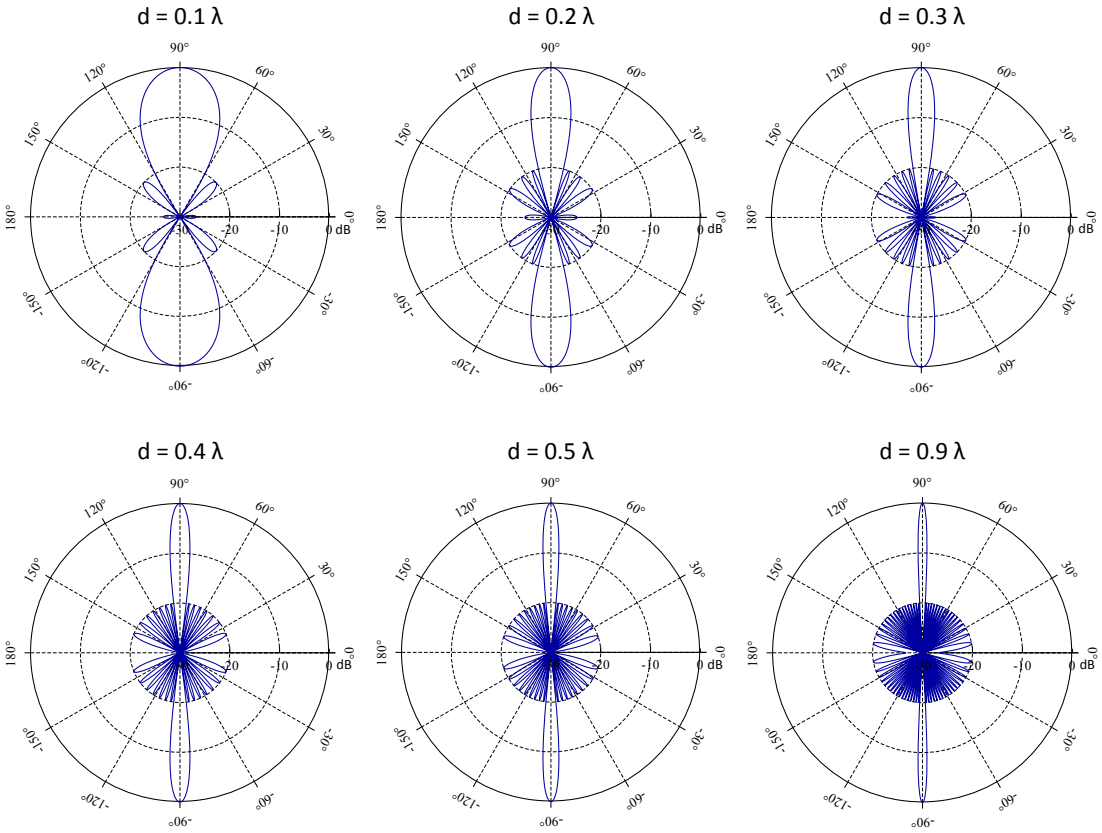

Figure 3.6. Illustration of the effect of *d* (element spacing) on AF beamwidth. A Dolph-Tschebyscheff (20 dB SLL) array with $N = 20$ elements is used for comparison.

Phase-Shifter Bits

The effect that the number of phase-shifter bits has on phase quantization grating lobes has been previously discussed and quantified in (3.28)-(3.29) and graphed in Fig. 3.2. A phase-shifter with many bits reduces the size of the quantization lobes, but it is in general more expensive than one with fewer bits. Increasing the number of bits also increases control complexity and cost.

Scan Range Considerations

The AF's gain is constant across all scan angles. However, since practical antennas are not isotropic, the single-element antenna's gain will decrease as the observation angle diverges from broadside. Since the array pattern is determined by the product of the array factor and the single-element pattern, the array's gain will decrease with increasing scan angles. If AF beamwidth is wide, the AF gain at angles which are lower than the intended scan angle can be large enough that when multiplied by the larger single-element gain, the array's gain will actually be larger at smaller angles than it is at the intended scan angle. This will effectively create a smaller scan angle than intended and can decrease the array's maximum scan angle.

Fig. 3.7 illustrates this by showing different scan angles for arrays of various sizes. The AF and single-element pattern are illustrated in thin red and blue, respectively. The product of these gives the array pattern which is shown in thick black. For a 4-element array, a 30° scan works well, but already the array points to an angle slightly less than 30°. For a 45° scan, the array points to an angle slightly larger than

30°, and for a 75° scan, the sidelobes have exceeded the magnitude of the main beam. The 8-element array scans significantly better, and the 16-element array only starts to lose angle at the 75° scan angle.

It has been shown that the number of elements in an array has a significant impact on the array's maximum scan angle and performance. Hence, the required scan angle and beamwidth should be taken into account when designing a phased array.

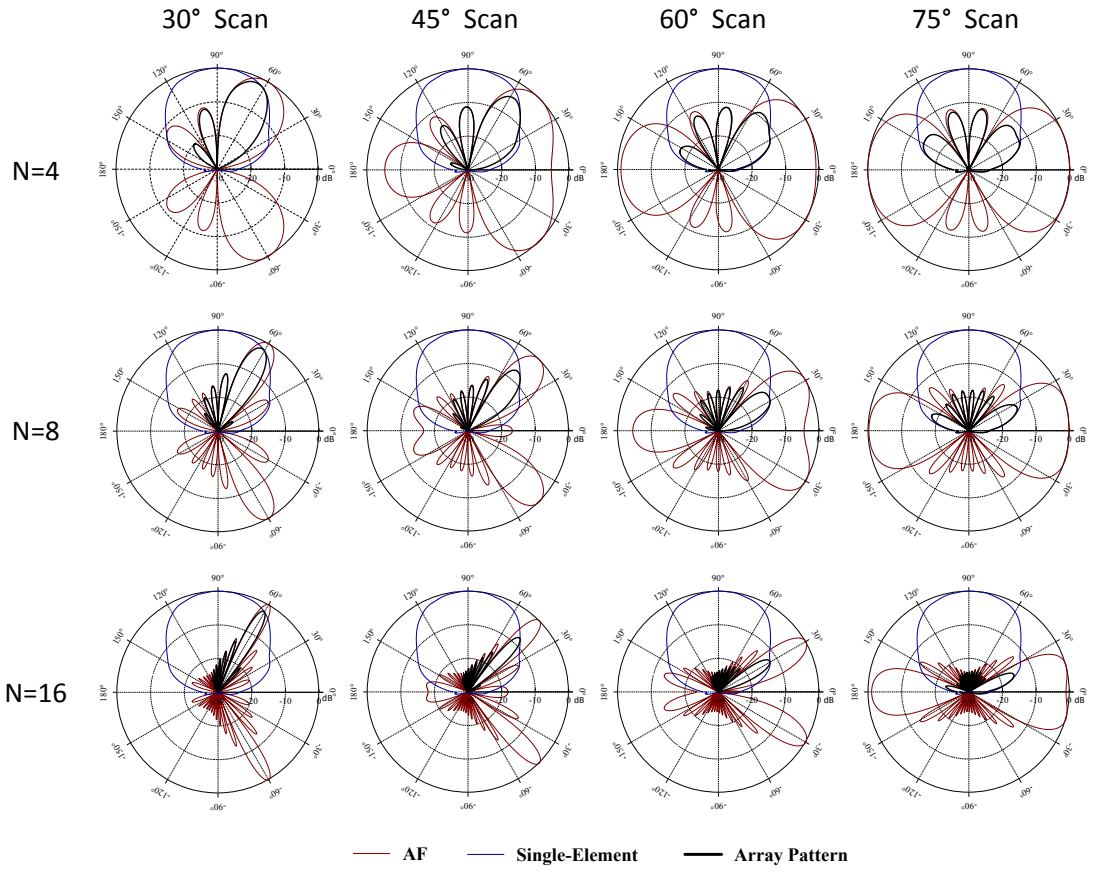

Figure 3.7. Illustration of the effect of N (number of elements) on scan angle. The AF and Single-Element patterns are shown in red and blue, respectively. The Array Pattern is the product of these two and is shown in black. The measured single-element E-plane pattern from the previous section (for Feed 1 at 10 GHz) and a uniform array with $d = \lambda/2$ are used to generate the plots.

4. PHASED ARRAY DEVELOPMENT

A. Antenna Array

The previously designed single-element antenna is to be used in a 4x1 array configuration. A uniform amplitude arrangement is chosen at this stage to simplify the design and avoid the need for amplifiers or attenuators. At a later date, computer-controlled amplifiers can be incorporated in the design to allow various amplitude schemes to be easily realized. The element spacing is chosen as 0.5λ at 10 GHz (1.5 cm) to minimize the effect of grating lobes while still maintaining a reasonably narrow beamwidth. This equates to 0.425λ at 8.5 GHz and 0.575λ at 11.5 GHz. A diagram of the array configuration can be seen in Fig. 4.1.

The array is fabricated in a manner similar to the method previously described for the single-element, with care being taken to ensure proper alignment; the fabricated array can be seen in Fig. 4.2. The four feeds on one side of the array will be combined into port 1, and the four feeds on the other side will be combined into port 2. The port numbering is defined from the numbering paradigm set by the single-element feed numbering (i.e., port 1 is created from the top feeds and port 2 is created from the bottom feeds).

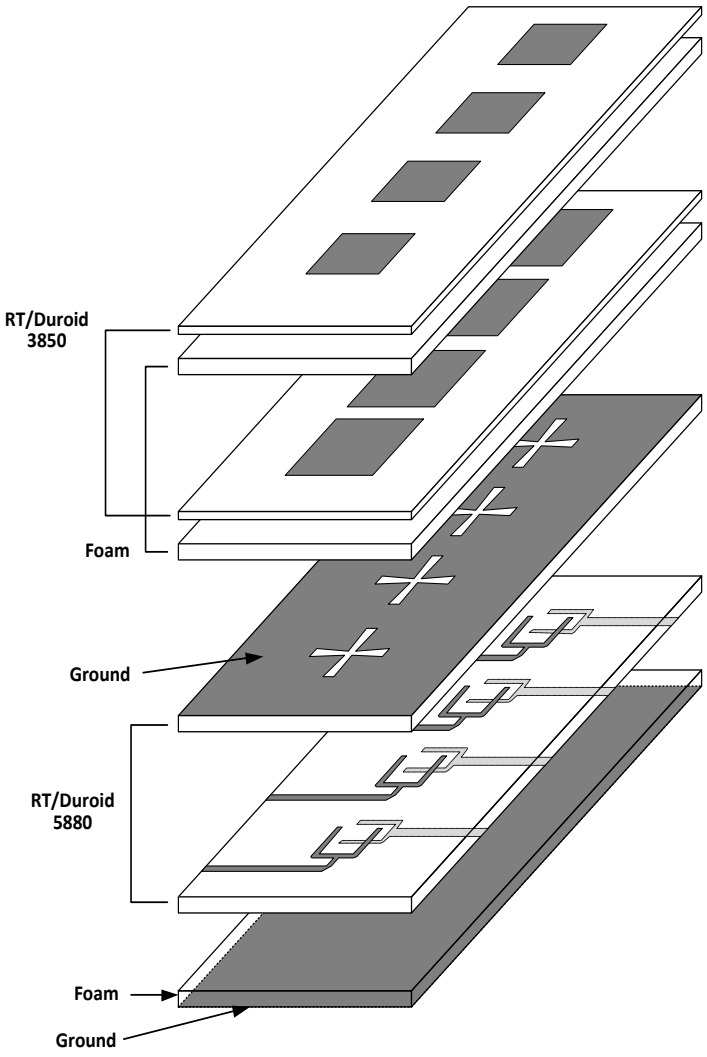

Figure 4.1. 4-element array design (stacked-patch, aperture-fed, dual-polarized stripline).

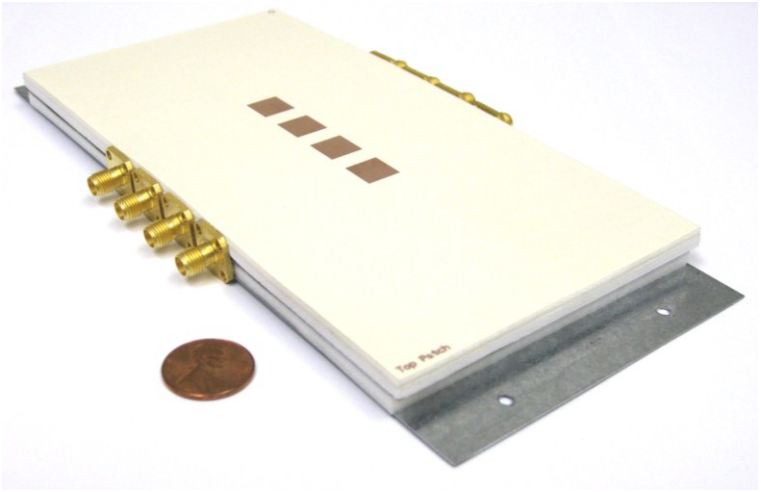

Figure 4.2. Photograph of the antenna array.

An Agilent 8510C network analyzer was used to measure the VSWR of the feeds as well as the isolation between the feeds. These measured values as well as simulated values can be seen in Figs. 4.3-4.4. Ignoring some small overruns, port 1's feeds have a simulated VSWR bandwidth of 45% (8 – 12.7 GHz) (f_0 = 10.4 GHz) and a measured VSWR bandwidth of 43% (7.9 – 12.2 GHz) (f_0 = 10.1 GHz). Port 2's feeds have a simulated VSWR bandwidth of 42% (8.3 – 12.7 GHz) (f_0 = 10.5 GHz) and a measured VSWR bandwidth of 41% (7.8 – 11.8 GHz) (f_0 = 9.8 GHz). This shift in bandwidth between simulated and measured values is similar to what was seen with the single-element and is the reason for the redesign. This places the center frequency close to 10 GHz. The simulated isolation between the ports' feeds is greater than 20 dB, and the measured isolation is greater than 18 dB throughout the VSWR bandwidth.

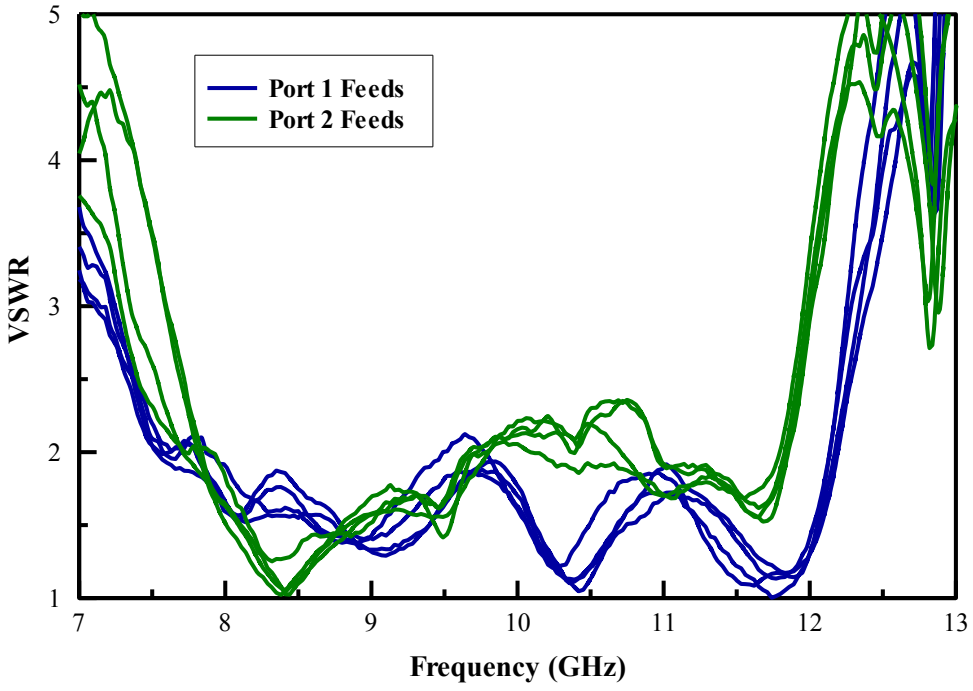

(a)

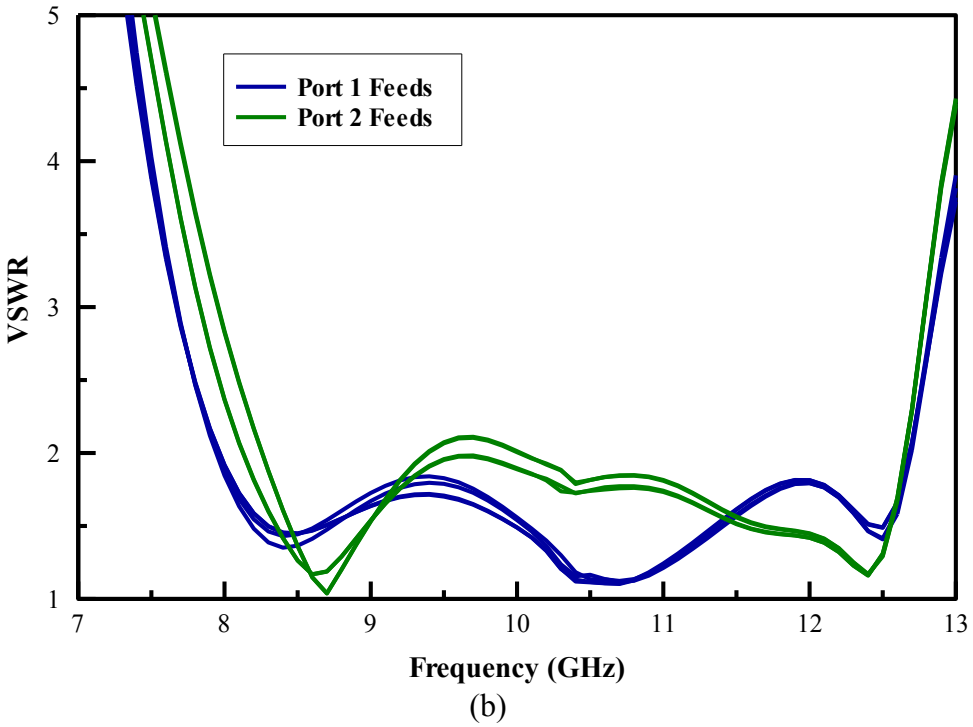

(b)

Figure 4.3. VSWR of the array feeds. (a) Measured and (b) simulated.

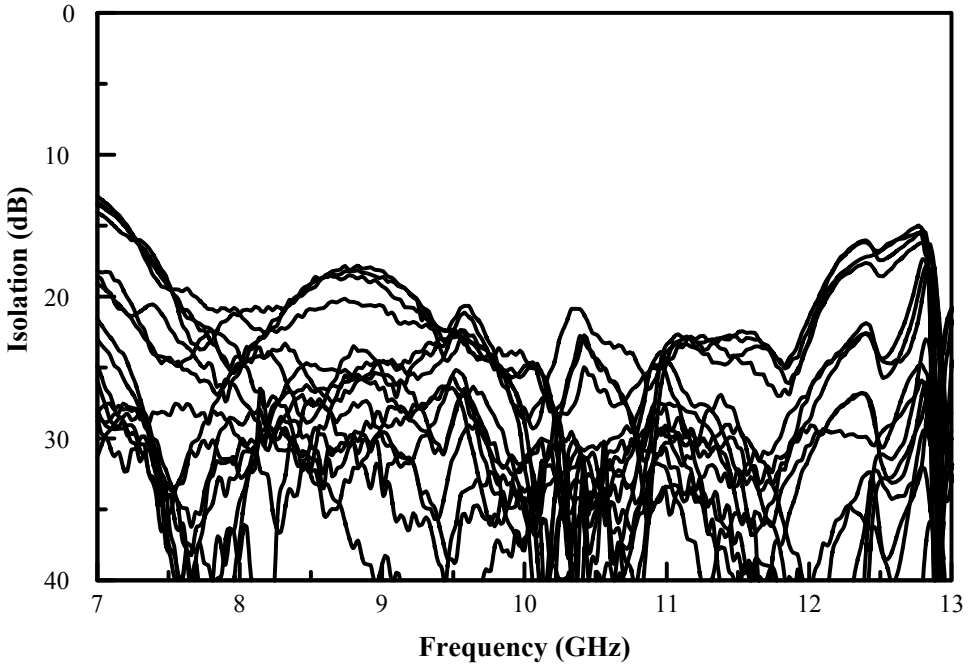

(a)

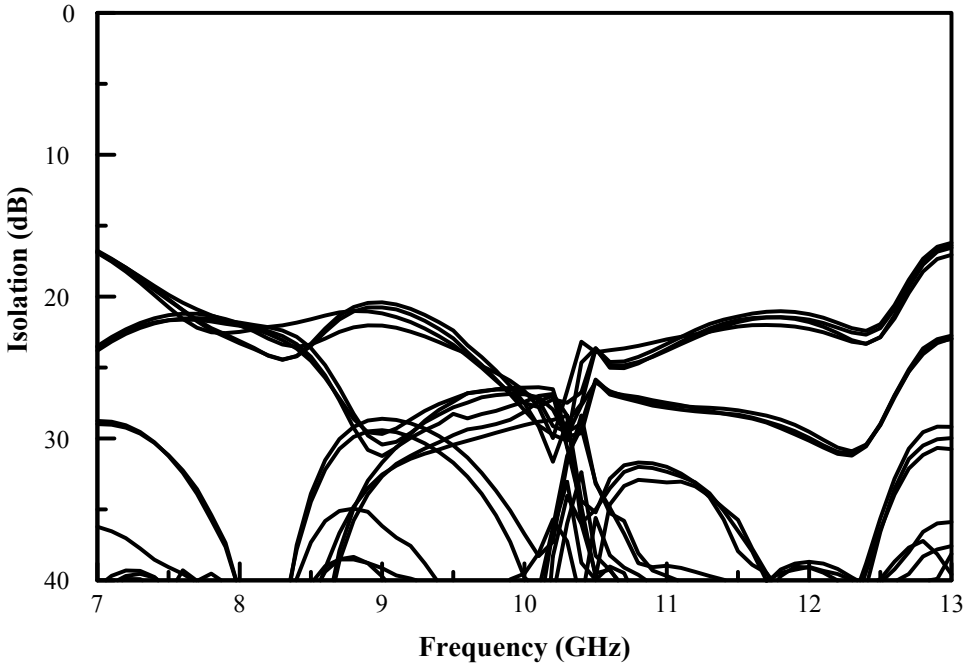

(b)

Figure 4.4. Isolation of the array feeds. (a) Measured and (b) simulated.

B. Power Divider

A 1-to-4 power divider must be used to evenly divide power between the four feeds of each port. Ideally, each output of the power divider will have the same amplitude and phase shift. However, the phase-shifters can be used to adjust for any difference in phase, but since variable amplifiers (or attenuators) are not used in this design, there is no way to adjust for an amplitude variation.

A corporate feed [24] arrangement is used to divide power since this can support a wide bandwidth. In this arrangement, a mitered T-junction [25] will be used to split the power into two, and then mitered T-junctions will be used to split that power again.

In addition to splitting power, the mitered T-junction will change the impedance from Z_0 at the input to $2*Z_0$ at the two outputs. This change in impedance must be accounted for with a transformer. The transformer will be placed before the T-junction rather than after it so that it changes the impedance from 50 to 25 Ω rather than from 100 to 50 Ω. This will prevent the use of high impedance lines which are narrow and sensitive to fabrication errors. It will also reduce the number of required transformers from six to three.

A single quarter-wave transformer can only support a narrow bandwidth, so it is better to use a multi-section transformer to increase the bandwidth. A two section transformer is sufficient and can be designed from a simple algorithm using a uniform geometric progression as presented in [26]. The characteristic impedance Z_0 is 50 Ω, and the load resistance R_L, which is the required impedance before the T-junction, is 25 Ω. The number of sections N will be 2. The impedance will be transformed into

intermediary impedances before finally reaching the final value. The step between these intermediary impedances is defined as:

$$Step = \left(\frac{R_L}{Z_0}\right)^{1/N} = \left(\frac{25}{50}\right)^{1/2} = 0.7071 \quad . \tag{4.1}$$

Then the intermediary impedances are defined as:

$$Z_i(1) = Step \text{ x } Z_0 = 35.6\ \Omega \tag{4.2}$$

$$Z_i(2) = Step \text{ x } Z_i(1) = 25\ \Omega \quad . \tag{4.3}$$

Finally, the characteristic impedance of each quarter-wave section can be defined as:

$$Z(1) = \sqrt{Z_i(0)Z_i(1)} = 42.04\ \Omega \tag{4.4}$$

$$Z(2) = \sqrt{Z_i(1)Z_i(2)} = 29.73\ \Omega \quad . \tag{4.5}$$

The power divider design can be seen in Fig. 4.5, and a photograph can be seen in Fig. 4.6. Note that there is not a 25 Ω line in the design because the input to the mitered T-junction is placed immediately following the conversion to 25 Ω.

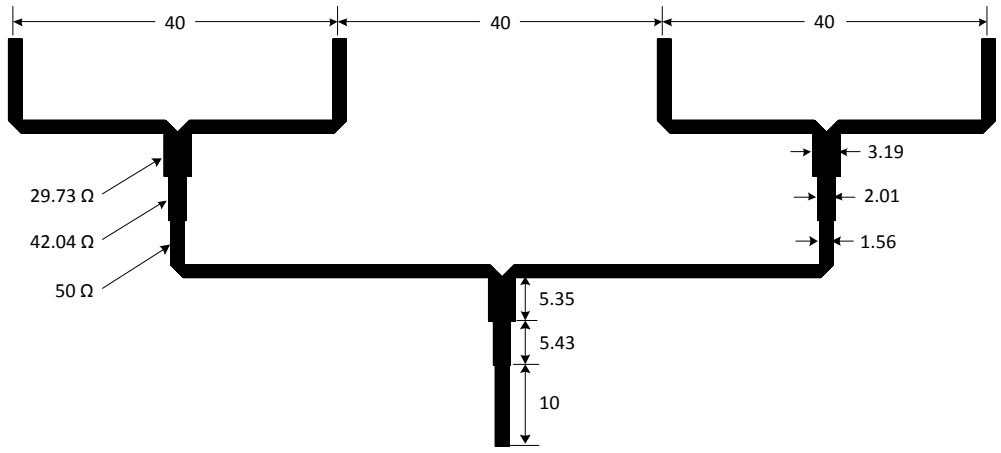

Figure 4.5. Schematic of the power divider (all units in mm).

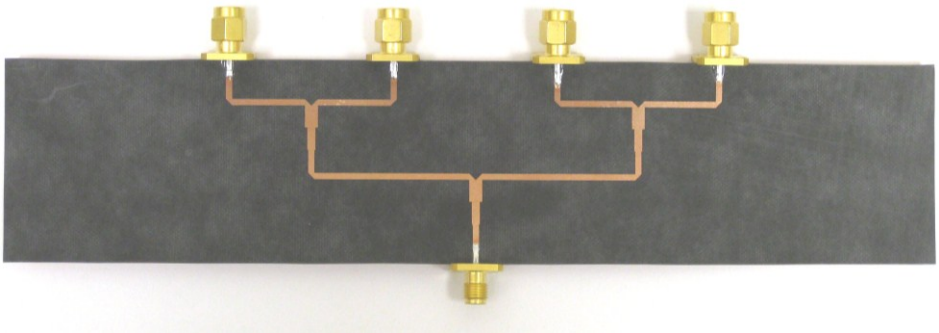

Figure 4.6. Photograph of the power divider.

The insertion loss of the power divider is measured with a network analyzer, and the results are displayed in Fig. 4.7. These are plots of the insertion loss and phase shift from the input to each of the outputs, so ideally the insertion loss and phase shift of all the outputs would be equal to one another. The simulation shows that, at every frequency, the insertion loss of any two outputs differ by less than 0.19 dB, and the phase shifts differ by less than 1°. The measurements show that the insertion losses

differ by less than 1.16 dB, and the phase shifts differ by less than 14°. This error in measured values is most likely due to fabrication errors, namely connector inconsistencies.

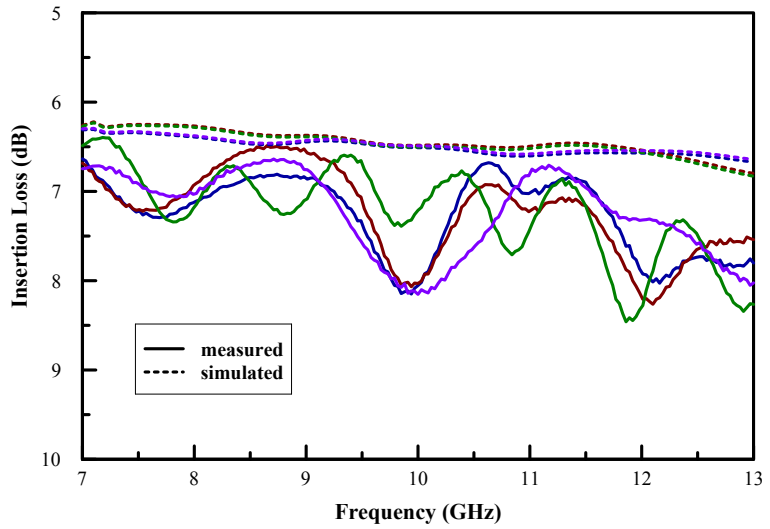

(a)

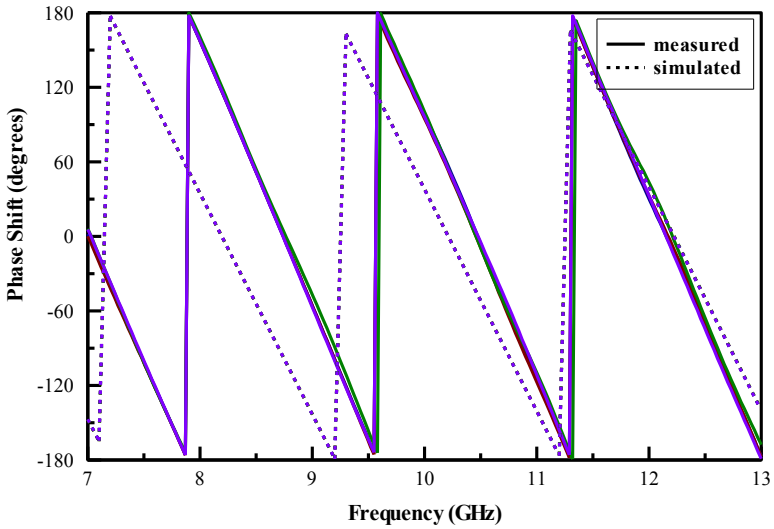

(b)

Figure 4.7. Measured and simulated (a) insertion loss and (b) phase shift of the power divider.

C. Phase-Shifters

Four digital phase-shifters are needed to control the phased array (one shifter for each element), and there are a number of varieties and options available on the market. Some of the phase-shifters are packaged as a sealed unit in a hardened case which is durable but also large and expensive. The other option is a monolithic microwave integrated circuit (MMIC) which is much cheaper and smaller. They are typically a few square millimeters and can be directly integrated into the antenna array. Using MMIC phase-shifters would allow the entire phased array (antenna, phase-shifters, and power divider) to be fabricated together and be very compact. The downside to the MMIC is that they can be very fragile, and if an integrated phase-shifter breaks then the whole array assembly must be discarded and rebuilt. The other downside is that special equipment is required to mount and connect MMICs, and unfortunately this lab does not have access to that equipment.

There is another option for using MMIC phase-shifters which overcomes this lab's inability to mount them. The companies which manufacture MMICs usually also make an evaluation board with the MMIC already mounted on a board and attached to external connections. Using evaluation boards would sacrifice some of the MMICs advantages since it would no longer be possible to fabricate the entire phased array together, and they are more expensive than the standalone MMICs. However, the evaluation boards are still smaller and less expensive than the sealed units. For these reasons, MMIC evaluation boards will be used in the system.

The Hittite HMC543LC4B phase-shifter is chosen for use in this system mainly for its price. It is a 4-bit digital phase-shifter which operates from 8 – 12 GHz. It has 360° coverage, so 4-bits means that the smallest possible adjustment is 22.5°. A photograph of the HMC543LC4B phase-shifter evaluation board can be seen in Fig. 4.8.

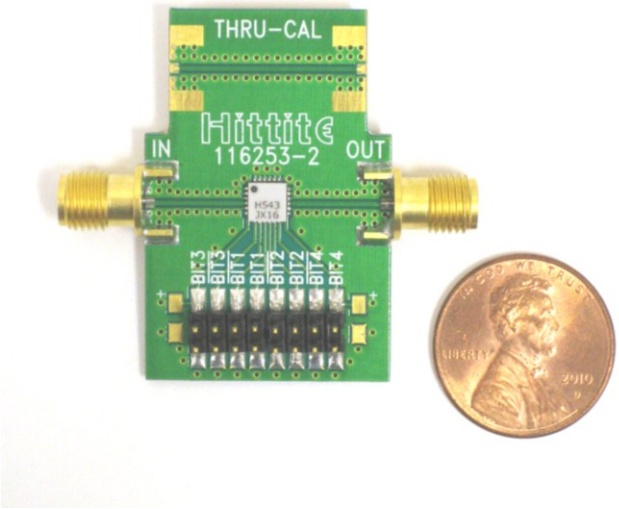

Figure 4.8. Photograph of the Hittite HMC543LC4B phase-shifter evaluation board.

The S-parameters of the phase-shifter are measured with a network analyzer, and the results can be seen in Figs. 4.9-4.10. Each line in the graphs represents a different phase setting. The insertion loss for each phase setting (Fig. 4.9) ranges from 6.3 – 8.3 dB which is a range of 2 dB. However, at any given frequency, the insertion loss varies by less than 1.6 dB, and at 10 GHz it varies by less than 0.6 dB. The variation in insertion loss increases for frequencies farther away from the center frequency of 10 GHz. This insertion loss variation will create a deviation from the

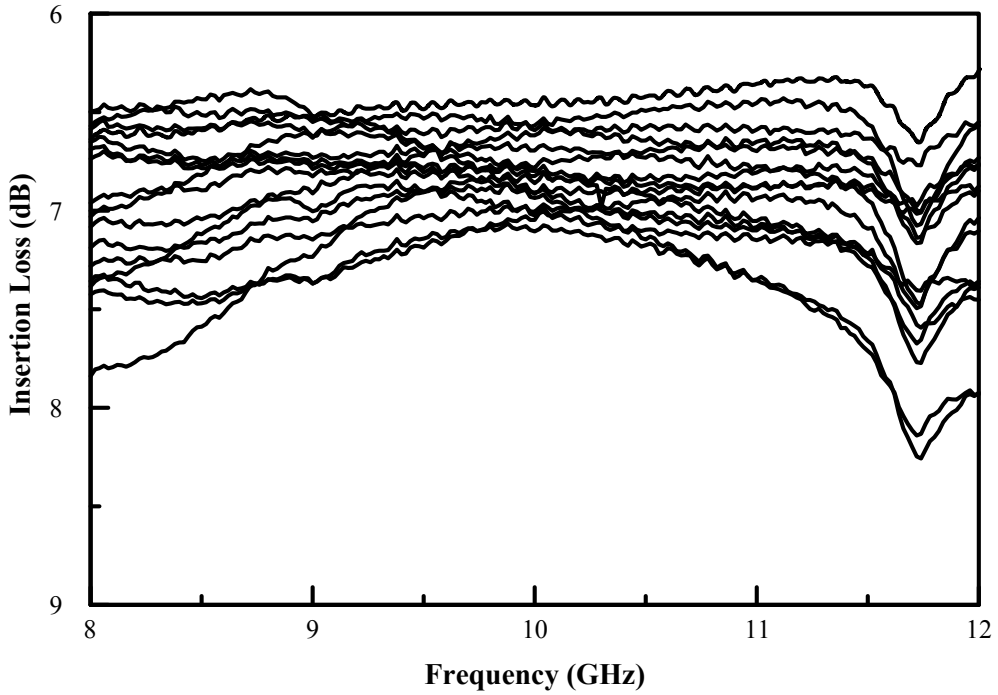

Figure 4.9. Measured insertion loss of the phase-shifter at all phase settings.

planned uniform amplitude distribution, and if variable amplifiers were included in the design, this variation could be accounted for.

Fig. 4.10a illustrates the relative phase shift of each setting where each setting is relative to the 0° state. Ideally each setting would be 22.5° from the previous setting, but some deviation exists. This deviation can be seen in Fig. 4.10b which illustrates the amount that each setting deviates, and it can be seen that there is a maximum deviation of 12°. This phase deviation can be corrected in the calibration. However, the phase shift error of each state is not consistent for all frequencies, and it can vary by as much as 18° (as a function of frequency) for some states. Hence, if the system is calibrated at

one frequency, there will be some phase error introduced at other frequencies by the inconsistencies of the phase-shifter. Of course this can be corrected by recalibrating at other frequencies and using different settings for different frequencies, but if the system is to be used in a broadband application, a single setting should be used.

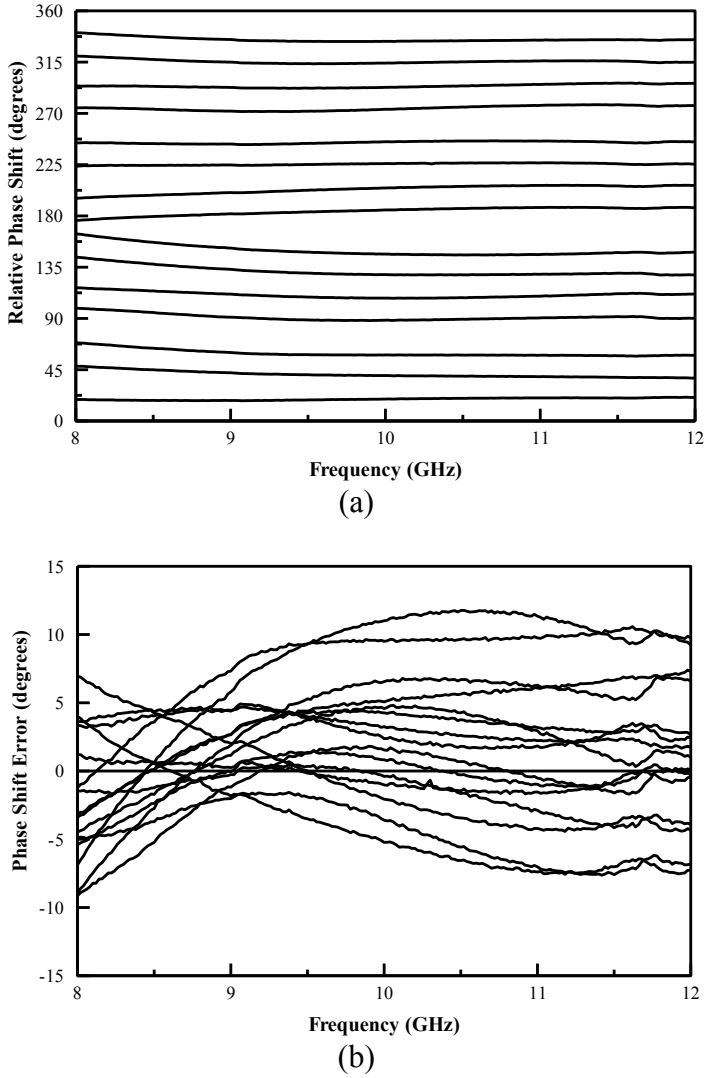

Figure 4.10. Measured (a) relative phase shift of the phase-shifter at all phase settings and (b) phase shift error.

D. Phase-Shifter Control

To steer the phased array, the phase-shifters must be digitally controlled by a computer. There are four 4-bit shifters, so 16 bits of information are required. LabVIEW [27] can be used in conjunction with a Data Acquisition (DAQ) device to provide the 16 bits. An NI USB-6509 Digital I/O device will serve as the DAQ with an NI CB-50 connector box providing the connection terminals. This DAQ provides 96 channels (operating on the 5 V TTL/CMOS standard) which will allow room for the array to grow at a later date. Photographs of the DAQ and connector box can be seen in Fig. 4.11.

(a) (b)

Figure 4.11. Photographs of (a) the NI USB-6509 DAQ and (b) the NI CB-50 connector box.

LabVIEW can be used to convert the desired phase to a 4-bit representation which can be sent to the phase-shifter. The conversion procedure is as follows:

1.) Shift phase to the range 0 - 360° [phase modulo 360]

2.) Convert phase to a 4-bit representation [round(phase/22.5)]

3.) If the result is 16, change this to 0 (16 is an overflow)

Outputs are sent in packets of 8 bits, so two phases should be combined into one 8-bit output as follows:

1.) (4-bit phase 1) + (4-bit phase 2) x 16

where the least significant bits (LSBs) are for shifter 1 and the most significant bits (MSBs) are for shifter 2. This procedure is used to develop an easy to use LabVIEW interface (Fig. 4.12), and the details of the implementation can be seen in the appendix.

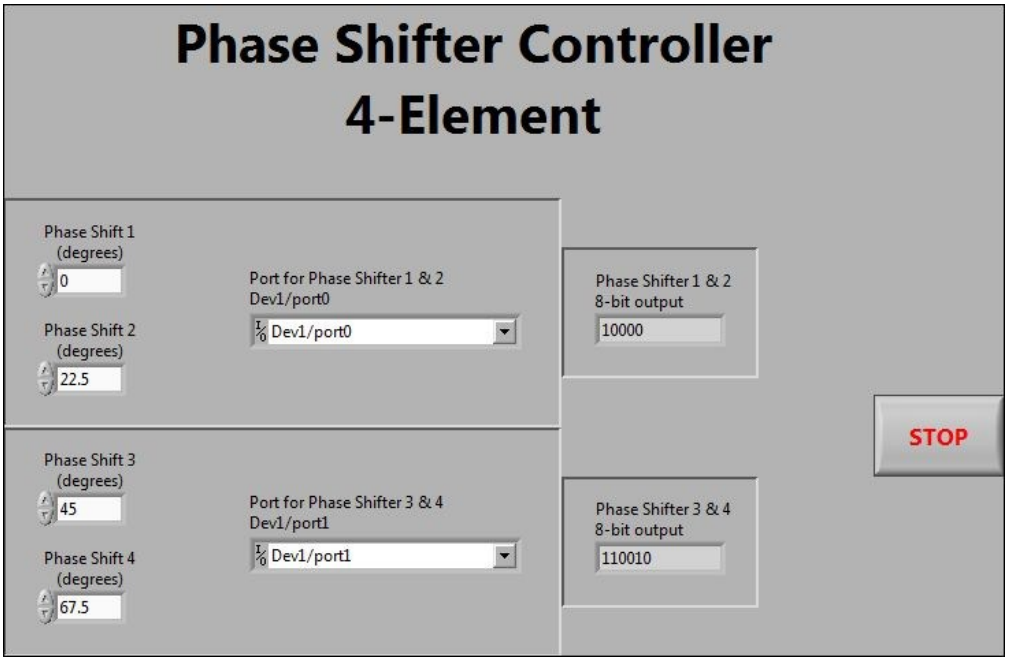

Figure 4.12. LabVIEW interface for controlling four 4-bit phase-shifters.

E. Phase-Shifter Logic Conversion

LabVIEW and the DAQ provide the standard 5 V TTL/CMOS logic, but unfortunately the phase-shifters require a complementary logic of 0/-3V. In this logic scheme, each bit of information requires two control lines (one with 0 V and the other with -3 V). A converting circuit must be designed to convert all 16 control bits into 32 bits of this 0/-3V complementary logic. A circuit design [28] as seen in Fig. 4.13 can be used to convert each bit.

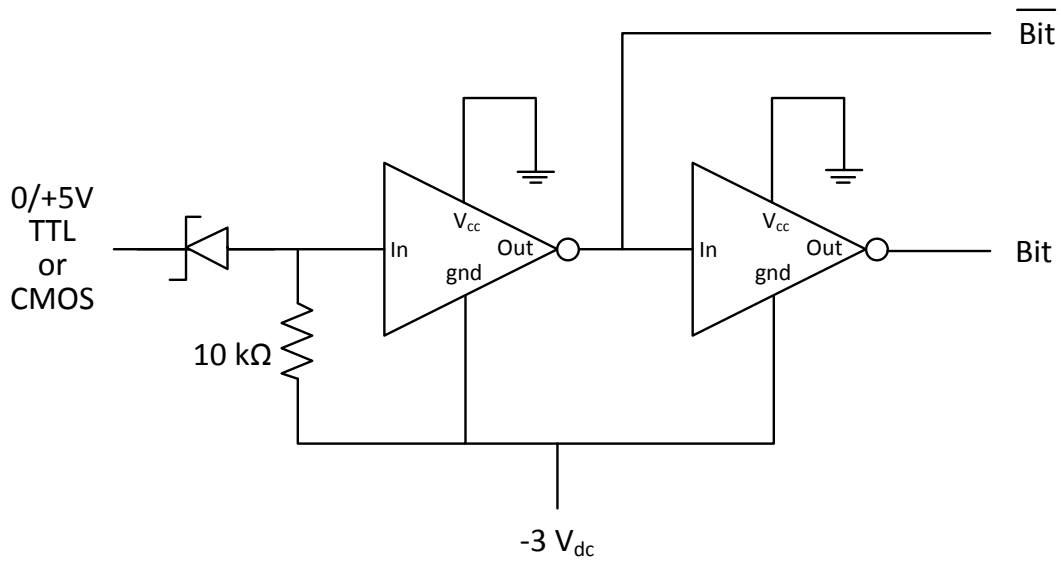

Figure 4.13. Circuit to convert 5 V TTL/CMOS logic to 0/-3V complementary logic.

This circuit contains two inverters (Philips Semiconductors 74HC04), a 10 kΩ resistor, and a zener diode (ON Semiconductor MMSZ4689T1, V_z = 5.1 V, I_{zt} = 50 μA). When the input is 5 V, the diode will conduct, and the 5 V zener voltage drop will cause 0 V to appear at the input of the first inverter. This will cause the inverter to connect its

gnd (which is connected to -3 V) to its output. Then -3 V will appear at the output $\overline{Bit}$, and the second inverter will connect its V_{cc} (which is connected to ground) to its output which is the output *Bit*. This will make $\overline{Bit}$ = -3 V and *Bit* = 0 V. When the input is 0 V, the diode will not conduct, and -3 V will appear at the input to the first inverter. This will cause the inverter to connect its V_{cc} (which is connected to ground) to its output. Then 0 V will appear at the output $\overline{Bit}$, and the second inverter will connect its *gnd* (which is connected to -3 V) to its output which is the output *Bit*. This will make $\overline{Bit}$ = 0 V and *Bit* = -3 V.

This circuit must be implemented 16 times in order to convert all of the bits. The most clean and efficient way to do this is with a Printed Circuit Board (PCB) which can be designed using Protel DXP 2004 [29]. The input and outputs for each bit are grouped together and placed on the left and right sides of the PCB. A connection for ground and a -3 V_{dc} source are placed at the bottom, and the inverter DIPs run down the center. The grounds and the -3 V_{dc} leads are connected on the backside of the board. The DXP schematic and a photograph of the assembled PCB can be seen in Fig. 4.14.

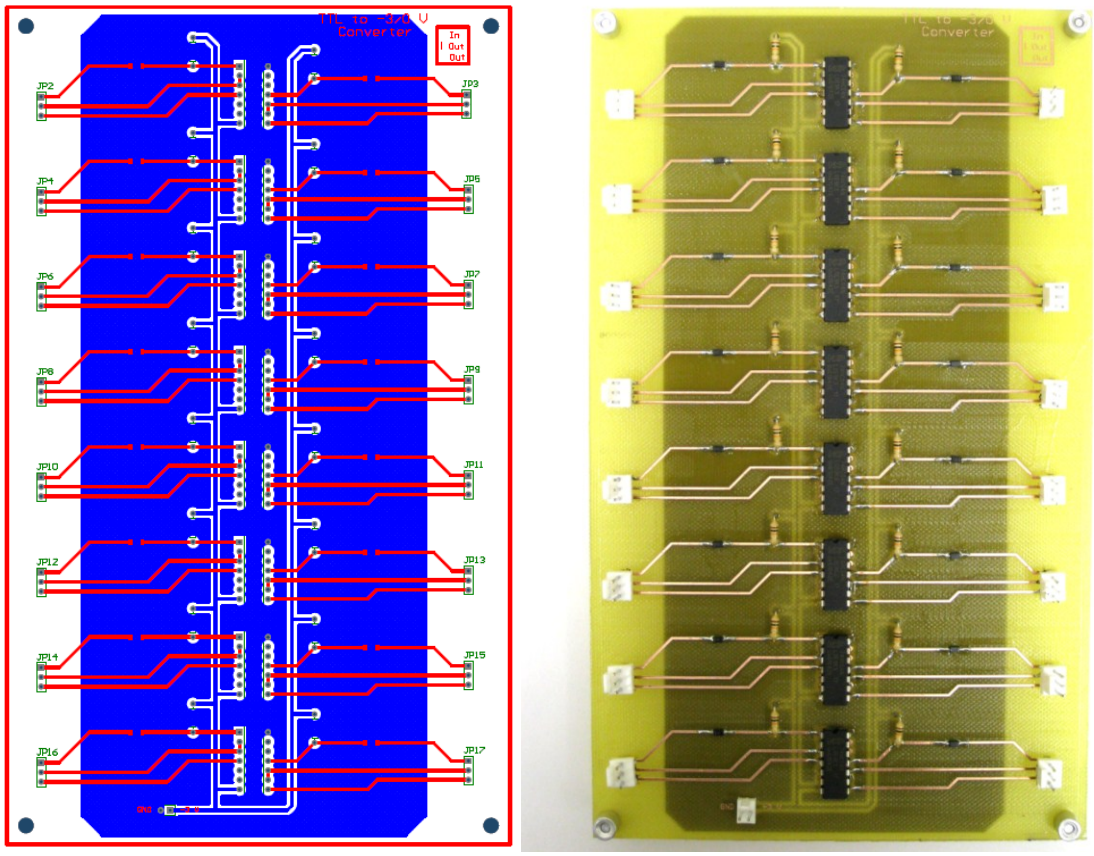

(a) (b)

Figure 4.14. PCB to convert 5 V TTL/CMOS logic to 0/-3V complementary logic. (a) Schematic and (b) photograph.

F. Phased Array Assembly

The antenna array, phase-shifters, and power divider are connected and fixed together using a bracket as illustrated in Fig. 4.15. Each polarization will be measured separately with the feeds for the other polarization terminated with 50 Ω loads as shown in the photograph. Three-inch coaxial cables (Mini-Circuits Hand-Flex 086-3SM+) are used to connect the antenna array to the phase-shifters since they can easily be formed to the necessary shape, and the phase-shifters and power divider are directly connected with SMA connectors.

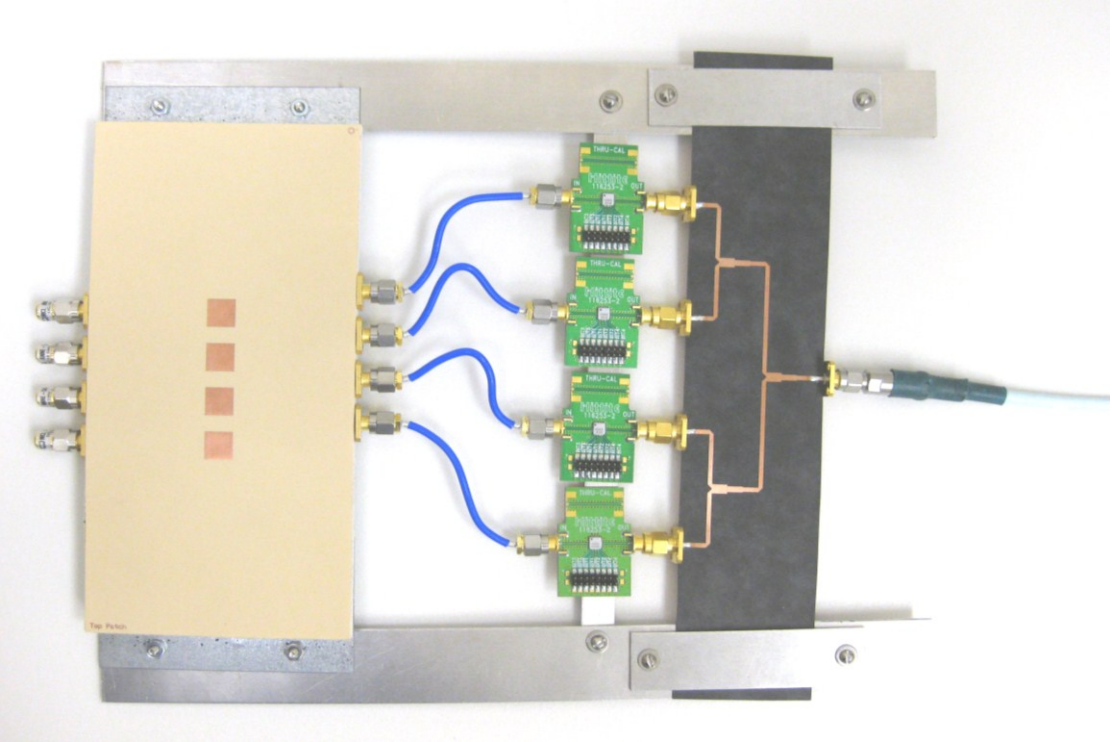

Figure 4.15. Photograph of the array assembly (antenna array, phase-shifters, and power divider) fixed together by a bracket.

The phase-shifters must be wired to the logic converter circuit and the LabVIEW DAQ. Due to the fragility of the phase-shifters, a protective shield is built to protect them from harmful external disturbances as shown in Fig. 4.16. The array assembly is surrounded by absorber to prevent reflections; this is done by placing the assembly in a large hollowed out chunk of absorber and then covering it with layers of absorber as shown in Fig. 4.17.

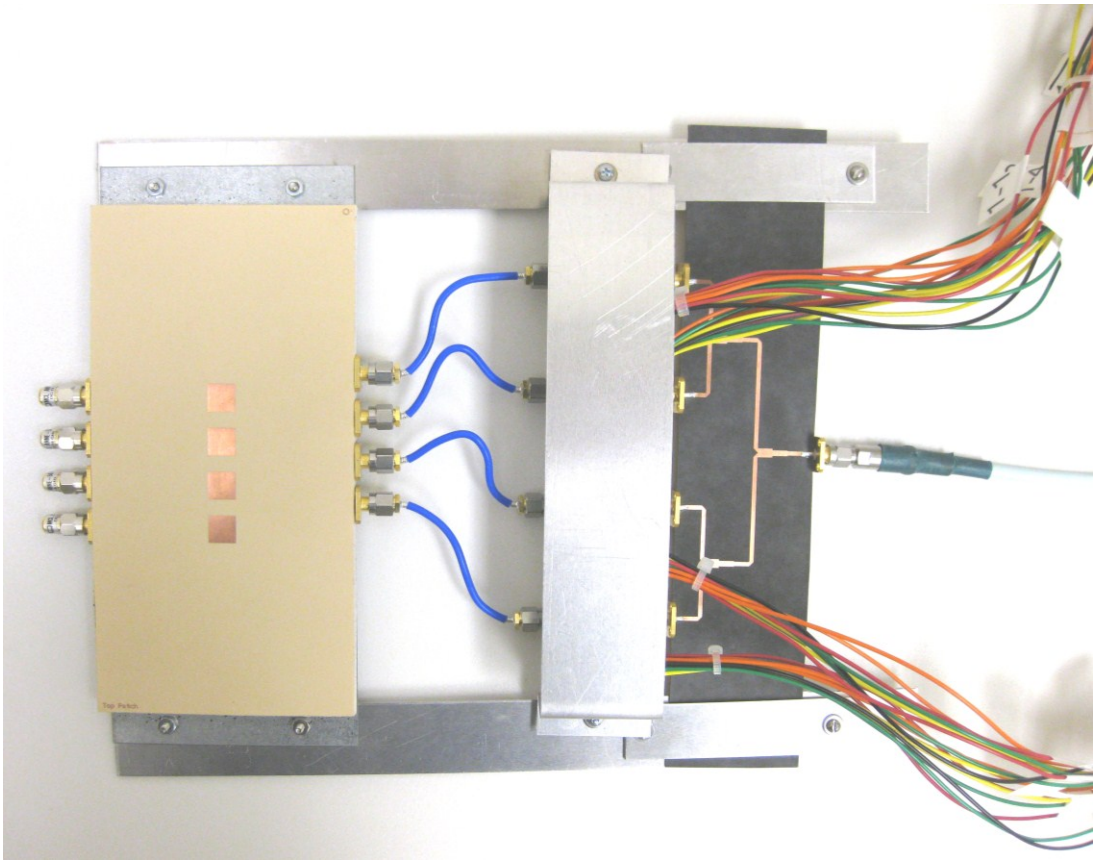

Figure 4.16. Photograph of the array assembly with a protective shield over the phase-shifters.

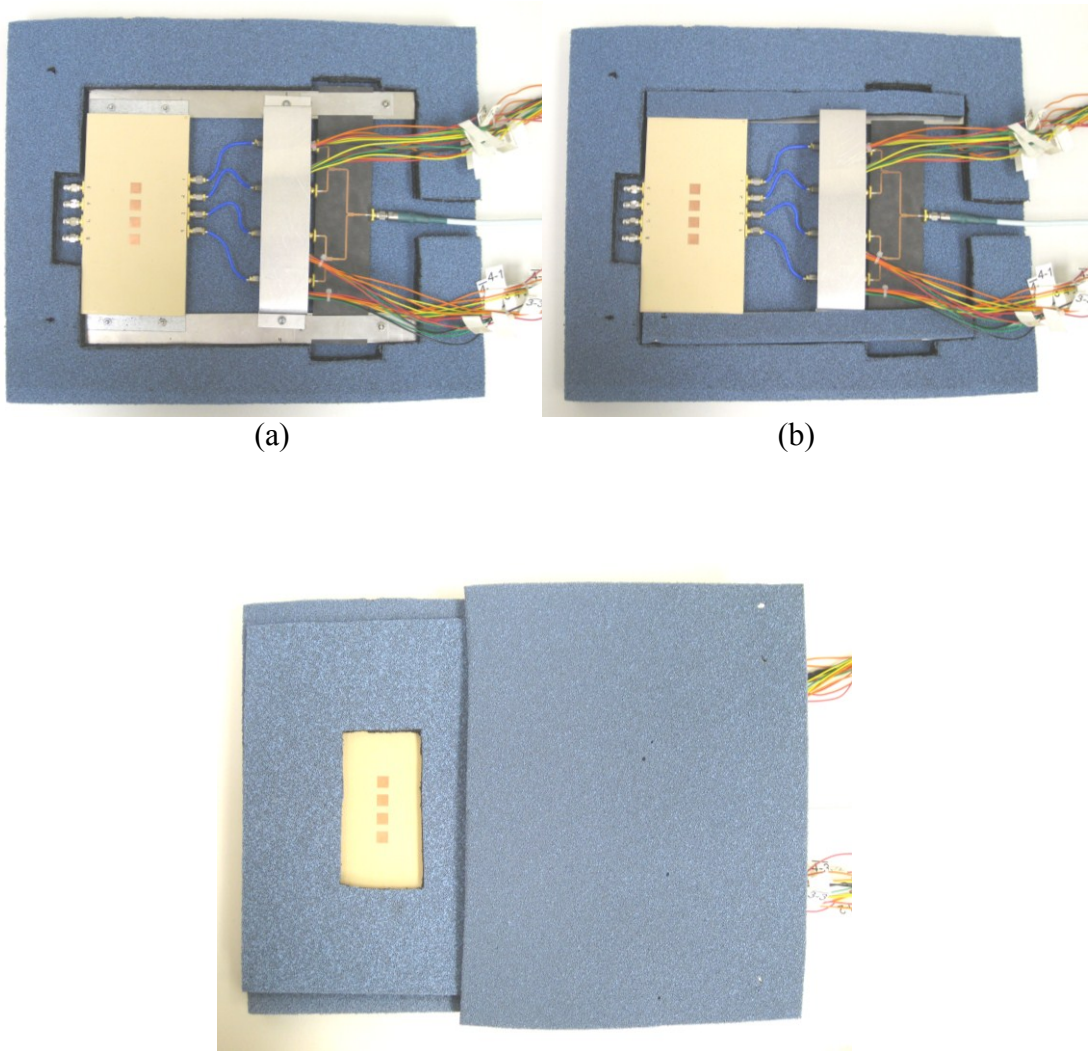

Figure 4.17. Photograph of the array assembly. (a) Placed in a hollowed out chunk of absorber, (b) protected by pieces of absorber, and (c) covered with layers of absorber.

To operate the phased array and take measurements in the anechoic chamber, the array assembly (Fig. 4.17) is mounted inside the chamber, and the wires controlling the phase-shifters are run under the chamber door so that the phase-shifter controlling equipment does not disturb the measurements. These wires are connected to the logic converter circuit which is connected to the connector box which is connected to the DAQ which is connected to a computer running LabVIEW. This arrangement is illustrated in Fig. 4.18, and a photograph can be seen in Fig. 4.19.

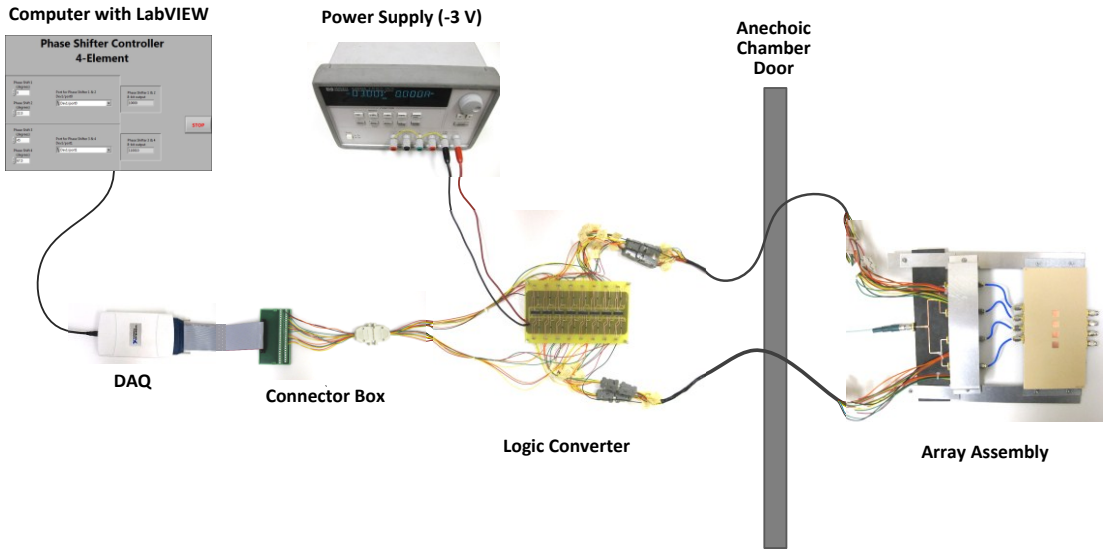

Figure 4.18. Diagram of the phased array system setup.

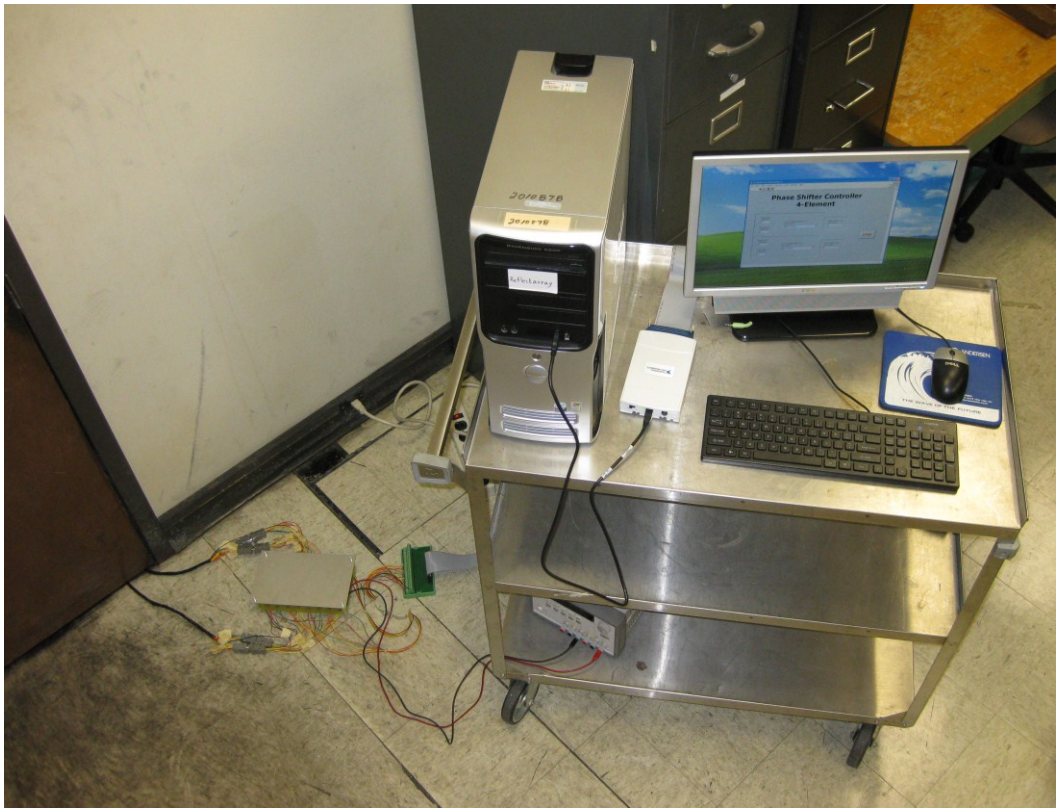

Figure 4.19. Photograph of the phased array system setup.

G. Phased Array Calibration

Before the phased array can be used for the first time, it must be calibrated. Unequal line lengths, phase-shifter errors, and mutual coupling [30] prevent simply offsetting each phase-shifter by identical phases to create the desired scan angle.

Unequal line lengths have the most dramatic effect on calibration. A simple method to calibrate the array is to merely measure the amount of phase shift that the input signal undergoes while traveling through the power divider, phase-shifter, and coaxial line on its way to each feed. The difference in measured phase shift for each

feed can then be subtracted from the desired shift of that feed. The measured phase shifts for lines 1 – 4 are -100°, 65°, 55°, and 60° respectively. There is a difference in phase shift between lines 1 and 4 of 165° which is quite large. However, using this calibration method, the effect of these unequal line lengths can be tuned out. One drawback of this technique is that it does not take into account the phase-shifter errors of each state (as seen in Fig. 4.10b) or mutual coupling [30].

All effects can be accounted for if a far-field phase-alignment calibration approach is used. For this calibration technique, the phased array system is assembled in an anechoic chamber (as seen in Fig. 4.18), and the antenna is oriented at broadside for the duration of the calibration. Each antenna element must be isolated by terminating the other elements' feeds. A far-field gain measurement is then made for all phase states of that element. This is repeated by then isolating the other elements, one at a time, and repeating the measurements for each element. Once a table containing the phase shift of each element for all phase states has been made, the phase settings to be used can be obtained from the calibration table. For example, if a scan angle of 0° is required, phase settings for each shifter should be chosen such that their values in the calibration table are equal. If the array is to be scanned to an angle θ_0, then the phase β between array elements should be

$$\beta = -kd \sin \theta_0 \tag{4.6}$$

where *d* is the separation between elements and *k* is the wave number. Then phase settings for each shifter should be chosen such that their values in the calibration table are x, x+β, x+2β, x+3β where x is any number. A plot of the data from one of the calibrations can be seen in Fig. 4.20.

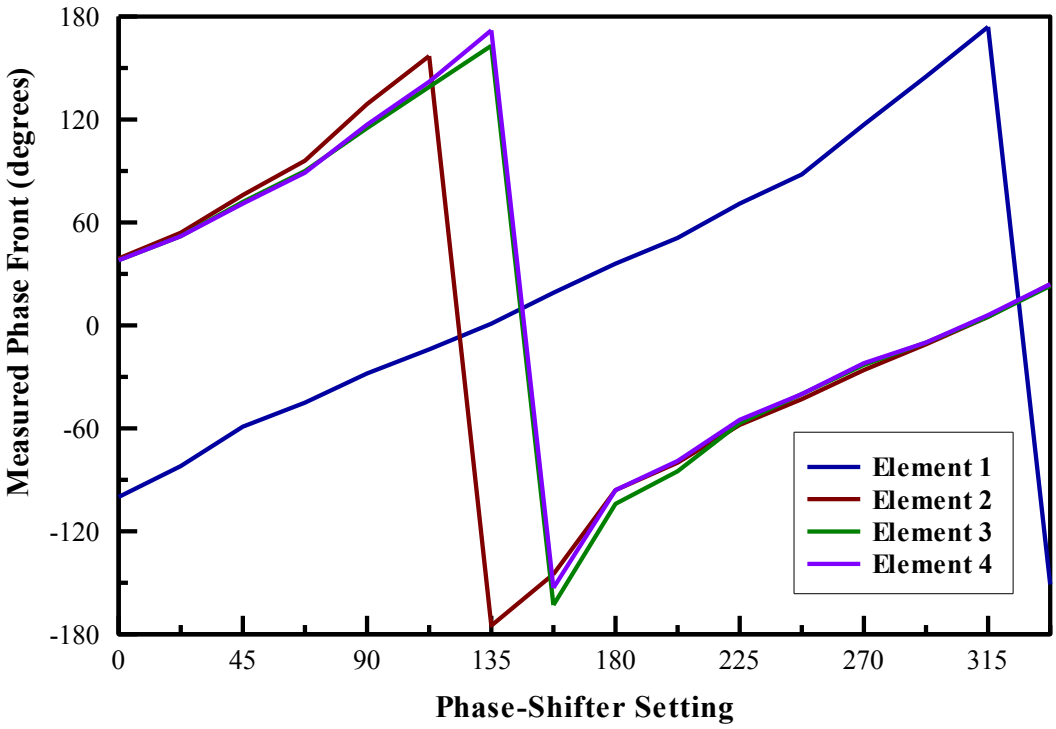

Figure 4.20. Plot of a typical calibration table for the four elements.

There is one small problem with using the far-field phase-alignment method for this phased array. The elements not under test must be terminated, and since variable amplifiers are not used, the only way to do this without disturbing the antenna position is to remove the phase-shifter control lines. This effectively isolates the unwanted elements, but it does this by reflecting power from the phase-shifter rather than

terminating the power. The reflected power from the unwanted elements will combine and interfere with the transmission to the element-under-test. The goal is to isolate the element-under-test and measure it under the same conditions that will be encountered in normal operation, but these reflections disturb that normal operating condition. However, the phase difference from terminating the unwanted elements with a 50 Ω load and unplugging their phase-shifters was measured to be less than 9°, and the variation of this change between elements was measured to be less than 4°. Therefore, the error introduced by unplugging the unwanted elements, rather than terminating them, is minimal.

A comparison of the far-field phase-alignment calibration method and the line length adjustment calibration method is illustrated for a 0° scan angle in Fig. 4.21. Both calibration methods work, but the far-field phase-alignment method gives a higher gain and a nicer beam shape. Consequently, the far-field phase-alignment method will be used.

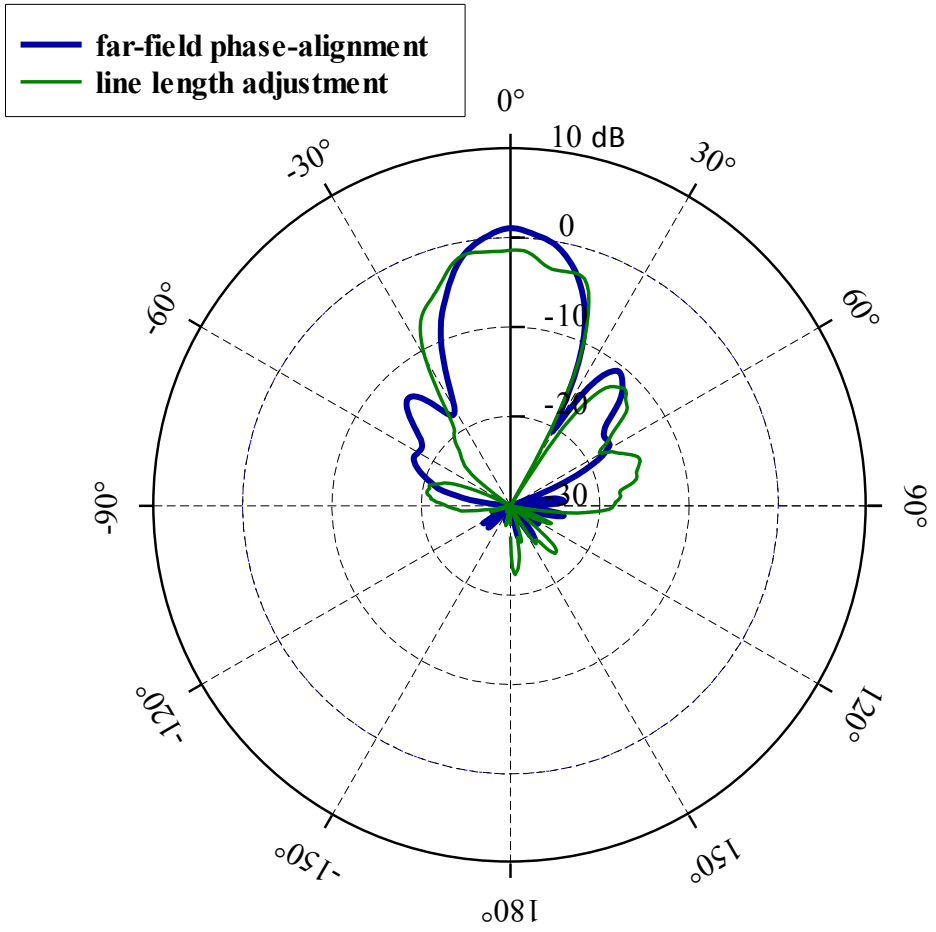

Figure 4.21. Comparison of two phased array calibration methods (the far-field phase-alignment method and the line length adjustment method). Measurement is for a 0° scan angle.

H. Pattern Measurements

The phased array system (Fig. 4.18) is calibrated at 10 GHz, and the pattern is measured from 8.5 to 12 GHz in increments of 0.5 GHz and for scan angles from 0 to 90° in increments of 10°. The array scans as intended and works fairly well, but there are a few abnormalities with the pattern and scan loss. The gain oscillates some with observation angle, and peak gain can sometimes increase with increasing scan angle. This could be caused by a number of factors such as: resonant modes caused by reflection and interaction with array assembly metal, phase quantization errors, calibration errors, and phase-shifter insertion loss variation with phase setting.

The effect from resonant modes caused by reflection and interaction with array assembly metal can be reduced by replacing the array assembly mounting structure with lexan and nylon screws as illustrated in Fig. 4.22a. Also, adding more absorber around the SMA connectors (Fig. 4.22b) and another layer of absorber on top (Fig. 4.22c) can help to prevent and attenuate any reflected waves.

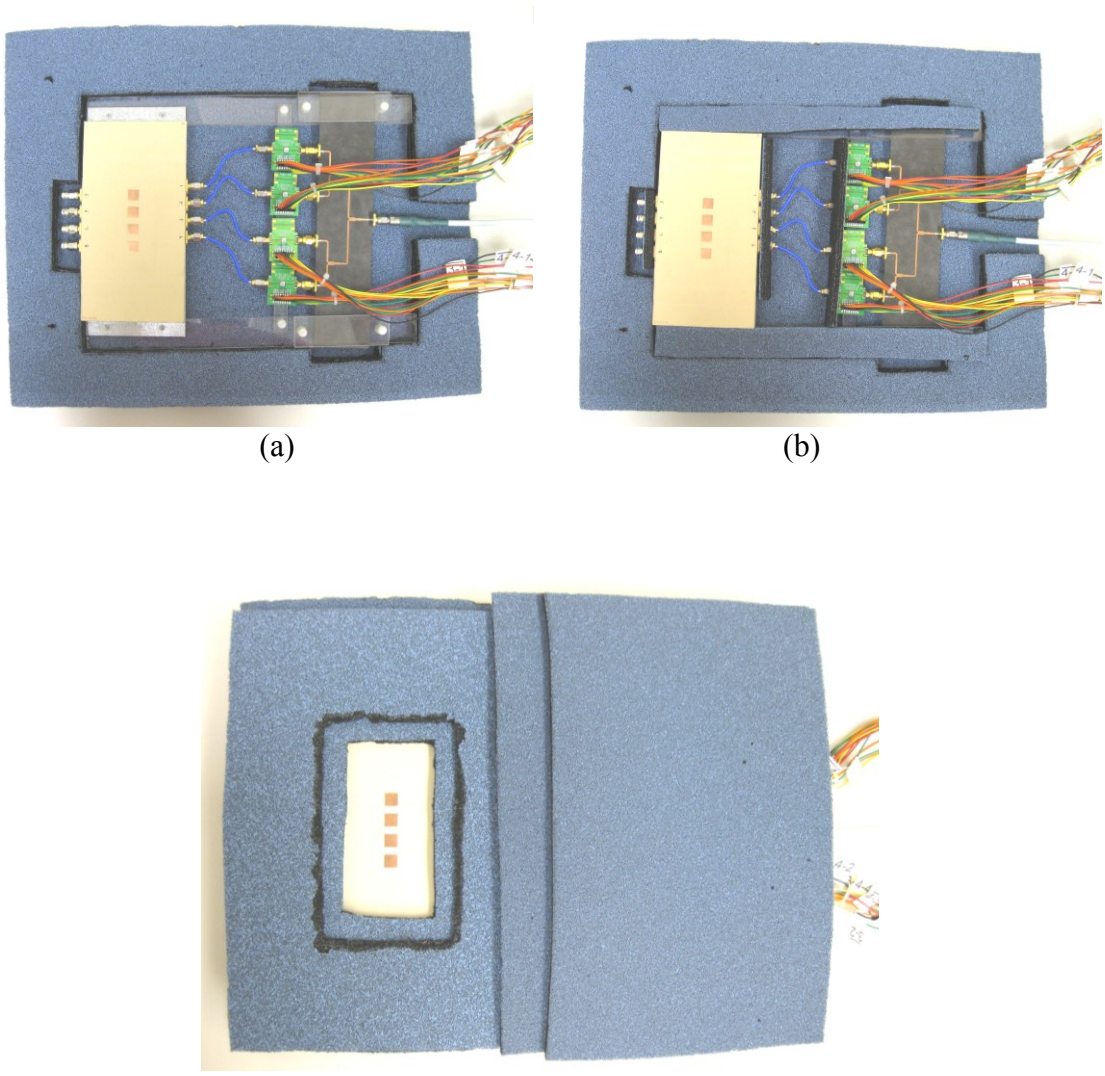

(a) (b)

(c)

Figure 4.22. Photograph of the array assembly with lexan and nylon screws. (a) Placed in a hollowed out chunk of absorber, (b) protected by pieces of absorber, and (c) covered with layers of absorber.

The phase quantization error can be reduced by strategically choosing the reference element which will result in minimum phase quantization error rather than choosing this reference element at random. Since the phase-shifter states are not separated by exactly 22.5°, reference element choice can make a significant difference in phase quantization error. The optimum phase settings for a given phase β can be found using a Matlab [31] program which can be seen in the appendix. If a reference element is chosen at random, the phase error from each element is usually less than 5-12°. However, if the Matlab program is used, the phase error from each element is usually less than 1-3°. This will increase the calibration accuracy and should more correctly align the phase fronts of the elements.

The revamped phased array assembly seen in Fig. 4.22 is calibrated at 10 GHz, and phase-shifter settings are chosen using the Matlab program. The array pattern is then measured as before. The results are similar, but the gain oscillation is reduced, and the scan loss is closer to expectation. Some of the measurements can be seen in Figs. 4.23-4.28.

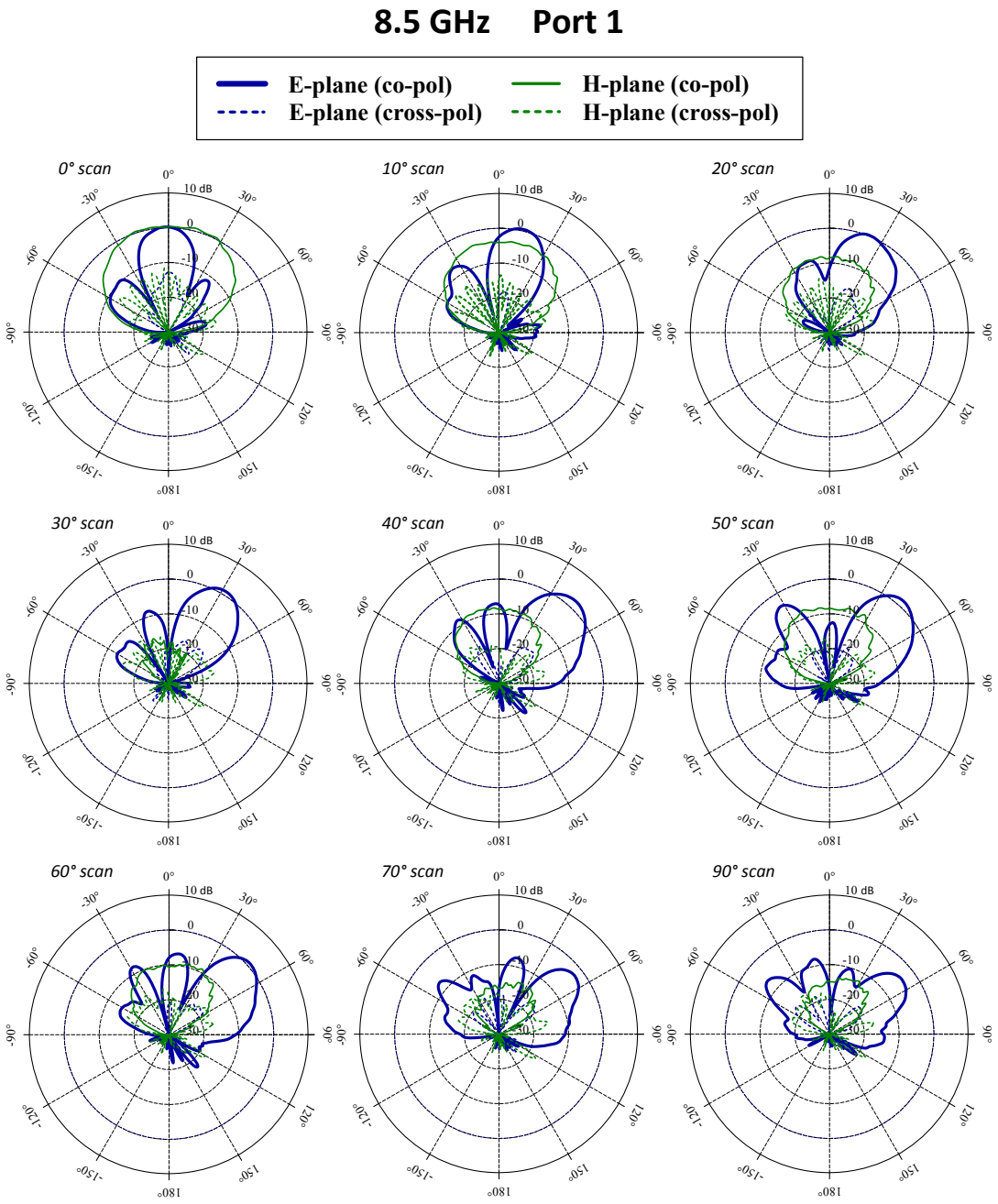

Figure 4.23. Measured radiation pattern of the 4-element phased array. Port 1 at 8.5 GHz.

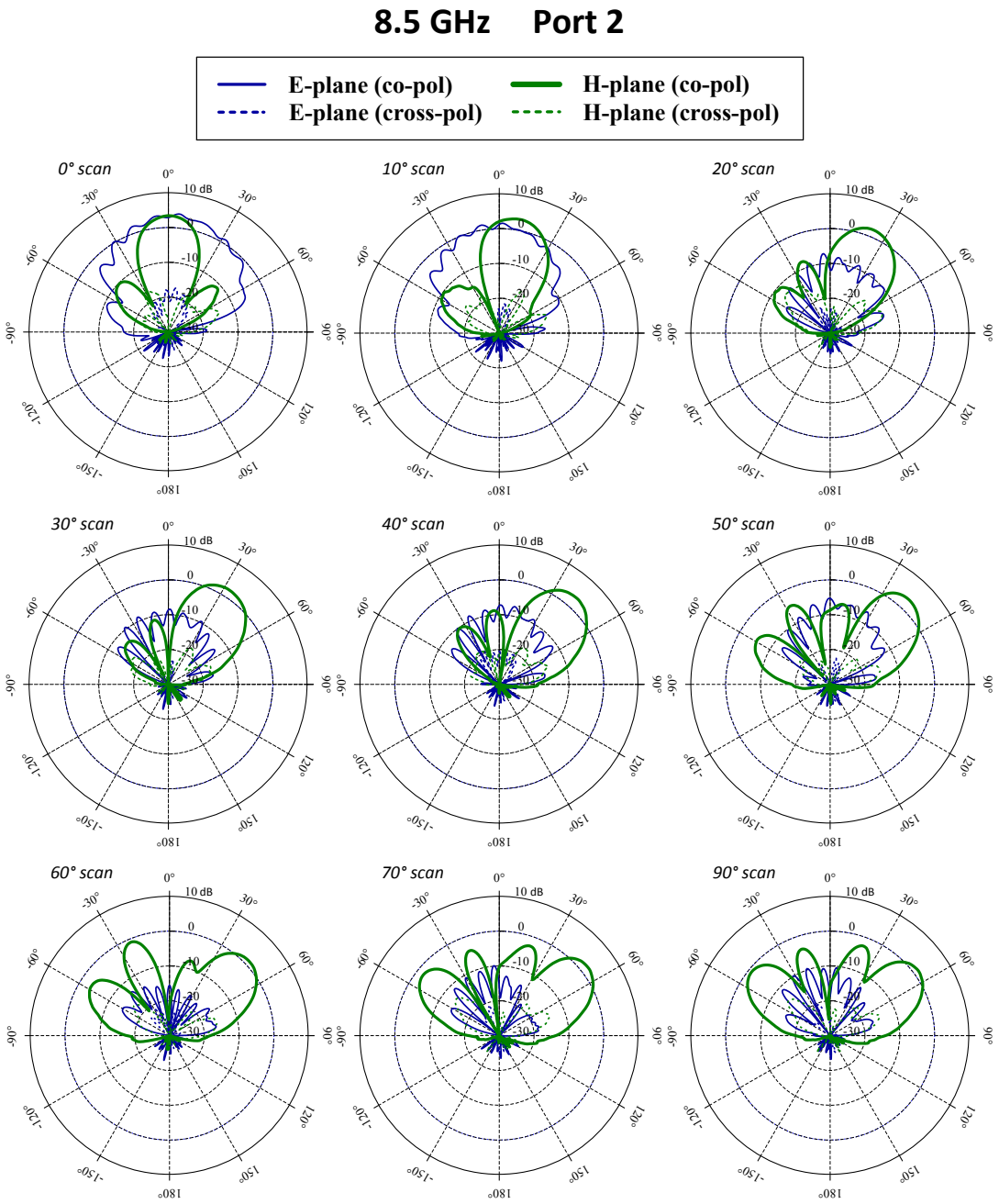

Figure 4.24. Measured radiation pattern of the 4-element phased array. Port 2 at 8.5 GHz.

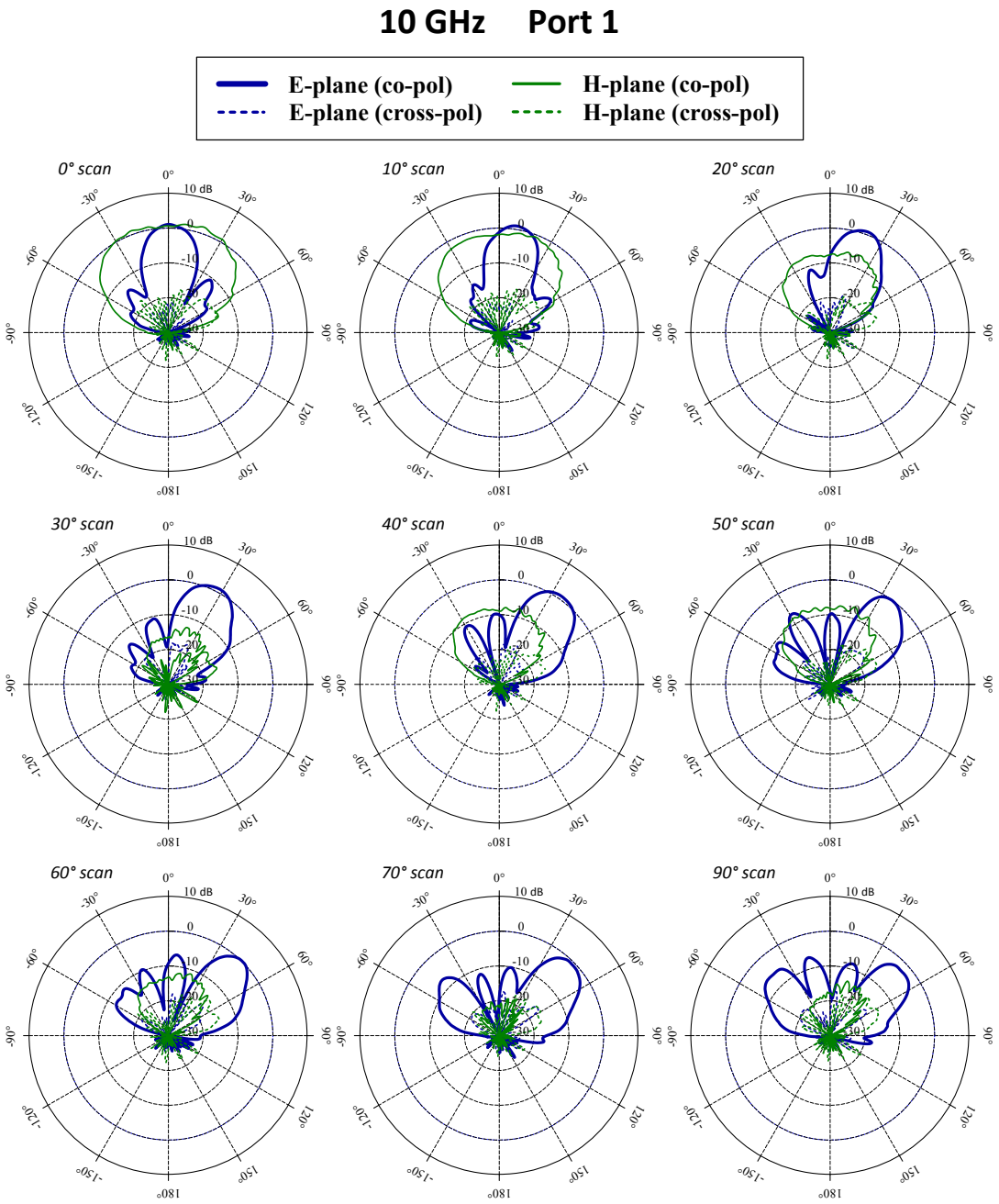

Figure 4.25. Measured radiation pattern of the 4-element phased array. Port 1 at 10 GHz.

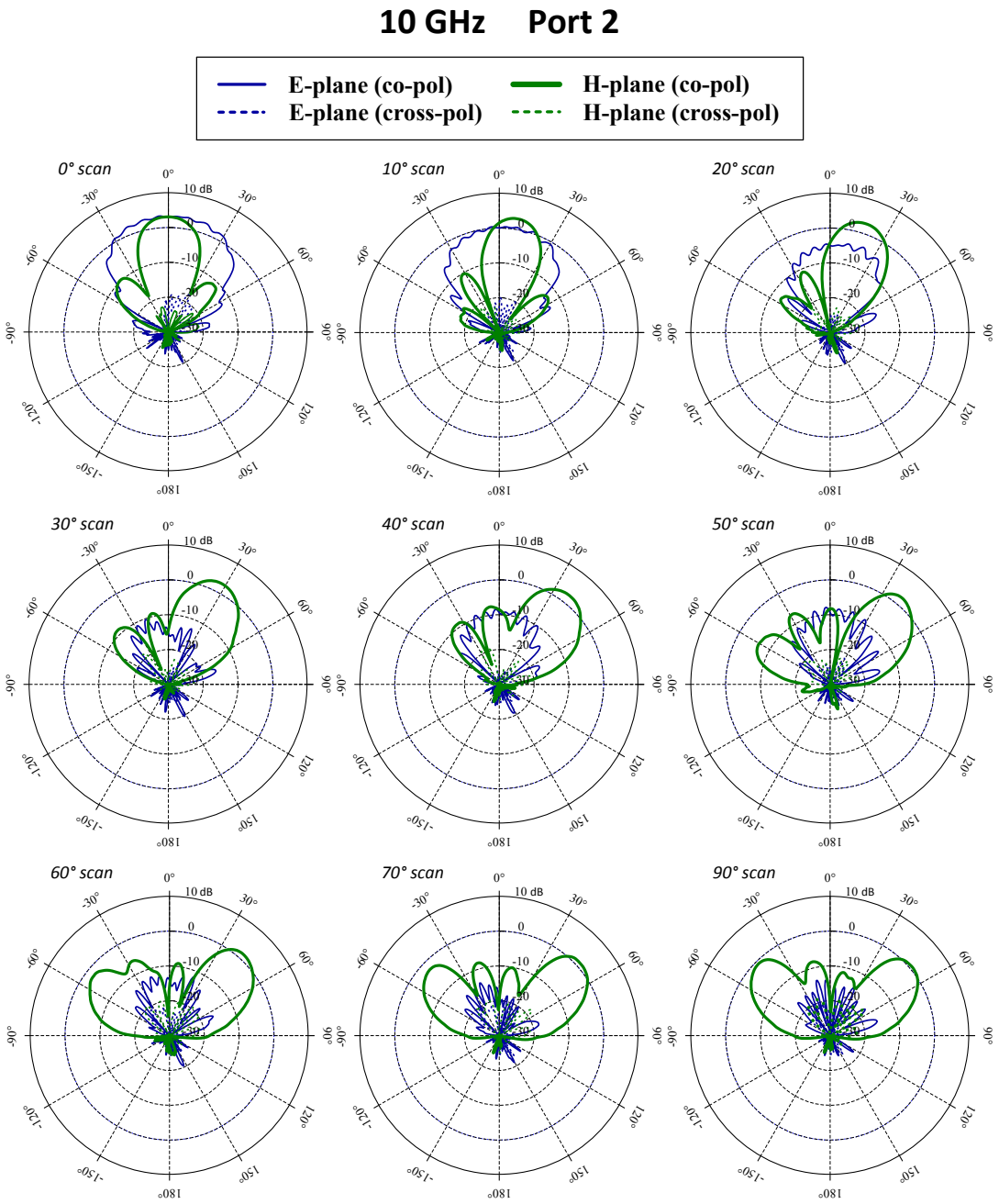

Figure 4.26. Measured radiation pattern of the 4-element phased array. Port 2 at 10 GHz.

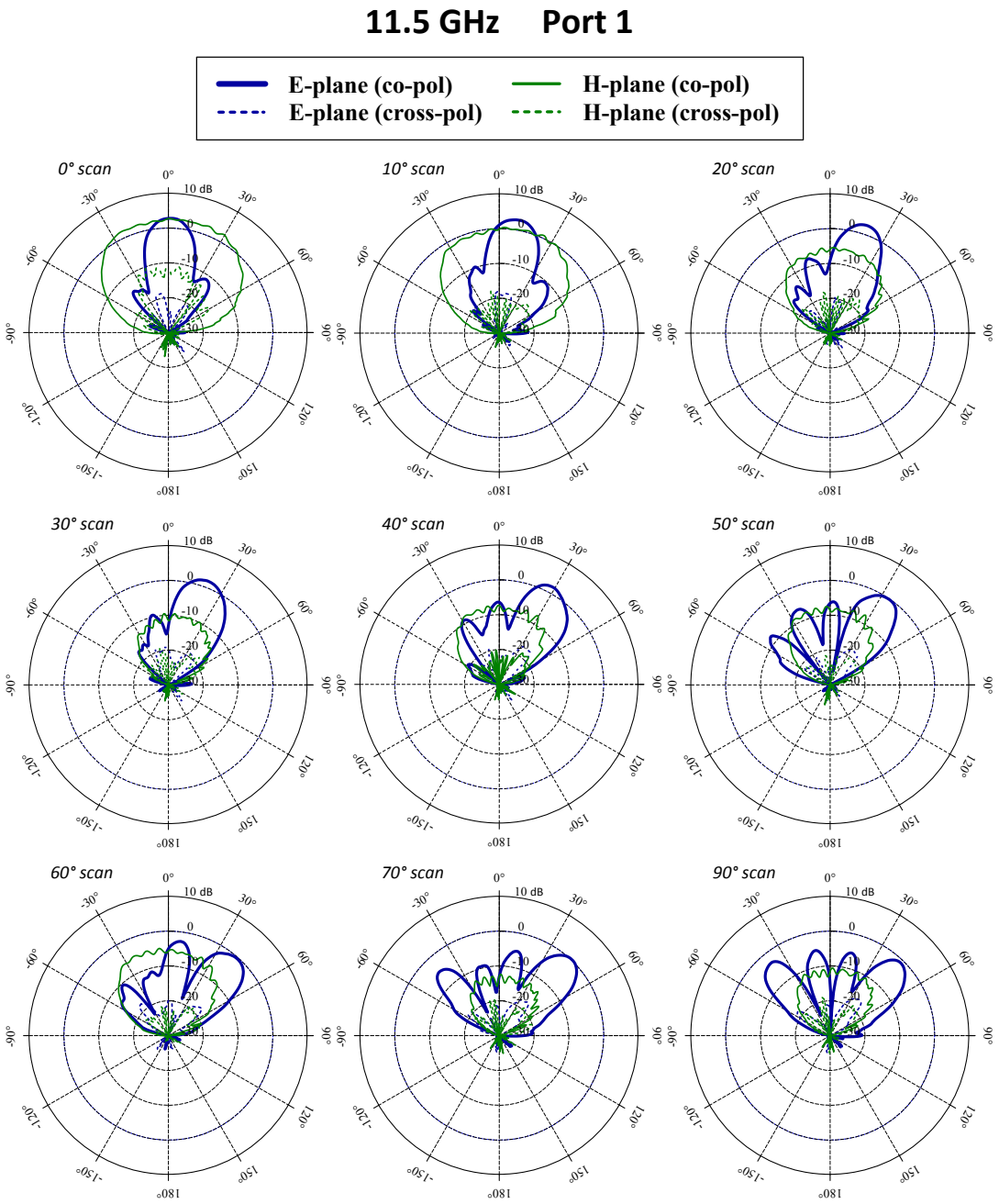

Figure 4.27. Measured radiation pattern of the 4-element phased array. Port 1 at 11.5 GHz.

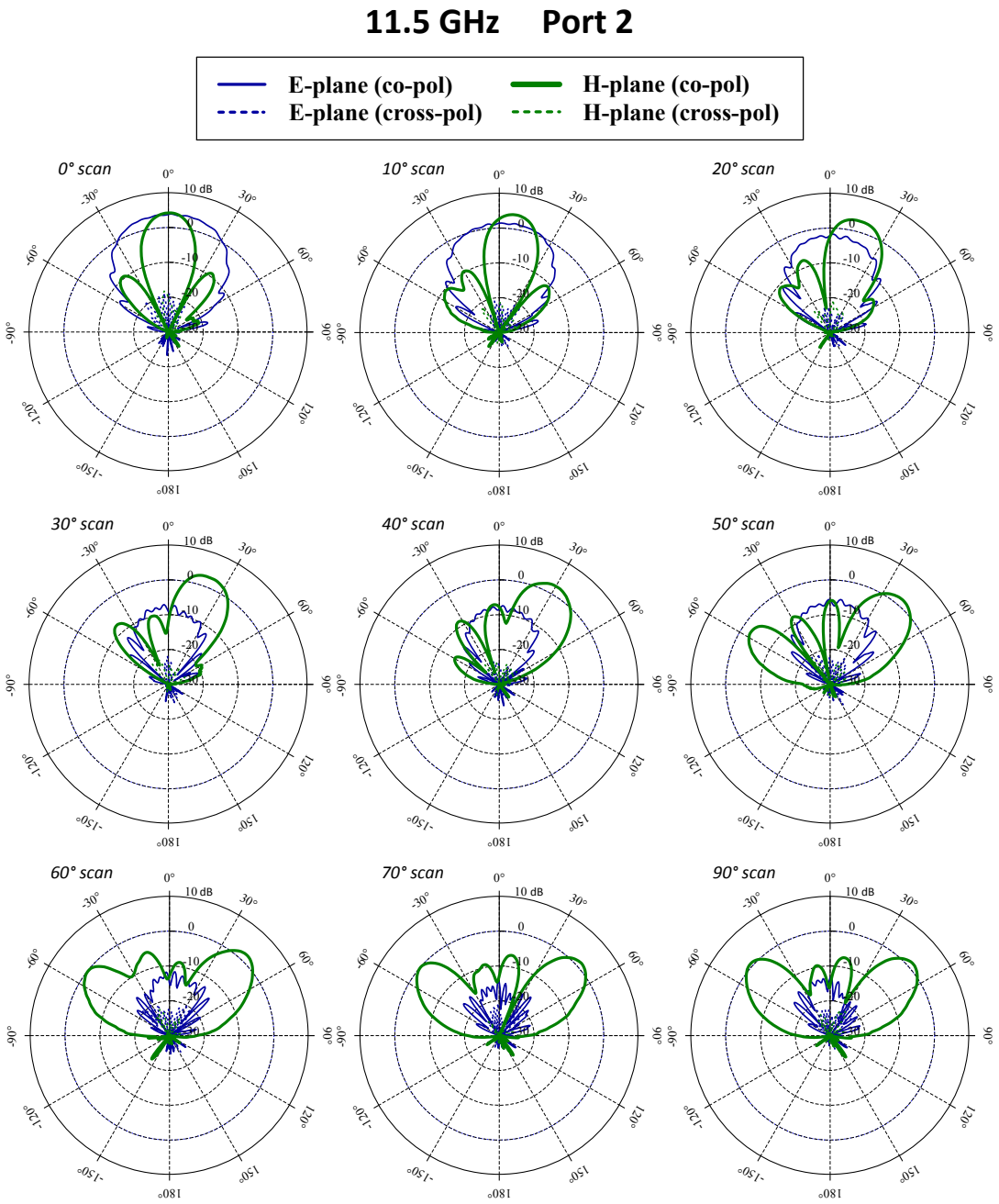

Figure 4.28. Measured radiation pattern of the 4-element phased array. Port 2 at 11.5 GHz.

Since this is a dual-polarized array, the E-plane is the scanning plane for port 1, and the H-plane is the scanning plane for port 2. At the center frequency (10 GHz), the array scans from a setting of 0° to 40° with virtually no change in peak gain (i.e., no scan loss). At the 50° setting, peak gain starts to decrease and continues through the 90° setting. This is caused by the directionality of the single-element antenna which is used. Also, the array steers to an angle slightly less than the setting would indicate. Again, this is due to the directionality of the single-element. The array factor points to the angle specified by the setting, but when it is multiplied by the single-element pattern, the 4-element array does not have an array factor with a narrow enough beamwidth to overcome the decrease in single-element gain.

The maximum scan angle of this array is approximately 45°. There are two sidelobes; the third lobe to appear is a grating lobe which becomes noticeable at a 50° scan, and at a 70° scan it dwarfs the sidelobes and approaches the magnitude of the main lobe. The sidelobes are around 10 dB below the main beam, and the cross-polarization levels are 15 - 20 dB below the main beam.

Port 1 has a measured HPBW (half-power beamwidth) of 21°-29° for the E-plane and 80°-89° for the H-plane. Port 2 has a measured HPBW of 23°-29° for the H-plane and 58°-67° for the E-plane. Note that the E-plane is the scanning plane for port 1, and the H-plane is the scanning plane for port 2. Since the single-element E-plane has a narrower beamwidth than its H-plane, it can be expected that for the array, the scanning plane of port 1 will have a narrower beamwidth than port 2, and the non-scanning plane

of port 2 will have a narrower beamwidth than port 1. This is seen in the measured HPBW.

At frequencies lower than 10 GHz, the element spacing d is less than 0.5λ. It can be seen from (4.6) that if β is constant and d decreases, then θ_0 must increase. Therefore, when β is set for a 10 GHz setting, frequencies lower than this will steer to a larger angle. The opposite is also true; higher frequencies will steer to a smaller angle. This effect is illustrated in Figs. 4.23-4.28.

At some frequencies, the main beam can actually increase in magnitude when the scan angle increases. According to theory, this should not happen, and it is probably due to two of the effects discussed earlier: the phase-shifter's phase instability with frequency and phase-shifter insertion loss variation with phase setting and frequency. The phased array is calibrated at 10 GHz. When other frequencies are used with this calibration, the phase shift can vary as seen in Fig. 4.10. This will effectively cause the calibration to be slightly off for different frequencies. Also, the phase-shifter insertion loss varies with phase setting and frequency, so the shifter setting at larger scan angles could potentially have less insertion loss than at lower scan angles. This would cause an increase in array gain for larger scan angles. This change in insertion loss with frequency and setting is illustrated in Fig. 4.9. These effects cause the slightly unusual results at some frequencies, but the array still behaves well and steers to approximately the desired scan angle at all frequencies using only a single calibration. Of course, non-calibration frequency anomalies can be corrected by a recalibration at any desired frequency.

I. Conclusion

The single-element antenna described in a previous section was used to create a 4x1 element phased array with a 0.5λ element separation at 10 GHz. A 1-to-4 power divider was designed to divide the power evenly between the four elements, and digitally controlled phase-shifters were used to steer the array. LabVIEW and a DAQ control the phase-shifters, and logic conversion circuits are required to convert from the standard 5 V TTL/CMOS logic of the DAQ to the 0/-3V complementary logic that the phase-shifters require. The array was calibrated at 10 GHz using a far-field phase-alignment method, and measurements were taken of the array's performance. The array successfully operates over a 3 GHz bandwidth with a maximum scan angle of approximately 45°.

The phased array can be improved with the addition of more elements. This will decrease the beamwidth of the array factor which will allow larger scan angles and form a more directed beam. Using a phase-shifter with a more consistent insertion loss and phase shift would also improve the array's performance. The addition of controllable amplifiers for each element could correct the phase-shifter's variable insertion loss problem and also allow for a non-uniform amplitude distribution which could narrow the array's beamwidth.

5. RECTENNA HISTORY

In wireless power transmission (WPT) systems, microwave power is transmitted wirelessly from one location to another where it is then converted into a useable form. The rectenna (rectifying antenna) is a crucial component in this system. It consists of a receiving antenna which collects microwave power and a rectifier which converts this microwave power into useable DC power. It is called a "rectenna" from the combination of "rectifier" and "antenna". The rectenna is used in numerous applications such as space power transmission (SPT) [32], wireless sensors [33], RFID tags [34], recycling ambient microwave energy [35], and powering devices in hazardous or difficult to reach places [36]. Since power transmission by wires is extremely efficient and cost effective, wireless power transmission is only a practical replacement in applications where it would be difficult or inconvenient to route power lines from the power source to the receiver or if power needs to be quickly delivered to an area without a useable power infrastructure such as for disaster relief.

Wireless power transmission was originally demonstrated by Heinrich Hertz in 1888 when he used a half-wavelength dipole spark gap to generate and transmit power at 500 MHz. He was able to detect this transmission at the receiver with the help of parabolic reflectors at both the transmitter and receiver. To generate this power, both sides of the dipole were charged with high-voltage which arced across the dipole gap and set up an oscillation along the length of the dipole which radiated from the antenna [37]-[38].

Nikola Tesla further demonstrated wireless power transmission in 1898 when he used Tesla coils to generate power at 150 kHz to light 200 light bulbs positioned 26 miles away [37] [39]. Tesla's high power wireless power transmission endeavors continued from 1899-1910 with limited success, but his activities did bring much attention to the idea [40].

During the 1920's and 1930's, researchers from the United States [41] and Japan [42] conducted feasibility studies into wireless power transmission and concluded that current technology was not sufficiently developed to make WPT feasible [37]. The major shortcoming was that devices did not exist which could transmit large amounts of electromagnetic power in a narrow beam. This shortcoming was addressed in the late 1930's when two microwave generating devices were invented. These were the velocity-modulated beam tube (now modified and known as the klystron tube) and the microwave cavity magnetron [38] [43]. Then in 1960, the US Department of Defense contracted Raytheon to build a very high-power, high-efficiency microwave tube (Amplitron) which had an output of 400 kW of CW power at 3 GHz and an efficiency of 80 percent [44]. This filled in the high-power microwave tube technology gap [38].

Another technology not sufficiently developed and preventing complete wireless power transmission systems was the conversion of microwave power to DC power [38]. The US Air Force contracted a number of companies to study the rectification of microwave power [45]. The most important study for WPT was one at Purdue University investigating the use of semiconductor diodes as an efficient rectifier [46].

Also during this time, Raytheon supported William Brown in developing a close-spaced thermionic diode rectifier to be used for a WPT demonstration [47].

In May of 1963 William Brown and others demonstrated a complete WPT system at Raytheon's Spencer Laboratory to a large group of US DOD officials who had sponsored the development of an Amplitron. For the demonstration, a magnetron was used to generate 400 W of microwave power which was transmitted to a receiver and used to drive a DC motor attached to a fan at 100 W [38].

Motivated by Raytheon's previous successes, the US Air Force expressed interest in powering aircraft with WPT. In October of 1964, William Brown and others demonstrated the sustained flight of a tethered helicopter powered by WPT [48]. This demonstration garnered much news coverage both on TV and the newspaper, including a spot on Walter Cronkite's CBS news program. This event validated the possibility of powering larger surveillance and communication aircrafts with WPT, and it was the first time that most people had heard of wireless power transmission or rectennas [37].

The Marshall Space Flight Center (MSFC) became interested in WPT as a means to power satellites from a central space station in low-Earth orbit [40] following a demonstration given by Brown in a board room where he powered a rectenna driven propeller from a 100 W microwave beam on the other side of the room [38]. This resulted in a contract in 1970 with Raytheon to build a high efficiency WPT system demonstration. An initial system was demonstrated at the MSFC in September 1970 with an overall DC-to-DC efficiency of 26%. The next few years of the contracts included work on improving rectenna design, microwave beam launching methods, and

measurement tools which culminated in a system with an overall DC-to-DC efficiency of 48%. Important improvements included using a large transmitting antenna with a Gaussian beam and minimal sidelobes. The use of a Gaussian beam meant that the power density at the center of the rectenna array may be 50 times higher than at the edge of the rectenna array. The spacing of the rectenna elements and the DC load of each element were adjusted to maximize absorbed power and efficiency [38].

In 1968, Dr. Peter Glaser introduced a concept which would change the future development of wireless power transmission [38]; this was the concept of the solar-power satellite (SPS) or space solar power (SSP) [49]. This describes a system whereby a geosynchronous satellite comprised of solar cells collects the sun's energy and transmits this energy via microwaves to a giant array of rectennas on earth's surface. The rectennas would then convert this microwave power to DC which would supply the power grid. This was proposed to be a new form of renewable energy which could potentially replace limited and polluting fossil fuels.

The proposed solar-power satellite concept led to a technical session on SPS in 1970 at the International Microwave Power Institute at Hague, and its papers were published in a special issue of the Journal of Microwave Power [50]. NASA also funded a study in 1973 on the feasibility of a satellite solar power station led by a four company team of Arthur D. Little, Raytheon, Grumman Aerospace, and Textron [51]. This led NASA to further support microwave power transmission with oversight from both the Jet Propulsion Laboratory (JPL) and Lewis Research Center (LeRC) [52]-[53]. One of the studies led to a demonstration in the Mojave Desert at JPL's Goldstone Facility in

1975 where power was transmitted one mile with a DC output of 30 kW [53]. This was an increase in transmitted power of 50 times and an increase in distance of 100 times over what had previously been demonstrated [40]. Another study led by LeRC from 1976-1977 led to a transition from a three-plane rectenna system to a two-plane system which eventually allowed the much lighter, cheaper, and simpler thin-film etched circuits to replace the old bulky standard [38]. Following this development, almost all rectennas have been etched on thin-film using photolithography.

Rectenna conversion efficiency continued to improve, and in 1977 Brown measured the highest microwave conversion efficiency ever recorded. He used a GaAs-Pt Schottky barrier diode and an aluminum bar dipole to achieve a 90.6% conversion efficiency [54].

In 1980, Canada created the Stationary High-Altitude Relay Program (SHARP) to develop a long endurance high-altitude aircraft powered by WPT [55]. In September of 1987, a 1/8 scale SHARP prototype flew for 20 minutes at an altitude of 150 meters under the power of WPT. The aircraft had a wingspan of 4.5 meters and was powered by a 10 kW source transmitted at 2.45 GHz by a parabolic dish antenna on the ground [37].

The 1980's saw the shift of WPT leadership from the United States to Japan. This was spurred by Japan's desire to meet their increasing energy demands with limited natural resources [37]. In 1983, Japan carried out their Microwave Ionosphere Nonlinear Interaction Experiment (MINIX) [56] where 830 W was transmitted from one

rocket to another in the ionosphere. This marked the first WPT experiments in the ionosphere [37].

Wireless power transmission systems tended to operate at 2.45 GHz because of its minimal attenuation through the atmosphere, abundant technology base, and its location in the center of the industrial, scientific, and medical (ISM) band. This was until ARCO Power Technologies designed a rectenna in 1991 at 35 GHz with a 72% conversion efficiency [57]. This frequency change reduced component size and aperture area; however the components at this frequency are both expensive and inefficient. Therefore, 5.8 GHz (also in the ISM research band) is used as a compromise between these frequencies because it decreases component size and aperture area without the expense and inefficiency incurred at 35 GHz. This rise in frequency, however, does result in higher attenuation through the atmosphere in thunderstorms [58].

In the 1990's, Japan conducted the Microwave Lifted Airplane Experiment (MILAX) which involved collaboration with a number of Japanese Universities and corporations [59]. A balsa wood airplane with a 2.5 meter wingspan was flown for 400 meters at an altitude of 15 meters which lasted 40 seconds. It was powered by a phased array transmitter operating at 2.411 GHz and mounted to a van. The van followed the airplane and transmitted power to rectennas mounted on the airplane [37].

In 1993, Japan conducted the International Space Year – Microwave Power Transmission in Space (ISY-METS) experiment to demonstrate WPT in space between two rockets [60]. One rocket transmitted 800 W of power to the other rocket at 2.45

GHz. The dual-polarized rectenna was developed by McSpadden and Chang at Texas A&M University [61].

In the late 1990's, dual and circular polarization became the preferred polarization for wireless power transmission, especially SSP. Microwaves passing through the earth's atmosphere undergo Faraday rotation which can cause alignment problems with linear polarization systems and severely degrade performance. Dual and circular polarization systems do not suffer this same performance degradation since broadside alignment of transmitting and receiving antennas is arbitrary. This allows both antennas of dual and circularly polarized systems to be rotated without any change in performance [37].

NASA reassessed the SSP concept with its "Fresh Look Study" from 1995-1997 and concluded that with recent technological advances, SSP could be feasible but still remained challenging [62]. This led to an SSP Exploratory Research and Technology (SERT) study in 1999 which involved researchers from around the United States. One result from the SERT study was Strassner and Chang's 2002 design of a circularly polarized rectenna array which utilized a folded dipole antenna called a dual rhombic loop antenna (DRLA). The DRLA is circularly polarized and has a large gain of 10.7 dBi. The array has a 78% RF-to-DC conversion efficiency and operates at 5.61 GHz [63]. Also in 2002, McSpadden and Mankins estimated that SPS systems have the potential to achieve 45% DC-to-DC efficiencies [64].

A serious problem which arises in WPT systems is that of beam alignment. If the microwave beam is narrow, as would be required for a long-range, high-efficiency

system, it is difficult to keep the transmitter and receiver properly aligned. This is especially problematic with SPS systems and aircraft applications since the transmission distance is large and the atmosphere can unpredictably alter the microwave beam's path. A proposed method to solve this problem is through the use of a retrodirective array [65]-[68]. This system uses a pilot beam to align the antennas and alter the direction that the transmitting antenna array is focused. The phase of the pilot beam is acquired by receivers located on each element of the transmitting array. This phase is then compared to a reference, phase conjugated and fed back to the phase controller for that element of the transmitting array.

There are some environmental concerns about the use of an SPS system. Electromagnetic exposure is the largest concern from the public, but it has been shown that potential exposure of the general public from a 5-GW reference SPS system would be 0.1 $\mu W/cm^2$ in most places and 10 $\mu W/cm^2$ in some small grating lobe areas. This is well below accepted environmental safety levels around the world which range from 100-10,000 $\mu W/cm^2$. Radio frequency interference should be a larger environmental concern. Many wireless systems operate at 2.45 GHz, and an SPS has the potential to disrupt these communications; unblocked harmonics are also a potential interference. Frequency allocation will be very important for a successful SPS system [69]. High powered microwave transmission from space will also cause some localized heating of the ionosphere. There is some concern that this could interfere with telecommunication systems [70], perturb the earth's magnetic field, or have some other environmental impact [71].

The application of wireless power transmission currently drawing the most attention is space solar power. This has become even more true with Japan's announcement that it plans to have a MW class SSP system in place in the 2020's and a commercial 1 GW class SSP system in place in the 2030's [72]. This stems from Japan's desire for unlimited clean energy to replace its limited energy resources and reliance on foreign oil. With this SSP commitment and the numerous other WPT applications, rectennas have a bright and promising future.

6. RECTENNA OPERATION THEORY *

A. Wireless Power Transmission System

Wireless power transmission (WPT) systems and wireless communication systems are based on the same technology with the Maxwell equations governing both. The fundamental difference between the two is efficiency.

In wireless communication systems, the microwave is simply a carrier of information, so bandwidth is required to encode this information, and noise is a major concern. Efficiency is not the top priority and only becomes problematic if the received power is below the noise level. However, WPT systems do not carry any information, so a very narrow band can be used, and noise is not a problem. Efficiency, however, is of paramount importance for a practical WPT system. It is dependent on component efficiencies as well as the ability to focus the microwave beam on the rectenna.

The wireless power transmission system consists of three core system blocks as seen in Fig. 6.1. The first block is the DC-to-RF transmission block which converts the DC (or AC) source power to RF power and also radiates this power. The source of the power is dependent on the application and could be photovoltaic solar cells for use in space solar power (SSP), or it could be a power plant for terrestrial applications. The power can be converted to RF by either a solid-state semiconductor circuit (below 10 GHz) or a microwave tube such as a magnetron or a klystron [38]. The efficiency of the

* Parts of this section are reprinted, with permission, from J. Hansen and K. Chang, "Diode modeling for rectenna design," in *IEEE Antennas and Propagation Society International Symposium (APSURSI)*, pp. 1077-1080, Spokane, WA, July, 2011.

first block η_t is the product of the DC-to-RF conversion efficiency and the transmission efficiency.

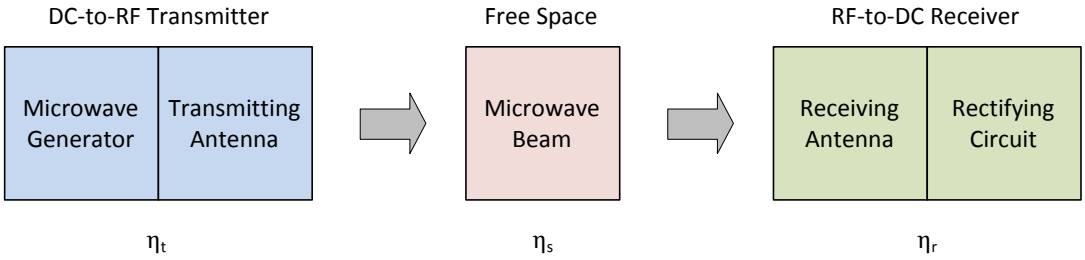

Figure 6.1. Block diagram of a wireless power transmission (WPT) system.

The second block is the free space transmission channel which accounts for propagation losses through the space separating the transmitter and receiver. Its efficiency η_s is the ratio of received power to transmitted power. For high-efficiency transmission, the microwave power must be transmitted with optimal power density. Goubau and Schwering showed that microwave power can be transmitted with efficiencies approaching 100% if the correct transmitting aperture is properly illuminated [73]-[74]. The efficiency is a function of the parameter τ [75] which is given by

$$\tau = \frac{\sqrt{A_r A_t}}{\lambda D} \tag{6.1}$$

where A_r and A_t are the aperture areas of the receiver and transmitter respectively, λ is the wavelength of the transmitted wave, and D is the distance between the transmitter and receiver. A graph of efficiency vs the parameter τ can be seen in [75]. This

presumes an aperture power density as seen in [75]. As the efficiency approaches 100%, the aperture power density approaches the shape of an edge truncated Gaussian curve. The efficiency can be approximated as

$$\eta = \left(1 - e^{-\tau^2}\right) \times 100\% \quad . \tag{6.2}$$

Larger values of τ result in higher efficiency, and the receiving and transmitting aperture areas are directly related to τ, so larger apertures result in higher transmission efficiency. Therefore, a compromise must be found between size and efficiency.

The final block is the RF-to-DC receiving block which receives the microwave power with the receiving antenna and converts this power into DC power with a rectifying circuit; this power conversion efficiency η_r determines the performance of the rectenna. This final block is called a rectenna from the combination of "rectifying" and "antenna". A block diagram of the basic components of a rectenna can be seen in Fig. 6.2 and includes an antenna, a harmonic rejection filter, a diode, a DC-pass filter (capacitor), and a load. The harmonic rejection filter allows microwaves to enter the rectifying circuit but rejects any harmonics created by the diode due to its non-linear behavior. This prevents diode harmonics from radiating back out through the antenna. The diode converts the microwave power into DC power, and the DC-pass filter reflects any unconverted microwave power back to the diode which prevents microwave power from reaching the load. By utilizing filters to block microwave power on both sides of the diode, any unconverted microwave power should be reflected back to the diode and eventually rectified to DC power, thereby improving conversion efficiency. The only

way that energy can escape from the system is in the form of DC at the output or as a reflected fundamental at the input. The DC output voltage is measured across the load. A method to further reduce harmonic radiation from the rectenna is through the use of frequency selective surfaces. In this scheme, a frequency selective surface which passes the fundamental frequency and blocks the second and third harmonics is placed in front of the rectenna. This will attenuate harmonics which attempt to radiate from the rectenna [76]-[77].

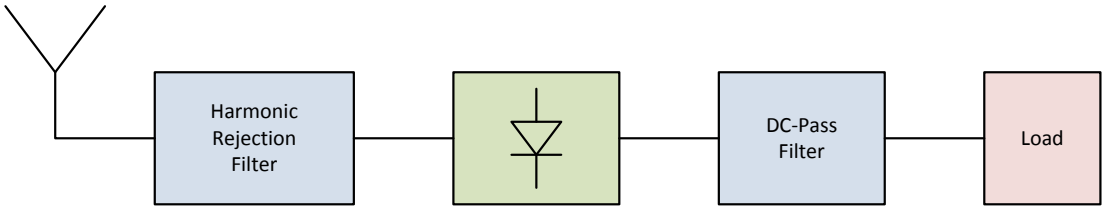

Figure 6.2. Block diagram of a rectenna.

Optimization of the rectifying circuit is important to maximize efficiency. The diode must be matched to the input power level, the input impedance, and the load. The distance between the diode and capacitor is crucial because in addition to reflecting microwave power, the capacitor is used to tune out the diode's reactance and improve conversion efficiency. This distance is typically a quarter-wavelength at the fundamental frequency, and since the capacitor can be considered a short at RF, this will have the diode seeing an open circuit at ω, 3ω, 5ω, . . . and a short circuit at 2ω, 4ω, 6ω, . . . This results in the blockage of microwave power (fundamental frequency and all

harmonics) and the passing of DC power. If the rectenna is properly designed then the efficiency becomes a property of diode parameters.

The conversion efficiency of the rectenna is calculated as

$$\eta = \frac{P_{DC}}{P_{received}} \times 100\% \tag{6.3}$$

where P_{DC} is the measured output power across the load at DC and $P_{received}$ is the RF power received by the rectenna's antenna. $P_{received}$ can be calculated using the Friis transmission equation [74] by

$$P_{received} = P_t G_t G_r \left(\lambda_0 / 4\pi r \right)^2 = A_{er} \frac{P_t G_t}{4\pi r^2} \tag{6.4}$$

where the effective area of the receiving antenna is

$$A_{er} = \frac{G_r \lambda_0^2}{4\pi} \quad . \tag{6.5}$$

P_t is the transmitted power, G_t and G_r are the transmitting and receiving antenna gains respectively, λ_0 is the free space wavelength, and r is the distance between the transmitter and the rectenna. Rectenna efficiencies are oftentimes given as a function of received power density S_D which can be calculated from

$$S_D = \frac{P_{received}}{A_{er}} = \frac{P_t G_t}{4\pi r^2} \quad . \tag{6.6}$$

The overall efficiency η_{all} of the wireless power transmission system is the ratio of DC output power at the rectenna to DC (or AC) input power and is given by

$$\eta_{all} = \eta_t \times \eta_s \times \eta_r \quad . \tag{6.7}$$

B. Rectenna Operation Theory

The basic rectenna rectifying circuit is based on a half-wave rectifier with a capacitor added in shunt. It is therefore important to understand the operation of a half-wave rectifier so that the rectenna's operation can be understood. An explanation of a half-wave rectifier can be found in [78] and rectenna operation theory is discussed in [58],[79]-[81]. Some of this information will be summarized here.

A half-wave rectifier and its voltage waveforms are illustrated in Fig. 6.3. Assuming an ideal diode and a perfect input sinusoid v_s, during the positive half-cycle ($v_s \geq 0$) the diode will not conduct which will cause all of the current to flow through the load R_L. During the negative half-cycle ($v_s \leq 0$), the current will flow through the diode,

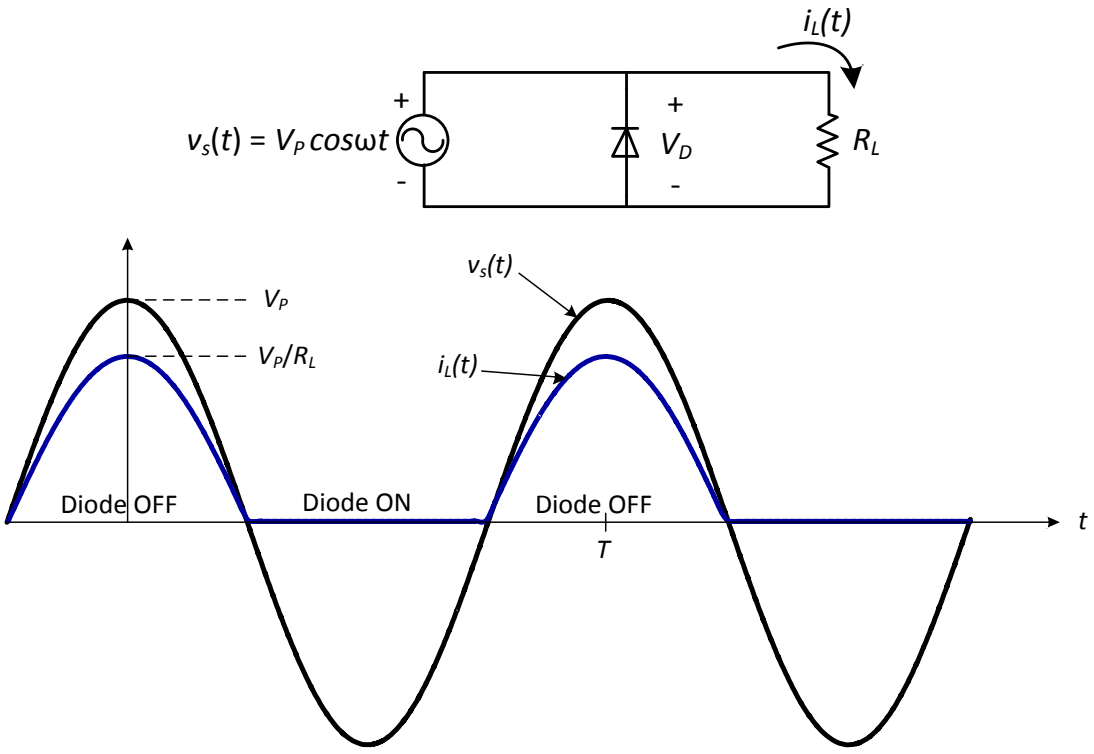

Figure 6.3. Half-wave rectifier circuit and waveforms.

bypassing the load. This will cause the current through R_L to be unidirectional and have a finite average value or a DC component. This is a rectification of the source current which can be used to generate DC from AC. The average rectified DC current $I_{L,DC}$ can be found from

$$I_{L,DC} = \frac{1}{T}\int_{T} i_L(t)\,dt = \frac{1}{T}\left(\int_{-T/4}^{T/4} \frac{V_P}{R_L}\cos\omega t\,dt\right) \tag{6.8}$$

where T is the period of the incident sinusoid and $\omega = 2\pi/T$. Solving this integral gives an average DC current of

$$I_{L,DC} = \frac{V_P}{\pi R_L}\ . \tag{6.9}$$

Applying Ohm's law gives an average rms DC voltage across the load of V_p/π.

If a capacitor (DC-pass filter) is added in shunt to this half-wave rectifier circuit, it will result in the waveform seen in Fig. 6.4. The voltage across the load is

$$v_L(t) = V_P\, e^{-t/R_L C} \tag{6.10}$$

where R_LC is the time constant and t is the time measured from the peak of the waveform where $v_L(t) = V_p$. The exponential decrease in the load voltage can be approximated by a straight line since the period is very short compared to the time constant at microwave frequencies. Equation (6.10) can be expanded using a power series [82] as

$$v_L(t) = V_P\, e^{-t/R_L C} = V_P\left[1 + \frac{-t/R_L C}{1!} + \frac{\left(-t/R_L C\right)^2}{2!} + \frac{\left(-t/R_L C\right)^3}{3!} + \ . \ . \ .\right] . \qquad (6.11)$$

Because of the straight line approximation for the exponential decay, the linear terms of (6.11) are kept while the rest are discarded. The minimum value of v_L is at $t = T$ and is then

$$V_{\min} = v_L(t = T) \approx V_P\left(1 - \frac{T}{R_L C}\right) = V_P\left(1 - \frac{1}{f R_L C}\right) \ . \qquad (6.12)$$

Once the voltage $v_L(t)$ deceases to V_{min}, the diode will be non-conducting and the source voltage will be rising above V_{min} which will again raise the load voltage v_L to its peak value of V_P. The peak-to-peak ripple voltage of V_L is

$$V_r = V_{\max} - V_{\min} = \frac{V_P}{f R_L C} \ , \qquad (6.13)$$

and the average rms DC voltage across the load is

$$V_{L,DC} = \frac{V_{\max} + V_{\min}}{2} = V_P\left(1 - \frac{1}{2 f R_L C}\right) \approx V_P \ . \qquad (6.14)$$

At microwave frequencies, the time constant $R_L C$ is much larger than the period T which gives rise to a small ripple voltage V_r, resulting in an average DC load voltage of approximately V_P. Consequently, it has been shown that by adding the shunt capacitor, the average DC load voltage is raised from V_P/π to approximately V_P.

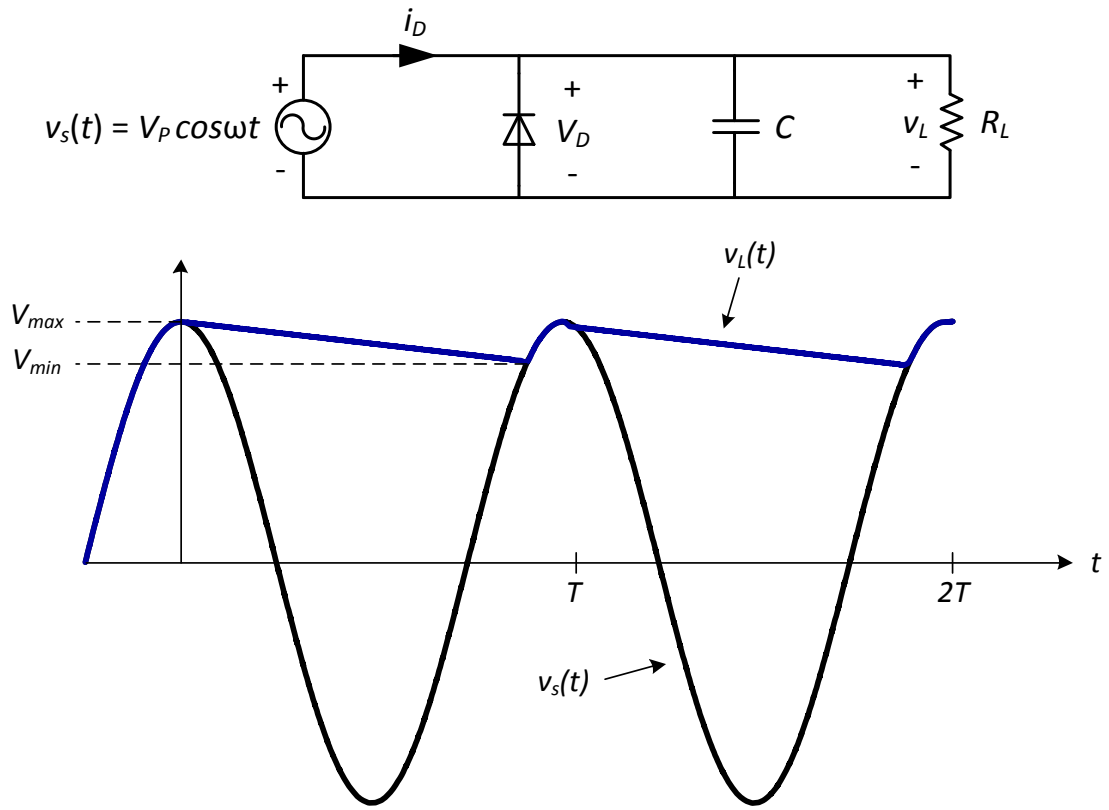

Figure 6.4. Half-wave rectifier with capacitor circuit and waveforms.

C. Analytical Model of Rectenna Efficiency

A simplified mathematical model described by Yoo [79]-[80] can be used to predict the conversion efficiency of the rectenna. This model makes a number of simplifications which prevent it from being accurate enough to be useful for precise rectenna design, but it does demonstrate rectenna behavior and reveal the effect of parameter variation on performance. It is only dependent on the simplified diode parameters and microwave circuit losses at the fundamental frequency. This model does not include harmonics created by the diode, and diode parasitics are excluded. It also assumes ideal diode characteristics (Fig. 6.5) such as: $R_j = 0$ for forward bias, $R_j = \infty$ for reverse bias, and no current through C_j during forward bias. Due to ideal condition assumptions, the results from this model can be considered as the maximum conversion efficiencies that would result from a diode with the same parameters.

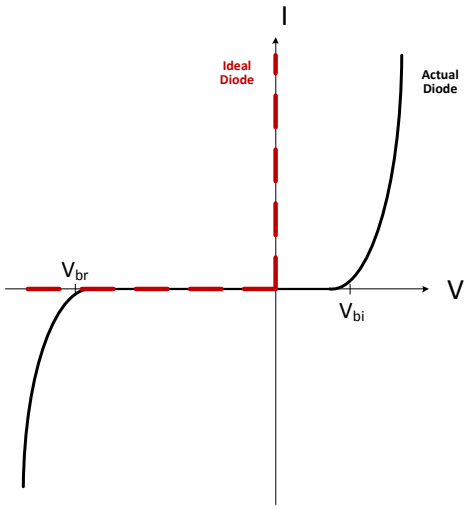

Figure 6.5. Voltage-Current curves of an ideal diode and an actual diode. The built-in turn-on voltage V_{bi} is the voltage at which forward current starts to flow through the diode. The reverse breakdown voltage V_{br} is the minimum reverse voltage which will cause reverse current flow through the diode.

The equivalent circuit of the diode rectifier which is used to derive the mathematical model is shown in Fig. 6.6. The nonlinear components R_j and C_j represent the diode junction with ideal diode conditions applied: junction resistance $R_j = 0$ for forward bias and $R_j = \infty$ for reverse bias. The voltage V_D is the voltage across the diode and the voltage V_j represents the voltage across the diode's junction. The diode's voltage waveforms are displayed in Fig. 6.7. The angle θ_{on} is the forward bias turn-on angle and ϕ is the phase lag of the junction voltage behind the incident diode voltage.

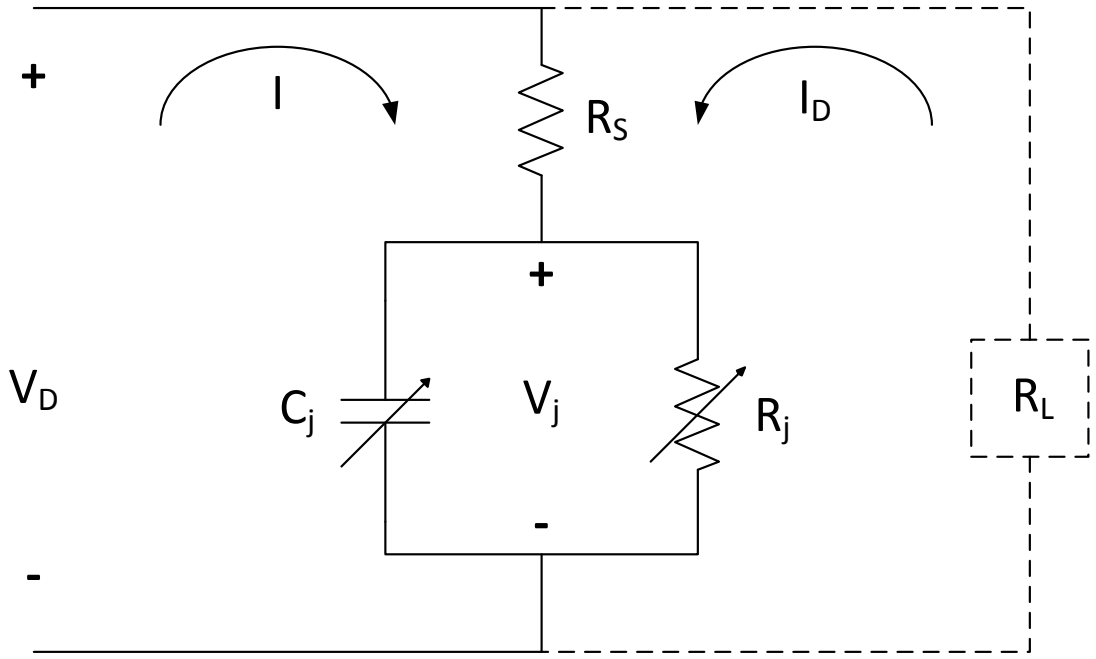

Figure 6.6. Equivalent circuit of the diode rectifier.

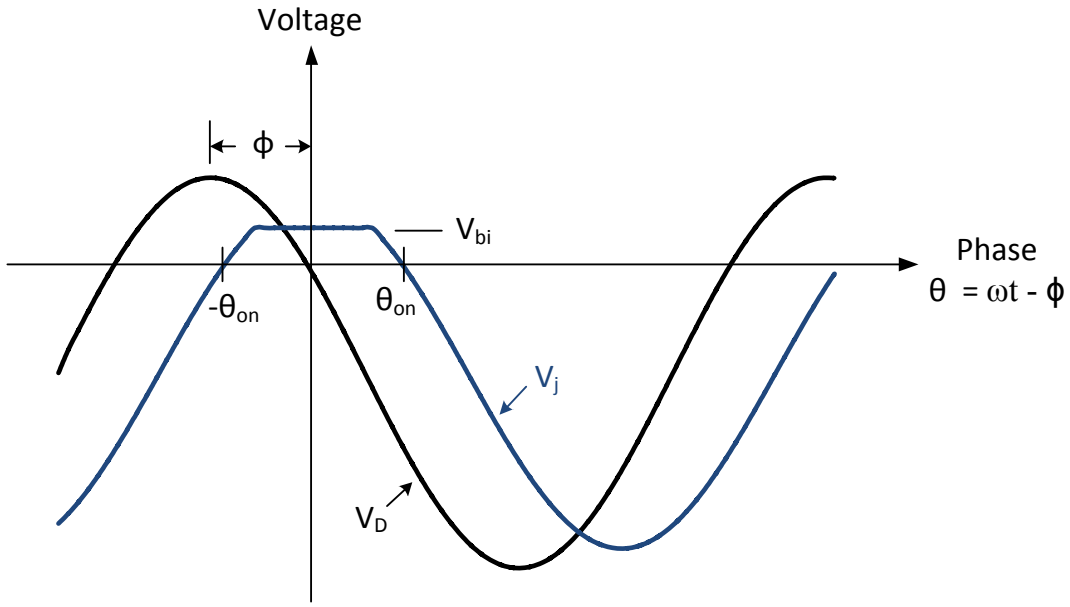

Figure 6.7. Voltage waveforms of the diode rectifier. V_D is the voltage across the physical diode, and V_j is the voltage across the diode junction.

The incident diode voltage V_D is composed of a fundamental frequency and a DC component. It can be expressed as

$$V_D = -V_0 + V_1 \cos(\omega t) \tag{6.15}$$

where V_0 is the self-biasing DC output voltage across the load R_L and V_1 is the peak voltage of the incident microwave signal. The incident microwave signal produces a DC output voltage which biases the diode. This biasing level increases through a few cycles and also as the input power level increases. The diode junction voltage is

$$V_j = \begin{cases} -V_{j0} + V_{j1}\cos(\omega t - \phi) & , \text{ when diode is off} \\ V_{bi} & , \text{ when diode is on} \end{cases} \tag{6.16}$$

where V_{j0} is the DC component of the diode junction voltage and V_{j1} is the peak voltage of the first harmonic of the diode junction voltage when the diode is off ($V_j < V_{bi}$). When the diode is on, the junction voltage V_j is equal to the built-in turn-on voltage of the diode V_{bi} which is set to zero in this derivation (ideal diode). The phase ϕ is the angle that the diode's junction voltage lags the incident microwave's voltage.

The DC output voltage V_0 can be determined from the junction voltage V_j. The average value of V_j in each cycle can be calculated as

$$V_{j,dc} = \frac{1}{2\pi}\int_{0}^{2\pi} V_j \, d\theta = \frac{1}{2\pi}\int_{-\theta_{on}}^{\theta_{on}} V_{bi} \, d\theta + \frac{1}{2\pi}\int_{\theta_{on}}^{2\pi-\theta_{on}} (-V_{j0} + V_{j1}\cos\theta)\, d\theta \,. \qquad (6.17)$$

The first term in (6.17) corresponds to the forward-biased region, and the second term corresponds to the reverse-biased region. Note that the phase lag ϕ is assumed to be zero for this derivation. Integrating (6.17) gives

$$V_{j,dc} = V_{bi}\frac{\theta_{on}}{\pi} - V_{j0}\left(1 - \frac{\theta_{on}}{\pi}\right) - \frac{V_{j1}}{\pi}\sin\theta_{on} \quad . \qquad (6.18)$$

Applying Kirchhoff's voltage law along the DC path as illustrated in Fig. 6.6 by the dotted line gives

$$V_0 = V_{j,dc}\frac{R_L}{R_S + R_L} \,. \qquad (6.19)$$

The diode switching occurs when the junction voltage V_j is equal to the turn-on voltage V_{bi} and $\omega t = \theta_{on}$, so from (6.16),

$$V_{bi} = V_j = -V_{jo} + V_{j1}\cos\theta_{on} \qquad (6.20)$$

which can be rearranged to give an expression for the turn-on angle

$$\cos\theta_{on} = \frac{V_{bi} + V_{j0}}{V_{j1}} \quad . \tag{6.21}$$

When the diode is off, R_j is infinite and Kirchhoff's voltage law can be applied to the RF loop in Fig. 6.6 to give

$$-V_D + IR_S + V_j = 0\,, \tag{6.22}$$

and since all current is flowing through C_j when the diode is off,

$$I = \frac{d(C_j V_j)}{dt}\,. \tag{6.23}$$

Equations (6.22) and (6.23) can be combined to give

$$I = \frac{d(C_j V_j)}{dt} = \frac{V_D - V_j}{R_S} \tag{6.24}$$

where C_j can be expressed as a harmonic function of V_D:

$$C_j = C_0 + C_1\cos(\omega t - \phi) + C_2\cos(2\omega t - 2\phi) + \ldots \tag{6.25}$$

Substituting (6.15), (6.16), and (6.25) into (6.24) and neglecting terms higher than the second harmonic gives

$$\omega R_S\left(C_1 V_{j0} - C_0 V_{j1}\right)\sin\theta = V_{j0} - V_0 + \left(V_1\cos\phi - V_{j1}\right)\cos\theta - V_1\sin\phi\sin\theta \tag{6.26}$$

where $\theta = \omega t - \phi$ for simplicity. Since this equation is valid whenever the diode is off, each sinusoidal term should separately be satisfied during the diode's off period as follows:

$$V_{j0} = V_0 \tag{6.27}$$

$$V_{j1} = V_1\cos\phi \tag{6.28}$$

$$V_1 \sin\phi = \omega R_S \left(C_0 V_{j1} - C_1 V_{j0} \right) \ . \tag{6.29}$$

An expression for the turn-on angle can be derived by combining (6.18), (6.19), (6.21), and (6.27) into

$$\tan\theta_{on} - \theta_{on} = \frac{\pi R_S}{R_L \left(1 + \frac{V_{bi}}{V_0} \right)} \ . \tag{6.30}$$

It can be seen that the ratio of R_s to R_L and the ratio of V_{bi} to V_0 are the only variables that determine θ_{on}. Note that the input power will affect V_0, but the expression for θ_{on} is not directly dependent on input power.

The diode efficiency η is defined as

$$\eta = \frac{P_{DC}}{P_{Loss} + P_{DC}} \tag{6.31}$$

where P_{DC} is the DC output power and P_{Loss} is the power dissipated by the diode. P_{DC} and P_{Loss} are defined as

$$P_{DC} = \frac{V_0^2}{R_L} \tag{6.32}$$

$$P_{Loss} = Loss_{on,R_S} + Loss_{off,R_S} + Loss_{on,diode} \tag{6.33}$$

where $Loss_{on,Rs}$ and $Loss_{off,Rs}$ are the losses from R_S when the diode is on and off, respectively. $Loss_{on,diode}$ is the loss from the diode when the diode is on. The loss terms of (6.33) can be expressed as

$$Loss_{on,R_S} = \frac{1}{2\pi} \int_{-\theta_{on}}^{\theta_{on}} \frac{\left(V_D - V_{bi} \right)^2}{R_S} d\theta \tag{6.34}$$

$$Loss_{off,R_S} = \frac{1}{2\pi}\int_{\theta_{on}}^{2\pi-\theta_{on}} \frac{\left(V_D - V_j\right)^2}{R_S} d\theta \tag{6.35}$$

$$Loss_{on,diode} = \frac{1}{2\pi}\int_{-\theta_{on}}^{\theta_{on}} \frac{\left(V_D - V_{bi}\right)V_{bi}}{R_S} d\theta \quad . \tag{6.36}$$

Since the junction resistance is assumed to be infinite during the off cycle of the diode, the loss through the diode during the off cycle is neglected. These power loss terms are the time-average products of the voltage across each element and the current through this element. The total power lost from the series resistance R_s can be found from using (6.15), (6.16), (6.24), and (6.28) in (6.34) and (6.35) and setting $\phi = 0$ as

$$L_{R_S} = \frac{1}{2\pi R_S}\left[\int_{-\theta_{on}}^{\theta_{on}} \left(-V_0 - V_{bi} + V_1\cos\theta\right)^2 d\theta + \left(\omega R_S C_j V_1\right)^2 \int_{\theta_{on}}^{2\pi-\theta_{on}} \sin^2\theta\, d\theta\right], \tag{6.37}$$

and the power lost from the diode junction can be found from substituting (6.15) into (6.36) and setting $\phi = 0$ as

$$L_{diode} = \frac{1}{2\pi R_S}\int_{-\theta_{on}}^{\theta_{on}} V_{bi}(-V_0 - V_{bi} + V_1\cos\theta)d\theta \quad . \tag{6.38}$$

During the diode off cycle, the voltage drop across R_s is so small that the phase difference ϕ can be set to zero in (6.28) to obtain

$$V_{j1} = V_1 \quad . \tag{6.39}$$

V_1 in (6.38) can be determined when the diode is off by substituting (6.16), (6.27), and (6.39) into (6.20) as

$$V_1 = \frac{V_0 + V_{bi}}{\cos\theta_{on}} \quad . \tag{6.40}$$

Finally, an expression for the diode efficiency η can be found by using (6.32), (6.33), (6.37), and (6.38) in (6.31). This gives

$$\eta_D = \frac{1}{1 + A + B + C} \tag{6.41}$$

where

$$A = \frac{R_L}{\pi R_S}\left(1 + \frac{V_{bi}}{V_0}\right)^2 \left[\theta_{on}\left(1 + \frac{1}{2\cos^2\theta_{on}}\right) - \frac{3}{2}\tan\theta_{on}\right] \tag{6.42}$$

$$B = \frac{R_S R_L C_j^2 \omega^2}{2\pi}\left(1 + \frac{V_{bi}}{V_0}\right)\left(\frac{\pi - \theta_{on}}{\cos^2\theta_{on}} + \tan\theta_{on}\right) \tag{6.43}$$

$$C = \frac{R_L}{\pi R_S}\left(1 + \frac{V_{bi}}{V_0}\right)\frac{V_{bi}}{V_0}\left(\tan\theta_{on} - \theta_{on}\right). \tag{6.44}$$

The input impedance of the diode can be found from the current I which flows through R_S during one cycle by utilizing a Fourier series as

$$I = I_0 + I_{1r}\cos(\omega t) + I_{1i}\sin(\omega t) \tag{6.45}$$

where I_0 is the DC component and I_{1r} and I_{1i} are the real and imaginary parts of the fundamental frequency component, respectively. Using (6.24) and $\theta = \omega t - \phi$, these current components are given by

$$I_0 = \frac{1}{2\pi R_S}\left[\int_{-\theta_{on}}^{\theta_{on}} \left(V_D - V_{bi}\right) d\theta + \int_{\theta_{on}}^{2\pi - \theta_{on}} \left(V_D - V_j\right) d\theta\right] \tag{6.46}$$

$$I_{1r} = \frac{1}{\pi R_S}\left[\int_{-\theta_{on}}^{\theta_{on}} \left(V_D - V_{bi}\right)\cos(\theta + \phi) d\theta + \int_{\theta_{on}}^{2\pi - \theta_{on}} \left(V_D - V_j\right)\cos(\theta + \phi) d\theta\right] \tag{6.47}$$

$$I_{1i} = \frac{1}{\pi R_S}\left[\int_{-\theta_{on}}^{\theta_{on}} \left(V_D - V_{bi}\right)\sin(\theta+\phi)d\theta + \int_{\theta_{on}}^{2\pi-\theta_{on}} \left(V_D - V_j\right)\sin(\theta+\phi)d\theta\right], \quad (6.48)$$

and the input impedance of the diode at the fundamental frequency expressed as a phasor is

$$Z_D = \frac{V_1}{I_{1r} - jI_{1i}} \quad . \quad (6.49)$$

Assuming that no current flows through C_j when the diode is on and that all of the current flows through C_j when the diode is off, the diode current in one cycle can be found from

$$I_{1r} - jI_{1i} = \frac{1}{\pi R_S}\int_{-\theta_{on}}^{\theta_{on}} \left(-V_0 - V_{bi} + V_1\cos\theta\right)\cos\theta\, d\theta + j\frac{\omega C_j V_1}{\pi}\int_{\theta_{on}}^{2\pi-\theta_{on}} \sin^2\theta\, d\theta \,. \quad (6.50)$$

The input impedance of the diode can then be written as

$$Z_D = \frac{\pi R_S}{\cos\theta_{on}\left(\frac{\theta_{on}}{\cos\theta_{on}} - \sin\theta_{on}\right) + j\omega R_S C_j\left(\frac{\pi-\theta_{on}}{\cos\theta_{on}} + \sin\theta_{on}\right)} \quad . \quad (6.51)$$

If impedance matching is utilized to tune out the reactance of the diode impedance, the diode input impedance can be simplified to

$$R_D = \frac{1}{\text{Real}(Y_D)} = \frac{\pi R_S}{\cos\theta_{on}\left(\frac{\theta_{on}}{\cos\theta_{on}} - \sin\theta_{on}\right)} \quad . \quad (6.52)$$

Equation (6.30) can be used to find the turn-on angle θ_{on}, and once this is known, (6.41)-(6.44) and (6.52) can be used to calculate the theoretical maximum conversion efficiency and input resistance of a diode as a function of fundamental diode parameters. As an

example, a plot of conversion efficiency versus a normalized parameter $\omega R_S C_j$ for different R_S/R_L ratios is displayed in Fig. 6.8. Also, plots of conversion efficiency and input resistance versus load resistance for a diode with parameters $C_j = 2$ pF and $R_S = 0.5$ Ω operating at 5.8 GHz are shown in Figs. 6.9-6.10.

The junction capacitance C_j can be calculated from

$$C_j = C_{j0}\sqrt{\frac{V_{bi}}{V_{bi} + |V_0|}} \tag{6.53}$$

where C_{j0} is the zero bias junction capacitance.

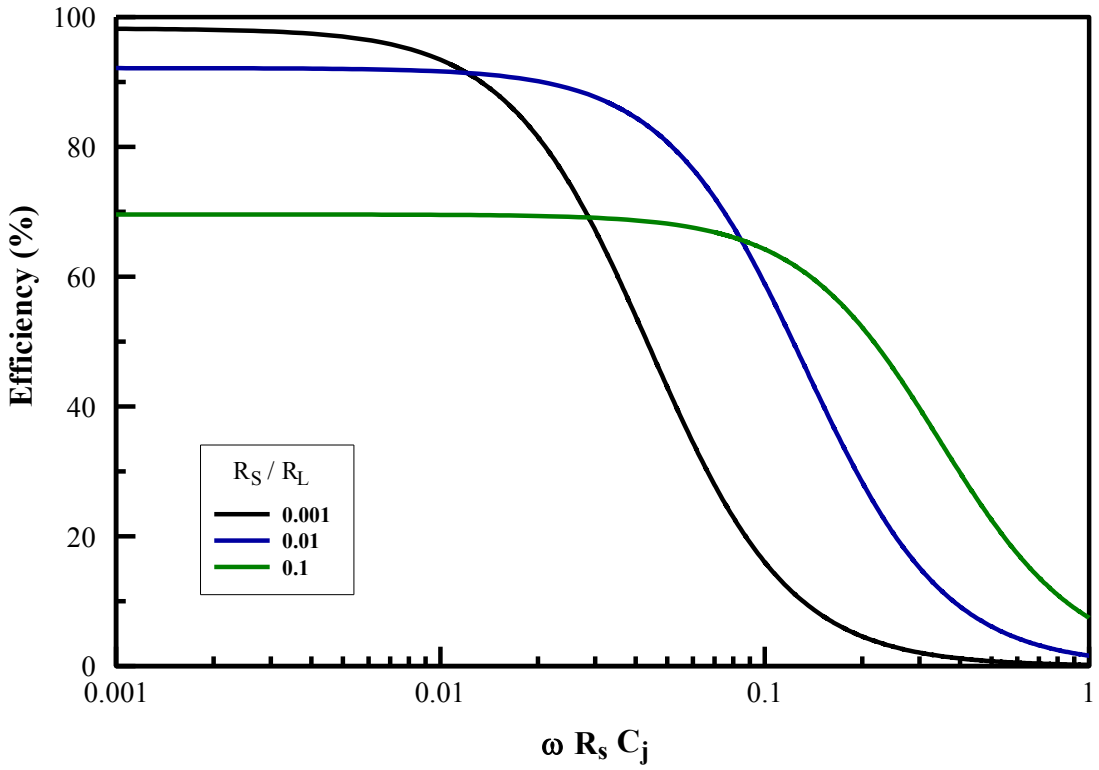

Figure 6.8. Conversion efficiency of an ideal diode versus the normalized parameter $\omega R_S C_j$ for different R_S/R_L ratios.

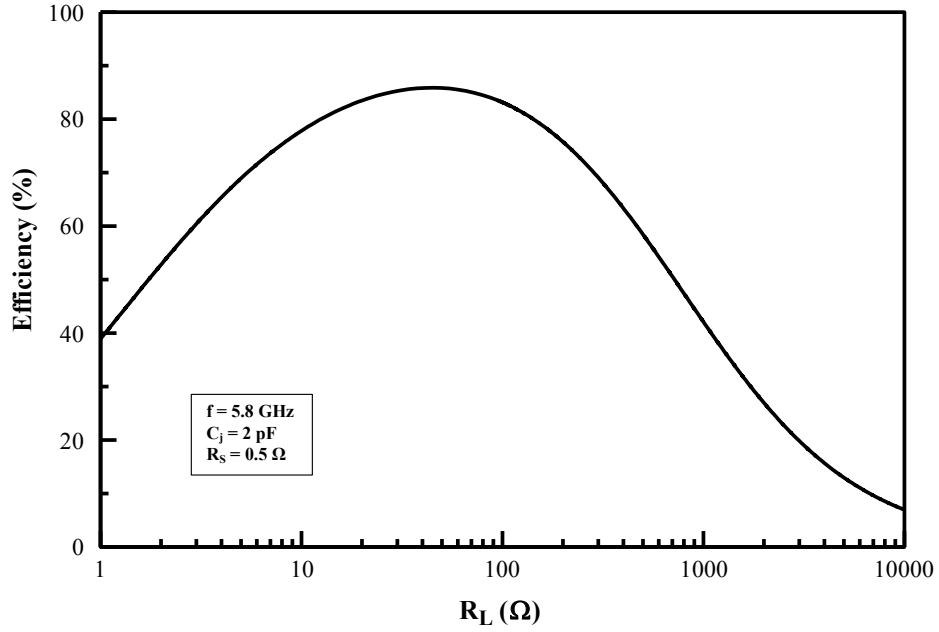

Figure 6.9. Conversion efficiency of an ideal diode versus load resistance (for a 5.8 GHz ideal diode with set parameters).

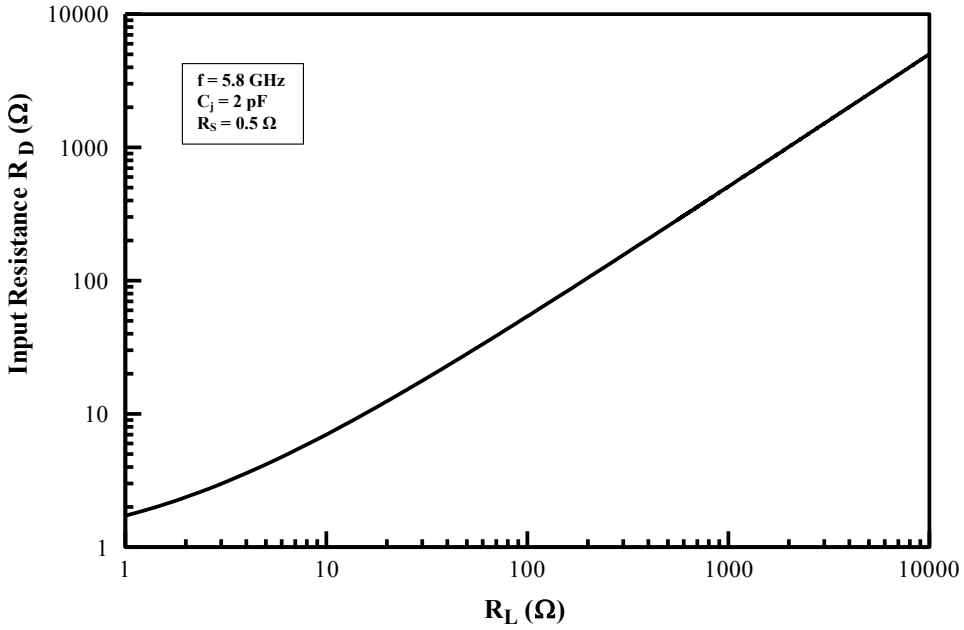

Figure 6.10. Input resistance of an ideal diode versus load resistance (for a 5.8 GHz ideal diode with set parameters).

D. Effect of Input Power on Rectenna Efficiency

The magnitude of the input power to the rectenna has a dramatic effect on its power conversion efficiency. With increasing input power, the diode conversion efficiency will rise to a point and then start to decrease [79].

At low input power levels, the conversion efficiency is low because the diode voltage is below or comparable to the turn-on voltage V_{bi} which means that the diode is not fully turned on. As the diode voltage exceeds the turn-on voltage, this effect disappears and the conversion efficiency levels off. Also, as power increases, the higher order harmonics will come into play and decrease efficiency. Finally, efficiency abruptly decreases when the power level increases to a point where the diode voltage swing exceeds the diode's breakdown voltage V_{br}. The critical point where the breakdown voltage effect takes over is when the power level is equal to $V^2_{br}/4R_L$. These effects combine to give a net conversion efficiency curve [79].

E. Diode Selection

The diode is the most crucial component in rectenna design because in a well-designed rectenna, it has the largest effect on efficiency. GaAs and Si diodes can both be used in a rectenna. GaAs is usually preferable for high efficiency because it has more than six times the electron mobility of Si, but Si has higher thermal conductivity which is better for long-term reliability.

Diode selection is dependent on system design parameters such as frequency and input power. In general, a small series resistance R_S and low turn-on voltage V_{bi} are

preferred because this will reduce rectenna losses. The diode's reverse breakdown voltage V_{br} limits the diode's power handling capacity and should be large enough to handle the expected power level. V_{br} and the DC output voltage V_0 should be chosen such that $V_0 < V_{br}/2$. Since all parameters are related to each other, diode parameter tradeoffs must be made.

7. DIODE MODEL *

A. Background and Introduction

Computer simulation has become an increasingly popular design tool for microwave circuits and systems, and the design of a rectenna is no exception. The capability of simulating a rectenna design will allow for the analysis of new ideas and tuning of parameters without the added expense and time of fabricating and measuring each new design to test its validity.

All parts of the rectenna, with the exception of the diode, can be easily modeled using standard microwave simulation software. The antenna and transmission lines can be modeled using EM modeling software such as IE3D [12] or HFSS [13], and the capacitor and load (resistor) are standard components which can be modeled in any software capable of circuit-level simulation, such as Agilent ADS [83]. However, diodes present a problem with off-the-shelf modeling because the parameters of different diodes vary from each other, so there is not a uniform standard model which works for all diodes. Models of a few popular diodes are usually included in circuit level simulator software or may be provided by the manufacturer, but if a diode, which is not provided with a model, is to be used in a rectenna then a model for this particular diode should be created. After this diode model is created, it will be possible to simulate the entire rectenna design and avoid unnecessary fabrication and testing.

Device models are usually not generic, and the limitations of the model must be appreciated. The model must be designed to work in the target application. For use in rectenna modeling, a nonlinear harmonic balance simulator is utilized, so the model must be compatible with this type of simulation.

A harmonic balance analysis [84]-[85] can be used to solve the steady-state of a nonlinear circuit which is excited by a single-tone. It works in the frequency domain by balancing currents and voltages until Kirchhoff's Current Law is satisfied at the fundamental frequency and a specified number of harmonics. An initial guess is made at node voltages which are used to calculate currents. These currents are then checked for adherence to Kirchhoff's Current Law. An iterative process is used to update the node voltages, and the procedure is repeated until Kirchhoff's Current Law is satisfied.

The model should imitate the operation of the device within the required simulation environment by generating similar characteristics to the physical diode by utilizing an analogous system. Device models can be either physical device models or equivalent circuit models.

Equivalent circuit models [86] are common for circuit design applications because they are relatively easy to implement, and they can seamlessly mimic the electrical performance of the device being modeled. However, it can be difficult to relate the model parameters to the physical device parameters because of the non-linear behavior, frequency dependence, and biasing of most devices. This can restrict the use of equivalent circuit models because they are generally not suitable for predicting the performance of new devices or modeling large-signal operation [87].

Physical device models are based on the physical operation of carrier transport and therefore provide greater insight into how the device operates. They are usually not restricted to certain applications like an equivalent circuit model, and they can be used to predict the performance of new devices. However, these advantages come at the price of requiring considerably more computer simulation time and memory [87].

B. Diode Equivalent Circuit

The diode might be the simplest modern solid-state device in existence and is probably the easiest to accurately characterize and model; the model can be both simple and accurate [88]. The equivalent circuit model of a diode takes much less computing power to evaluate than a physical device model, and it is simple and accurate under a wide range of conditions. It is for these reasons that a standard diode equivalent circuit will be the basis of the rectenna's diode model. The standard diode model which will be used is illustrated in Fig 7.1 [89].

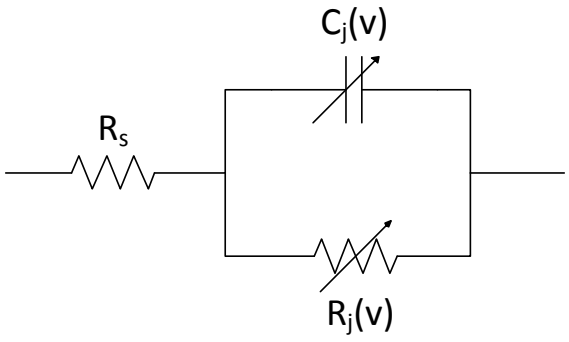

Figure 7.1. Equivalent circuit of the diode.

Mathematical expressions for the voltage-dependent parameters can be obtained from analytical expressions based on the internal physics of the diode [90]. The parasitic series resistance R_s represents the spreading resistance which is associated with the bonding wire, the semiconductor substrate, and the ohmic contact. The series resistance is also nonlinear but only varies slightly under forward bias, so it can be treated as linear [88].

The voltage-dependent resistor R_j is interchangeable with a voltage-dependent current source I_j. This nonlinear current can be expressed by a simple expression which is derived assuming that conduction occurs primarily by means of the thermionic emission of electrons over a barrier. Conduction by other means such as tunneling does occur with a limited scope, but this thermionic emission assumption is valid for Schottky diodes operating close to room temperature with moderate doping densities [88]. The nonlinear current source follows the Shockley equation:

$$I_j = I_0\left(e^{V_j/nV_t} - 1\right) \tag{7.1}$$

where V_t is the thermal voltage which is equal to kT/q and has a value of 25.69 mV at 25°C, k is Boltzmann's constant, T is absolute temperature, q is the electron charge, and V_j is the voltage across the junction. The model parameters I_0 and n are used to model the effects of the junction and differ from diode to diode. The current parameter or saturation current I_0 is a proportionality constant, and the ideality factor n accounts for imperfections in the junction [88].

The voltage-dependent capacitor C_j is the junction capacitance. In a Schottky diode, a reverse-biased junction creates a wider depletion region, and more electrons move to the anode which leaves behind more positive charge. A forward-biased junction creates a narrower depletion region, and fewer electrons move to the anode which results in less stored charge. This creates a situation where a negative voltage increases the amount of negative charge stored on the anode and a positive voltage reduces the amount of negative charge stored [88]. This results in the junction behaving as a nonlinear capacitor [89] which can be expressed as

$$C_j = \frac{C_0}{\left(1 - V_j / V_0\right)^{\gamma}} \tag{7.2}$$

where V_0 is the diffusion potential, C_0 is the zero-voltage junction capacitance, γ is the grading coefficient, and V_j is the voltage across the junction. It can be assumed that the junction is uniformly doped and the transition between regions is abrupt ($\gamma = 0.5$) [88] which simplifies the equation to

$$C_j = C_0 \sqrt{\frac{V_0}{V_0 - V_j}} \ . \tag{7.3}$$

The diode comes in a package, and at microwave frequencies the effect of this packaging must be taken into account. The packaging creates parasitics which limit the performance of the diode. A package parasitic inductance L_p is added to account for the inductance of wires or conductors used to connect the die inside to the exterior terminations. A package parasitic capacitance C_p and a beam-lead parasitic capacitance

C_b are added to account for the capacitance due to the dielectric constant of the solid packaging. The modified equivalent circuit can be seen in Fig 7.2 [89].

The values of the equivalent circuit's parameters can be calculated by measuring the diode's small-signal S-parameters. The voltage dependence can be determined by measuring the small-signal S-parameters at various bias levels and combining these measurements to create a large-signal model [91]. The procedure involves altering the values of the circuit parameters until the S-parameters of the equivalent circuit sufficiently match the measured S-parameters. An optimization procedure is generally required for this multi-variable procedure, and unique solutions usually do not exist [92]. Software packages can be used to fit the S-parameters [93], but if this software is not available, another method must be used.

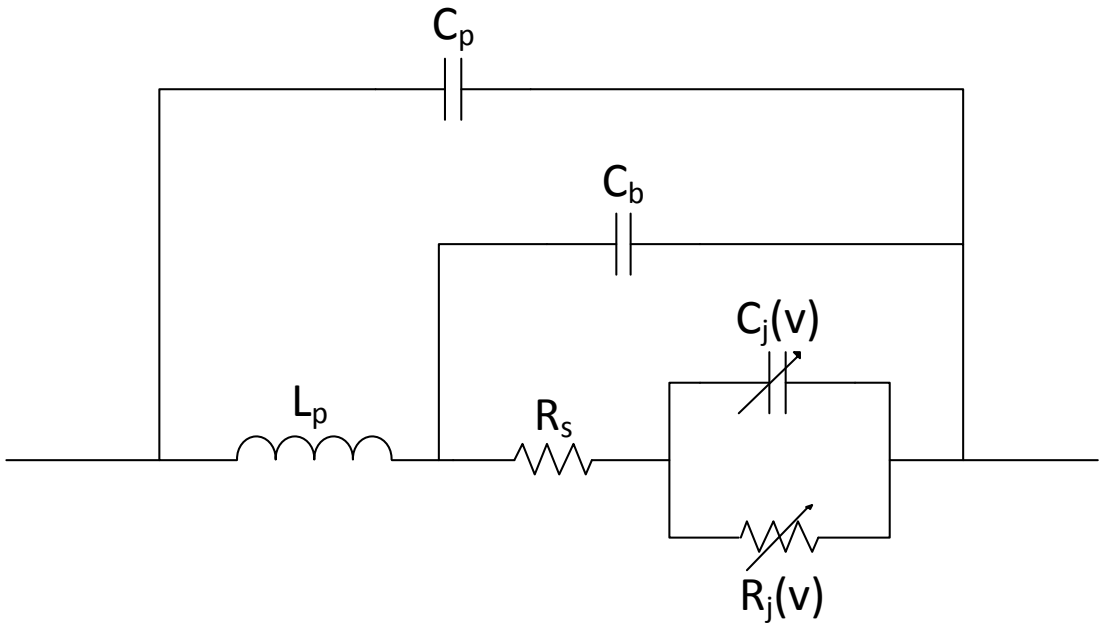

Figure 7.2. Equivalent circuit of the diode (including package parasitics).

C. Measurements

A popular diode used in rectenna design is the M/A-COM GaAs Schottky barrier diode (MA4E1317). This diode will be modeled for use in a 5.8 GHz rectenna system.

The current-voltage curve at DC should be measured so that the DC components of the model (R_s and R_j) can be calculated [94]. This can be done with a curve tracer, or a high resolution voltmeter and ammeter can be used if a curve tracer is not available. The diode must be mounted on a test board to allow the measurement equipment to contact the diode terminals, so care must be taken not to add any extra resistance with the test board. A silver adhesive (Diemat DM6030Hk/F954) is used to connect the diode to the test board. Also, the diode characteristics will be permanently altered if it is burned out. This can happen if over 100 mW is applied to the diode or if the breakdown region is reached. The diode can reach varying degrees of being burned out. Sometimes once burned out, it will become an open or a short, but other times it will just start to permanently behave differently by allowing more current to flow for the same applied voltage. Extra care must be taken to ensure that the diode is not burned out to any degree before the measurements are complete. Seven diodes were measured to ensure that the measurements of a "typical" diode were used to create the model. One of the measured curves of "typical" values can be seen in Fig 7.3.

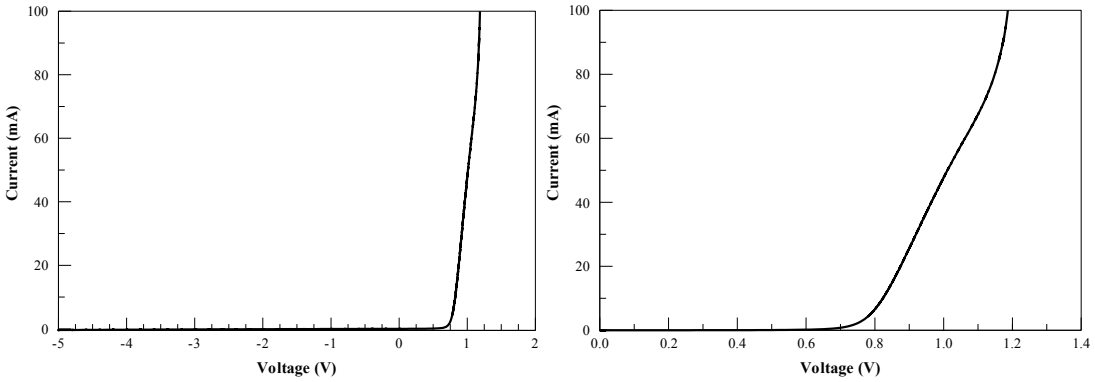

(a) (b)

Figure 7.3. (a) Diode DC measurements and (b) zoomed in view.

S-parameter measurements of the diode must be taken at numerous bias levels using the Thru-Reflect-Line (TRL) calibration method [95]. A network analyzer is used to measure the S-parameters as ratios of complex voltage amplitudes. These S-parameters should be measured at the diode reference plane as shown in Fig 7.4. However, the measurement plane is at a point within the network analyzer, and losses and phase delays will be introduced to the measurement caused by cables, connections, and transitions that must be in place for the network analyzer to connect to the diode. These losses and phase delays can be lumped into a two-port error box placed at both ports of the diode between the measurement plane and the device plane (Fig 7.5). The TRL calibration method can be used to characterize these error boxes before the measurements of the diode are made. The effects of the error boxes can then be removed from the measurements, leaving only the error-corrected S-parameters of the diode.

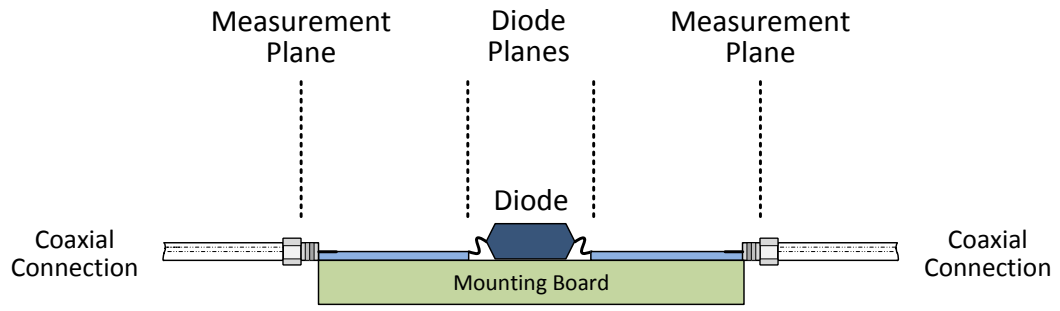

Figure 7.4. Measurement and Device Planes for S-parameter measurements of a diode.

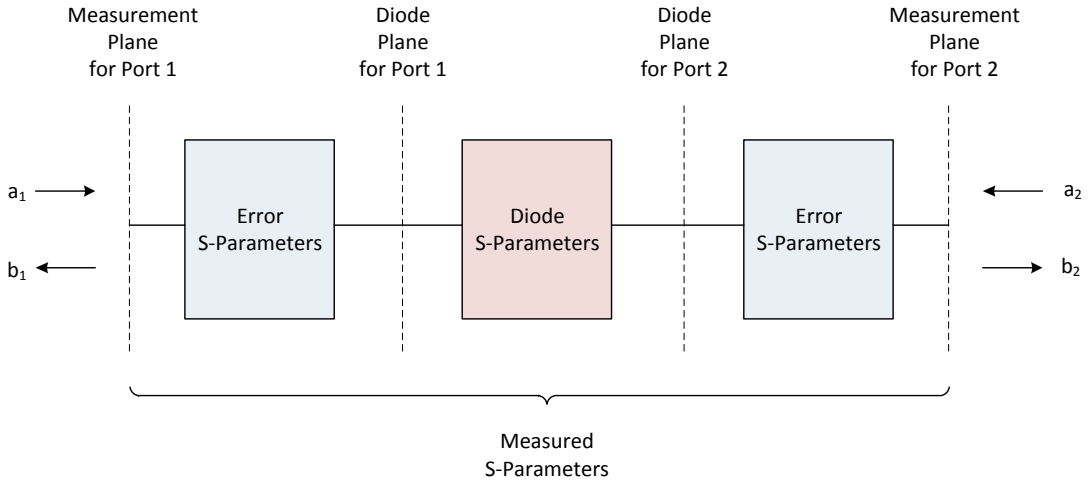

Figure 7.5. Block diagram of a diode's S-parameter measurements.

Three connections are used by the TRL method to determine the error boxes. The Thru connection is made by connecting port 1 directly to port 2 at the device plane. This can be realized by using the same test fixture that will be used for the diode measurement but with the diode removed; the two device planes will be moved infinitesimally close to each other. The Reflect connection is made by terminating each measurement port with a load having a large reflection coefficient. This can be realized by using the same test fixture that will be used for the diode measurement but with the connections to the ports terminated at the device plane. The Line connection is made by connecting port 1 to port 2 through a length of matched transmission line. This can be realized by using the same test fixture as is used for the Thru connection but with an extra length of transmission line added [11]. A diagram of the calibration connections can be seen in Fig 7.6.

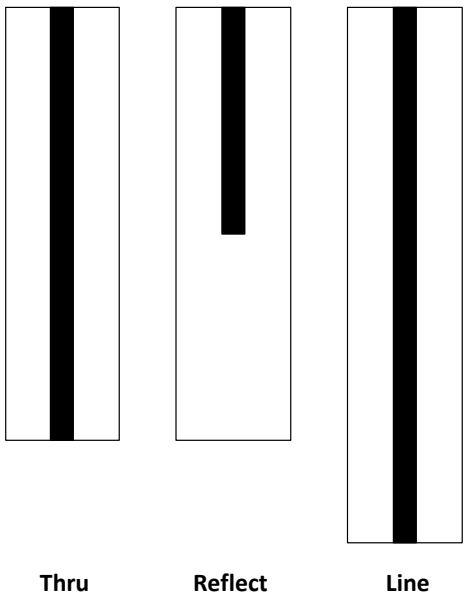

Figure 7.6. Calibration set for TRL measurement.

The S-parameters should be measured over a span of frequencies, but the TRL method places a restriction on the range of frequencies that can accurately be measured. The optimal extra length of the Line (beyond the Thru length) is ¼ wavelength (or 90° of insertion phase) at the center of the frequency range. The insertion phase of the ¼ wavelength Line [96] will vary with frequency as:

$$\text{phase (degrees)} = (360 \times \text{frequency} \times \text{electrical length}) / c \tag{7.4}$$

which can be rearranged to give the electrical length of a ¼ wavelength at the center frequency

$$\text{electrical length (cm)} = 15 / (f_1(\text{GHz}) + f_2(\text{GHz})) \tag{7.5}$$

where f_1 is the start frequency and f_2 is the stop frequency. The insertion phase requirement is that the phase φ over the operating frequency should be $20° \leq \varphi \leq 160°$ [96].

To capture 5.8 GHz and its second harmonic, a frequency range of 4 to 13 GHz is measured which has a center frequency of $f_0 = 8.5$ GHz. The electrical length for this range is calculated from (7.5) as 0.8824 cm. The phase delays from the added ¼ wavelength at the start and stop frequency are calculated from (7.4) as

$$\text{phase (@ 4 GHz)} = 42° \tag{7.6}$$

$$\text{phase (@ 13 GHz)} = 138° \tag{7.7}$$

which meet the insertion phase requirement.

The Thru, Reflect, Line, and numerous diode mounts are etched on 20 mil RT/Duroid 5880 substrate which has a dielectric constant of 2.2. A Thru line length of 110 mm is used, and the physical length of the extra ¼ wavelength on the Line is 6.46

mm. The strip width is 1.52 mm to provide a 50 Ω line at the center frequency. The calibration sets and a diode mount can be seen in Fig 7.7.

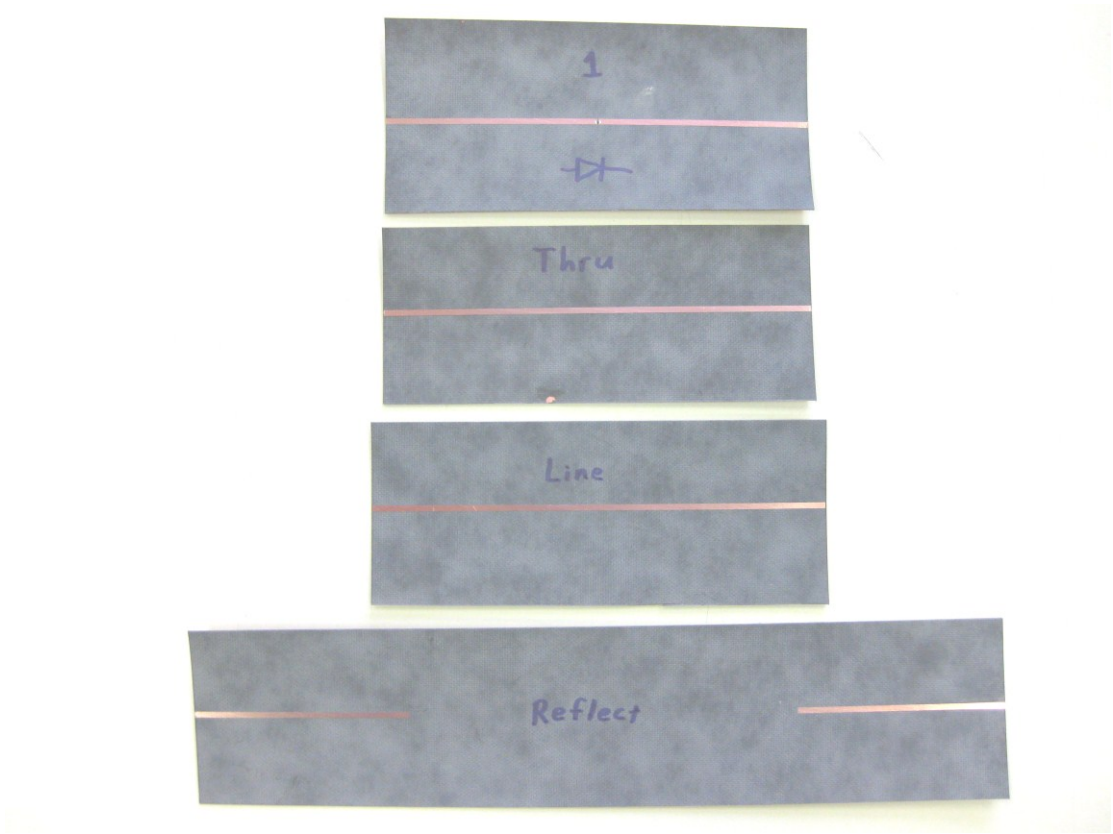

Figure 7.7. Etched calibration set and test fixture for diode TRL measurement.

To calibrate the network analyzer and measure the diode, a measurement setup should be constructed as illustrated in Fig 7.8. Bias-Tees must be used on both sides of the test fixture so that the diode can be biased to various voltages without damaging the network analyzer. The Bias-Tees should be in place (as they will be used for diode measurement) when the calibration sets are used so that the effects of the Bias-Tees are accounted for in the error box calculation. It is important to note that there is some resistance in the Bias-Tees which will result in a voltage drop across the Bias-Tee when a DC current flow is established. Therefore, not all of the voltage provided by the DC-voltage source will appear as a bias across the diode, so a voltmeter should be used to measure the actual bias being applied to the diode.

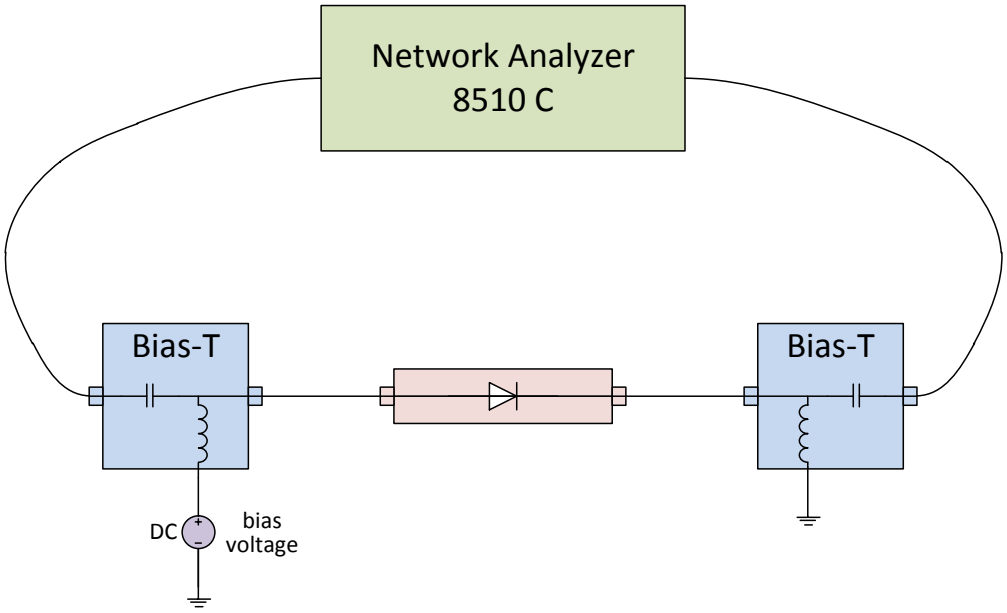

Figure 7.8. Setup for TRL calibrated S-parameter measurement of a diode.

The Agilent 8510C network analyzer can be set to compute the error boxes and directly apply them to the measured S-parameters by entering the correct settings and letting the network analyzer know what kind of calibration set is being used. There is some difficulty in creating consistent connections for all calibration sets and diode mounts. Ten diodes were measured at sixteen bias levels with a Thru length of 110 mm. One of the better measurement sets can be seen in Figs. 7.9-7.10. Some oscillation with frequency can be seen in the figures which is a result of inconsistent connections. Another set of four diodes was measured with a new calibration set which has a Thru length of 37.88 mm in an attempt to reduce some of the transmission line effects on the measurements, but the same oscillation with frequency occurred. The new measurements had fewer oscillations across the frequency range because the shortened length could not support as many wavelengths, but the oscillations had similar amplitude variations. This confirmed that the oscillations were indeed due to connection inconsistencies.

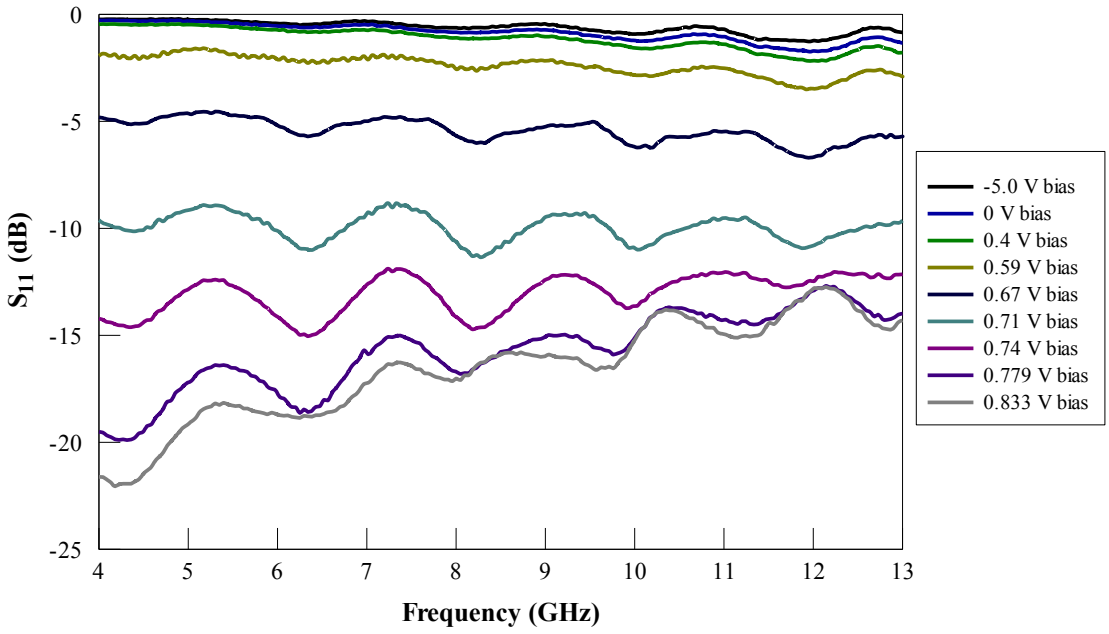

(a)

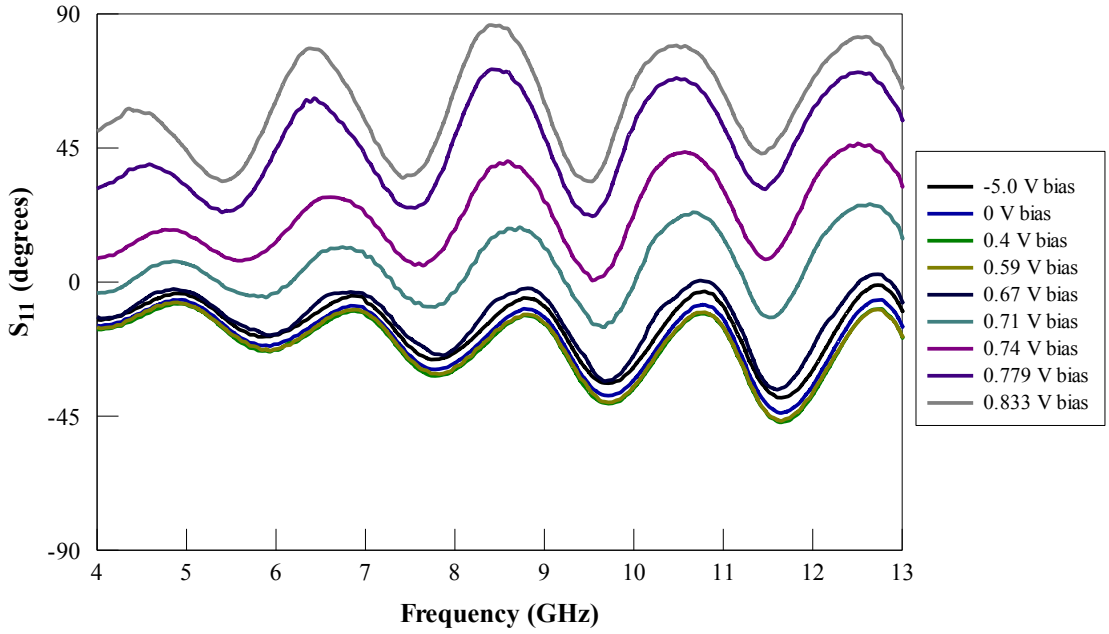

(b)

Figure 7.9. S-parameter (S_{11}) measurements at various bias voltages. (a) Magnitude and (b) phase.

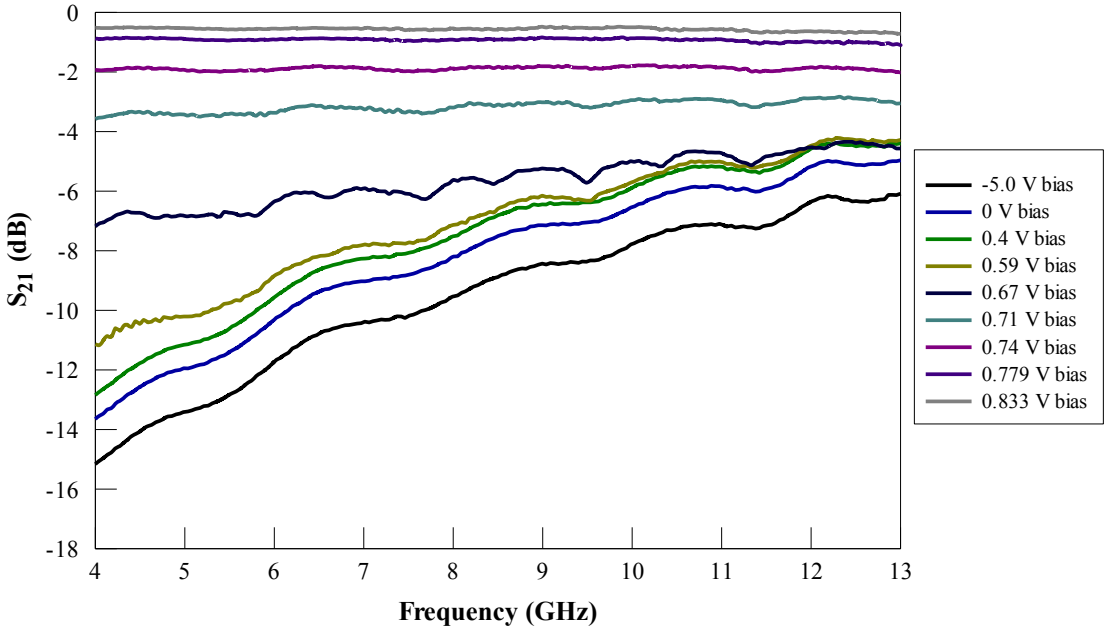

(a)

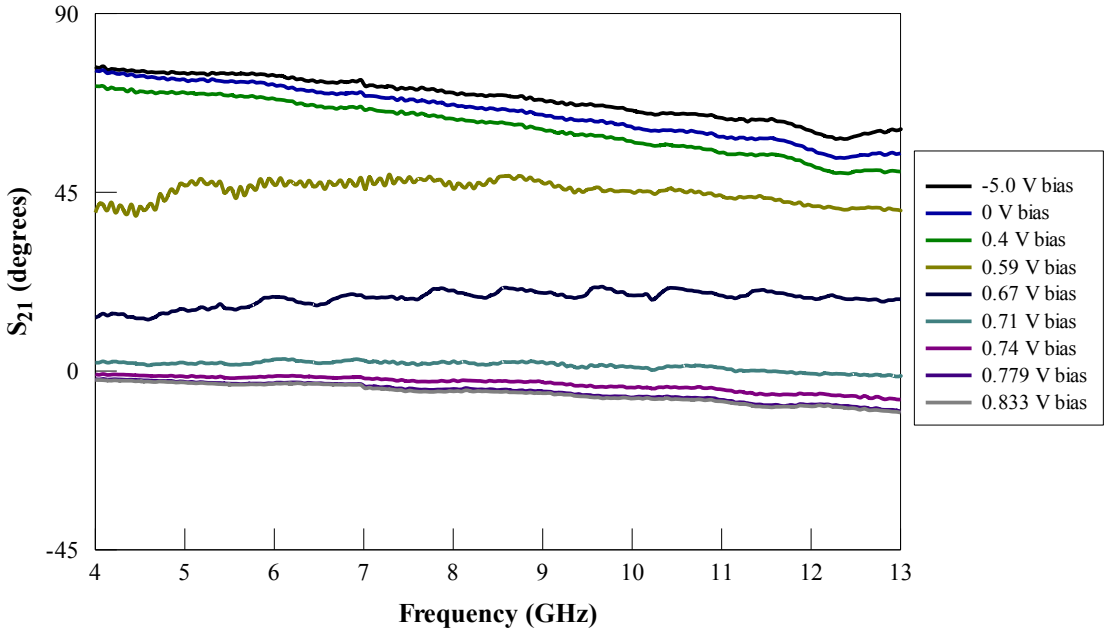

(b)

Figure 7.10. S-parameter (S_{21}) measurements at various bias voltages. (a) Magnitude and (b) phase.

D. Model Parameter Extraction

Once measurements of the diode's DC current-voltage relation and its small signal S-parameters at various bias levels are successfully taken, the equivalent circuit parameters can be fit to the measurements.

The DC parameters R_s and I_j (interchangeable with R_j) can be fit to the DC current-voltage data because at DC these are the only components with any effect. The equivalent circuit will reduce to Fig 7.11. Note the relation $V_j = V_D - R_s I_j$, where V_D is the measured voltage across the diode and I_j is the measured diode current. The current-voltage curve can be broken down into two regions: the exponential region and the linear region (Fig 7.12) [97]. At low current, the junction resistance R_j is very large. When current increases, the junction resistance decreases, so at some point the junction resistance will become negligibly small. The diode's series resistance will then become the dominant resistor, and the curve will become linear. This means that when current increases, the ohmic effect takes over. In the exponential region, R_j dominates, so

$$I_j = I_0\left(e^{V_j/nV_t} - 1\right) \tag{7.8}$$

can be fit to this region where I_j is used in place of R_j. This curve can be transformed into a linear curve so that linear regression techniques can be utilized:

$$I_j = I_0\left(e^{V_j/nV_t} - 1\right) \tag{7.9}$$

$$\log(I_j) = \log(I_0) + \frac{1}{nV_t}\log(e)\,V_j \ . \tag{7.10}$$

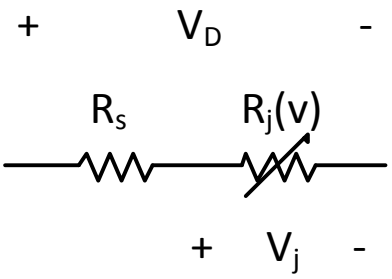

Figure 7.11. Equivalent circuit of the diode at DC.

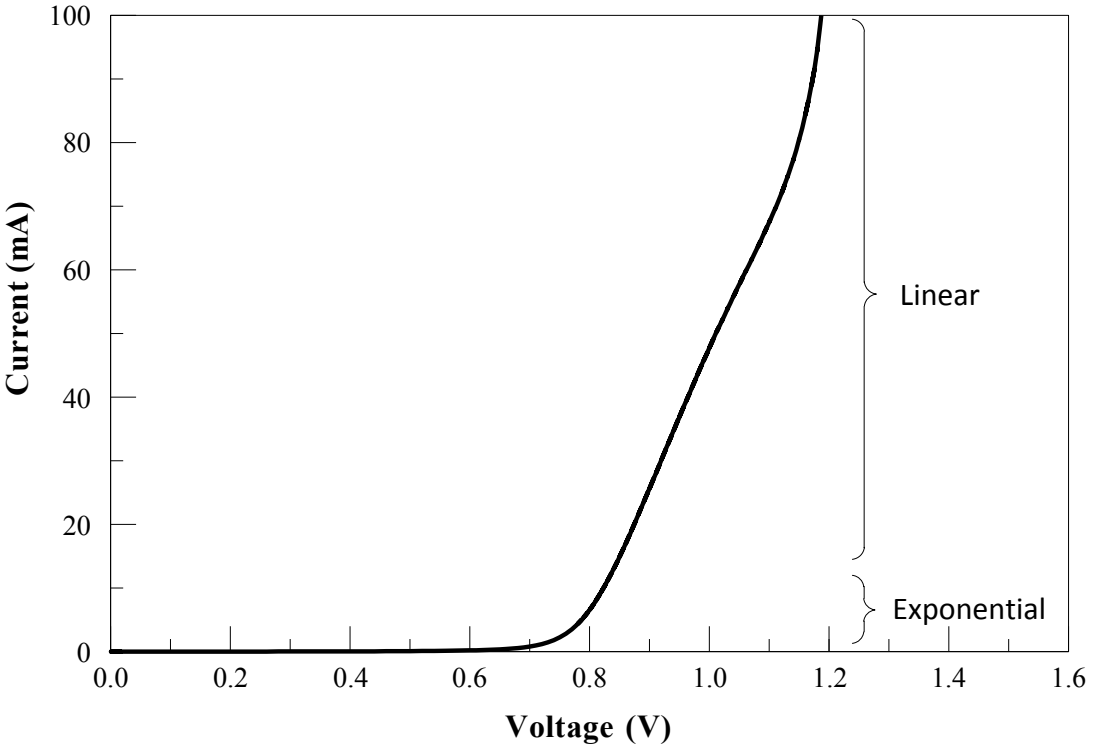

Figure 7.12. Linear and exponential regions of the diode's DC current-voltage curve.

Note that the "-1" in (7.9) is dropped with minimal effect. Equation (7.10) is of the linear form y = m x + b where

$$y = \log(I_j) \tag{7.11}$$

$$b = \log(I_0) \tag{7.12}$$

$$m = \frac{1}{nV_t}\log(e) \tag{7.13}$$

$$x = V_j \tag{7.14}$$

which can be fit to the data in the exponential region using a linear regression. In the linear region, R_s dominates, so

$$R_s = V_D / I_j \tag{7.15}$$

can be fit to this region. R_s is simply the inverse of the curve's slope in the linear region. There is a gradual transition between the exponential region and the linear region, so the slope should be measured at some distance from the exponential region to insure that R_j's effect is minimal. The model parameters are calculated to be:

$$R_s = 4\ \Omega \tag{7.16}$$

$$I_0 = 10^{-14}\ \text{A} \tag{7.17}$$

$$n = 1.06\ . \tag{7.18}$$

The curve is fit with an R^2 value [98] of 0.9901 and is illustrated in Fig 7.13 along with the measured data. Alternatively, a nonlinear regression can be used to fit the curve if capable software is available.

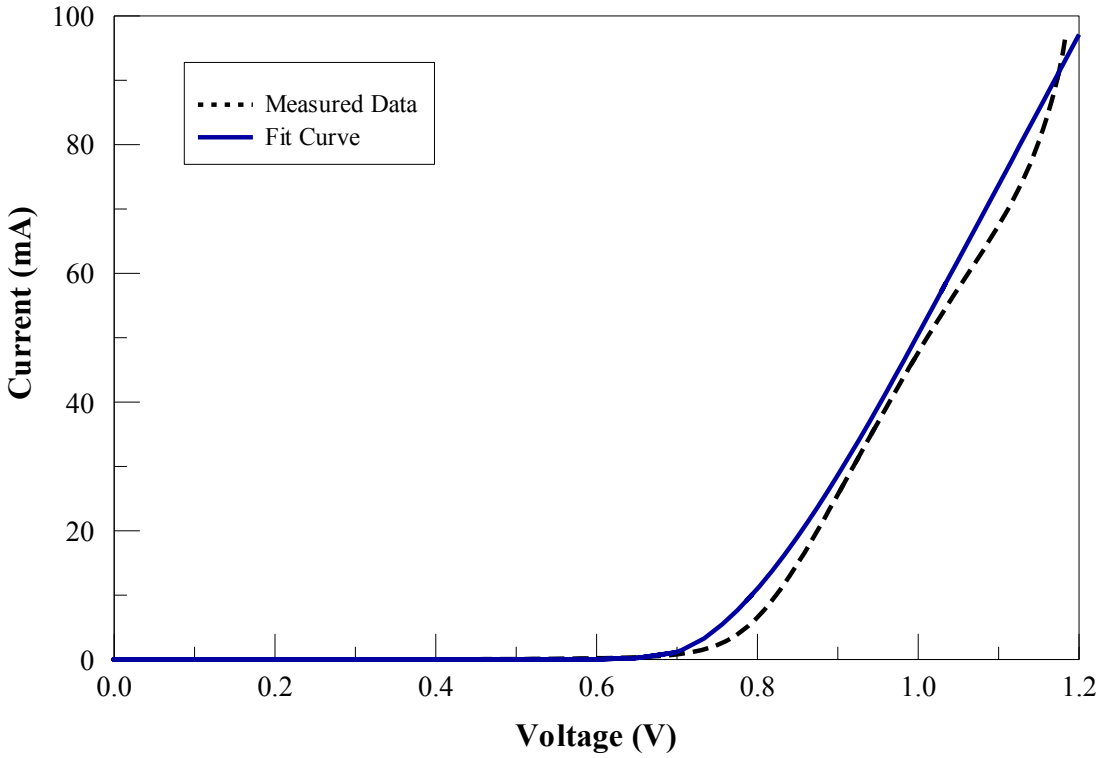

Figure 7.13. Diode DC measurements and fit curve.

Now that R_s and I_j are determined, the other model parameters can be found from the S-parameters. Using Agilent ADS, the S-parameters of the model can be observed for different parameter values. R_s and I_j can be permanently fixed, and then the parasitics can be set to different values while C_j is varied to different bias levels to create a match with measurements over all bias levels. This works successfully when the diode is in the non-conducting region. However, at bias levels in the forward region, the model could not match the measured S-parameters. The restriction of a fixed R_s and I_j prevented the freedom necessary to fully match to the S-parameters.

E. Alternate Model Parameter Extraction Method

It can be difficult to choose correct values for the model parameters, and once parameter values are chosen, they are usually not unique. A convenient method to fit the data using only the S-parameters is to systematically isolate the voltage-independent components from the voltage-dependent components [99]. Circuit components can be added to the diode model to cancel the effect of the voltage-independent components so that only the voltage-dependent components remain as contributing elements. Fig 7.14 illustrates the addition of $-R_s$, $-L_p$, $-C_b$, and $-C_p$ (which are the negatives of the voltage-independent components) to the equivalent circuit which serve to cancel out the voltage-independent components. This leaves only the voltage-dependent components C_j and R_j. When the circuit is simplified to only C_j and R_j in parallel as shown in Fig 7.14, the Y-parameters of this reduced circuit will be a series of straight lines as illustrated in Fig 7.15. The real part of Y_{11} will be $1/R_j(V_j)$ and the imaginary part of Y_{11} will be $\omega C_j(V_j)$ which are both straight lines as a function of frequency.

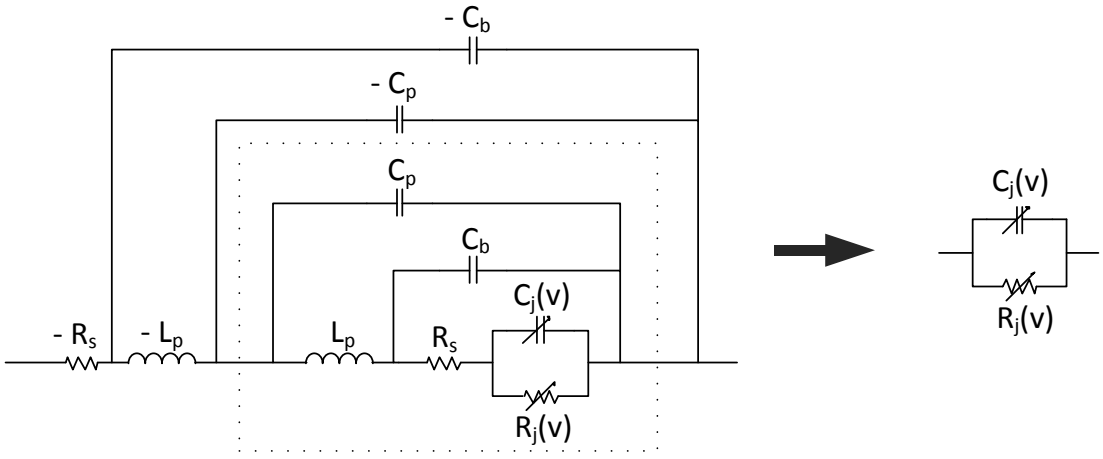

Figure 7.14. Components added to cancel the voltage-independent components' effect. The components within the dotted box represent the diode model. This can be replaced with S-parameters.

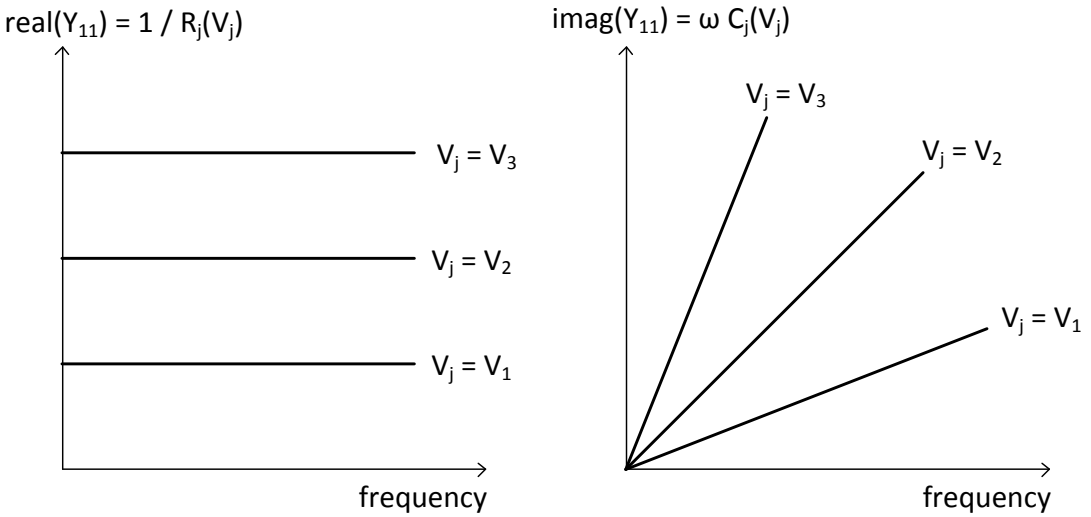

Figure 7.15. Y-parameters of remaining voltage-dependent components. The different lines represent different bias voltages.

Using the Agilent ADS circuit simulator, the equivalent circuit representation of the diode can be replaced by the diode's measured S-parameters and the negative components added as shown in Fig 7.16. The values of Y_{11} can be calculated from the S-parameters [11] by

$$Y_{11} = \left.\frac{I_1}{V_1}\right|_{V_2=0} = Y_0 \frac{(1-S_{11})(1+S_{22})+S_{12}S_{21}}{(1+S_{11})(1+S_{22})-S_{12}S_{21}} \quad . \tag{7.19}$$

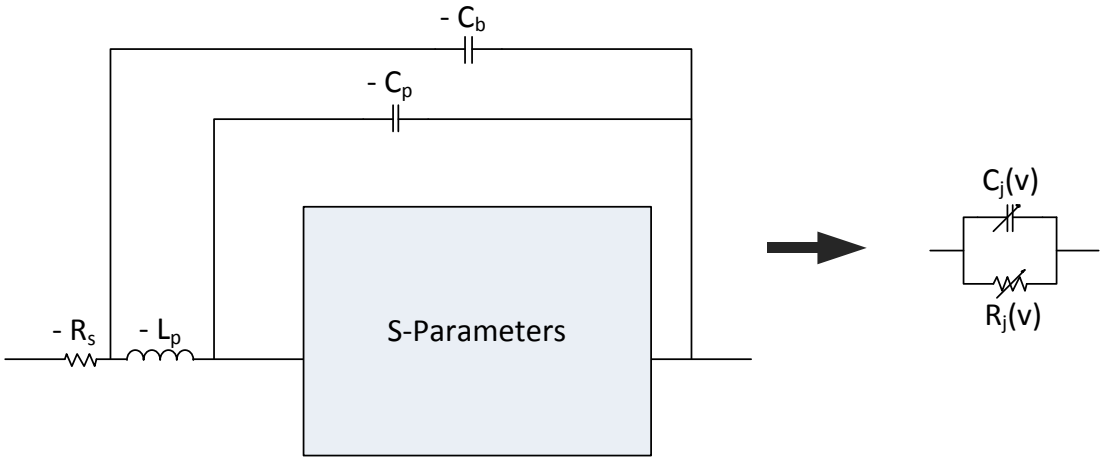

Figure 7.16. Components added to cancel the voltage-independent components' effect. The S-parameters replace the equivalent circuit of the diode. When negative components are set to the correct values, then only C_j and R_j of the diode model will affect the Y-parameters.

If the negative components are set to the correct values, then only C_j and R_j will have any effect on the Y-parameters. Therefore, to find the correct values of the negative components, the values of these components can be varied while observing the resulting Y-parameters. When the Y-parameters are a series of straight lines of the form shown in Fig 7.15, then the effect of the voltage-independent parameters has been cancelled out and their values successfully determined. By following this procedure, these voltage-independent parameters are determined to be:

$$R_s = 0.5\ \Omega \tag{7.20}$$

$$L_p = 0.26\ \text{nH} \tag{7.21}$$

$$C_p = 0.01\ \text{pF} \tag{7.22}$$

$$C_b = 0.04\ \text{pF}\ . \tag{7.23}$$

The values of the voltage-dependent components (as a function of bias voltage) can then be determined from the Y-parameters that result from the previous step. Each straight line on the Y-parameter graph represents a value at a different bias voltage. Since

$$\text{real}(Y_{11}) = 1/R_j(V_j) \tag{7.24}$$

$$\text{imag}(Y_{11}) = \omega C_j(V_j)\ , \tag{7.25}$$

$R_j(V_j)$ can be determined from the real part of Y_{11}, and $C_j(V_j)$ can be determined from the imaginary part of Y_{11}.

F. R_j Calculation

The parameter R_j can be calculated from the real part of Y_{11}. Each horizontal line on the real(Y_{11}) graph gives a value for R_j at a different bias voltage as shown in Fig 7.15. This can be used to create a series of (V_j, R_j) data points (one data point for each bias voltage). The $R_j(V_j)$ data is then converted to a current by

$$I_j = V_j / R_j \,, \tag{7.26}$$

and the equation

$$I_j = I_0 \left(e^{V_j / nV_t} - 1 \right) \tag{7.27}$$

is fit to the data points using a least squares method which gives:

$$I_0 = 1.193 \text{ x } 10^{-11} \text{ A} \tag{7.28}$$

$$n = 1.290 \,. \tag{7.29}$$

The I_j curve is fit with an R^2 value [98] of 0.9812. This curve and the (V_j, I_j) data points are illustrated in Fig 7.17. I_j can be implemented in Agilent ADS as a nonlinear current source by using a symbolically defined device.

A "soft exponential" should be used in place of a regular exponential in the computer calculations to prevent overflow. If the argument of the exponential (V_j/nV_t) is large, taking the exponential of this large argument can cause an overflow error. The "soft exponential" can be defined to be equal to a regular exponential for arguments less than some cutoff value and to be a linear extrapolation of the exponential for arguments greater than the cutoff value. This can be implemented in Agilent ADS as:

max_exp = 1.0e20

max_arg = ln(max_exp)

exp_soft(x) = if (x < max_arg) then exp(x) else (x+1-max_arg)*max_exp endif

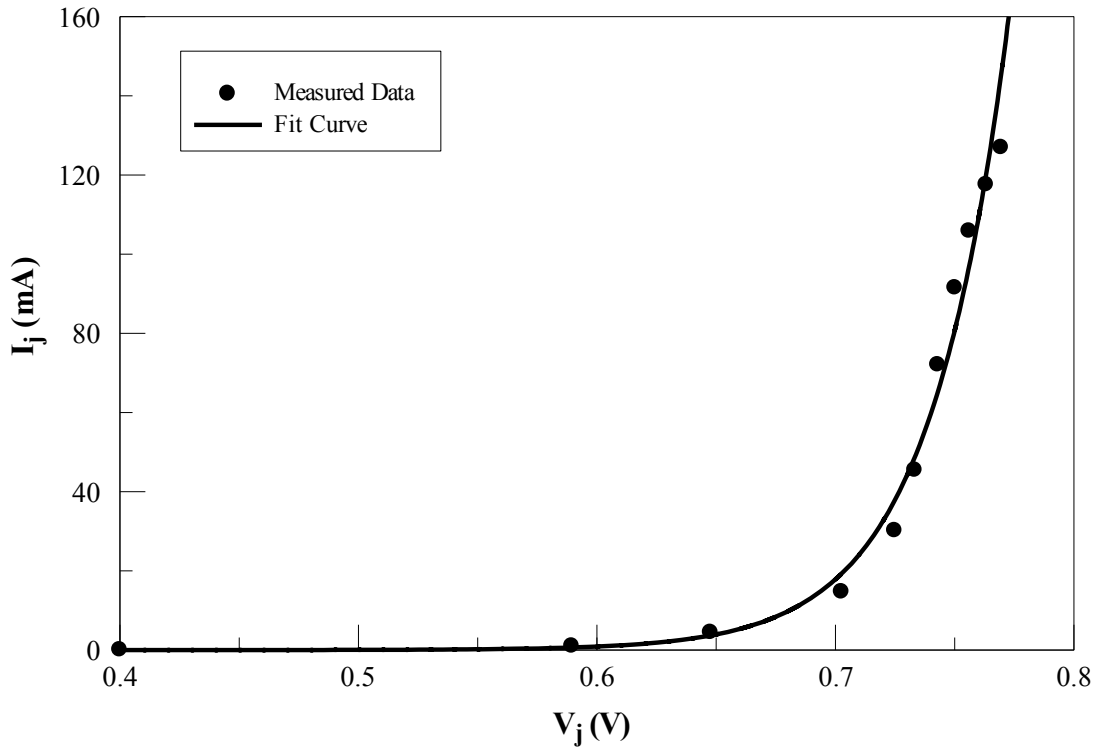

Figure 7.17. I_j curve fit to data.

G. C_j Calculation

The parameter C_j can be calculated from the imaginary part of Y_{11}. Each straight line on the imag(Y_{11}) graph gives a value for C_j at a different bias voltage as shown in Fig 7.15. This can be used to create a series of (V_j, C_j) data points (one data point for each bias voltage). Agilent ADS has a nonlinear capacitor device which can be used to implement C_j. This device requires input in the form of a polynomial, so the $C_j(V_j)$ data must be forced into the form of a polynomial [100].

A polynomial of a large degree (20-25) must be used in order to satisfactorily force the polynomial to behave as an exponential over the desired range, but only sixteen data points exist. If a 20-25 degree polynomial is fit to only sixteen data points using a least squares method then the data is overfit, and the polynomial will fit correctly at the data points but will wildly oscillate between data points. This does not adequately represent the exponential form of the data. Artificial data points can be created by linearly interpolating between real data points, allowing the use of as many data points as desired. A 20-25 degree polynomial can then be fit to the artificial data points (using a least squares method) and effectively fit the form of an exponential within the desired range. Note that the polynomial blows up outside of the range. Polynomials of such a large degree are required to adequately fit the form of an exponential since this is not a polynomial's usual form. A 20 degree polynomial and a 25 degree polynomial are fit to the data using this method with resulting R^2 values [98] of 0.7152 and 0.9339, respectively. These curves and the (V_j, C_j) data points are illustrated in Fig 7.18.

The polynomials are:

20 deg $C_j(V_j)$ =

$2.251953845934267 \times 10^{-14} + 3.928708106450134 \times 10^{-14} V_j - 1.872605744144919 \times 10^{-13} V_j^2 - 8.010052760857773 \times 10^{-13} V_j^3 + 1.035723793272987 \times 10^{-12} V_j^4 + 6.019608944715903 \times 10^{-12} V_j^5 + 3.292217192099333 \times 10^{-12} V_j^6 - 1.188012141308037 \times 10^{-11} V_j^7 - 2.021997434144966 \times 10^{-11} V_j^8 - 6.795781565984654 \times 10^{-12} V_j^9 + 1.408246385109605 \times 10^{-11} V_j^{10} + 2.231293123305528 \times 10^{-11} V_j^{11} + 1.691875529472090 \times 10^{-11} V_j^{12} + 8.293398780762461 \times 10^{-12} V_j^{13} + 2.844367116709308 \times 10^{-12} V_j^{14} + 7.004768751099705 \times 10^{-13} V_j^{15} + 1.238874503528577 \times 10^{-13} V_j^{16} + 1.540283747327346 \times 10^{-14} V_j^{17} + 1.280357467024890 \times 10^{-15} V_j^{18} + 6.396262419195184 \times 10^{-17} V_j^{19} + 1.453338557125182 \times 10^{-18} V_j^{20}$.

25 deg $C_j(V_j)$ =

$1.646738462080980 \times 10^{-14} - 3.841968572067818 \times 10^{-14} V_j + 1.353667676256704 \times 10^{-13} V_j^2 + 1.603431782387508 \times 10^{-12} V_j^3 + 1.725111435338492 \times 10^{-13} V_j^4 - 1.363440404577148 \times 10^{-11} V_j^5 - 1.692864176044302 \times 10^{-11} V_j^6 + 3.576722607831512 \times 10^{-11} V_j^7 + 9.264821210126666 \times 10^{-11} V_j^8 + 2.660693196199393 \times 10^{-11} V_j^9 - 1.334940731727817 \times 10^{-10} V_j^{10} - 1.929241277273865 \times 10^{-10} V_j^{11} - 7.342053211680040 \times 10^{-11} V_j^{12} + 9.197717732432363 \times 10^{-11} V_j^{13} + 1.623743979314330 \times 10^{-10} V_j^{14} + 1.323625389434068 \times 10^{-10} V_j^{15} + 7.171379278258487 \times 10^{-11} V_j^{16} + 2.826579043343990 \times 10^{-11} V_j^{17} + 8.387264303460990 \times 10^{-12} V_j^{18} + 1.895653489292848 \times 10^{-12} V_j^{19} + 3.256194634903012 \times 10^{-13} V_j^{20} + 4.188460909887590 \times 10^{-14} V_j^{21} + 3.913242592828937 \times 10^{-15} V_j^{22} + 2.510211233005998 \times 10^{-16} V_j^{23} + 9.894061095862421 \times 10^{-18} V_j^{24} + 1.807503156397230 \times 10^{-19} V_j^{25}$.

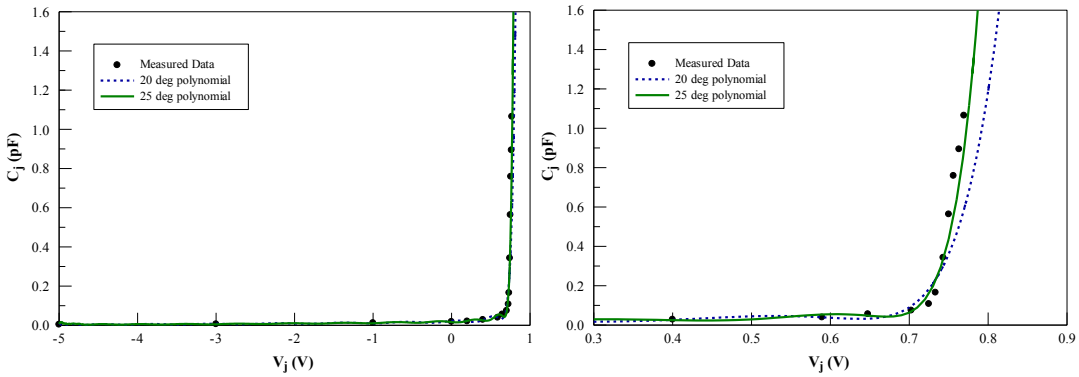

Figure 7.18. (a) C_j polynomials (of 20 and 25 degree) fit to data and (b) zoomed in view.

The equivalent circuit can now be constructed in Agilent ADS by using a current source to represent R_j and a nonlinear capacitor to represent C_j. This equivalent circuit shows a good match to the measured S-parameters with a slight S-parameter oscillation with changing bias voltage; this is due to the oscillatory properties of the polynomial which was used to represent C_j. This might be acceptable, however a major problem results when a harmonic balance simulation is run using this model. There is a huge convergence problem which is a byproduct of the nonlinear capacitor [101]-[102]. This makes the model very difficult to use for the design of a rectenna and severely limits its utility as a design tool.

H. C_j Calculation (Charge-Based Model)

A charge-based model can be used to represent the voltage-dependent capacitor in place of the nonlinear capacitor component to correct the convergence problem in the harmonic balance simulation [103]. The equation for junction capacitance in the reverse bias region has been previously defined as

$$C_{jr}(V_j) = C_0 \sqrt{\frac{V_0}{V_0 - V_j}} \tag{7.30}$$

where C_{jr} signifies that this is valid only for the reverse bias region. Since

$$Q(v) = \int_v C(\hat{v})\, d\hat{v} + Q_0 \ , \tag{7.31}$$

(7.30) can be integrated with respect to V_j to obtain an equation for charge:

$$Q_{jr}(V_j) = -2C_0 \sqrt{V_0 (V_0 - V_j)} \tag{7.32}$$

where a boundary condition of $Q_j(V_0) = 0$ is enforced. $C_{jr}(V_j)$ and $Q_{jr}(V_j)$ can be extended into the forward region using linear extrapolation. A variable α (where $0<\alpha<1$) must be introduced to define the reverse region as $V_j \leq \alpha V_0$ and the forward region as $V_j > \alpha V_0$. This is necessary to extend the range of the equations into the forward-region while preventing $C_{jr}(V_j)$ from blowing up at $V_j = V_0$. $C_{jr}(V_j)$ is extended to the forward-region by linear extrapolation as

$$C_{jf}(V_j) = C_{jr}(\alpha V_0) + C_{jr}'(\alpha V_0)(V_j - \alpha V_0) \ , \tag{7.33}$$

which can be integrated with respect to V_j to obtain an equation for charge in the forward-region:

$$Q_{jf}(V_j) = \left[V_j - \alpha V_0\right]\left[C_{jr}(\alpha V_o)\right] + C'_{jr}(\alpha V_0)\left[\frac{(V_j - \alpha V_0)^2}{2}\right] + Q_{jr}(\alpha V_0) \qquad (7.34)$$

where a boundary condition of $Q_{jf}(\alpha V_0) = Q_{jr}(\alpha V_0)$ is enforced. This can be rewritten as

$$Q_{jf}(V_j) = \frac{C_0}{\sqrt{1-\alpha}}\left(V_j - \alpha V_0 + \frac{(V_j - \alpha V_0)^2}{4V_0(1-\alpha)}\right) + Q_{jr}(\alpha V_0)\ . \qquad (7.35)$$

So the final equations for $C_j(V_j)$ and $Q_j(V_j)$ are defined as

$$C_j(V_j) = \begin{cases} C_{jr}(V_j)\ ,\ V_j \le \alpha V_0 & \text{(reverse bias)} \\ C_{jf}(V_j)\ ,\ V_j > \alpha V_0 & \text{(forward bias)} \end{cases} \qquad (7.36)$$

$$Q_j(V_j) = \begin{cases} Q_{jr}(V_j)\ ,\ V_j \le \alpha V_0 & \text{(reverse bias)} \\ Q_{jf}(V_j)\ ,\ V_j > \alpha V_0 & \text{(forward bias)} \end{cases} \qquad (7.37)$$

with $C_{jr}(V_j)$, $C_{jf}(V_j)$, $Q_{jr}(V_j)$, and $Q_{jf}(V_j)$ defined in (7.30), (7.33), (7.32), and (7.35) respectively. It is important to note that $C_j(V_j)$ and $Q_j(V_j)$, as well as their first derivatives, are continuous. $C_j(V_j)$ can be fit to the data points using a least squares method which gives:

$$C_0 = 1.771 \text{ x } 10^{-14} \text{ F} \qquad (7.38)$$

$$V_0 = 0.7424 \text{ V} \qquad (7.39)$$

$$\alpha = 0.9942\ . \qquad (7.40)$$

The C_j curve is fit with an R^2 value [98] of 0.9985. Note that in addition to correcting the convergence problem, the charge-based model allows a more natural curve to be fit and increases C_j's match to the data. The fit curve for C_j and the (V_j, C_j) data points can be seen in Fig 7.19. C_j can be implemented in Agilent ADS with a symbolically defined device. A weighting function of 1 in an ADS symbolically defined

device is defined as jω and is used when a time derivative is required. Q_j is defined in (7.37) as a function of C_0, V_0, and α, and since

$$I = \frac{d}{dt}\big(Q(v)\big) \ , \tag{7.41}$$

a weighting function of 1 can be used on an expression for Q_j to define the current through the nonlinear capacitor. This is the charge-based model of a voltage-dependent capacitor.

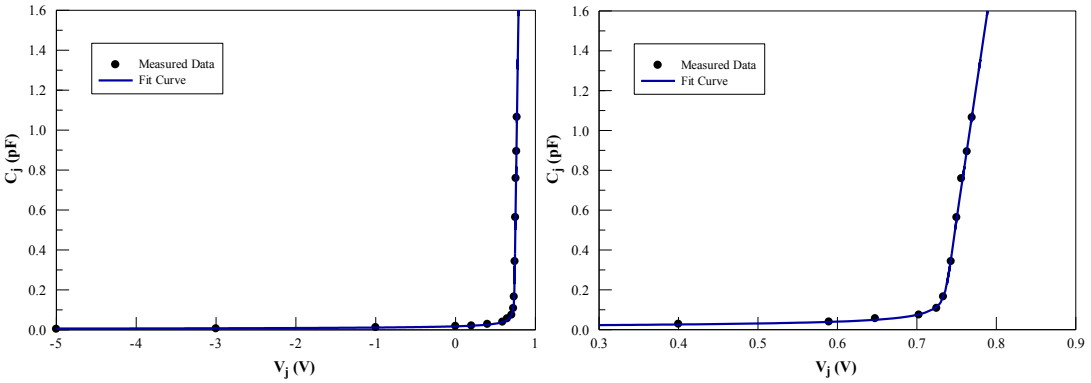

Figure 7.19. (a) C_j exponential curve fit to data and (b) zoomed in view.

I. Final Model

The final diode model is created using equations (7.27) and (7.37) with parameter values (7.20)-(7.23), (7.28)-(7.29), and (7.38)-(7.40). The implementation of this model in Agilent ADS [83] can be seen in Fig 7.20. Note that the variable capacitor C_j and variable resistor R_j are both implemented as symbolically defined devices.

The S-parameters of the model show a good match to the measured S-parameters; a comparison can be seen at a few of the bias voltages in Figs. 7.21-7.22. Sixteen bias levels were measured, but only a few are shown in order to make the graphs more readable. This diode model can be used in an electromagnetic simulator, such as Agilent ADS, in conjunction with the other rectenna components (which are easily modeled) to simulate a rectenna's performance. This will greatly improve rectenna design time and prevent unnecessary fabrication and testing. An example of using this model for the design of a rectenna system is included in the next section.

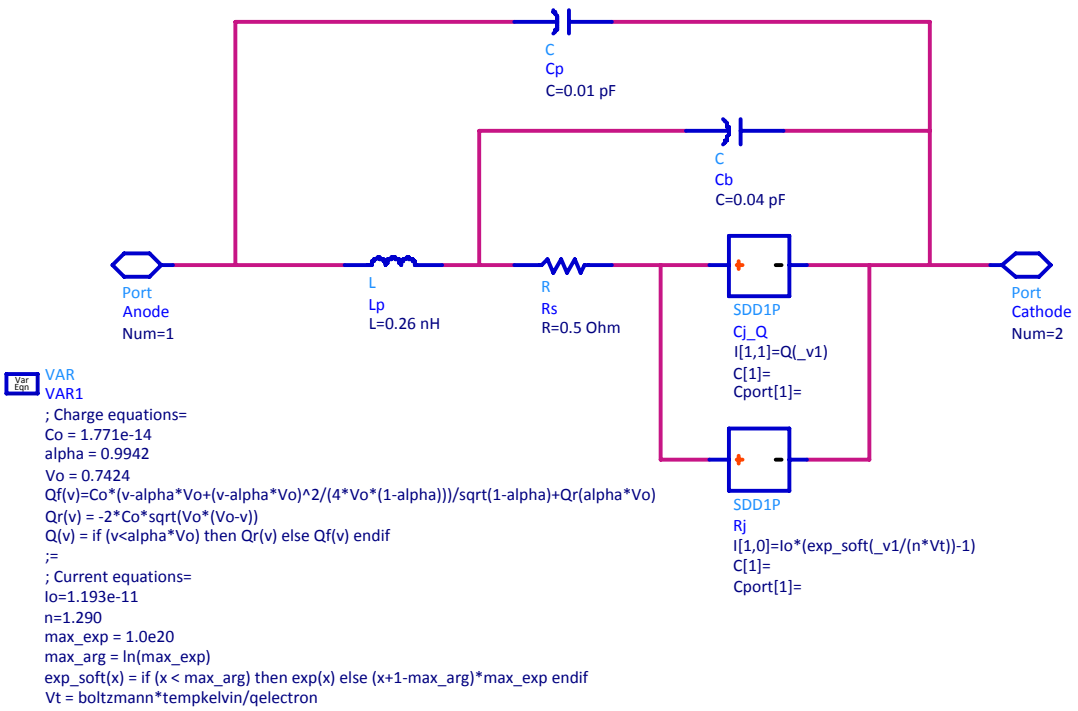

Figure 7.20. Schematic of the diode model in Agilent ADS.

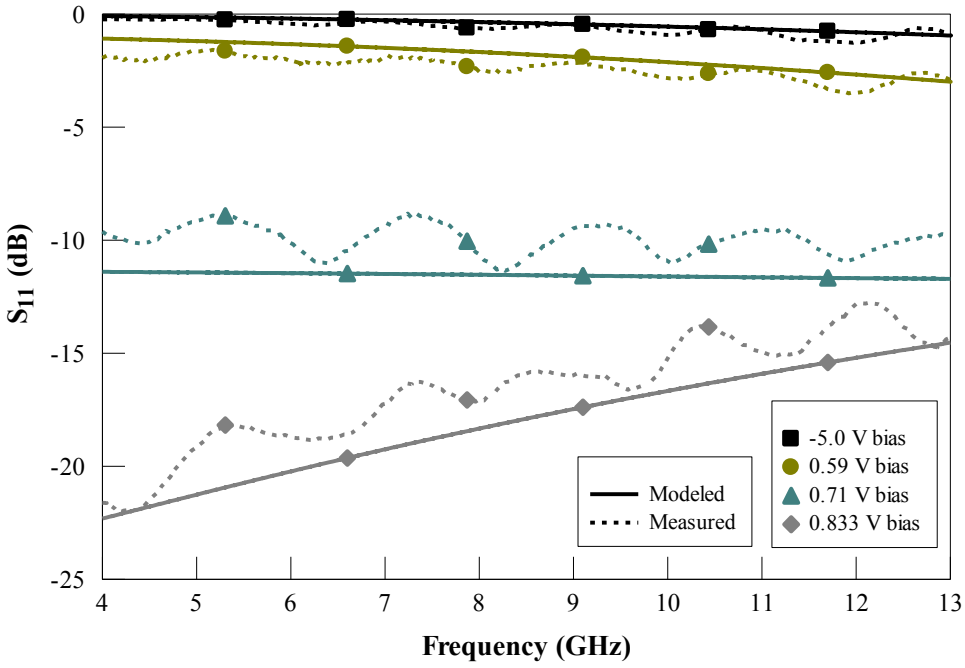

(a)

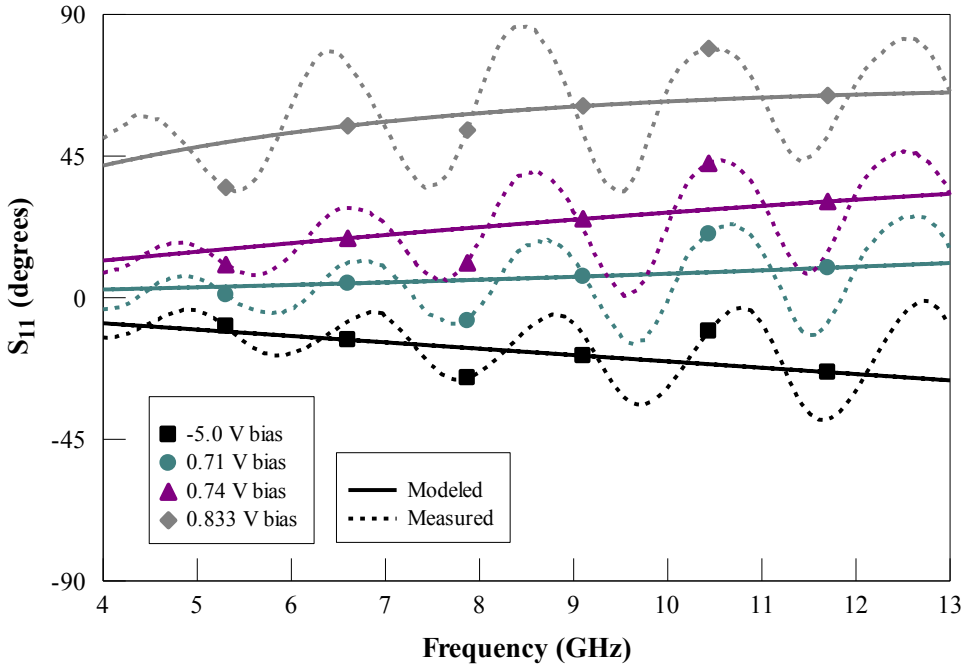

(b)

Figure 7.21. Comparison of S-parameter (S_{11}) measurements and modeled (simulated) values at various bias voltages. (a) Magnitude and (b) phase.

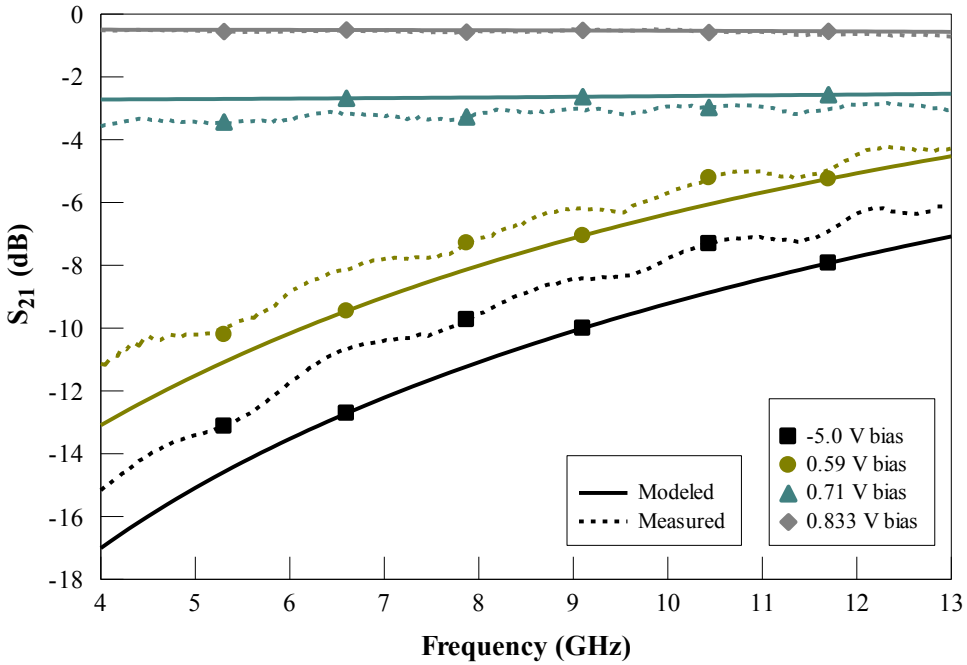

(a)

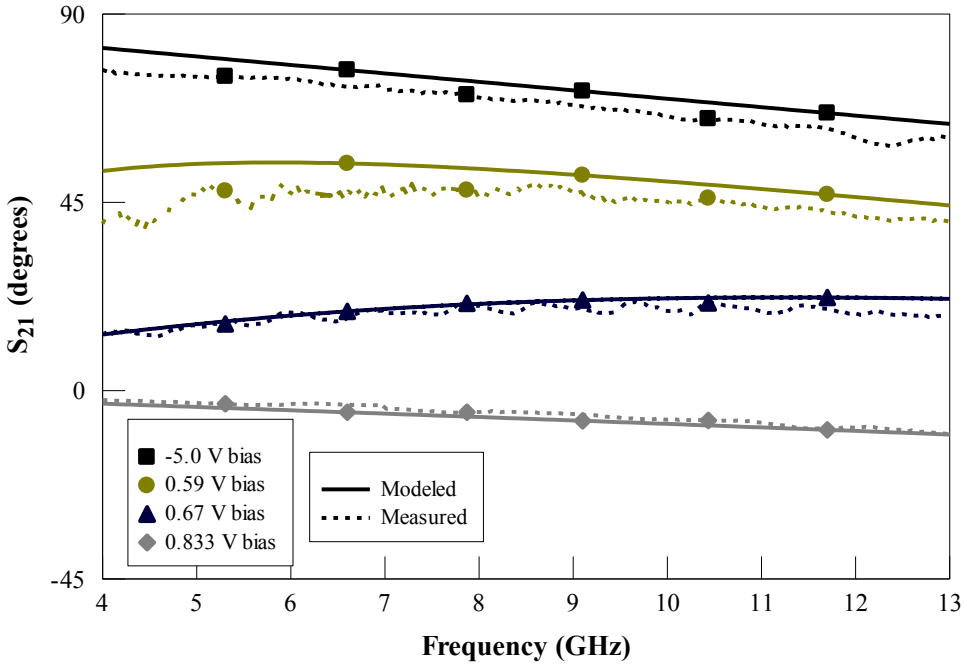

(b)

Figure 7.22. Comparison of S-parameter (S_{21}) measurements and modeled (simulated) values at various bias voltages. (a) Magnitude and (b) phase.

J. Conclusion

A diode model based on an equivalent circuit was created to aid in rectenna design. A method which systematically isolates the model's voltage-dependent components from its voltage-independent components was used to calculate the parameters. This method is based on measured S-parameters of the diode at various bias levels. The voltage-independent components were found by adjusting their values such that the Y-parameters appeared as a series of straight lines. The voltage-dependent components were then derived by fitting curves to data points obtained from the straight-lined Y-parameters. A charge-based capacitor model was used in lieu of an ADS nonlinear capacitor component to avoid harmonic balance convergence issues.

The model was implemented in Agilent ADS using symbolically defined devices for both the voltage-dependent current source and the voltage-dependent capacitor (implemented as a charge source). The simulated S-parameters of the model showed a good match to the measured S-parameters over all the bias levels. This model can be used in ADS to simulate the entire rectenna design as will be shown in the next section.

8. RECTENNA DESIGN *

A. Design and Fabrication

The most important component of a microwave wireless power transmission (WPT) system is the rectenna which consists of a receiving antenna and a rectifying circuit. The antenna receives the microwave power, and the rectifying circuit converts the microwave power into DC power.

The proposed rectenna design for 5.8 GHz operation is illustrated in Fig. 8.1. It consists of an aperture-coupled high-gain single-patch antenna, a split ring resonator (SRR) filter to suppress harmonic signals, a diode for RF-to-DC conversion, a DC-pass filter (capacitor), and a load.

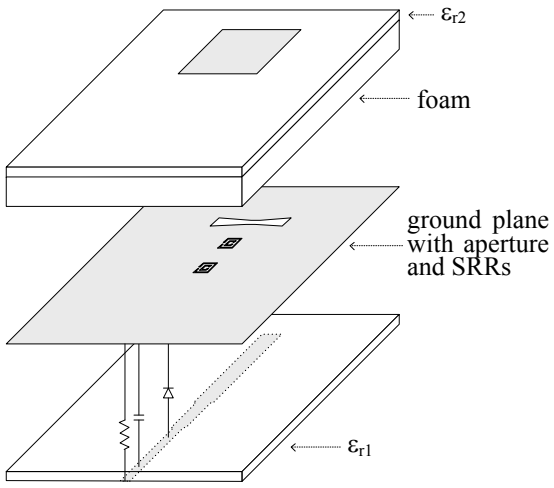

Figure 8.1. Rectenna design (exploded view).

* Parts of this section are reprinted, with permission, from J. Hansen, C. Ahn, and K. Chang, "A 5.8 GHz high gain, aperture coupled rectenna utilizing a split ring resonator filter," in *IEEE Antennas and Propagation Society International Symposium (APSURSI)*, pp. 1-4, Toronto, July, 2010.

The role of the antenna is to efficiently receive microwave power from free space. A high gain antenna is important because it will allow the rectenna to receive more power for a given incident power due to its increased effective aperture area. This will allow for longer distance WPT and a smaller physical receiving area. A patch is utilized because of its simplicity, flatness, and ease of fabrication and integration [1][104]. The length of the patch can be initially approximated [5] by

$$L \approx 0.49\lambda_d = 0.49\frac{\lambda_0}{\sqrt{\varepsilon_r}} \tag{8.1}$$

and optimized using IE3D [12]. The antenna must also be tuned to maximize its gain. The antenna is measured to have a gain of 9.3 dBi, and the radiation pattern can be seen in Fig. 8.2.

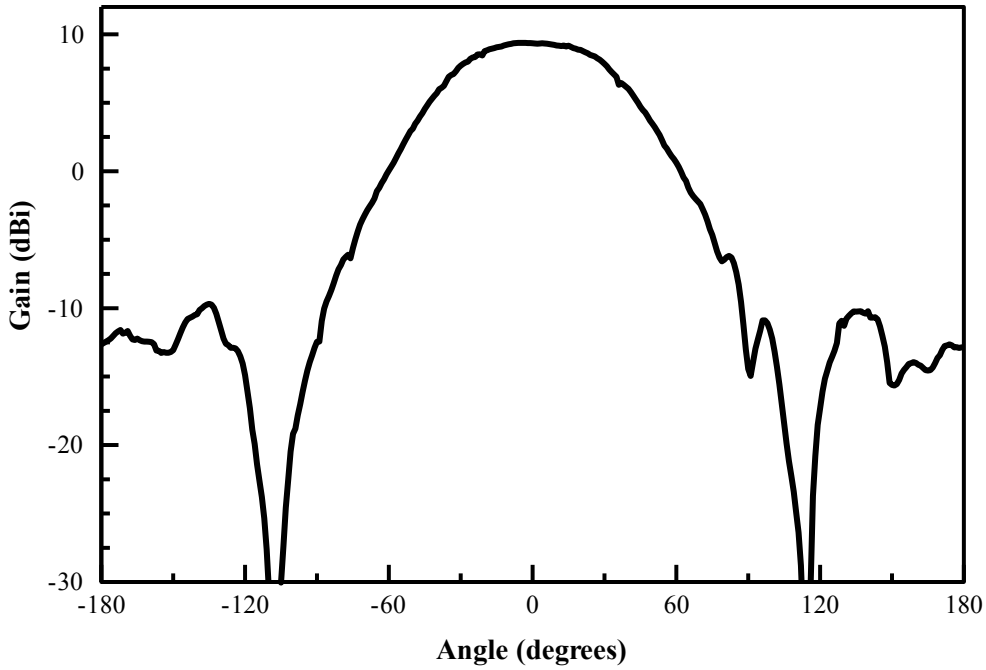

Figure 8.2. Measured radiation pattern.

An aperture-coupled feed [105] is employed because of its inherent isolation between the feeding circuit and the patch. This serves to isolate the antenna operation from the rectifying operation and prevents any inadvertent coupling between the two [1][104]. This will also serve to simplify the design process since the antenna and the rectifier can be designed independently due to very limited coupling between the two.

Novel compact split ring resonators (SRRs) are utilized as the band-reject filter to pass 5.8 GHz and block the second harmonic at 11.6 GHz. This is necessary since the diode creates harmonics due to its non-linear behavior. Most of this harmonic power is contained in the second harmonic, so blocking this harmonic is the most important. The return loss of the patch and filter combination is measured to be 0.86 dB at the second harmonic while the return loss of the patch alone is 5.79 dB at the second harmonic (Fig. 8.3). This is an additional 4.93 dB of suppression provided by the filter.

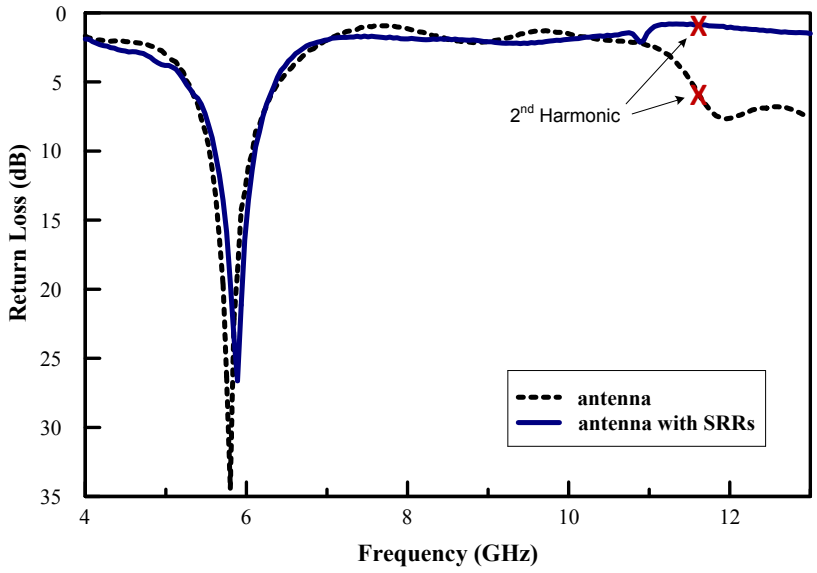

Figure 8.3. Measured return loss of the antenna with and without the split ring resonator (SRR) filter.

The split ring resonator is a defective ground structure which is implemented by etching the structure into the ground plane. This disturbs the shield current in the ground plane and changes the characteristics of the transmission line. A magnetic resonance is induced in the rings of the SRR by the split in the ring and by the gap between the two rings. The splits in the rings allow this type of structure to support wavelengths much larger than the diameter of the rings; this makes SRRs a compact filter [106]-[107]. A split ring resonator is illustrated in Fig. 8.4. The dimensions used for this filter are: a = 1.89 mm, b = 3.01 mm, g = 0.19 mm, t = 0.24 mm, and c = 0.15 mm.

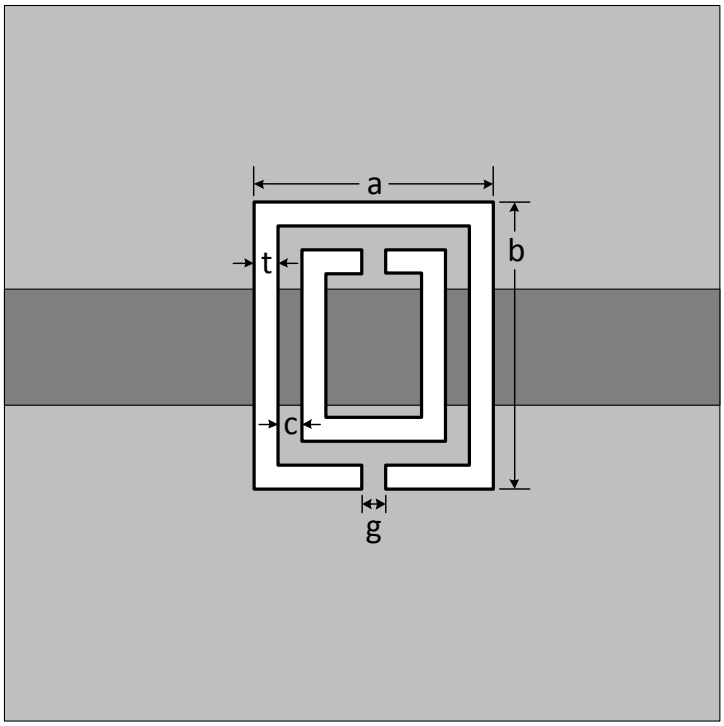

Figure 8.4. Split ring resonator (SRR) in the defective ground plane. The transmission line is also illustrated below the SRR.

A flip-chip type GaAs Schottky barrier diode (MA4E1317) is used to rectify the microwave power, and a broadband capacitor (C08BLBB1X5UX) is used as a DC-pass filter to reflect any unconverted microwave power back to the diode and prevent microwave power from reaching the load. A silver adhesive (Diemat DM6030Hk/F954) is used to attach both the diode and capacitor to the microstrip line. The distance between the diode and the capacitor is crucial because in addition to reflecting the microwave power, the capacitor is used to tune out the diode's reactance and improve conversion efficiency. Setting the distance between the diode and capacitor to a quarter-wavelength will make the capacitor appear as either an open or a short at RF for the fundamental frequency and all of the harmonics. This will create a situation where the microwave energy is reflected back from the capacitor. The SRRs will also reflect the harmonics on the other side of the diode, so any harmonics should be reflected between the SRRs and the capacitor until they are eventually converted to DC by the diode.

Optimization of the rectifying circuit is important to maximize efficiency. The diode must be matched to the input power level and to the load. It has been found that this diode matches well with a 120 Ω line, so the 50 Ω line is converted to a 120 Ω line by way of a quarter-wavelength transformer after the SRRs. The characteristic impedance of the quarter-wavelength transformer can be found [3] by

$$Z_{0T} = \sqrt{Z_i Z_t} \tag{8.2}$$

where Z_{0T} is the characteristic impedance of the quarter-wavelength transformer, Z_i is the input impedance (50 Ω), and Z_t is the terminating impedance (120 Ω). The optimum load value should also be selected to maximize efficiency.

The rectenna is designed using IE3D [12] and is illustrated in Fig. 8.5. The feedline and rectifying circuit are etched on one side of a 20 mil RT/Duroid 5880 substrate with a dielectric constant of 2.2, and the aperture is etched on the other side. Via holes are necessary to connect the diode and capacitor to ground. The patch element is etched on a 2 mil RT/Duroid 3850 substrate with a dielectric constant of 2.9 and is supported by a 3.2 mm thick layer of lightweight foam (Cuming C-FOAM PF-4/PSA) with a low (1.06) dielectric constant. Photographs of the rectenna can be seen in Fig. 8.6.

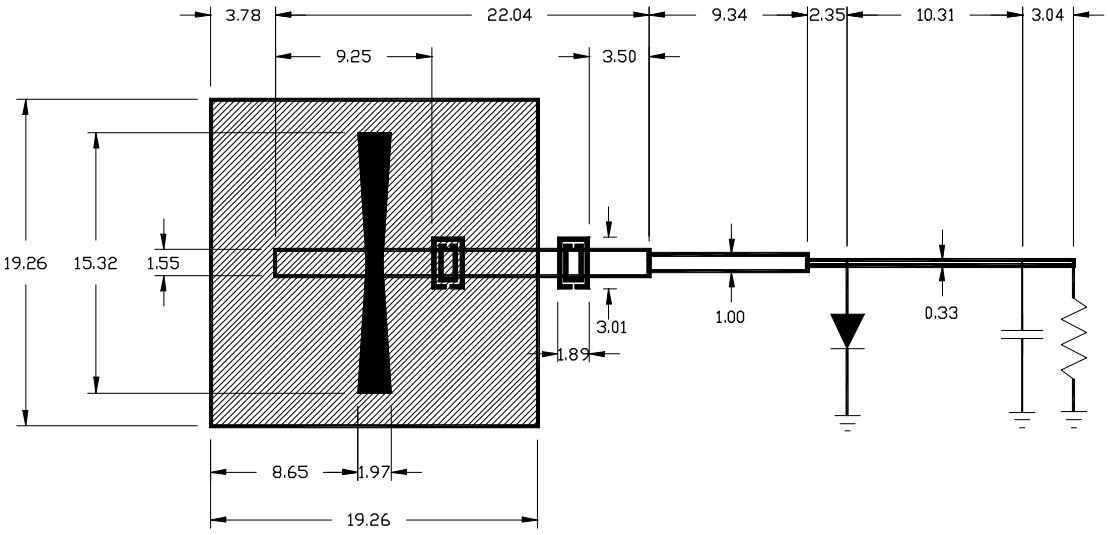

Figure 8.5. Rectenna design (all dimensions in mm).

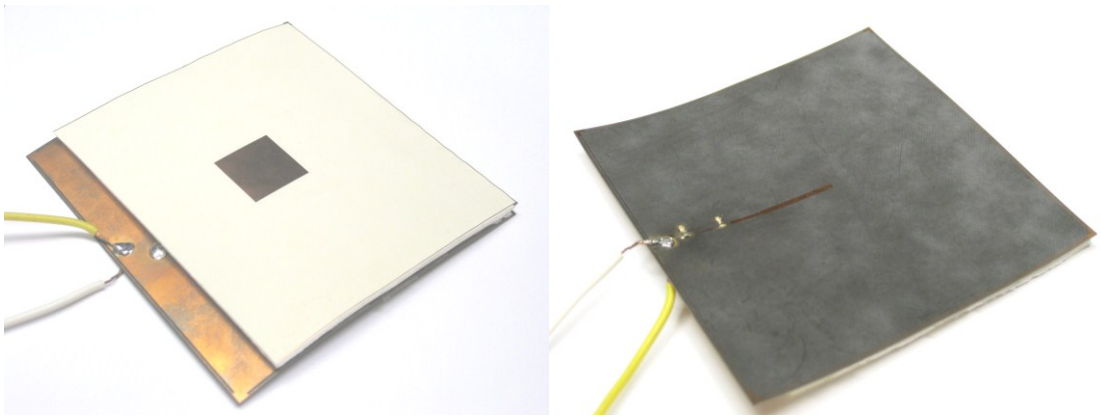

(a) (b)

Figure 8.6. Photographs of the rectenna. (a) Top view and (b) bottom view.

B. Efficiency Measurement

In order to measure the rectenna efficiency, a known power is transmitted from a standard horn antenna, and the resulting voltage is measured across the rectenna's load. The efficiency η can be calculated by

$$\eta = \frac{P_{DC}}{P_{rec}} = \frac{\left(V_D^2 \big/ R_L \right)}{P_t G_t G_r \left(\lambda_0 \big/ 4\pi r \right)^2} \tag{8.3}$$

where P_{DC} is the DC output power of the rectenna and P_{rec} is the power received by the rectenna. V_D is the voltage measured across the load, and R_L is the load resistance. The received power P_{rec} is calculated using the Friis transmission equation [3] where a standard NARDA horn antenna with a 15 dB gain (G_t) is used to transmit the microwave power (P_t) to the rectenna. The rectenna gain (G_r) is 9.3 dB, λ_0 is the free space

wavelength at 5.8 GHz, and r is the distance between the transmitter and the rectenna. The transmitted power (P_t) can be varied to determine the efficiency of the rectenna at different power densities. The load (R_L) can also be varied to determine the rectenna's optimum load. Power density S_D and effective area A_{er} can be calculated [3] as

$$S_D = \frac{P_t G_t}{4\pi r^2} \tag{8.4}$$

$$A_{er} = \frac{G_r \lambda_0^2}{4\pi} \tag{8.5}$$

which can be used to express received power P_{rec} as

$$P_{rec} = S_D A_{er} \ . \tag{8.6}$$

The measurement setup used for this procedure can be seen in Fig. 8.7. A frequency synthesizer is used to generate the 5.8 GHz signal and an isolator is used to protect the synthesizer. A power amplifier must be used so that the transmitted power is sufficiently high to cover the rectenna's entire operating range. A coupler is used immediately before the transmitting antenna so that the transmitted power can be measured. Most of the power is coupled to the antenna, but a small portion is coupled to a power meter. An attenuator must be used before the power meter to adjust the power to a level which is readable by the power meter. A network analyzer is used to characterize the coupler and determine how much power is coupled to the transmitting antenna and how much is coupled to the power meter. In this way, the power meter can be used to measure the transmitted power. The rectenna is set at a fixed distance in the far field, and the voltage across its load is measured for various transmitted power levels.

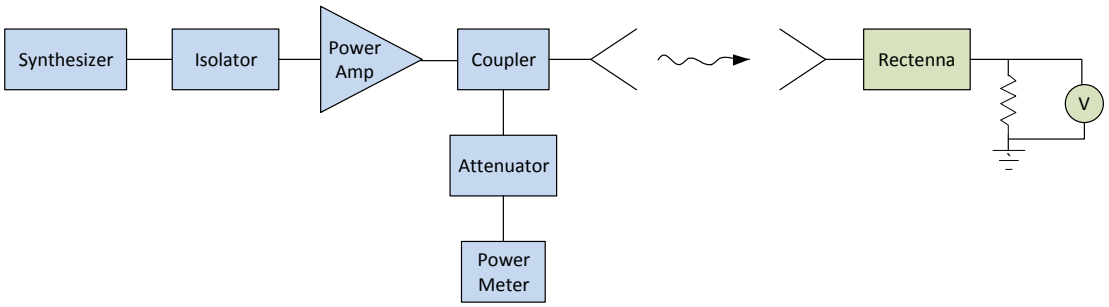

Figure 8.7. Equipment setup for efficiency measurement.

The measured voltage for various loads and power levels can be seen in Fig. 8.8. Higher load values result in higher output voltages. The measured voltage is converted to an efficiency by (8.3), and the results can be seen in Fig. 8.9. A peak efficiency of 73% was measured with a 100 ohm load and occurred at roughly 100 mW received power which is the maximum power rating of the diode. Loads of 80, 90, 110, and 120 ohms were also measured and produced nearly identical results to the 100 ohm load. Other loads ranging from 50 to 500 ohms were measured and showed a predictable decrease in performance the farther the values deviated from 100 ohms. The efficiency of some of the other loads can be seen in the figure.

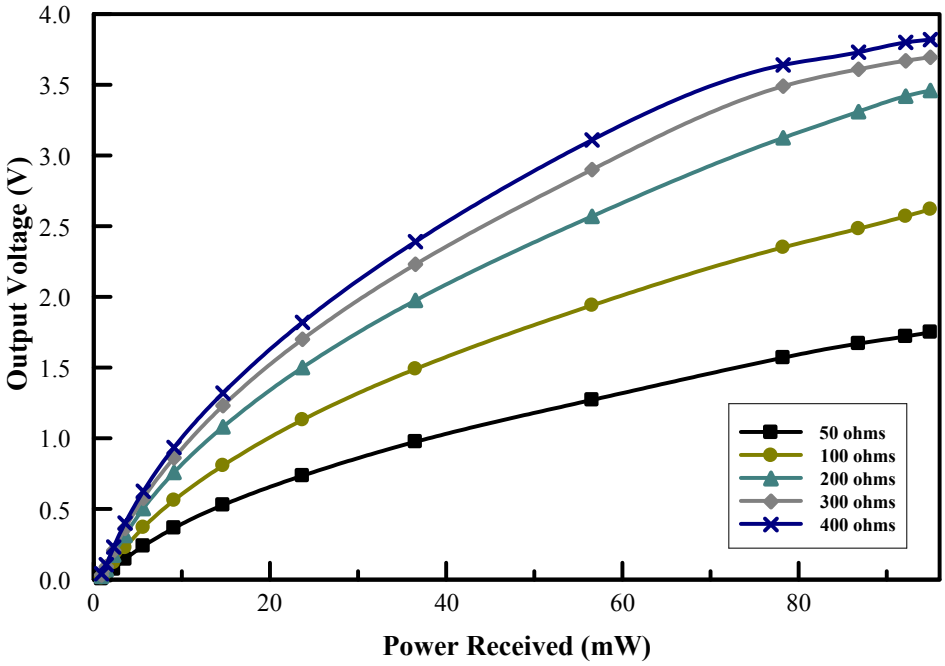

Figure 8.8. Measured rectenna output voltage.

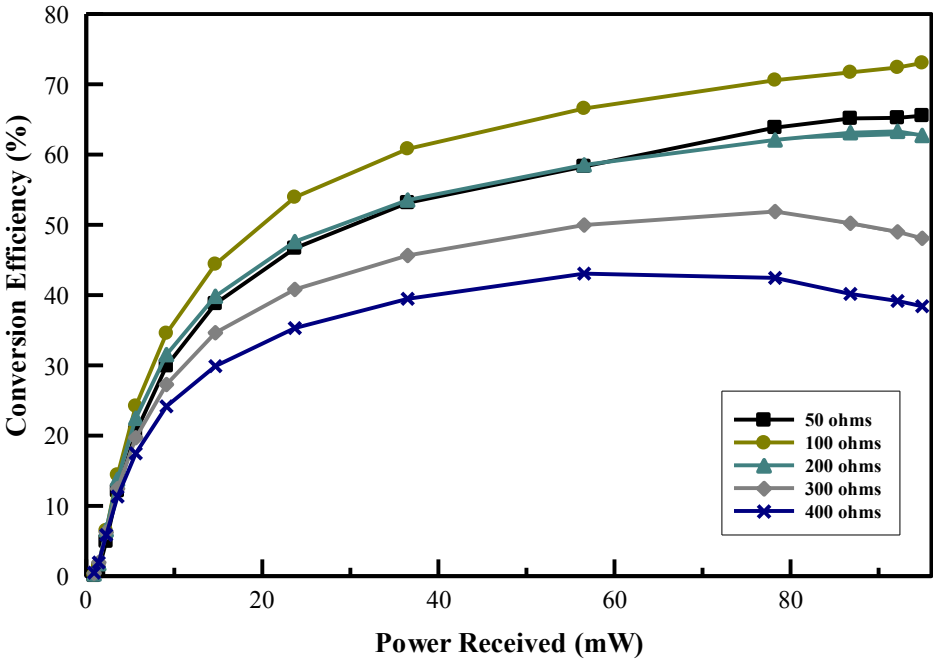

Figure 8.9. Measured RF-to-DC conversion efficiency.

C. Comparison to Model

The rectenna model described in the previous section can be utilized to model this rectenna design, and the simulated results can be compared to the measured results. IE3D [12] can be used to generate S-parameters of the antenna and filter section of the rectenna. These S-parameters can then be used in Agilent ADS [83] along with the diode model, a capacitor, and a resistor to simulate the entire rectenna design. A harmonic balance simulation can then be run with various values for input power and load resistance to verify against the measured results.

The Agilent ADS schematic can be seen in Fig. 8.10. A variable power source and DC-blocking capacitor are used to represent the source of power to the rectenna. Then S-parameters of the filter section (generated from IE3D) are used to represent the rectenna's transmission line up to the quarter-wavelength transformer. The quarter-wavelength transformer and the 120 Ω line (up to the diode) are represented by transmission line components in ADS. The diode is represented by a model component described in the previous section. This is followed by a capacitor with transmission lines on either side and finally a variable resistor. The power source and load can be varied to give output voltages for various power levels and loads.

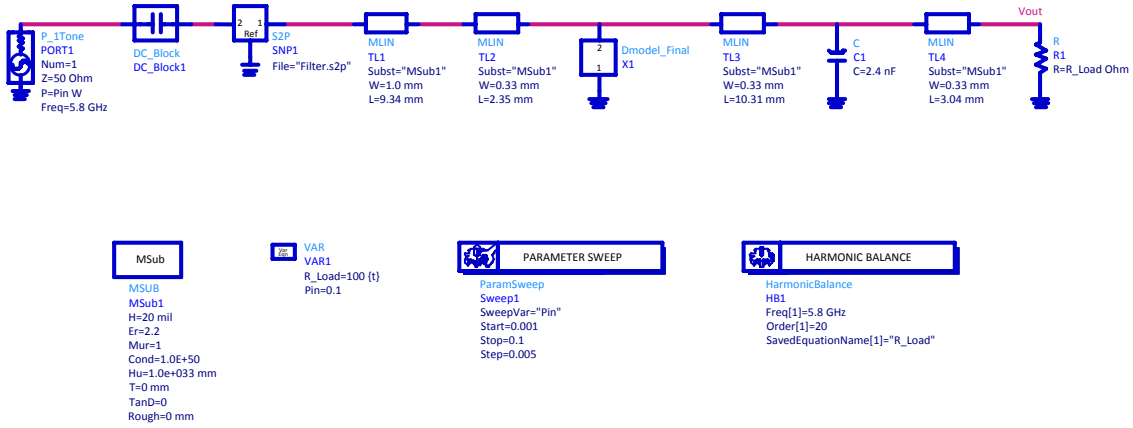

Figure 8.10. Schematic of rectenna simulation in Agilent ADS.

A comparison of measured and simulated output voltages can be seen in Fig. 8.11. The simulated results show a very good match to the measured results. A comparison of measured and simulated efficiency can be seen in Fig. 8.12. Since the output voltage is squared to calculate the efficiency, any error in voltage is magnified in efficiency error. This results in an increased difference between measured and simulated results for efficiency, but the results are still good, and more importantly both the measured and simulated results show an optimum load value of 100 ohms.

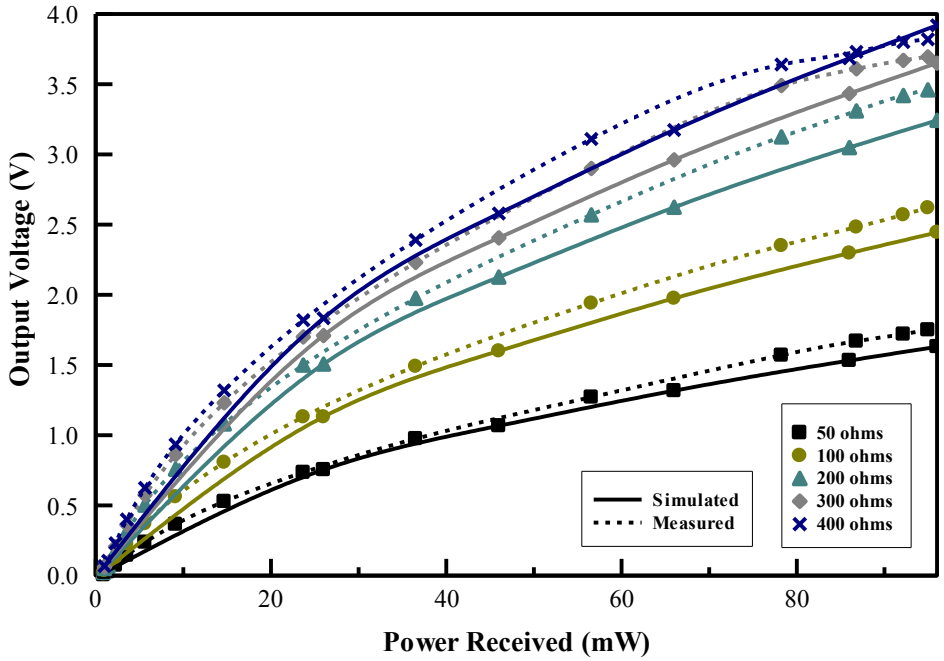

Figure 8.11. Comparison of measured and simulated rectenna output voltage.

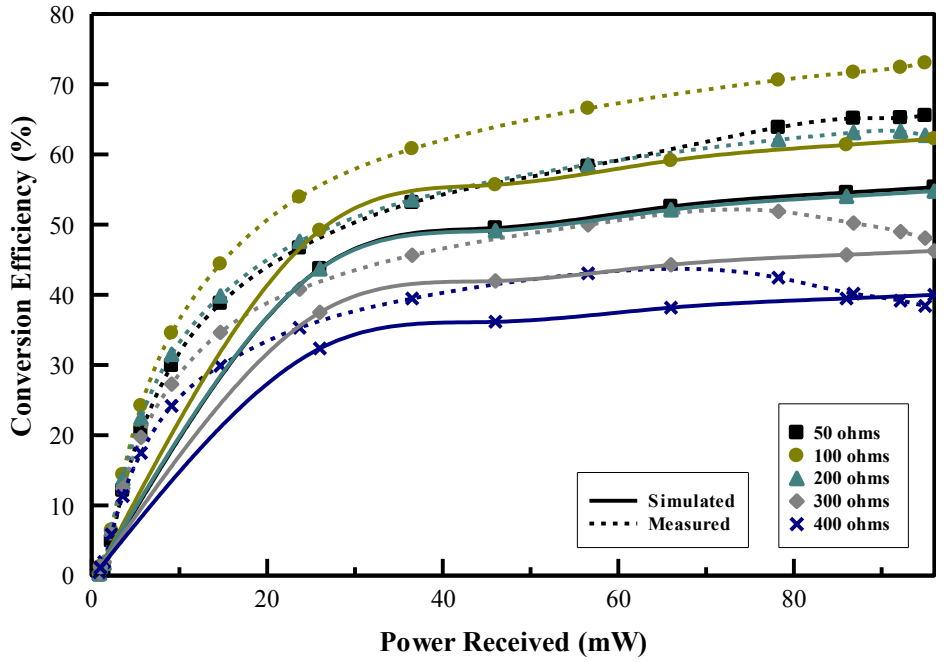

Figure 8.12. Comparison of measured and simulated RF-to-DC conversion efficiency.

D. Conclusion

A 5.8 GHz rectenna was successfully developed with an antenna gain of 9.3 dBi, a second harmonic suppression of 4.93 dB from split ring resonators (SRRs), and a conversion efficiency of 73%. Aperture-coupling was employed to isolate the rectifying operation from the receiving operation. The design was also used to further verify the diode model created for the rectenna in the previous section. The measurements showed a good match to the simulated model.

9. CONCLUSION

A broadband, dual-polarized antenna was designed, fabricated, and measured. The design was tuned using electromagnetic simulation software, but a shift in measured bandwidth necessitated a redesign to account for this unavoidable shift. Feed 1 was measured to have a 42% VSWR bandwidth with f_0=10.0 GHz, and feed 2 was measured to have a 38% VSWR bandwidth with f_0=10.1 GHz. Gain was measured to be 5 – 8 dBi, and the half-power beamwidth was measured to be 50 - 90°. The gain measurements showed a cross-polarization isolation of greater than 20 dB, and the S-parameter isolation between the feeds was measured to be greater than 17 dB. With the exception of the frequency shift, the measured results matched well to the simulation.

This antenna was then used in a broadband, dual-polarized phased array application. A 4x1 antenna array was created from the previously designed single-element which served to increase the gain and allow the antenna pattern to be steered. To feed the antenna array with a uniform amplitude distribution, a 1-to-4 power divider was created, and digital phase-shifters were used to control each element's phase, thereby steering the pattern. A LabVIEW program was created with a simple interface in order to facilitate control of the phase-shifters. After calibrating the phased array at 10 GHz, the array pattern was measured over the target bandwidth for various scan angles. The array performed well over a 3 GHz bandwidth and produced a maximum scan angle of 45°.

Adding more elements to the phased array would greatly improve its performance. The beamwidth could be narrowed and the maximum scan angle increased. Additionally, including controllable amplifiers for each element would permit the use of non-uniform amplitude distributions which could narrow the beamwidth and/or decrease sidelobes. Controllable amplifiers could also increase the calibration accuracy by removing the effect of variable line attenuation on each element. Lastly, using phase-shifters with a more consistent phase shift and insertion loss would also increase the array performance.

Rectennas are a key component of wireless power transmission systems, and the ability to simulate rectenna designs can expedite and improve their development. A diode model which is based on an equivalent circuit was created to serve as an integral part of a complete rectenna model. The model component values were determined from a series of S-parameter measurements (at various bias levels) using a method which systematically isolates the model's voltage-dependent components from its voltage-independent components. The model was implemented in Agilent ADS using symbolically defined devices for both the voltage-dependent current source and the voltage-dependent capacitor, and the model's simulated S-parameters matched well to the measured S-parameters over all bias levels.

An aperture-coupled, high-gain patch rectenna was then designed, fabricated, and measured. This rectenna design was modeled using the previously described method which allowed for a verification of the model's accuracy. The model simulation showed

a good match to the measured results, and both gave the same optimum load value. This demonstrated the model's usefulness for rectenna simulation and design.

REFERENCES

[1] R. Waterhouse, *Microstrip Patch Antennas: A Designer's Guide*. Boston: Kluwer, 2003.

[2] R. Garg, P. Bhartia, I. Bahl, and A. Ittipibbon, *Microstrip Antenna Design Handbook*. Boston: Artech House, 2001.

[3] K. Chang, *RF and Microwave Wireless Systems*. New York: Wiley, 2000.

[4] C. A. Balanis, *Antenna Theory: Analysis and Design*, 2nd ed. New York: Wiley, 1997.

[5] R. C. Johnson, *Antenna Engineering Handbook*, 3rd ed. New York: McGraw-Hill, 1993.

[6] E. Nishiyama, M. Aikawa, and S. Egashira, "Three-element stacked microstrip antenna with wide-band and high-gain performances," in *IEEE Antennas Propagat. Society Int. Symp.*, vol. 2, pp. 900-903, 2003.

[7] V. Rathi, G. Kumar, and K. P. Ray, "Improved coupling for aperture coupled microstrip antennas," *IEEE Trans. Antennas Propagat.*, vol. 44, no. 8, pp. 1196-1198, Aug. 1996.

[8] D. M. Pozar, "Microstrip antennas," *Proc. IEEE*, vol. 80, no. 1, pp. 79-91, 1992.

[9] S. D. Targonski, R. B. Waterhouse, and D. M. Pozar, "Design of wide-band aperture-stacked patch microstrip antennas," *IEEE Trans. Antennas Propagat.*, vol. 46, no. 9, pp. 1245-1251, Sept. 1998.

[10] D. G. Kim, "Design of stripline-fed dual-polarization aperture-coupled stacked microstrip patch phased array antenna for wideband application," M.S. thesis, Dept. Elect. Comput. Eng., Texas A&M Univ., College Station, TX, 2010.

[11] D. M. Pozar, *Microwave Engineering*, 2nd ed. New York: Wiley, 1998.

[12] IE3D Version 14.61. Computer Software. Zealand Software Inc., Freemont, CA, 2009.

[13] HFSS: 3D Full-wave Electromagnetic Field Simulation. Version 12.0.0. Computer Software. Ansoft LLC., Pittsburgh, PA, 2009.

[14] D. Kim, C. You, and W. Hwang, "Effect of adhesive bonds on electrical performance in multi-layer composite antenna," *Composite Structures*, vol. 90, no. 4, pp. 413-417, Oct. 2009.

[15] P. Coquet, R. Sauleau, K. Shinohara, H. Lhermite, and T. Matsui, "Multi-layer microstrip antennas on quartz substrates: technological considerations and performances at 60 GHz," *Microw. Optical Technol. Lett.*, vol. 40, no. 1, pp. 41-47, Jan. 2004.

[16] S. Drabowitch, A. Papierkik, H. D. Griffiths, J. Encinas, and B. L. Smith, *Modern Antennas*, 2nd ed. Dordrecht, The Netherlands: Springer, 2005.

[17] N. Fourikis, *Advanced Array Systems, Applications and RF Technologies*. San Diego: Academic Press, 2000.

[18] D. G. Fang, *Antenna Theory and Microstrip Antennas*. Boca Raton: CRC Press, 2010.

[19] R. J. Mailloux, *Phased Array Antenna Handbook*, 2nd ed. Boston: Artech House, 2005.

[20] C. J. Miller, "Minimizing the effects of phase quantization errors in an electronically scanned array," in *Proc. Symp. Electronically Scanned Array Techniques and Applications*, RADC-TDR-64-225, vol. 1, pp. 17-38, 1964.

[21] T. C. Cheston and J. Frank, "Array Antennas," in *Radar Handbook*, M. E. Skolnik, Ed. New York: McGraw-Hill, 1990.

[22] R. C. Hansen, "Linear Arrays," in *The Handbook of Antenna Design*, vol. 2. London, England: Peter Peregrinus, 1986.

[23] R. J. Mailloux, "Array grating lobes due to periodic phase, amplitude, and time delay quantization," *IEEE Trans. Antenn. Propag.*, vol. 32, no. 12, pp. 1364-1368, Dec. 1984.

[24] J. R. James and P. S. Hall, *Handbook of Microstrip Antennas*, Vol. 1. London: Peter Peregrinus, 1989.

[25] J. R. James and P. S. Hall, *Handbook of Microstrip Antennas*, Vol. 2. London: Peter Peregrinus, 1989.

[26] R. Rhea, "The Yin-Yang of Matching: Part 2 – Practical Matching Techniques," *High Frequency Electron.*, pp. 28-40, Apr. 2006.

[27] LabVIEW 2010 Service Pack 1. Version 10.0.1. Computer Software. National Instruments, Austin, TX, 2010.

[28] *Hittite Microwave Corporation: HMC543 Data Sheet* v02.0209, Hittite, Chelmsford, MA.

[29] Altium DXP 2004. Build 8.1.4.1717. Computer Software. Altium Limited, Sydney, NSW, Australia, 2004.

[30] D. M. Pozar, "The active element pattern," *IEEE Trans. Antennas Propagat.*, vol. 42, no. 8, pp. 1176-1178, Aug. 1994.

[31] Matlab: The Language of Technical Computing. Version 7.1.0.246 (R14) Service Pack 3. Computer Software. MathWorks, Inc., Natick, MA, 2005.

[32] K. Itoh, Y. Akiba, T. Ohgane, and Y. Ogawa, "Fundamental study on SPS rectenna printed on a sheet of copper clad laminate," *Space Solar Power Review*, vol. 5, pp. 149-162, 1985.

[33] M. Ali, G. Yang, and R. Dougal, "A new circularly polarized rectenna for wireless power transmission and data communication," *IEEE Antennas Wireless Propag. Lett.*, vol. 4, pp. 205-208, 2005.

[34] B. Strassner and K. Chang, "Passive 5.8-GHz radio-frequency identification tag for monitoring oil drill pipe," *IEEE Trans. Microw. Theory Tech.*, vol. 51, no. 2, pp. 356-363, Feb. 2003.

[35] J. A. Hagerty, F. B. Helmbrecht, W. H. McCalpin, R. Zane, and Z. B. Popovic, "Recycling ambient microwave energy with broad-band rectenna arrays," *IEEE Trans. Microw. Theory Tech.*, vol. 52, no. 3, pp. 1014-1024, Mar. 2004.

[36] S. Lim, K. M. K. H. Leong, and T. Itoh, "Adaptive power controllable retrodirective array system for wireless sensor server applications," *IEEE Trans. Microw. Theory Tech.*, vol. 53, no. 12, pp. 3735-3743, Dec. 2005.

[37] B. H. Strassner and K. Chang, "Rectifying antennas (rectennas)," in *Encyclopedia of RF and Microwave Engineering*. Hoboken, NJ: Wiley, 2005, vol. 5, pp. 4418-4428.

[38] W. C. Brown, "The history of power transmission by radio waves," *IEEE Trans. Microw. Theory Tech.*, vol. MTT-32, no. 9, pp. 1230-1242, Sept. 1984.

[39] M. Cheney, *Tesla: Man Out of Time.* Englewood Cliffs, NJ: Prentice-Hall, 1981.

[40] W. C. Brown, "The history of wireless power transmission," *Solar Energy*, vol. 56, no. 1, pp. 3-21, 1996.

[41] "Electric light without current," *Literary Dig.*, vol. 112, no. 3, p. 30, Jan. 1932.

[42] H. Yagi and S. Uda, "On the feasibility of power transmission by electric waves," in *Proc. 3rd Pan-Pacific Sci. Congr.*, vol. 2, pp. 1305-1313, Tokyo, Japan, 1926.

[43] H. Boot and J. Randall, "Historical notes on the cavity magnetron," *IEEE Trans. Electron Devices*, vol. ED-23, no. 7, July 1976.

[44] J. F. Showron, G. H. MacMaster, and W. C. Brown, "The super power CW amplitron," *Microw. J.*, Oct. 1964.

[45] E. C. Okress, *Microwave Power Engineering*, vols. I, II. New York: Academic, 1968.

[46] R. H. George and E. M. Sabbagh, "An efficient means of converting microwave energy to dc using semiconductor diodes," in *IEEE Intern. Conv. Rec., Electron Devices, Microwave Theory Tech.*, vol. 11, pt. 3, Mar. 1963, pp. 132-141.

[47] W. C. Brown, "Thermionic diode rectifier," in *Microwave Power Engineering*, vol. I, E. C. Okress, Ed. New York: Academic, 1968, pp. 295-298.

[48] W. C. Brown, J. R. Mims, and M. I. Heenan, "An experimental microwave-powered helicopter," *IEEE Int. Convention Record*, vol. 13, no. 5, pp. 225-235, Mar. 1965.

[49] P. Glaser, "Power from the sun: Its future," *Sci. Mag.*, vol. 162, no. 3856, pp. 857-861, Nov. 1968.

[50] "Satellite solar power station and microwave transmission to earth," *J. Microw. Power*, vol. 5, no. 4, Dec. 1970.

[51] P. E. Glaser, O. E. Maynard, J. Mackovciak, Jr., and E. L. Ralph, "Feasibility study of a satellite solar power station," NASA Contractor Rep. CR 2357, MTIS N74-17784, 1974.

[52] R. M. Dickinson and W. C. Brown, "Radiated microwave power transmission system efficiency measurements," Tech. Memo 33-727, Jet Propulsion Lab., Cal. Inst. Technol., Mar. 15, 1975.

[53] R. M. Dickinson, "Evaluation of a microwave high-power reception-conversion array for wireless power transmission," Tech. Memo 33-741, Jet Propulsion Lab., Cal. Inst. Technol., Sept. 1, 1975.

[54] W. C. Brown, "Electronic and mechanical improvement of the receiving terminal of a free-space microwave power transmission system," Tech. Rep. PT-4964, Raytheon Company, NASA Rep. CR-135194, Aug. 1977.

[55] J. Schlesak, A. Alden, and T. Ohno, "SHARP rectenna and low altitude flight trials," in *IEEE Global Telecommunications Conf.*, New Orleans, LA, Dec. 2-5, 1985.

[56] H. Matsumoto, H. Hirata, Y. Hashino, and N. Shinohara, "Theoretical analysis of nonlinear interaction of intense electromagnetic wave and plasma waves in the ionosphere," *Electron. Commun. Jpn. Pt. 3,* vol. 78, no. 11, pp. 104-114, Nov. 1995.

[57] P. Koert, J. Cha, and M. Macina, "35 and 94 GHz rectifying antenna systems," in *Proc. 2nd Intern. Symp. SPS 91 – Power from Space*, pp. 541-547, Paris, France, Aug. 27-30, 1991.

[58] J. O. McSpadden, L. Fan, and K. Chang, "Design and experiments of a high-conversion-efficiency 5.8-GHz rectenna," *IEEE Trans. Microw. Theory Tech.*, vol. 46, no. 12, pp. 2053-2060, Dec. 1998.

[59] Y. Fujino, T. Ito, N. Kaya, H. Matsumoto, K. Kawabata, H. Sawada, and T. Onodera, "A rectenna for MILAX," in *Proc. 1st Wireless Power Transmission Conf.*, pp. 273-277, Texas, Feb. 1993.

[60] N. Kaya, H. Matsumoto, and R. Akiba, "Rocket experiment METS: Microwave energy transmission in space," *Space Power*, vol. 11, no. 3-4, pp. 267-274, 1992.

[61] J. McSpadden, A. M. Brown, K. Chang, and N. Kaya, "Receiving rectifying antenna for the international space year – Microwave energy transmission in space (ISY-METS) rocket experiment," *IEEE Aerosp. Electron. Syst. Mag.*, vol. 9, no. 11, pp. 36-41, Nov. 1994.

[62] H. Feingold *et al.*, "Space solar power – A fresh look at the feasibility of generating solar power in space for use on earth," Space Applications Int. Corp. (SAIC), Schaumburg, IL, Rep. SAIC-97/1005, NASA Contract NAS3-26565, Apr. 4, 1997.

[63] B. Strassner and K. Chang, "Highly efficient C-band circularly polarized rectifying antenna array for wireless microwave power transmission," *IEEE Trans. Antenn. Propag.*, vol. 51, no. 6, pp. 1347-1356, 2003.

[64] J. McSpadden and J. Mankins, "Space solar power programs and microwave wireless power transmission technology," *IEEE Microwave Magazine*, vol. 3, no. 4, pp. 46-57, 2002.

[65] L. –H. Hsieh, B. H. Strassner, S. J. Kokel, C. T. Rodenbeck, M. Y. Li, K. Chang, F. E. Little, G. D. Arndt, and P. H. Ngo, "Development of a retrodirective wireless microwave power transmission system," in *IEEE AP-S Antenn. Propag. Int. Symp. Dig.*, vol. 2, pp. 393-396, Jun. 2003.

[66] C. Rodenbeck, M. Li, and K. Chang, "A phased-array architecture for retrodirective microwave power transmission from the space solar power satellite," in *IEEE MTT-S Int. Microw. Symp. Dig.*, vol. 3, pp. 1679-1682, Jun. 2004.

[67] K. Hashimoto and H. Matsumoto, "Microwave beam control system for solar power satellite," *IEEE Proc., Asia-Pacific Radio Sci. Conf.*, pp. 616-617, Aug. 2004.

[68] Y. –J., Ren and K. Chang, "New 5.8-GHz circularly polarized retrodirective rectenna arrays for wireless power transmission," *IEEE Trans. Microw. Theory Tech.*, vol. 54, no. 7, pp. 2970-2976, 2006.

[69] J. Osepchuk, "How safe are microwaves and solar power from space?," *IEEE Microwave Magazine*, vol. 3, no. 4, pp. 58-64, Dec. 2002.

[70] P. Glaser, "Environmental implications of the solar power satellite concept," *Space Power*, vol. 6, no. 4, pp. 279-285, 1985.

[71] M. Lee and S. Kuo, "Earth's magnetic field perturbations as the possible environmental impact of the conceptualized solar power satellite," *J. Geophysical Research*, vol. 89, no. A12, pp. 11043-11047, Dec. 1984.

[72] S. Sasaki, "SSPS development road map," in *60th Int. Astronautical Congr. 2009*, vol. 7, pp. 5976-5981, Oct. 2009.

[73] W. C. Brown, "The technology and application of free-space power transmission by microwave beam," *Proceedings of the IEEE*, vol. 62, no. 1, pp. 11-25, Jan. 1974.

[74] G. Goubau and F. Schwering, "On the guided propagation of electromagnetic wave beams," *IRE Trans. Antennas Propagat.*, vol. 9, no. 3, pp. 248-263, May 1961.

[75] G. Goubau, "Microwave power transmission from an orbiting solar power station," *J. Microwave Power*, vol. 5, Dec. 1970.

[76] J. McSpadden, T. Yoo, and K. Chang, "Theoretical and experimental investigation of a rectenna element for microwave power transmission," *IEEE Trans. Microw. Theory Tech.*, vol. 40, pp. 2359-2366, Dec. 1992.

[77] Z. Wang, K. Hashimoto, N. Shinohara, and H. Matsumoto, "Frequency-selective-surface for microwave power transmission," *IEEE Trans. Microw. Theory Tech.*, vol. 47, pp. 2039-2042, Oct. 1999.

[78] A. Sedra and K. Smith, *Microelectronic Circuits*, 4th ed. New York: Oxford, 1998.

[79] T. –W. Yoo and K. Chang, "Theoretical and experimental development of 10 and 35 GHz rectennas," *IEEE Trans. Microw. Theory Tech.*, vol. 40, no. 6, pp. 1259-1266, Jun. 1992.

[80] T. –W. Yoo, "Experimental and theoretical study on 35 GHz RF-to-DC power conversion receiver for millimeter-wave beamed power transmission," Ph.D. dissertation, Dept. Elect. Eng., Texas A&M Univ., College Station, TX, 1993.

[81] B. H. Strassner II, "Microwave rectifying circuits and antennas for radio frequency identification and wireless power transmission applications," Ph.D. dissertation, Dept. Elect. Eng., Texas A&M Univ., College Station, TX, 2002.

[82] D. Swillinger, *CRC Standard Mathematical Tables and Formulae*, 30th ed. Boston: CRC Press, 1996.

[83] Advanced Design System 2008 Update 2. Computer Software. Agilent Technologies, Santa Clara, CA, 2008.

[84] S. A. Maas, *Nonlinear Microwave Circuits*. Norwood: Artech House, 1988.

[85] R. Gilmore and L. Besser, *Practical RF Circuit Design for Modern Wireless Systems*, Vol. 2, *Active Circuits and Systems*. Norwood: Artech House, 2003.

[86] F. Giannini and G. Leuzzi, *Nonlinear Microwave Circuit Design*. Chichester, England: Wiley, 2004.

[87] C. M. Snowden, *Introduction to Semiconductor Device Modelling*. Singapore: World Scientific, 1986.

[88] S. A. Maas, *Nonlinear Microwave and RF Circuits*, 2nd ed. Boston: Artech House, 2003.

[89] U. L. Rohde and D. P. Newkirk, *RF/Microwave Circuit Design for Wireless Applications*. New York: Wiley, 2000.

[90] C. M. Snowden, *Semiconductor Device Modelling*. London: Short Run, 1988.

[91] K. K. Tantwai, "Microwave-frequency non-linear universal model for PIN diode," in *Int. Workshop Physics Semiconductor Devices*, pp. 119-122, 2007.

[92] C. M. Snowden, *Semiconductor Device Modelling*. London: Springer-Verlag, 1989.

[93] IC-CAP: Device Modeling Software. Computer Software. Agilent Technologies, Santa Clara, CA.

[94] D. B. Estreich, "A simulation model for Schottky diodes in GaAs integrated circuits," *IEEE Trans. Comput.-Aided Des. Integr. Circuits Syst.*, vol. 2, no. 2, pp. 106-111, April 1983.

[95] G. F. Engen and C. A. Hoer, "Thru-reflect-line: An improved technique for calibrating the dual six-port automatic network analyzer," *IEEE Trans. Microw. Theory Tech.*, vol. MTT-27, no. 12, pp. 987-993, Dec. 1979.

[96] *Network Analysis: Applying the 8510 TRL calibration for non-coaxial measurements*, (Product Note 8510-8A), Agilent, Santa Clara, CA, 2000.

[97] S. A. Maas, *Microwave Mixers*, 2nd ed. Boston: Artech House, 1993.

[98] J. L. Devore, *Probability and Statistics for Engineering and the Sciences*, 5th ed. Pacific Grove: Duxbury, 2000.

[99] Y. H. Liew and J. Joe, "Large-signal diode modeling – an alternative parameter-extraction technique," *IEEE Trans. Microw. Theory Tech.*, vol. 53, no. 8, pp. 2633-2638, Aug. 2005.

[100] M. R. Deshpande *et al.*, "Tunnel diode non-linear model for microwave circuits and active antennas," in *IEEE MTT-S Int. Microw. Symp. Dig.*, pp. 403-406, 2001.

[101] D. E. Root and B. Hughes, "Principles of nonlinear active device modeling for circuit simulation," in *32nd ARFTG Conf. Dig.*, vol. 14, pp. 1-24, Dec. 1988.

[102] M. V. Calvo and A. D. Snider, "Resolution of linear/nonlinear inconsistencies in charge-conservative FET models," in *Southeastcon '96., Proc. IEEE*, pp. 428-431, 1996.

[103] *Custom Modeling with Symbolically-Defined Devices* [Online]. Available: http://www.agilent.com

[104] C. A. Balanis, *Modern Antenna Handbook*. Hoboken, NJ: Wiley, 2008.

[105] D. M. Pozar, "Microstrip antenna aperture-coupled to a microstripline," *Electron. Lett.*, vol. 21, no. 2, pp. 49-50, 1985.

[106] B. We, B. Li, T. Su, and C. H. Liang, "Equivalent-circuit analysis and lowpass filter design of split-ring resonator DGS," *J. Electromagn. Waves Appl.*, vol. 20, no. 14, pp. 1943-1953, 2006.

[107] B. Wu, B. Li, and C. Liang, "Design of lowpass filter using a novel split-ring resonator defected ground structure," *Microw. Optical Technol. Lett.*, vol. 49, no. 2, pp. 288-291, Feb. 2007.

APPENDIX A

MATLAB ARRAY PATTERN VISUALIZATION GUI

This appendix presents a Matlab GUI program which can be used to visualize the effect of different parameters on an array pattern. The phase shift between elements can be varied with a slider to see the effect in real time. Amplitude distribution can be chosen from: Uniform, Binomial, and Dolph-Tschebyscheff; for the Dolph-Tschebyscheff, the sidelobe levels (in dB) can be chosen. The distance between elements and the number of elements can be adjusted. Also, the pattern can be digitized, and the number of bits can be selected.

The plot can be visualized in rectangular or polar coordinates, it can be normalized, and it can be displayed in dB. Also, the array factor, the element pattern, or a combination of the two (real array pattern) can be displayed. The element pattern is input in the Matlab code.

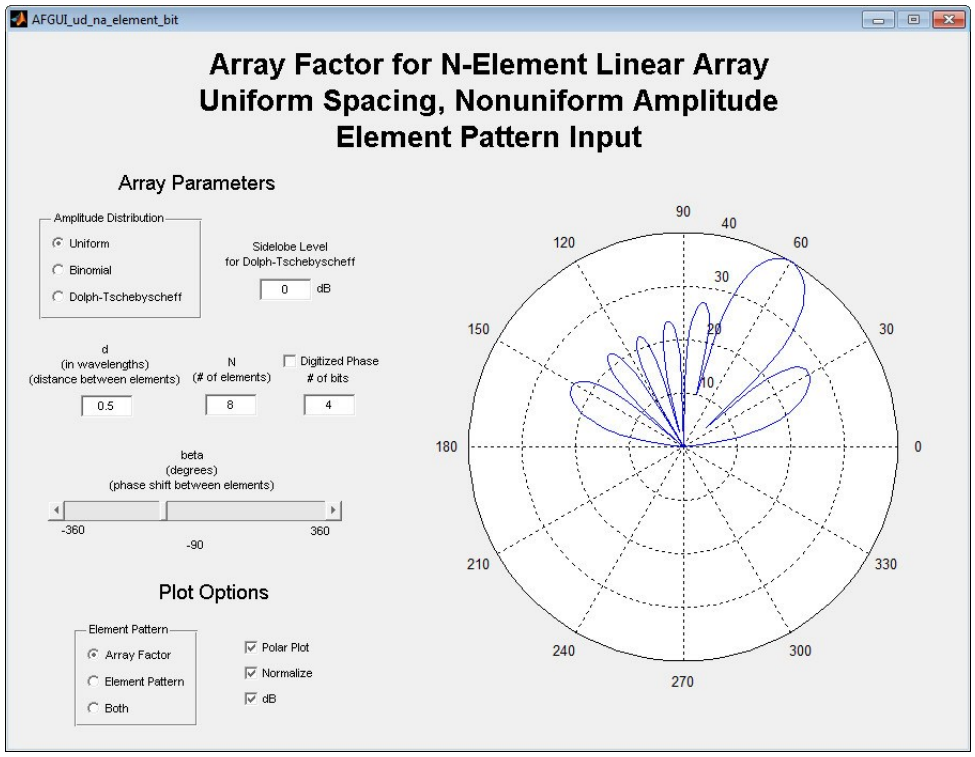

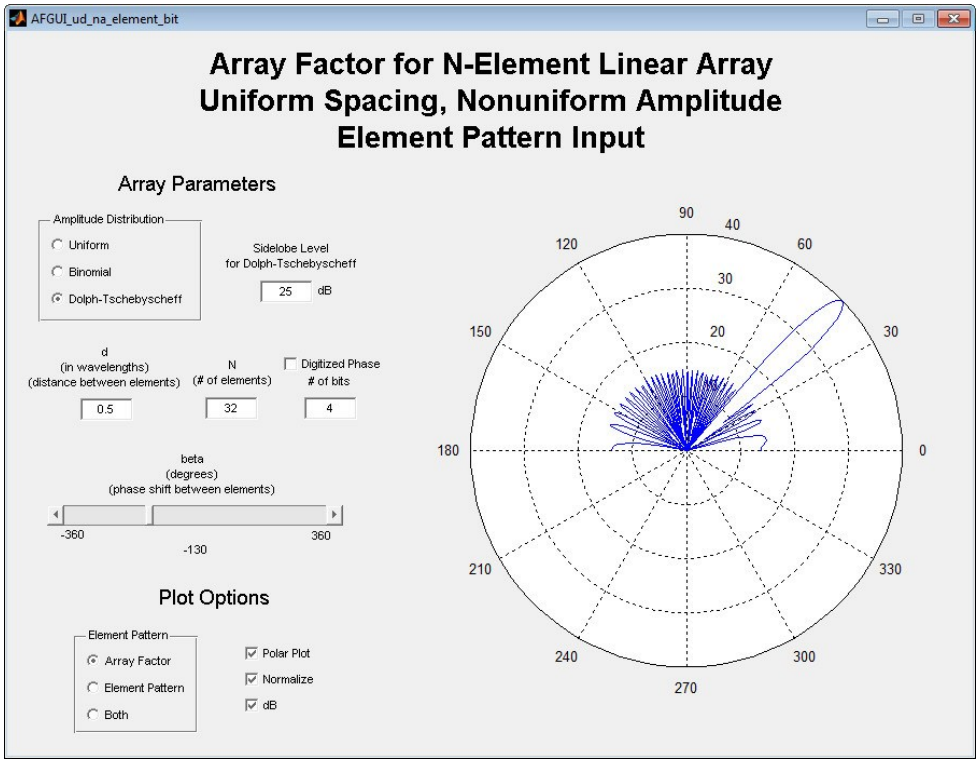

Figure A.1. User interface shown with different settings.

```
function varargout = AFGUI_ud_na_element_bit(varargin)
% AFGUI_UD_NA_ELEMENT_BIT M-file for AFGUI_ud_na_element_bit.fig
%      Jonathan Hansen
%      Array Factor for N-Element Linear Array
%      with Uniform Spacing and Non-uniform Amplitude
%      Allows an Element Pattern to be used and combined with the AF
%
%      Array Factor is calculated with broadside at 90 degrees.
%      IE3D defines a broadside of 0 degrees so this must be shifted.
%
%      Plots the array factor for given parameters.
%         Array Parameters
%           Amplitude Distribution
%              Uniform
%              Binomial
%              Dolph-Tschebyscheff
%         Sidelobe Level for Dolph-Tschebyscheff (in dB)
%         Distance between elements (d) in wavelengths
%         Number of Elements (N)
%         Digitize the phase shift or allow continuous number of bits for digitized
%         Phase shift between elements (beta) (in degrees)
%      Plot Options
%         Element Pattern Options
%            only plot the Array Factor
%            only plot the Element Pattern
%            plot the product of the Array Factor & Element Pattern
%         Polar or Cartesian coordinates
%         Normalize or Non-normalized data
%         dB or Ratio
%
%      AFGUI_UD_NA_ELEMENT_BIT, by itself, creates a new AFGUI_UD_NA_ELEMENT_BIT or raises the existing
%      singleton*.
%
%      H = AFGUI_UD_NA_ELEMENT_BIT returns the handle to a new AFGUI_UD_NA_ELEMENT_BIT or the handle to
%      the existing singleton*.
%
%      AFGUI_UD_NA_ELEMENT_BIT('CALLBACK',hObject,eventData,handles,...) calls the local
%      function named CALLBACK in AFGUI_UD_NA_ELEMENT_BIT.M with the given input arguments.
%
%      AFGUI_UD_NA_ELEMENT_BIT('Property','Value',...) creates a new AFGUI_UD_NA_ELEMENT_BIT or raises the
%      existing singleton*.  Starting from the left, property value pairs are
%      applied to the GUI before AFGUI_ud_na_element_bit_OpeningFunction gets called.  An
%      unrecognized property name or invalid value makes property application
%      stop.  All inputs are passed to AFGUI_ud_na_element_bit_OpeningFcn via varargin.
%
%      *See GUI Options on GUIDE's Tools menu.  Choose "GUI allows only one
%      instance to run (singleton)".
%
% See also: GUIDE, GUIDATA, GUIHANDLES

% Begin initialization code - DO NOT EDIT
gui_Singleton = 1;
gui_State = struct('gui_Name',       mfilename, ...
                   'gui_Singleton',  gui_Singleton, ...
                   'gui_OpeningFcn', @AFGUI_ud_na_element_bit_OpeningFcn, ...
                   'gui_OutputFcn',  @AFGUI_ud_na_element_bit_OutputFcn, ...
                   'gui_LayoutFcn',  [] , ...
                   'gui_Callback',   []);
if nargin && ischar(varargin{1})
    gui_State.gui_Callback = str2func(varargin{1});
end
```

```
if nargout
   [varargout{1:nargout}] = gui_mainfcn(gui_State, varargin{:});
else
   gui_mainfcn(gui_State, varargin{:});
end
% End initialization code - DO NOT EDIT


% --- Executes just before AFGUI_ud_na_element_bit is made visible.
function AFGUI_ud_na_element_bit_OpeningFcn(hObject, eventdata, handles, varargin)
% This function has no output args, see OutputFcn.
% hObject    handle to figure
% eventdata  reserved - to be defined in a future version of MATLAB
% handles    structure with handles and user data (see GUIDATA)
% varargin   command line arguments to AFGUI_ud_na_element_bit (see VARARGIN)

% Choose default command line output for AFGUI_ud_na_element_bit
handles.output = hObject;

set(handles.AmpSelect_buttongroup,'SelectionChangeFcn',@AmpSelect_buttongroup_SelectionChangeFcn);
set(handles.AFSelect_buttongroup,'SelectionChangeFcn',@AFSelect_buttongroup_SelectionChangeFcn);

% UIWAIT makes AFGUI_ud_na_element_bit wait for user response (see UIRESUME)
% uiwait(handles.figure1);

% Initialize Global Variables
global beta beta_deg N phase_step d DigitizedPhase PolarPlot dBPlot NormalizePlot theta theta_deg cos_theta Element small_num
       amp AmpSelect AFSelect SidelobeLeveldB NormalizeF

ElementPatterndB = [-1992.211761 -1992.211761 -1992.211761 -1992.211761 -1992.211761 -1992.211761 -1992.211761
-1992.211761 -1992.211761 -1992.211761 -1992.211761 -1992.211761 -1992.211761 -1992.211761 -1992.211761 -1992.211761
-1992.211761 -1992.211761 -64.79668478 -9.892406686 -7.550849379 -5.933740436 -4.323770356 -2.719428108 -1.173279813
0.275782952 1.60549158 2.805027952 3.870468998 4.801781819 5.600990775 6.27107541 6.81529526 7.236761195 7.538153908
7.721537197 7.788239005 7.738786378 7.572887395 7.289457145 6.886687733 6.362165265 5.713041126 4.936273125
4.028968638 2.988893838 1.815271463 0.510088106 -0.919724216 -2.45876601 -4.078482087 -5.737493634 -7.438667667
-9.871805941 -64.81794103 -1992.211761 -1992.211761 -1992.211761 -1992.211761 -1992.211761 -1992.211761 -1992.211761
-1992.211761 -1992.211761 -1992.211761 -1992.211761 -1992.211761 -1992.211761 -1992.211761 -1992.211761 -1992.211761
-1992.211761 -1992.211761];
ElementPatterndB = circshift(ElementPatterndB,[0,90]);          % shift by 90 deg to have broadside at 90 deg instead of 0 deg
ElementPattern = 10 .^ (ElementPatterndB ./ 20);                % convert dB to ratio
ElementPattern = ElementPattern ./ max(ElementPattern);         % normalize the Element Pattern

Element_theta = [-3.14159265 -3.05432619 -2.96705973 -2.87979327 -2.7925268 -2.70526034 -2.61799388 -2.53072742
-2.44346095 -2.35619449 -2.26892803 -2.18166156 -2.0943951 -2.00712864 -1.91986218 -1.83259571 -1.74532925 -1.65806279
-1.57079633 -1.48352986 -1.3962634 -1.30899694 -1.22173048 -1.13446401 -1.04719755 -0.95993109 -0.87266463 -0.78539816
-0.6981317 -0.61086524 -0.52359878 -0.43633231 -0.34906585 -0.26179939 -0.17453293 -0.08726646 0 0.08726646 0.17453293
0.26179939 0.34906585 0.43633231 0.52359878 0.61086524 0.6981317 0.78539816 0.87266463 0.95993109 1.04719755
1.13446401 1.22173048 1.30899694 1.3962634 1.48352986 1.57079633 1.65806279 1.74532925 1.83259571 1.91986218
2.00712864 2.0943951 2.18166156 2.26892803 2.35619449 2.44346095 2.53072742 2.61799388 2.70526034 2.7925268
2.87979327 2.96705973 3.05432619 3.14159265];
Element_theta_deg = Element_theta * 180 / pi;   % observation angle (degrees)

theta_deg = 0 : 1 : 180;            % observation angle (degrees) [specify range & resolution]
theta = theta_deg * pi / 180;       % observation angle (radians)
cos_theta = cos(theta);             % pre-compute cos(theta) to save time later.

% Interpolate element pattern to new set of thetas
Element = interp1( Element_theta_deg, ElementPattern, theta_deg );
```

```
small_num = 1e-11;                  %  to prevent divide by zero problem
d = 0.5;                            % distance between elements
N = 10;                             % number of elements
phase_step_deg = 360 / (2 ^ 50);    % number of steps (degrees) for digitized phase-shifter (phase_step_deg = 360 / 2^#bits)
phase_step = phase_step_deg * pi/180;  % number of steps (radians) for digitized phase-shifter
beta_deg = 0;                       % phase shift between elements (degrees)
beta = beta_deg * pi/180;           % phase shift between elements (radians)
DigitizedPhase = 0;                 % true = digitize the phase of each element with the number of bits specified
PolarPlot = 0;                      % true = display polar plot; false = display cartesian plot
dBPlot = 0;                         % true = plot in dB
NormalizePlot = 0;                  % true = normalize data for the plot
AmpSelect = 1;                      % uniform amplitude distribution
AFSelect = 1;                       % display array factor only
SidelobeLeveldB = 0;                % Sidelobe Level of 0 dB
compute_amps(hObject, eventdata, handles);
plot_data(hObject, eventdata, handles);
guidata(hObject, handles);  % updates the handles structure


% --- Outputs from this function are returned to the command line.
function varargout = AFGUI_ud_na_element_bit_OutputFcn(hObject, eventdata, handles)
% varargout  cell array for returning output args (see VARARGOUT);
% hObject    handle to figure
% eventdata  reserved - to be defined in a future version of MATLAB
% handles    structure with handles and user data (see GUIDATA)

% Get default command line output from handles structure
varargout{1} = handles.output;


% --- Executes on slider movement.
function sliderBeta_Callback(hObject, eventdata, handles)
% hObject    handle to sliderBeta (see GCBO)
% eventdata  reserved - to be defined in a future version of MATLAB
% handles    structure with handles and user data (see GUIDATA)

% Hints: get(hObject,'Value') returns position of slider
%        get(hObject,'Min') and get(hObject,'Max') to determine range of slider
global beta beta_deg N phase_step d DigitizedPhase PolarPlot dBPlot NormalizePlot theta theta_deg cos_theta Element small_num
       amp AmpSelect AFSelect SidelobeLeveldB NormalizeF
beta_deg = get(hObject,'Value');
beta = beta_deg * pi/180;
beta_string = num2str(beta_deg);

% need to convert the answer into String type to display it
set(handles.display_beta,'String',beta_string);
plot_data(hObject, eventdata, handles);

guidata(hObject, handles);  % updates the handles structure


% --- Executes during object creation, after setting all properties.
function sliderBeta_CreateFcn(hObject, eventdata, handles)
% hObject    handle to sliderBeta (see GCBO)
% eventdata  reserved - to be defined in a future version of MATLAB
% handles    empty - handles not created until after all CreateFcns called

% Hint: slider controls usually have a light gray background.
if isequal(get(hObject,'BackgroundColor'), get(0,'defaultUicontrolBackgroundColor'))
   set(hObject,'BackgroundColor',[.9 .9 .9]);
end
```

```
function editSL_Callback(hObject, eventdata, handles)
% hObject    handle to editSL (see GCBO)
% eventdata  reserved - to be defined in a future version of MATLAB
% handles    structure with handles and user data (see GUIDATA)

% Hints: get(hObject,'String') returns contents of editSL as text
%        str2double(get(hObject,'String')) returns contents of editSL as a double
global beta beta_deg N phase_step d DigitizedPhase PolarPlot dBPlot NormalizePlot theta theta_deg cos_theta Element small_num
       amp AmpSelect AFSelect SidelobeLeveldB NormalizeF
SidelobeLeveldB = str2double(get(hObject,'String'));
compute_amps(hObject, eventdata, handles);
if NormalizePlot
   compute_normalize(hObject, eventdata, handles);
end
plot_data(hObject, eventdata, handles);
guidata(hObject, handles);  % updates the handles structure


% --- Executes during object creation, after setting all properties.
function editSL_CreateFcn(hObject, eventdata, handles)
% hObject    handle to editSL (see GCBO)
% eventdata  reserved - to be defined in a future version of MATLAB
% handles    empty - handles not created until after all CreateFcns called

% Hint: edit controls usually have a white background on Windows.
%       See ISPC and COMPUTER.
if ispc && isequal(get(hObject,'BackgroundColor'), get(0,'defaultUicontrolBackgroundColor'))
   set(hObject,'BackgroundColor','white');
end


function editN_Callback(hObject, eventdata, handles)
% hObject    handle to editN (see GCBO)
% eventdata  reserved - to be defined in a future version of MATLAB
% handles    structure with handles and user data (see GUIDATA)

% Hints: get(hObject,'String') returns contents of editN as text
%        str2double(get(hObject,'String')) returns contents of editN as a double
global beta beta_deg N phase_step d DigitizedPhase PolarPlot dBPlot NormalizePlot theta theta_deg cos_theta Element small_num
       amp AmpSelect AFSelect SidelobeLeveldB NormalizeF
N = str2double(get(hObject,'String'));
compute_amps(hObject, eventdata, handles);
if NormalizePlot
   compute_normalize(hObject, eventdata, handles);
end
plot_data(hObject, eventdata, handles);
guidata(hObject, handles);  % updates the handles structure


% --- Executes during object creation, after setting all properties.
function editN_CreateFcn(hObject, eventdata, handles)
% hObject    handle to editN (see GCBO)
% eventdata  reserved - to be defined in a future version of MATLAB
% handles    empty - handles not created until after all CreateFcns called

% Hint: edit controls usually have a white background on Windows.
%       See ISPC and COMPUTER.
if ispc && isequal(get(hObject,'BackgroundColor'), get(0,'defaultUicontrolBackgroundColor'))
   set(hObject,'BackgroundColor','white');
end
```

```
function editd_Callback(hObject, eventdata, handles)
% hObject    handle to editd (see GCBO)
% eventdata  reserved - to be defined in a future version of MATLAB
% handles    structure with handles and user data (see GUIDATA)

% Hints: get(hObject,'String') returns contents of editd as text
%        str2double(get(hObject,'String')) returns contents of editd as a double
global beta beta_deg N phase_step d DigitizedPhase PolarPlot dBPlot NormalizePlot theta theta_deg cos_theta Element small_num
       amp AmpSelect AFSelect SidelobeLeveldB NormalizeF
d = str2double(get(hObject,'String'));
if NormalizePlot
   compute_normalize(hObject, eventdata, handles);
end
plot_data(hObject, eventdata, handles);
guidata(hObject, handles);  % updates the handles structure


% --- Executes during object creation, after setting all properties.
function editd_CreateFcn(hObject, eventdata, handles)
% hObject    handle to editd (see GCBO)
% eventdata  reserved - to be defined in a future version of MATLAB
% handles    empty - handles not created until after all CreateFcns called

% Hint: edit controls usually have a white background on Windows.
%       See ISPC and COMPUTER.
if ispc && isequal(get(hObject,'BackgroundColor'), get(0,'defaultUicontrolBackgroundColor'))
   set(hObject,'BackgroundColor','white');
end


function editbits_Callback(hObject, eventdata, handles)
% hObject    handle to editbits (see GCBO)
% eventdata  reserved - to be defined in a future version of MATLAB
% handles    structure with handles and user data (see GUIDATA)

% Hints: get(hObject,'String') returns contents of editbits as text
%        str2double(get(hObject,'String')) returns contents of editbits as a double
global beta beta_deg N phase_step d DigitizedPhase PolarPlot dBPlot NormalizePlot theta theta_deg cos_theta Element small_num
       amp AmpSelect AFSelect SidelobeLeveldB NormalizeF
phase_step_deg = 360 / (2 ^ str2double(get(hObject,'String')));      % number of steps (degrees) for digitized phase-shifter
                                                                     % (phase_step_deg = 360 / 2^#bits)
phase_step = phase_step_deg * pi/180;                                % number of steps (radians) for digitized phase-shifter
if NormalizePlot
   compute_normalize(hObject, eventdata, handles);
end
plot_data(hObject, eventdata, handles);
guidata(hObject, handles);  % updates the handles structure


% --- Executes during object creation, after setting all properties.
function editbits_CreateFcn(hObject, eventdata, handles)
% hObject    handle to editbits (see GCBO)
% eventdata  reserved - to be defined in a future version of MATLAB
% handles    empty - handles not created until after all CreateFcns called

% Hint: edit controls usually have a white background on Windows.
%       See ISPC and COMPUTER.
if ispc && isequal(get(hObject,'BackgroundColor'), get(0,'defaultUicontrolBackgroundColor'))
   set(hObject,'BackgroundColor','white');
end
```

```
% --- Executes on button press in checkboxDigitized.
function checkboxDigitized_Callback(hObject, eventdata, handles)
% hObject    handle to checkboxDigitized (see GCBO)
% eventdata  reserved - to be defined in a future version of MATLAB
% handles    structure with handles and user data (see GUIDATA)

% Hint: get(hObject,'Value') returns toggle state of checkboxDigitized
global beta beta_deg N phase_step d DigitizedPhase PolarPlot dBPlot NormalizePlot theta theta_deg cos_theta Element small_num
       amp AmpSelect AFSelect SidelobeLeveldB NormalizeF
DigitizedPhase = get(hObject,'Value');
if NormalizePlot
   compute_normalize(hObject, eventdata, handles);
end
plot_data(hObject, eventdata, handles);
guidata(hObject, handles);  % updates the handles structure


% --- Executes on button press in checkboxPolar.
function checkboxPolar_Callback(hObject, eventdata, handles)
% hObject    handle to checkboxPolar (see GCBO)
% eventdata  reserved - to be defined in a future version of MATLAB
% handles    structure with handles and user data (see GUIDATA)

% Hint: get(hObject,'Value') returns toggle state of checkboxPolar
global beta beta_deg N phase_step d DigitizedPhase PolarPlot dBPlot NormalizePlot theta theta_deg cos_theta Element small_num
       amp AmpSelect AFSelect SidelobeLeveldB NormalizeF
PolarPlot = get(hObject,'Value');
plot_data(hObject, eventdata, handles);
guidata(hObject, handles);  % updates the handles structure


% --- Executes on button press in checkboxdB.
function checkboxdB_Callback(hObject, eventdata, handles)
% hObject    handle to checkboxdB (see GCBO)
% eventdata  reserved - to be defined in a future version of MATLAB
% handles    structure with handles and user data (see GUIDATA)

% Hint: get(hObject,'Value') returns toggle state of checkboxdB
global beta beta_deg N phase_step d DigitizedPhase PolarPlot dBPlot NormalizePlot theta theta_deg cos_theta Element small_num
       amp AmpSelect AFSelect SidelobeLeveldB NormalizeF
dBPlot = get(hObject,'Value');
plot_data(hObject, eventdata, handles);
guidata(hObject, handles);  % updates the handles structure


% --- Executes on button press in checkboxNormalize.
function checkboxNormalize_Callback(hObject, eventdata, handles)
% hObject    handle to checkboxNormalize (see GCBO)
% eventdata  reserved - to be defined in a future version of MATLAB
% handles    structure with handles and user data (see GUIDATA)

% Hint: get(hObject,'Value') returns toggle state of checkboxNormalize
global beta beta_deg N phase_step d DigitizedPhase PolarPlot dBPlot NormalizePlot theta theta_deg cos_theta Element small_num
       amp AmpSelect AFSelect SidelobeLeveldB NormalizeF
NormalizePlot = get(hObject,'Value');
if NormalizePlot
   compute_normalize(hObject, eventdata, handles);
end
plot_data(hObject, eventdata, handles);
guidata(hObject, handles);  % updates the handles structure
```

```
% --- Executes on button press in AmpSelect_buttongroup
function AmpSelect_buttongroup_SelectionChangeFcn(hObject, eventdata)

global beta beta_deg N phase_step d DigitizedPhase PolarPlot dBPlot NormalizePlot theta theta_deg cos_theta Element small_num
        amp AmpSelect AFSelect SidelobeLeveldB NormalizeF

% retrieve GUI data, i.e. the handles structure
handles = guidata(hObject);

switch get(eventdata.NewValue,'Tag')   % Get Tag of selected object
   case 'radiobuttonUniform'
     % execute this code when radiobuttonUniform is selected
     AmpSelect = 1;  % Uniform

   case 'radiobuttonBinomial'
     % execute this code when radiobuttonBinomial is selected
     AmpSelect = 2;  % Binomial

   otherwise % 'radiobuttonDolph'
     % execute this code when radiobuttonDolph is selected
     AmpSelect = 3;  % Dolph-Tschebyscheff
end

compute_amps(hObject, eventdata, handles);
if NormalizePlot
   compute_normalize(hObject, eventdata, handles);
end
plot_data(hObject, eventdata, handles);

guidata(hObject, handles);  % updates the handles structure


% --- Executes on button press in AFSelect_buttongroup
function AFSelect_buttongroup_SelectionChangeFcn(hObject, eventdata)

global beta beta_deg N phase_step d DigitizedPhase PolarPlot dBPlot NormalizePlot theta theta_deg cos_theta Element small_num
        amp AmpSelect AFSelect SidelobeLeveldB NormalizeF

% retrieve GUI data, i.e. the handles structure
handles = guidata(hObject);

switch get(eventdata.NewValue,'Tag')   % Get Tag of selected object
   case 'radiobuttonArrayFactor'
     % execute this code when radiobuttonArrayFactor is selected
     AFSelect = 1;  % Display only Array Factor

   case 'radiobuttonElementPattern'
     % execute this code when radiobuttonElementPattern is selected
     AFSelect = 2;  % Display only Element Pattern

   otherwise  % 'radiobuttonBoth'
     % execute this code when radiobuttonBoth is selected
     AFSelect = 3;  % Display both the Array Factor and the Element Pattern
end

plot_data(hObject, eventdata, handles);

guidata(hObject, handles);  % updates the handles structure
```

```
% --- Compute Amplitudes
function compute_amps(hObject, eventdata, handles)

global beta beta_deg N phase_step d DigitizedPhase PolarPlot dBPlot NormalizePlot theta theta_deg cos_theta Element small_num
        amp AmpSelect AFSelect SidelobeLeveldB NormalizeF

% axes(handles.axes1)

switch AmpSelect
   case 2  % Binomial
      P_mat = pascal(N);  % create Pascal's Matrix
      amp = (P_mat( N : N-1 : (N-1)*N+1 ))';  % create row N
   case 3  % Dolph-Tschebyscheff
      amp = chebwin(N,SidelobeLeveldB);
   otherwise  % case 1 - Uniform
      amp = ones(N,1);
end

guidata(hObject, handles);  % updates the handles structure


% --- Compute Normalizing Factor
function compute_normalize(hObject, eventdata, handles)

global beta beta_deg N phase_step d DigitizedPhase PolarPlot dBPlot NormalizePlot theta theta_deg cos_theta Element small_num
        amp AmpSelect AFSelect SidelobeLeveldB NormalizeF

% maximum should be at broadside for beta=0;
theta_n = pi/2;
beta_n = 0;

psi = 2*pi * d * cos(theta_n) + beta_n;
NormalizeF = 0;
for n = 1 : N
   NormalizeF = NormalizeF + amp(n)*exp(j*(n-1)*psi);
end

NormalizeF = abs(NormalizeF);

guidata(hObject, handles);  % updates the handles structure


% --- Plot the data
function plot_data(hObject, eventdata, handles)

global beta beta_deg N phase_step d DigitizedPhase PolarPlot dBPlot NormalizePlot theta theta_deg cos_theta Element small_num
        amp AmpSelect AFSelect SidelobeLeveldB NormalizeF

axes(handles.axes1)


% Calculate AF
AF = zeros( 1 , size(theta,2) );     % initialize & reserve memory for AF
pi_d_2 = 2 * pi * d;                 % precompute to save time
if  DigitizedPhase                   % digitize the phase shift of each element
   for k = 1 : size(theta,2)
      psi_beta = pi_d_2 * cos_theta(k);  % psi - beta
      for n = 1 : N
         el_shift = (n-1)*beta;  % phase shift for individual element
         dig_el_shift = round(el_shift / phase_step) * phase_step;  % digitized phase shift for individual element
         AF(k) = AF(k) + amp(n) * exp( j*((n-1)*psi_beta + dig_el_shift) );
```

```
        end
    end
else  % the phase-shifter is continuous
    for k = 1 : size(theta,2)
        psi = pi_d_2 * cos_theta(k) + beta;
        for n = 1 : N
            AF(k) = AF(k) + amp(n)*exp(j*(n-1)*psi);
        end
    end
end
AF = abs(AF);  % take magnitude of complex array factor

% Normalize AF (if required)
if NormalizePlot  % normalize the array factor
    AF = AF ./ NormalizeF;
end

% Multiply AF by Element Pattern if required
switch AFSelect
    case 2  % display only element pattern
        AF = Element;
    case 3  % display array factor and element pattern
        AF = AF .* Element;
end

% Convert AF to dB (if required)
if dBPlot  % plot in dB
    AF = 20*log10(AF);
end

% Plot AF
if PolarPlot  % plot in polar coordinates
    if dBPlot
        if NormalizePlot
            dBshift = 40;               % all data below -dBshift will be set to dBshift
            AF = AF + dBshift;          % shift AF to positive values
            AF = (AF>0) .* AF;          % set negative AF values to 0
        else  % plot is not normalized
            dBshift = min(AF);
            AF = AF - dBshift;          % shift negative dB values for polar plot
        end
    end
    polar(theta,AF);
else  % plot in rectangular coordinates
    plot(theta_deg,AF);
    xlabel('angle (deg)');
    if dBPlot
        if (AFSelect == 1)
            ylabel('Array Factor (dB)');
        elseif (AFSelect == 2)
            ylabel('Element Pattern (dB)');
        else
            ylabel('Array Pattern (dB)');
        end
    else
        if (AFSelect == 1)
            ylabel('Array Factor');
        elseif (AFSelect == 2)
            ylabel('Element Pattern');
        else
            ylabel('Array Pattern');
        end
    end
    set(gca,'XTick',0:30:180)  % set tick marks to 30 deg increments
```

```
    if NormalizePlot
        if dBPlot
            axis([0  180  -40  0])
        else
            axis([0  180  0  1])
        end
    end
end

guidata(hObject, handles);  % updates the handles structure
```

APPENDIX B

LABVIEW PHASE-SHIFTER CONTROLLER

1. PhaseToBinary.vi

This LabVIEW virtual instrument converts a phase shift (in degrees) into a 4-bit number which will control a 4-bit phase-shifter.

Figure B.1. PhaseToBinary.vi icon.

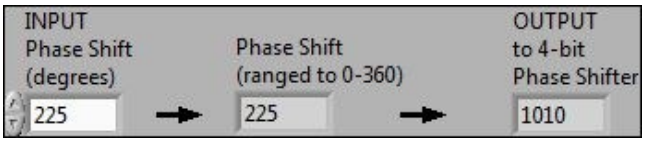

Figure B.2. PhaseToBinary.vi front panel.

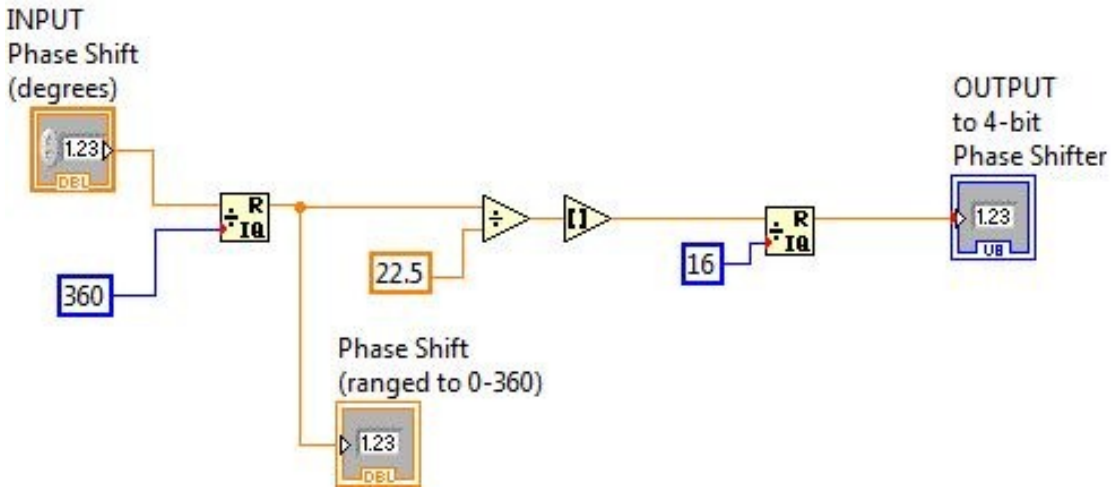

Figure B.3. PhaseToBinary.vi diagram.

2. PhaseToBinaryDB.vi

This LabVIEW virtual instrument converts two phase shifts (in degrees) into an 8-bit number which will control two 4-bit phase-shifters. "Phase Shift 1" will be the LSBs. PhaseToBinary.vi is used in the implementation.

Figure B.4. PhaseToBinaryDB.vi icon.

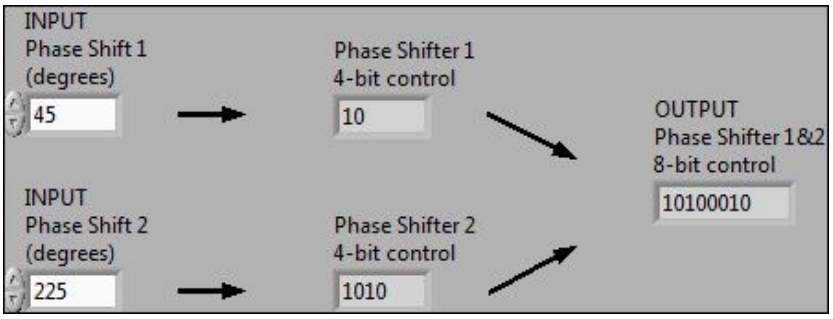

Figure B.5. PhaseToBinaryDB.vi front panel.

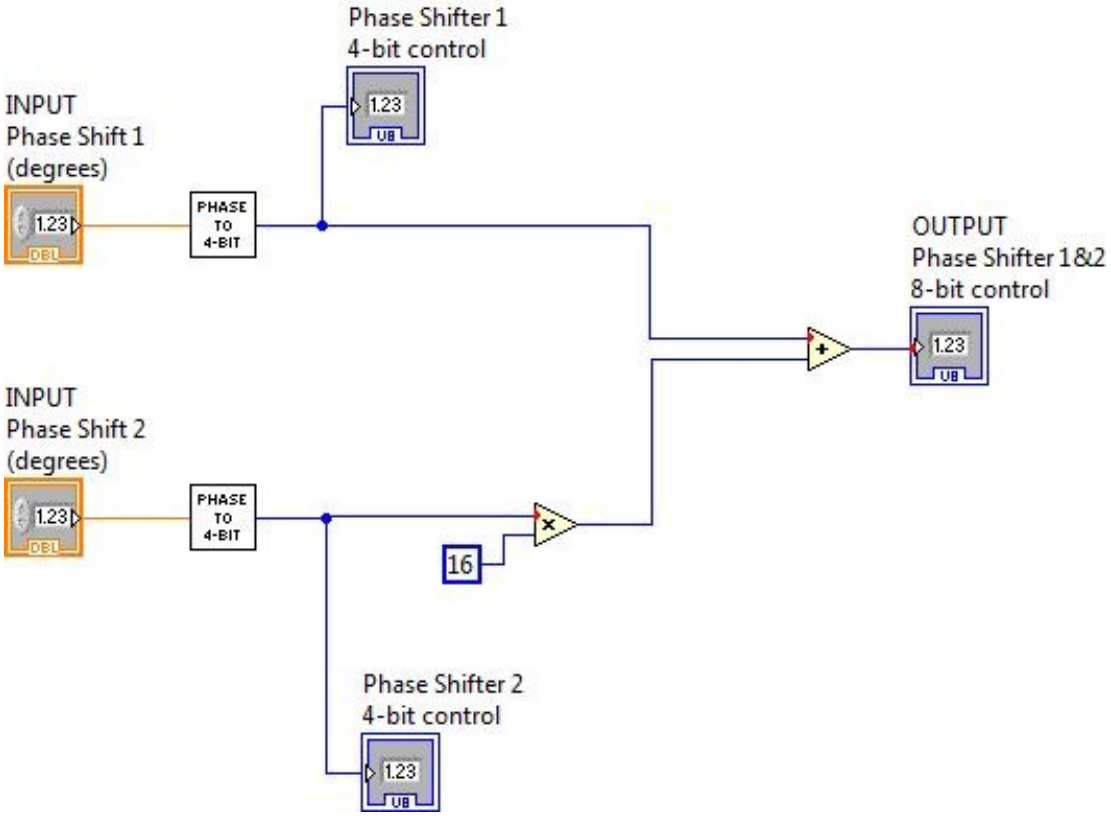

Figure B.6. PhaseToBinaryDB.vi diagram.

3. 4_ElementControl.vi

This LabVIEW virtual instrument controls four 4-bit phase-shifters. Phase-shifters 1 & 2 are on one port, and phase-shifters 3 & 4 are on another. Phase-shifter 1 & 3 are the LSBs of their respective ports, and phase-shifters 2 & 4 are the MSBs of their respective ports. PhaseToBinaryDB.vi is used in the implementation.

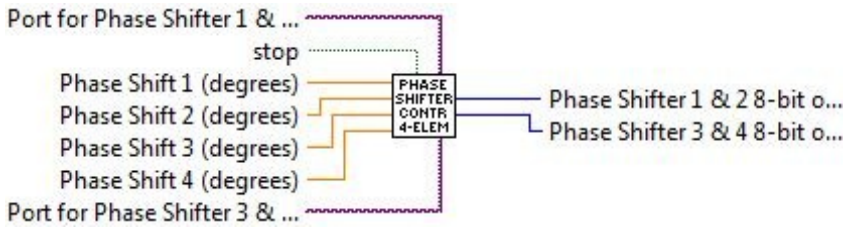

Figure B.7. 4_ElementControl.vi icon.

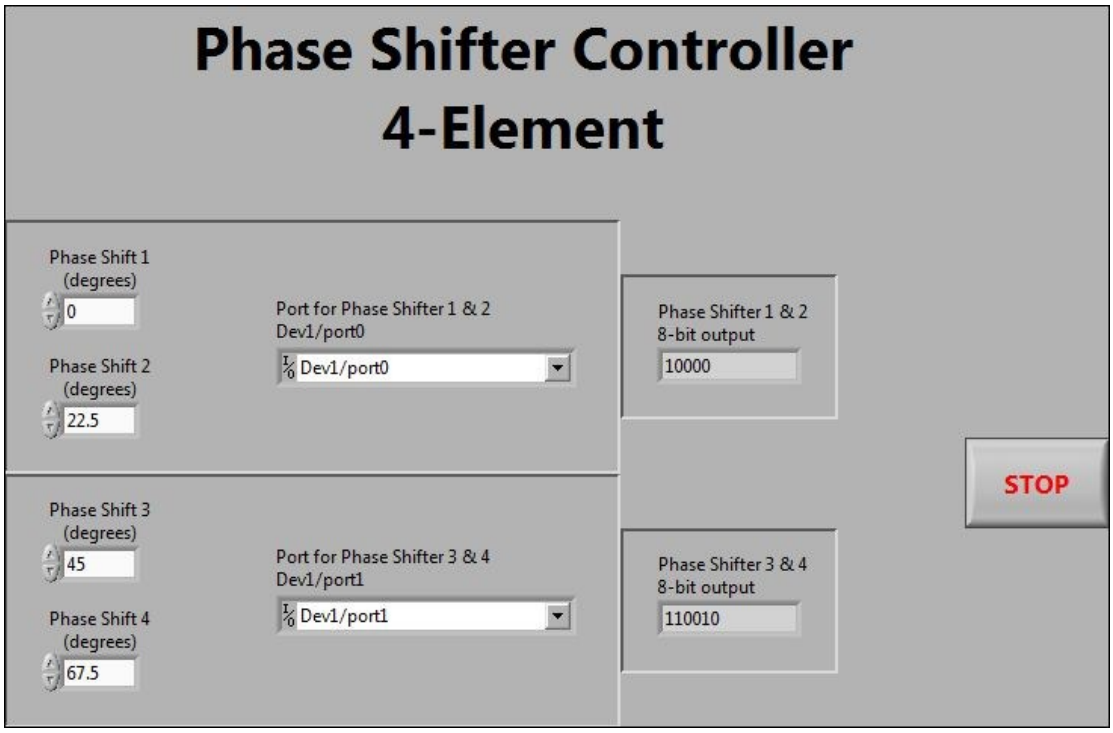

Figure B.8. 4_ElementControl.vi front panel.

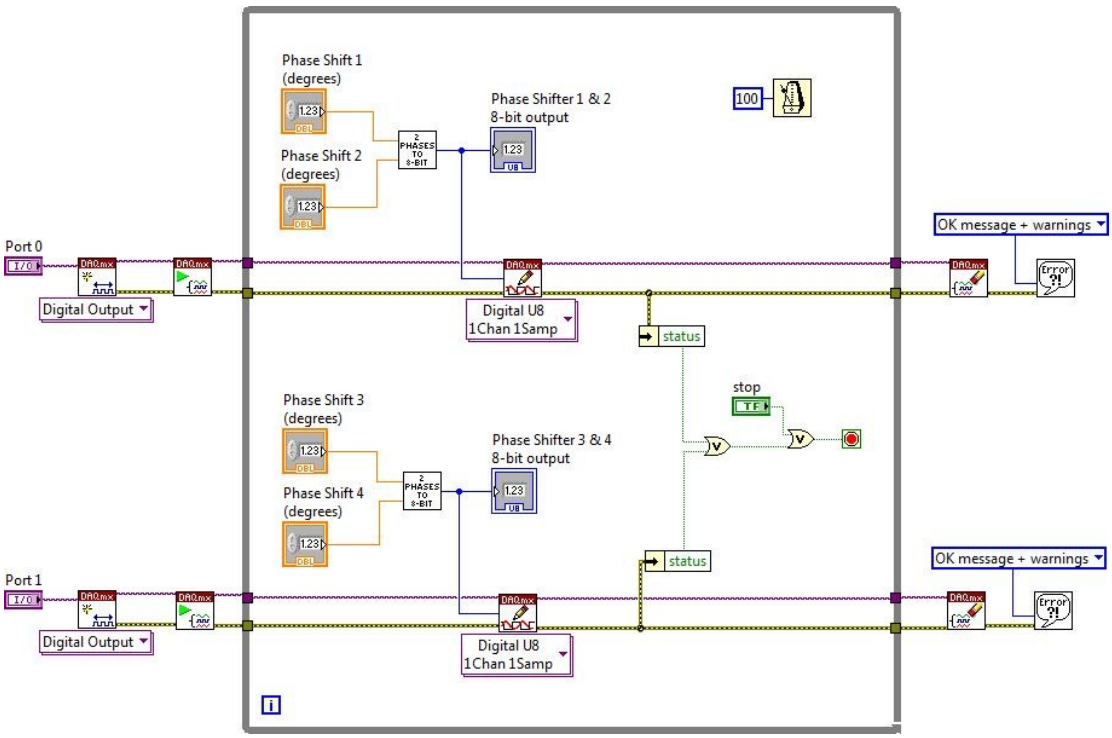

Figure B.9. 4_ElementControl.vi diagram.

APPENDIX C

MATLAB PHASE FINDER

This appendix presents a Matlab program which can be used to find the optimum phase-shifter settings from a calibration table to minimize phase quantization error.

```
% find_phases.m
% Jonathan Hansen
%
% For a list of 4 phase-shifters with 16 phase settings each, find the
% values of each shifter for the desired phase front that will minimize the
% error from the ideal values.

clear all   % removes all variables, globals, functions and MEX links.
clc         % clear the command window


%%%%%  Begin Settings  %%%%%%%%%%%%%%%%%%%%%%%%%%%%%%%%%%%%%%%%%%%%%%%%%%%%%%%%%%%

% MeasPhase is the measured phase for each setting of each phase-shifter
% rows 1-4 are phase-shifters 1-4
% columns 1-16 are the phase settings for each phase-shifter
MeasPhase = zeros( 4, 16 );  % initialize & reserve memory for MeasPhase
MeasPhase(1,:) = [-100 -82 -59 -45 -28 -14 1 19 36 51 71 88 117 145 174 -151];
MeasPhase(2,:) = [39 54 76 96 129 157 -175 -145 -96 -80 -58 -43 -26 -11 5 24];
MeasPhase(3,:) = [38 52 72 90 115 139 163 -163 -104 -85 -57 -40 -23 -10 5 23];
MeasPhase(4,:) = [38 52 71 89 117 142 172 -153 -96 -79 -55 -40 -22 -10 6 24];

% PhaseSetNames contains the name of each phase setting #1-16
PhaseSetNames = 0 : 22.5 : 337.5;

% ideal angle increase for each phase-shifter
IdealShift = -180*sind(40)

% number of best matches to save
NumOptions = 5;

% number of iterations to test for good matches
num_it = 720;

%%%%%  End Settings  %%%%%%%%%%%%%%%%%%%%%%%%%%%%%%%%%%%%%%%%%%%%%%%%%%%%%%%%%%%%
```

```
% vector of best sum of squares errors (each row is the error for a different set)
% best match is at index 1
BestError_ss = 1e50*ones(NumOptions,1);

% matrix of best setting values
% (each row is a set of settings) (each column is a different set)
% best match is at index 1
BestSettings = ones(NumOptions,4);

% i is the ideal phase shift of the first shifter
for i=0:360/num_it:360-360/num_it;  % cycle through 360 degrees

   % ideal phase settings for each phase-shifter #1-4
   if IdealShift == 0
      IdealPhase = [i i i i];
   else
      IdealPhase = i : IdealShift : i+(3*IdealShift);
   end

   for k=1:4            % cycle through each shifter
      for kk=1:16     % cycle through each setting
         % array of differences between the ideal phase & each measured phase for each phase setting
         sub_ang_array(kk) = abs((sub_ang(IdealPhase(k),MeasPhase(k,kk))));
      end
      [error(k),index(k)] = min(sub_ang_array);  % find best phase setting for this try (iteration i)
   end
   error_ss = sum(error.^2);  % sum of squares error over all 4 phase-shifters for this try (iteration i)

   if (error_ss<BestError_ss(NumOptions))  % if this try is better than the last setting in the list
      if sum(ismember(BestSettings,index,'rows'))  % if duplicate setting
         ind = find(ismember(BestSettings,index,'rows'),1);  % index of duplicate setting
         if BestError_ss(ind) > error_ss   % if new error for setting is better than stored error for same setting
            BestError_ss(ind) = error_ss; % store better error
            %  Sort modified setting
            j = ind;
            while (j>1) && (BestError_ss(j) < BestError_ss(j-1))
               [BestError_ss(j) BestError_ss(j-1)] = deal(BestError_ss(j-1),BestError_ss(j));       % swap j & (j-1)
               [BestSettings(j,:) BestSettings(j-1,:)] = deal(BestSettings(j-1,:),BestSettings(j,:));  % swap j & (j-1)
               j = j-1;
            end
         end
      else  % not a duplicate setting
         BestSettings(NumOptions,:) = index;       % replace last stored setting with new one
         BestError_ss(NumOptions) = error_ss;      % replace last stored setting with new one
         % Sort new setting
         j = NumOptions;
         while (j>1) && (BestError_ss(j) < BestError_ss(j-1))
            [BestError_ss(j) BestError_ss(j-1)] = deal(BestError_ss(j-1),BestError_ss(j));      %  swap j & (j-1)
            [BestSettings(j,:) BestSettings(j-1,:)] = deal(BestSettings(j-1,:),BestSettings(j,:)); %  swap j & (j-1)
            j = j-1;
         end
      end
   end

end
```

```
%%%%%  Begin Output  %%%%%%%%%%%%%%%%%%%%%%%%%%%%%%%%%%%%%%%%%%%%

% vector of sum of squares error for each found setting
BestError_ss

% BestSettings array with setting values replaced by setting names
BestSettingsNames = PhaseSetNames(BestSettings)

%%%%%  End Output  %%%%%%%%%%%%%%%%%%%%%%%%%%%%%%%%%%%%%%%%%%%%%
```

APPENDIX D

MATLAB DIODE MODELING (C_j POLYNOMIAL FIT)

This appendix presents a Matlab program used for diode modeling to fit a polynomial to data points for C_j.

```
% Fit_Cj_Poly.m
% Jonathan Hansen
% fit a polynomial for Cj vs Vj to data points

clear all   % removes all variables, globals, functions and MEX links.
clc         % clear the command window
hold off   % clears the current plot when a new plot is made

% define (Vj,Cj) data points
Vj = [-5, -3, -1, 0, 0.2, 0.4, 0.5895, 0.6477, 0.7026, 0.7249, 0.7333, 0.7430, 0.7502, 0.7561, 0.7632, 0.7695];
Cj = [3.6728e-15, 6.1213e-15, 1.2243e-14, 1.8364e-14, 2.0813e-14, 2.8158e-14, 3.9177e-14, 5.6316e-14, 7.4680e-14,
      1.0774e-13, 1.6528e-13, 3.4280e-13, 5.6316e-13, 7.5905e-13, 8.9372e-13, 1.0651e-12];

Vj = Vj';  % must be column vector for fit
Cj = Cj';  % must be column vector for fit

% fit a curve to the data using linear interpolation between data points
fitobject1 = fit(Vj,Cj,'linearinterp')  % linear interpolation

% plot raw data
plot(Vj,Cj,'o')
hold on  % holds the current plot

% create data points from the linear interpolated curve (fitobject1)
x = -5:0.0001:0.75;
y = feval(fitobject1,x)';

% create a polynomial from the linear interpolated curve data
P20 = polyfit(x,y,20);  % 20 degree polynomial
P25 = polyfit(x,y,25);  % 25 degree polynomial

% plot fit polynomials
xx = (-5: 0.001: 0.9)';    % x data for plotting
f20 = polyval(P20,xx);  % create vector data of fit polynomial
f25 = polyval(P25,xx);  % create vector data of fit polynomial
plot(xx,f20,'r')
plot(xx,f25,'b')
axis([-5  0.9  0  0.2e-11])
```

APPENDIX E

MATLAB DIODE MODELING (C_j EXPONENTIAL FIT)

This appendix presents a Matlab program used for diode modeling to fit an exponential equation to data points for C_j. The function Cjerror.m is called from Fit_Cj_Exp.m to calculate the sum of squares error for a given set of parameters.

```
% Fit_Cj_Exp.m
% Jonathan Hansen
% fit an exponential curve for Cj vs Vj to data points
%
% Cr(v) = Co * sqrt(Vo/(Vo-v))                              , v < alpha*Vo
% Cf(v) = Cr(alpha*Vo) + Cr'(alpha*Vo) * (v-alpha*Vo)   , v > alpha*Vo
%
% adjust Co, alpha, & Vo for least squares error between equation & data

clear all   % removes all variables, globals, functions and MEX links.
clc         % clear the command window

% define (Vj,Cj) data points
Vj = [-5, -3, -1, 0, 0.2, 0.4, 0.5895, 0.6477, 0.7026, 0.7249, 0.7333, 0.7430, 0.7502, 0.7561, 0.7632, 0.7695];
Cj = [3.6728e-15, 6.1213e-15, 1.2243e-14, 1.8364e-14, 2.0813e-14, 2.8158e-14, 3.9177e-14, 5.6316e-14, 7.4680e-14,
      1.0774e-13, 1.6528e-13, 3.4280e-13, 5.6316e-13, 7.5905e-13, 8.9372e-13, 1.0651e-12];

% define parameters for fminsearch
MaxFunEvals = 100000;   % Maximum number of function evals allowed (default = 200*numberofvariables = 600)
MaxIter     = 100000;   % Maximum number of iterations allowed (default = 200*numberofvariables = 600)
TolX        = 1e-15;    % Termination tolerance on x (default = 1e-4)
TolFun      = 1e-15;    % Termination tolerance on the function value  (default = 1e-4)

% initial values for parameters
Co = 1.452e-14;
Co = Co * 1e14;  % scale Co by 1e-14 (works better for fminsearch)
Vo = 0.7214;
alpha = 0.9907;

% set options for fminsearch
options = optimset('MaxFunEvals', MaxFunEvals, 'MaxIter', MaxIter, 'TolX', TolX, 'TolFun', TolFun);

% search for minimized Cj error as defined in Cjerror
[x,fval,exitflag,output] = fminsearch('Cjerror',[Co,Vo,alpha],options);
CO    = x(1) * 1e-14  % Co needs to be scaled back to correct value
VO    = x(2)
ALPHA = x(3)
fval        % sum of squares error
exitflag    % 1 = converged, 0 = max iter reached, -1 = term by output func
output      % summary
```

```
% plot best fit curve & raw data
x = -5 : 0.001 : ALPHA*VO;     % x for reverse bias
xx = ALPHA*VO : 0.001: 0.9;   % x for forward bias
Cr = CO .* sqrt(VO./(VO-x));
diff_Cr = 0.5*CO/VO*(1-ALPHA)^(-3/2);   % derivative of Cr
Cf = CO*sqrt(VO/(VO-VO*ALPHA)) + diff_Cr * (xx-ALPHA*VO);
plot(Vj,Cj,'o', x,Cr,'m', xx,Cf,'g');
axis([0  1  0  1.8e-12])


%%%%%%%%%%%%%%%%%%%%%%%%%%%%%%%%%%%%%%%%%%%%%%%%%%%%%%%%%%%%%%%%%%%%%%%%%%%%%%%


function error = Cjerror(x)
% Jonathan Hansen
% calculates the sum of squares error between measured data and a function
%
% Cr(v) = Co * sqrt(Vo/(Vo-v))                                  , v < alpha*Vo
% Cf(v) = Cr(alpha*Vo) + Cr'(alpha*Vo) * (v-alpha*Vo)   , v > alpha*Vo

% extract function parameters from input variable
Co = x(1);
Vo = x(2);
alpha = x(3);

% raw data
Vj = [-5, -3, -1, 0, 0.2, 0.4, 0.5895, 0.6477, 0.7026, 0.7249, 0.7333, 0.7430, 0.7502, 0.7561, 0.7632, 0.7695];
Cj = [3.6728e-15, 6.1213e-15, 1.2243e-14, 1.8364e-14, 2.0813e-14, 2.8158e-14, 3.9177e-14, 5.6316e-14, 7.4680e-14,
      1.0774e-13, 1.6528e-13, 3.4280e-13, 5.6316e-13, 7.5905e-13, 8.9372e-13, 1.0651e-12];

xdata = Vj;
ydata = Cj * 1e14;   % scale Cj by 1e14

% large error for unacceptable input values
LARGE_ERROR = 1e50;

if (alpha >=1 || Co <= 0 || Vo <=0)  % unacceptable values
   error = LARGE_ERROR;
else
   Cr_at_Vo_alpha = Co * sqrt( 1 / (1-alpha) );  % Cr(Vo*alpha)
   Vo_alpha = Vo * alpha;

   error = 0;  % initialize sum of squares error
   for k = 1 : size(xdata,2)
      if xdata(k) < Vo_alpha  % reverse bias
         Cr = Co * sqrt( Vo / (Vo-xdata(k)) );
         error = error + (Cr-ydata(k))^2;
      else  % forward bias
         diff_Cr = 0.5*Co/Vo*(1-alpha)^(-3/2);  % derivative of Cr
         Cf = Cr_at_Vo_alpha + diff_Cr * (xdata(k)-Vo_alpha);
         error = error + (Cf-ydata(k))^2;
      end
   end
end
```

VITA

Jonathan Noel Hansen received his Bachelor of Science degree in electrical engineering from Texas A&M University, College Station, TX in 2001 where he graduated *summa cum laude*. He then received his Ph.D degree in electrical engineering from Texas A&M University in 2011.

From 2001 to 2008, he was with Lockheed Martin Aeronautics, Fort Worth, TX, where he supported avionics software design, implementation, and validation for F-35 sensor fusion. He also provided research and development expertise for revolutionary technology, internal projects.

Mr. Hansen may be reached at the Department of Electrical and Computer Engineering, Texas A&M University, 214 Zachry Engineering Center, College Station, Texas 77843-3128. His email is JonHansen98@gmail.com.